

106-901

RESEARCH PROGRAMME ON  
MAGNETOPLASMDYNAMIC POWER GENERATION  
Contracts N62558-3127 and N62558-4180

FINAL TECHNICAL SUMMARY REPORT

1 April 1964 to 31 July 1964

Advanced Research Projects Agency  
Order No. 209-62, Amendment Nos. 2 and 6  
Contract period : 1 December 1961 to  
31 July 1964  
Contract amount : \$382,500  
Contractor : International Research  
and Development Co Ltd  
Principal Investigator : Dr. B.C. Lindley

International Research and Development Co Ltd  
Newcastle upon Tyne 6  
England

REPRODUCTION IN WHOLE OR IN PART IS PERMITTED  
FOR ANY PURPOSE OF THE UNITED STATES GOVERNMENT

# DISCLAIMER NOTICE

THIS DOCUMENT IS THE BEST  
QUALITY AVAILABLE.

COPY FURNISHED CONTAINED  
A SIGNIFICANT NUMBER OF  
PAGES WHICH DO NOT  
REPRODUCE LEGIBLY.

PART 1 : MFD CLOSED LOOP

## CONTENTS

	Page
CHAPTER 1 INTRODUCTION and SUMMARY	1.1
1.1 General	1.1
1.2 MPD closed-cycle loop	1.1
1.3 Plasma physics	1.2
Bibliography of technical reports and publications by IRD staff on MPD power generation	1.3
PART 1 : MPD CLOSED LOOP	
CHAPTER 2 LOOP OPERATION	
2.1 Introduction	2.1
2.2 Modifications and re-assembly	2.1
2.3 RHT 33	2.3
2.4 RHT 34	2.4
2.5 RHT 35	2.5
CHAPTER 3 POWER GENERATION EXPERIMENTS	
3.1 Introduction	3.1
3.2 Flow properties	3.1
3.3 Electrical properties	3.2
3.4 Discussion	3.5
3.5 Conclusions	3.7
CHAPTER 4 CESIUM INJECTION AND RECOVERY	
4.1 Operating problems	4.1
4.2 Cyclone separation	4.2
4.3 Electrostatic precipitation	4.13
4.4 Ultrasonic cesium removal systems	4.17
4.5 Cesium vaporization and superheat	4.18
CHAPTER 5 GENERATOR DUCT	
5.1 Specification	5.1
5.2 Electrically-conducting layers	5.2
5.3 Electrodes	5.2
5.4 Generator duct wall heater development	5.3



CHAPTER 6 INSTRUMENTATION

6.1	Introduction	6.1
6.2	Generator characteristics	6.2
6.3	Spectroscopic techniques	6.4
6.4	Temperature measurement development	6.5

CHAPTER 7 FUTURE PROGRAMME

PART 2 : PLASMA PHYSICS

CHAPTER 8 MICROWAVE STUDIES OF NON-EQUILIBRIUM PLASMA

8.1	General	8.1
8.2	Microwave bridge	8.2
8.3	Bridge theory and calibration	8.2
8.4	Identification of $TM_{020}$ mode	8.4
8.5	Electron concentration measurements in argon afterglow	8.4
8.6	Electron measurements in cesium afterglow	8.6
8.7	Cesium ion mobility	8.8
8.8	Diffusion, recombination and attachment	8.11
8.9	Preliminary experimental studies of photoionisation	8.12

CHAPTER 9 ATOMIC BEAM EXPERIMENT

9.1	General	9.1
9.2	Experimental equipment	9.2
9.3	Experimental results	9.5

CHAPTER 10 MICROWAVE STUDIES OF THERMALLY-EXCITED PLASMAS

10.1	Thermal ionization experiment	10.1
10.2	New design of equipment	10.2

APPENDIX HEAT TRANSFER AND PRESSURE LOSS CALCULATIONS FOR He-He RECUPERATIVE HEAT EXCHANGER

A.1	Design data	A.1
A.2	Geometry	A.1
A.3	Heat transfer	A.1
A.4	Pressure losses	A.7
A.5	Physical properties of He	A.8

**BLANK PAGE**

## CHAPTER 1

### INTRODUCTION AND SUMMARY

by

B.C. Lindley

#### 1.1 GENERAL

This Final Technical Summary Report covers the final stage of the IRD programme on MPD power generation with part support from the Advanced Research Projects Agency. The objectives and achievements in this energy conversion programme have been detailed in previous Technical Summary Reports<sup>24,45</sup>; a bibliography of the main technical reports and publications by IRD staff on MPD power generation is given at the end of this chapter.

#### 1.2 MPD CLOSED-CYCLE LOOP

The MPD closed-loop facility has demonstrated reliable operation during this further four-month period, resulting in a substantial amount of data with cesium-seeding. Much of the operation with power extraction has been at duct static gas temperatures in the region of 1500°K. Measured plasma electrical conductivities of about 1 mho/m are in excess of the calculated values based on thermal equilibrium ionization<sup>46</sup>. Several watts power have been available and there are reasons to expect a considerable improvement on this level. For example, cesium seeding fractions have been less than 0.1 atomic per cent (well below the optimum), electrically-conducting layers have been present in the MPD duct, the electrode configuration has not been optimum and the magnetic field has been restricted to 1T.

The main unsolved technical problems in the loop (and which are important in large-scale concepts) are related to the electrically-conducting layer which develops on the generator duct walls and to efficient removal of cesium from the helium downstream of the generator. However, considerable progress has been made towards effective solutions of both these problems.

A continuing programme of research on the IRD closed-loop facility is required to provide a full range of data. It is believed that the current development of an externally-heated MPD duct section will, by permitting isothermal operation, go far towards eliminating thermal boundary layers and associated effects on plasma behaviour. Flow boundary layer effects remain significant and a facility permitting much larger cross-section ducts will undoubtedly be required. Ideally, such a project would be initiated in 1965, by which time much more basic data will be available.

### 1.3 PLASMA PHYSICS

The most significant advances in the plasma physics programme were achieved on the microwave cavity and atomic beam experiments. The microwave transmission experiment yielded a set of measurements of electron concentration as a function of temperature for a cesium-helium mixture but ran into further metallurgical and mechanical difficulties which are currently being corrected. No further results have been obtained on the electrical conductivity experiments described in the last report (IRD 64-39, bibliography number 45), effort having been transferred to the other experiments.

BIBLIOGRAPHY OF TECHNICAL REPORTS AND PUBLICATIONS

BY IRD STAFF ON MPD POWER GENERATION

- 1 LINDLEY, B.C. The direct conversion of thermal to electrical energy by ionized gas streams NRC 60-7 January 1960
- 2 LINDLEY, B.C. The direct conversion of thermal to electrical energy NRC 60-8 January 1960
- 3 LINDLEY, B.C. The direct generation of electricity Parts 1 and 2 Nuclear Power Vol 5, no. 50, p 100, 1960; Vol 5, no. 51, p 80, 1960
- 4 McNAB, I.R. The electrical properties of cesium-helium mixtures NRC 61-12 March 1961
- 5 LINDLEY, B.C. and McNAB, I.R. Microwave diagnostics for helium-cesium plasmas. Proceedings of the Fifth International Conference on Ionization Phenomena in Gases North-Holland 1961
- 6 LINDLEY, B.C. Magnetoplasmadynamic electrical power generation British Power Engineering October 1961
- 7 LINDLEY, B.C. An investigation into the characteristics of pebble bed reactor cores Report NRC 62-4 February 1962
- 8 MAITLAND, A. Some consequences of ion slip in a plasma flowing through a magnetic field Nature Vol 194, p 670-1 May 1962
- 9 McNAB, I.R. and LINDLEY, B.C. Electron temperature in the rapid expansion of a plasma flow NRC 61-122 May 1962
- 10 McNAB, I.R. and ROBINSON, C.A. Electron-ion recombination in magnetoplasmadynamic power generators Report NRC 62-90 1962
- 11 LINDLEY, B.C. Closed-cycle magnetoplasmadynamic electric power generation Proceedings of the International Conference on Gas Discharges and the Electricity Supply Industry Butterworths 1962
- 12 LINDLEY, B.C. A magnetoplasmadynamic power generation experiment using helium-cesium Third Symposium on Engineering Aspects of Magnetohydrodynamics University of Rochester 1962
- 13 DUNN, M.H. and MAITLAND, A. Energy obtainable from a Carnot engine with a thermally ionized gas as the working fluid J. Appl. Phys. Vol 33, no. 12, p 3598-9 December 1962

- 14 McNAB, I.R. and ROBINSON, C.A. The viscosity of gaseous cesium at temperatures up to 3000°K IRD 63-10 February 1963
- 15 MAITLAND, A. and DUNN, M.H. Thermal ionization in a system with a distribution of ionization potentials Phys. of Fluids Vol 6, no. 4, p 586-9 April 1963
- 16 McNAB, I.R. and ROBINSON C.A. Electron-ion recombination in MPD generators Magnetoplasmdynamic Electrical Power Generation IEE Conference Report Series No. 4 1963
- 17 ARTHUR, G. and HEPWORTH, M.A. Ceramic materials for MPD power generation Magnetoplasmdynamic Electrical Power Generation IEE Conference Report Series No. 4 1963
- 18 LINDLEY, B.C. Some economic and design considerations of large-scale MPD generators Magnetoplasmdynamic Electrical Power Generation IEE Conference Report Series No. 4 1963
- 19 CRAMPTON, F.J.P. and WILKINSON, T.S. An open-cycle MPD generator optimization study Magnetoplasmdynamic Electrical Power Generation IEE Conference Report Series No. 4 1963
- 20 LINDLEY, B.C. A magnetoplasmdynamic power generation experiment Advances in Magnetohydrodynamics Pergamon Press 1963
- 21 LINDLEY, B.C. A closed-cycle MPD experiment Magnetoplasmdynamic Electrical Power Generation IEE Conference Report Series No. 4 1963
- 22 MAITLAND, A. A criterion for assessing methods of producing non-equilibrium ionization Magnetoplasmdynamic Electrical Power Generation IEE Conference Report Series No. 4 1963
- 23 WILSON, G.W. and ROBERTS, D.C. Superconducting magnets for magnetoplasmdynamic Electrical Power Generation IEE Conference Report Series No.4 1963
- 24 Research programme on magnetoplasmdynamic power generation Technical summary report for 1 December 1961 to 30 November 1962 IRD 63-1 June 1963
- 25 LINDLEY, B.C. Oil-fired MPD power generation Paper 29 Section VI World Petroleum Congress June 1963 (also IRD 63-46)
- 26 McNAB, I.R. The viscosity of helium-cesium mixtures IRD 63-59 July 1963

- 27 McNAB, I.R. and McNEILL, P.C. Density-time profiles for an electric propulsion unit efflux. 5th AGARD Combustion and Propulsion Colloquium, Athens. July 1963 (also IRD 63-63).
- 28 McNAB, I.R. and COOPER, N.A. Flow processes in MPD generators. IRD 63-82 October 1963
- 29 McNAB, I.R. and LINDLEY, B.C. Electron temperature in the rapid expansion of a plasma flow. Advances in Magnetohydrodynamics Pergamon Press 1963
- 30 McNAB, I.R. Power conversion in space IEE Conference on Electric Propulsion (to be published) February 1964
- 31 McNAB, I.R. A non-equilibrium electron mode for kilowatt-range MPD space power. Sixth AGARD Combustion and Propulsion Colloquium, Cannes March 1964 (to be published)
- 32 FINNISTON, H.M. and THRING, M.W. Basic research aspects of MPD power generation (prepared for the Advisory Council on Research and Development of the Ministry of Power) April 1964
- 33 FINNISTON, H.M. Industrial collaborative programme on MHD generation (prepared for the Advisory Council on Research and Development of the Ministry of Power) April 1964
- 34 LINDLEY, B.C. Magnetoplasma dynamic generation. II The future power plant I.Mech.E. Fluid Mechanics Convention, Cambridge. April 1964 (to be published)
- 35 ROBINSON, C.A. and McNab, I.R. Viscosity of partially-ionized gaseous cesium. J.App.Phys. June 1964
- 36 BALFOUR, D. and HARRIS, J.H. Photoionization in MPD generators. International Symposium on Magnetohydrodynamic Electrical Power Generation. Paris, July 1964
- 37 JOLLY, A.B. and NEWCOMBE, J. Cross section measurements and transport properties in seeded inert gas MPD generators. International Symposium on Magnetohydrodynamic Electrical Power Generation. Paris, July 1964
- 38 SANDS, A. and BALFOUR, D. Electrical conductivity and breakdown in cesium vapour. International Symposium on Magnetohydrodynamic Electrical Power Generation. Paris, July 1964
- 39 ARTHUR, G. Compatibility studies of some refractory materials with cesium vapour. International Symposium on Magnetohydrodynamic Electrical Power Generation. Paris, July 1964

- 40 CRAMPTON, F.J.P. and WILKINSON, T.S. Liquefied natural gas applied to oxygen-enrichment and magnet cooling in open cycle MPD generators. International Symposium on Magnetohydrodynamic Electrical Power Generation Paris, July 1964
- 41 LINDLEY, B.C., BROWN, R. and McNAB, I.R. MPD experiments with a helium-cesium loop. International Symposium on Magnetohydrodynamic Electrical Power Generation. Paris, July 1964
- 42 LINDLEY, B.C. and McNAB, I.R. Optimization of large-scale nuclear MPD systems. International Symposium on Magnetohydrodynamic Electrical Power Generation. Paris, July 1964
- 43 LINDLEY, B.C. Nuclear magnetoplasmadynamic energy conversion. Third Geneva Conference on the Peaceful Uses of Atomic Energy September 1964 (To be published)
- 44 DUNN, P.D., LINDLEY, B.C. and WRIGHT, J.K. A survey of MHD research in the United Kingdom. World Power Conference, Lausanne, September 1964 (to be published)
- 45 Research programme on magnetoplasmadynamic power generation: technical summary report 1 December 1963 to 31 March 1964  
Part 1: MPD closed loop  
Part 2: Plasma physics  
Part 3: Theoretical  
IRD 64-36 May 1964
- 46 McNAB, I.R. Extra-thermal electrical conductivity measurements in an MPD generator Nature Vol 204, no. 4955, p 275 October 1964



## CHAPTER 2

### LOOP OPERATION

by

R. Brown, W.J. Slater, V. Brown, K. Cass, J. Davidson and G. Johnson

#### 2.1 INTRODUCTION

A flow diagram of the present loop is shown in Fig. 2.1. Basic design details, manufacture and test of the individual loop components have been described in an earlier Technical Summary Report (IRD 63-1). Further description of the main aspects of loop development, the details of 33 high temperature runs with helium alone and 20 cesium-seeded power generation runs is given in Technical Summary Report IRD 64-36 .

During the 20 cesium-seeded runs in March 1964 the efficiency of cesium removal from the helium flow was low (<2 per cent). Consequently, it was necessary to completely strip the closed loop circuit using oxidation and alcohol dissolution techniques. Approximately one-third (100 gm) of the cesium throughput was located in the precooler outlet, the remainder being dispersed in the lubricating oil of the helium circulator. No deterioration of any components due to the presence of cesium was apparent. The closed loop facility was re-assembled with modifications and additions. Three runs (RHT 33, 34 and 35) were then undertaken.

#### 2.2 MODIFICATIONS AND RE-ASSEMBLY

##### 2.2.1 Helium circulator

The opportunity was taken before re-assembly of the circulator to reduce the end float of the rotor from 0.037 in. to 0.015 in. to minimize internal end leakage and improve the pressure ratio across the circulator. The reduction was achieved by machine grinding across one of the large end faces, reducing its overall thickness to give the required rotor float.

Later figures for circulator performance indicate that a further reduction in rotor float will be necessary for optimum efficiency of the unit. On re-assembly the circulator was checked and found to be leak-tight ( $<10^{-5} \mu\text{l/sec}$ ) under static and dynamic conditions.

### 2.2.2 Oil filtration

The activated charcoal oil filtration unit was found to be contaminated with traces of cesium compounds. The filter units were replaced and vacuum-outgassed at 300°C.

### 2.2.3 High temperature helium heater

The high temperature heater with element and inner radiation shields of fine-grained graphite was the subject of intensive development over the period from February 1963 to March 1964. Major development problems were associated with the electrical power connection to the top (hot) end of the electrical resistance element. The final form of the heater components used successfully during the power generation runs in March 1964 (RHT 32) is shown in Fig. 2.2. The high temperature heater system was completely stripped down after RHT 32. No deterioration of any component was evident and the heater was re-assembled and vacuum-outgassed to a central core temperature of 2200°C. Up to the present time the heater performance has continued to be satisfactory, approximately 100 hr of high temperature vacuum-outgassing and 60 hr high temperature operation with helium flow having been achieved without further disassembly of the heater system. The heater is in a highly active state when operable, readily absorbing gaseous impurities; during periods when the loop is closed down or under modification the high temperature heater is arranged to be pressurized, to a little above atmospheric, with high-purity helium.

### 2.2.4 Cesium injection

To allow seeded operation of the loop in March 1964 an extremely simple cesium injection system was devised and operated. A variable and metered supply of pure helium displaced a constant cesium feed from a storage tank to the loop through a hypodermic needle. A more robust, reliable microfeed mechanical piston displacement system has since been developed (Chapter 4). Preliminary tests were carried out with a facility capable of containing and injecting 1 kgm cesium and from this a small capacity (50 cm<sup>3</sup>) cesium displacement cylinder was developed (Fig. 4.1) employing a cesium reservoir heater tank allowing for rapid refilling of the cylinder. Up to the present time the efficiency of cesium removal from the helium flow has not been better than 12 per cent. Cumulative contamination of circulator oil from cesium carry over allows a maximum of 20 seeded runs of up to 15 sec duration at up to 1 gm/sec cesium flow (a total cesium throughput of about 300 gm) to be carried out during any one high temperature run, and the small-capacity injection system is adequate. The system was chemically cleaned, charged with cesium, calibrated and attached to loop in preparation for RHT 33.

A by-pass with 6 in. vacuum valves was arranged between the heat-exchanger outlet and pre-cooler inlet, allowing for the introduction and isolation of various cesium removal systems. Initially a single stage cyclone separator and an electrostatic precipitator unit were fitted (Chapter 4).

### 2.2.5 Generator duct

To complete the re-assembly of the loop and allow for high temperature clean-up with helium flow, a temporary generator duct system was fitted (Fig. 2.3), comprising two stainless steel (18/8) side walls plasma-spray-coated with alumina, high density recrystallized alumina top and bottom walls with 3 tantalum 0.5 in. x 0.5 in. flush electrode pairs and 9 alumina spray-coated tantalum pin pairs. The system was arranged for investigation of the characteristics of the generator in a subsonic mode; the pin pairs were arranged to extend by different amounts into the gas stream to indicate plasma properties in the core of the flow.

### 2.3 RHT 33

When major modifications have been made (in particular to the high temperature graphite heater) it is necessary to operate the loop with high temperature gas flow to transport and clean up particulate and gaseous impurities. The main objective of RHT 33 was to ensure that the loop was again reliably operable throughout a high temperature cycle, and to ensure cleanliness in preparation for the power generation experiment with the 16 electrode pair boron nitride duct system (RHT 35).

With the generator duct fitted the loop was completed; mass spectrometer and pressure rise techniques showed overall leakage to be less than  $\sim 10^{-5} \mu\text{l/sec}$ . The loop was checked out and charged to 1 ata with helium. Cold circulation was carried out for approximately 30 min until the  $\text{O}_2$  and  $\text{N}_2$  impurity levels in the helium were  $< 5$  ppm (Fig. 2.4). Power was applied to the high temperature heater, reaching thermal equilibrium at  $1770^\circ\text{K}$  (nozzle inlet indicated helium temperature) after 8 hr. The rate of helium temperature rise over this period was controlled to restrict the level of desorbed hydrogen to  $< 50$  ppm. Electrical resistance measurements taken between electrodes, pins and earth throughout the temperature rise indicated a declining generator duct surface resistance (from  $> 1$  Mohm at  $300^\circ\text{K}$  to  $< 100$  ohm at  $1770^\circ\text{K}$ ). From this it was concluded that electrically-conducting surface layers were depositing on the generator duct inner surfaces. At this steady temperature condition several cesium seeded runs were carried out, injecting between 0.1 and 0.5 atomic percent cesium for periods up to 15 sec. Although the cesium injection was successful, very low powers were extracted with magnetic fields of up to 1T (less than 1V indicated and total current of  $\sim 10$  mA) and over successive runs with time intervals of approximately 15 min the generator performance continued to deteriorate. The generator system was similar to that used during the cesium-seeded runs (RHT 32): with the significant reduction in generator performance it was decided that theoretical interpretation of results from RHT 33 would be impossible and injection of cesium was discontinued.

During the heating cycle the observed pressures along the generator indicated a restriction to flow which increased with increasing temperature to reduce the helium mass flow from 9 gm/sec at 800°K to 4.8 gm/sec at 1770°K.

After 2 hr at 1770°K the interelectrode leakage resistance, although extremely low, appeared to stabilize; it was concluded that the gas flow was clean and power was reduced and the circulation discontinued.

The high temperature transfer section and generator case were removed from the loop, using helium blow-off techniques, the remaining sections of the loop and the high temperature helium heater being isolated under helium pressure.

Inspection of the generator section showed that electrically-conducting layers had deposited on the wall inner surfaces. Indicated resistances were less than 1 ohm/cm across the interelectrode spaces. Bowing of the stainless steel side walls had occurred (Fig. 2.5); the more serious effect, which must have occurred at high temperature, would explain the secondary nozzle effect noticed during RHT 33.

#### 2.4 RHT 34

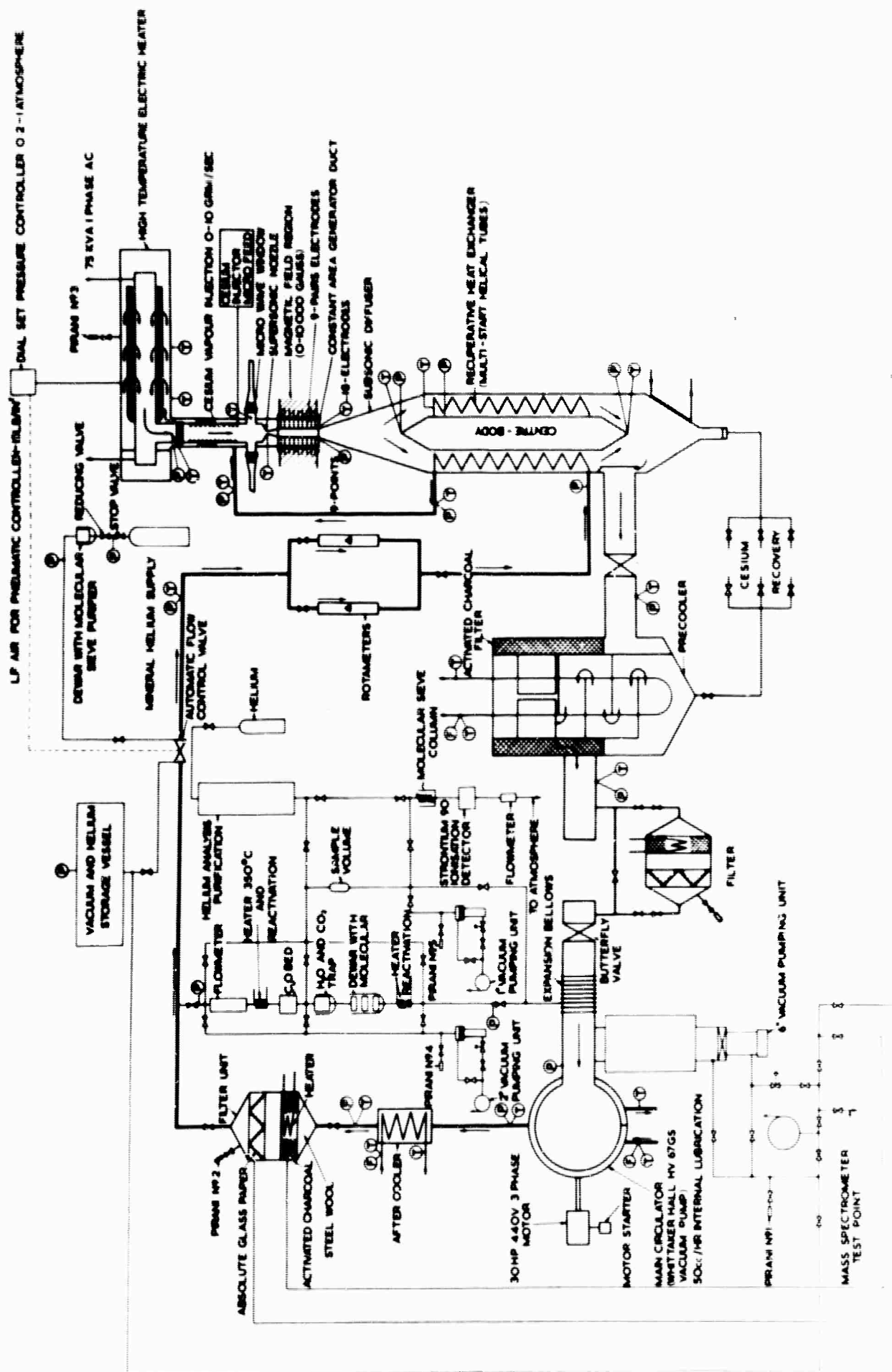
A new high temperature tantalum (0.02 in. thick) transfer section and cesium vaporizer, boron nitride nozzle and 16 (W10%/Ta 90%) strip electrode boron nitride generator duct were assembled (Section 5 and Figs. 5.1, 5.2 a, 5.2 b, and 5.3) and fitted into the loop. The objective of RHT 34 was to determine whether a high temperature thermal cycle with helium flow to a temperature level lower than that of RHT 33 could be carried out without deterioration of the electrical resistivity of the duct inner wall.

The loop was evacuated and recharged with helium. Cold circulation was maintained until gaseous impurities were <5 ppm (Fig. 2.6). Power was applied to the high temperature heater and rapid heating of the helium flow was achieved without measurement of significant desorbed gaseous impurities (nozzle inlet temperature >1550°K in 45 min). During the temperature rise the interelectrode resistances and electrode leakage resistances to earth remained similar to those expected for boron nitride. The 1550°K nozzle inlet temperature was maintained for a further 30 min without a significant change in duct electrical resistance characteristics. Fig. 2.7 shows the axial distribution along the generator pairs at 1400°K (nozzle inlet temperature). The internal surfaces of the tantalum high temperature transfer section viewed axially through the high temperature heater outlet window remained highly polished.

The power on the heater was reduced in stages to zero and the loop circulation stopped. Throughout the cooling cycle the generator duct wall resistances recovered to their original values. The loop was closed down under a positive pressure of helium.

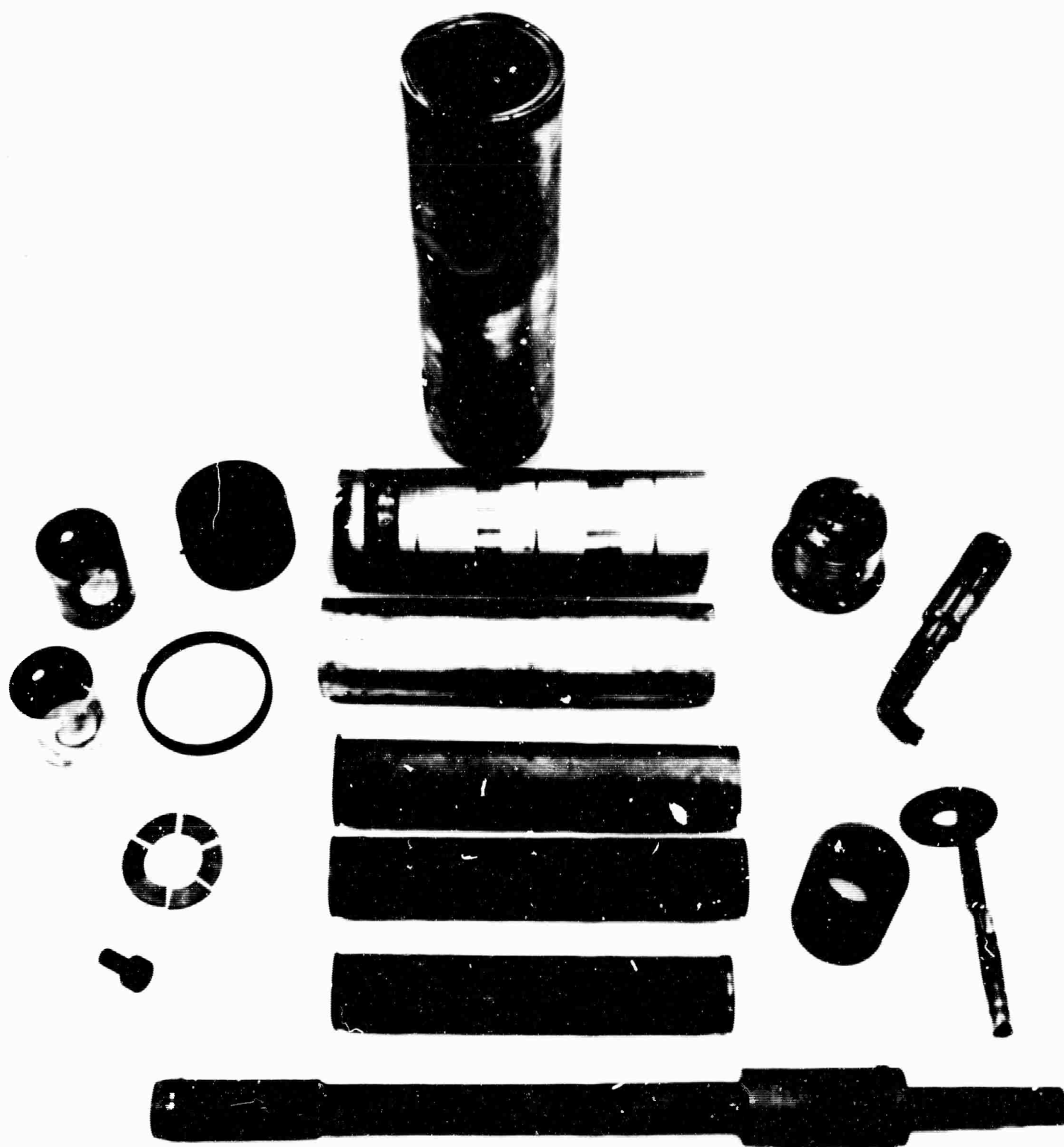
## 2.5 RHT 35

The objectives and the theoretical appreciation of results for RHT 35 are discussed in detail in Chapter 3. The loop was unchanged from RHT 34. Cold circulation was carried out to reduce gaseous impurities to  $< 5$  ppm (Fig. 2.8). During a period of approximately 15 hr cesium-seeded power generation experiments were carried out at three steady temperature levels. At the two lower levels (approximately  $1310^{\circ}\text{K}$  and  $1690^{\circ}\text{K}$  indicated nozzle inlet temperature) the visual appearance of the high temperature transfer section and the electrical resistance measurements along the generator indicated clean conditions. At the highest temperature level ( $\sim 1900^{\circ}\text{K}$ ) the inner walls of the tantalum transfer section became dull and apparently coated, the effect being coincidental with a declining interelectrode and earth leakage resistance along the generator. Generator performance during seeded operation progressively deteriorated and, as it was apparent that further results would be difficult to analyze seeded operation was discontinued and the loop cooled and closed down under helium pressure.



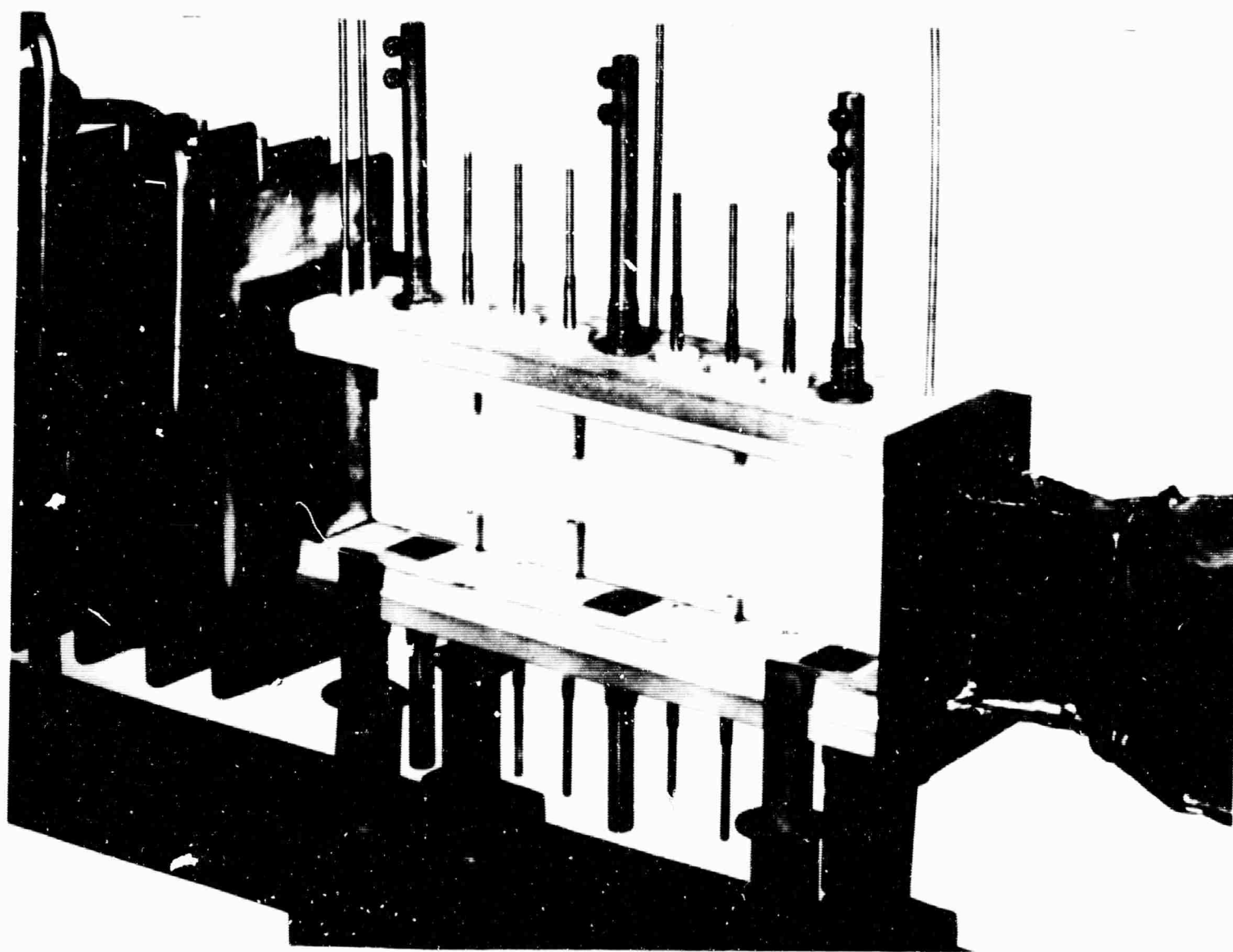
FLOW DIAGRAM

FIG 2.1



HIGH TEMPERATURE HEATER COMPONENTS

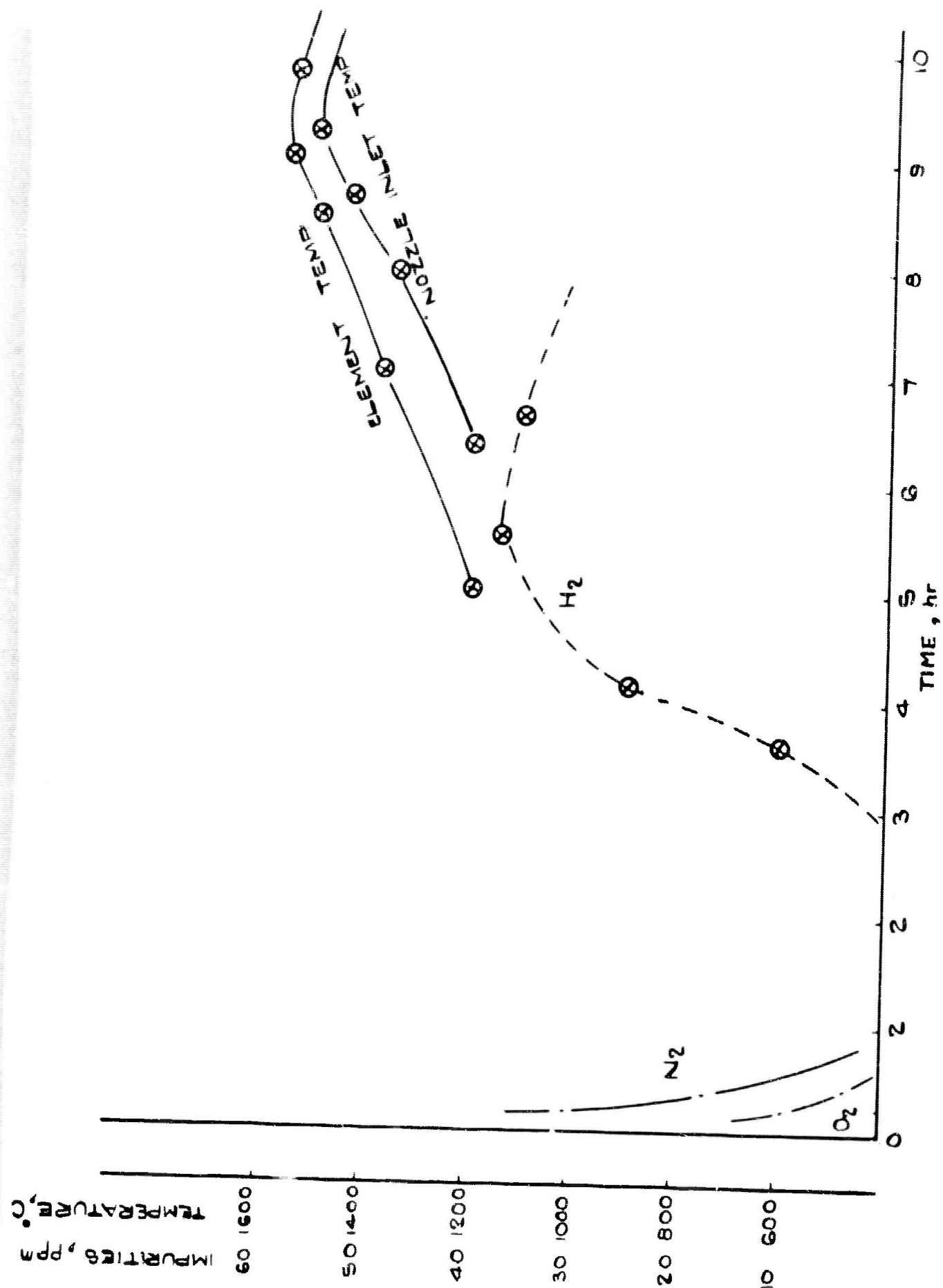
FIG 2.2



TEMPORARY GENERATOR DUCT SYSTEM

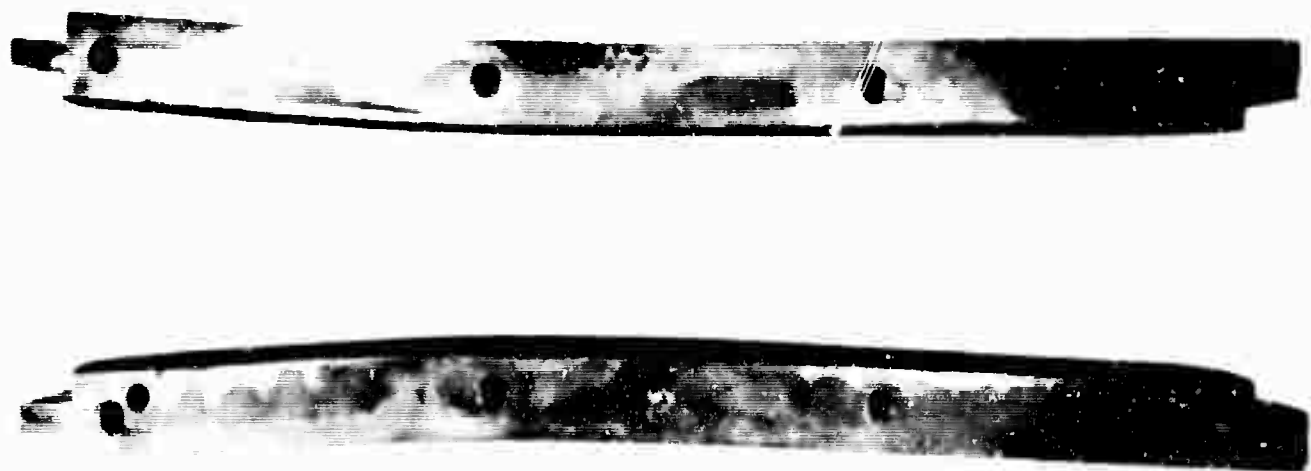
FIG2.3





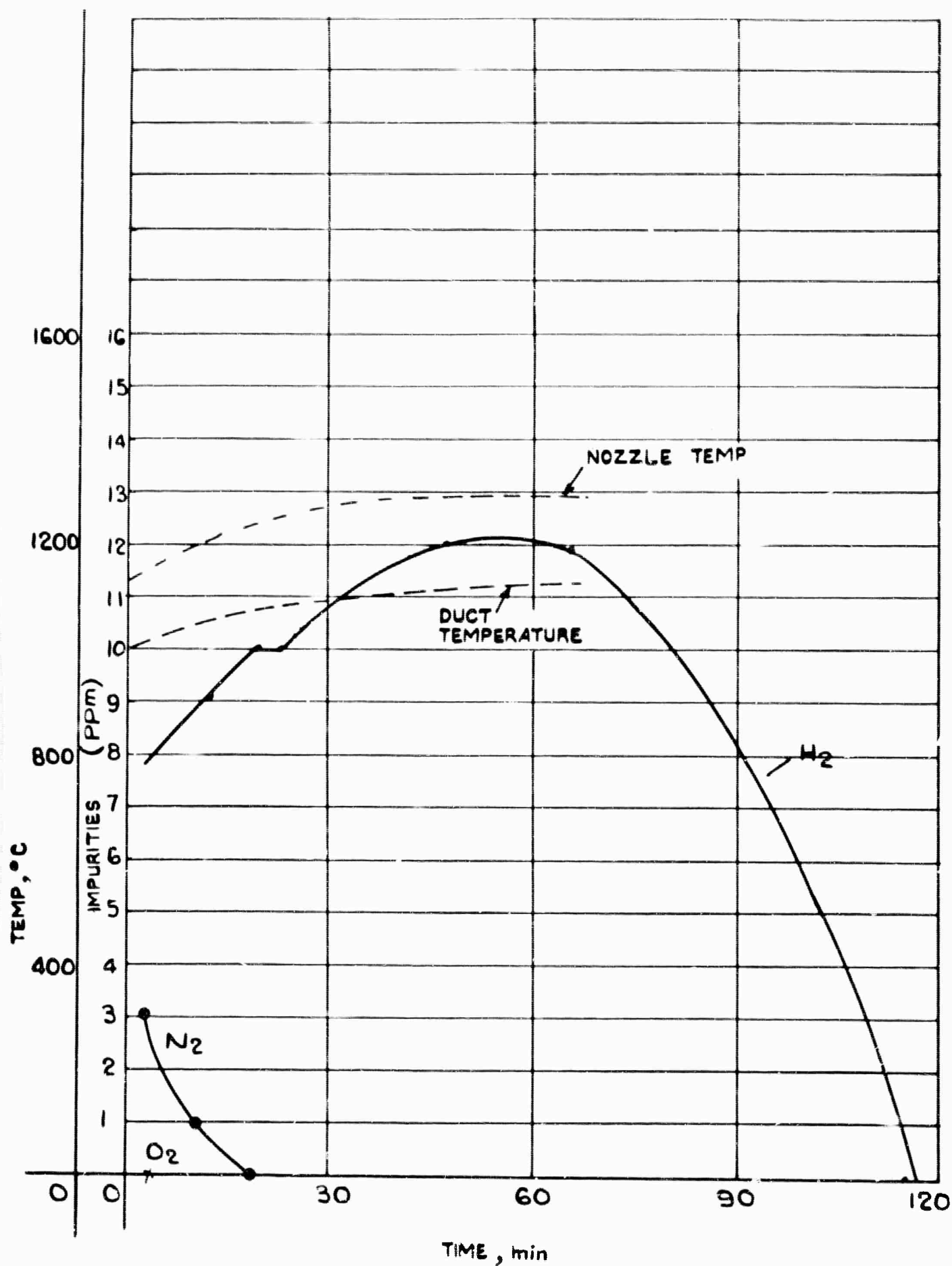
HELIUM PURITY RHT 33

FIG 2-4



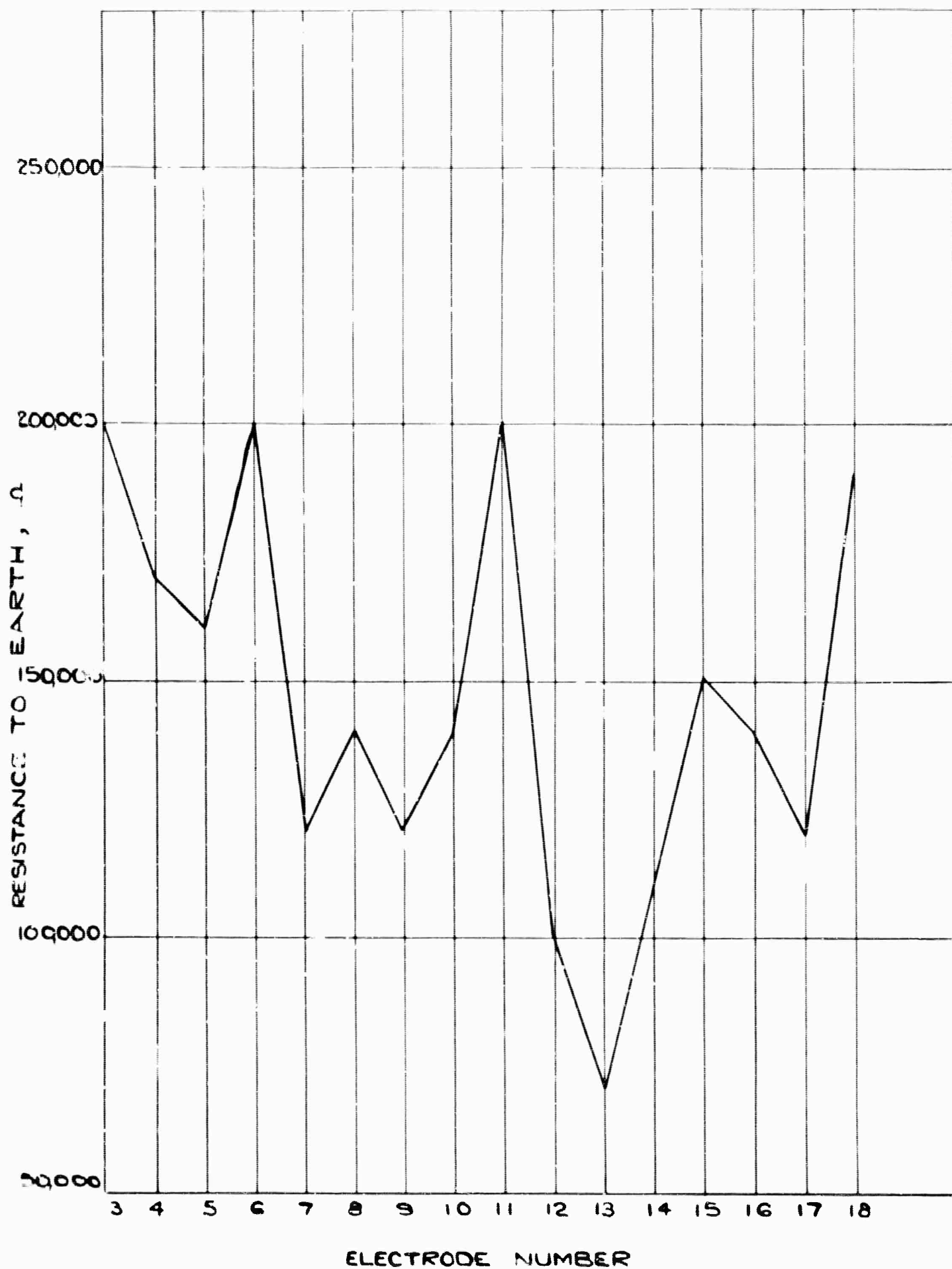
BOWING OF STAINLESS STEEL SIDEWALLS

FIG 2-5



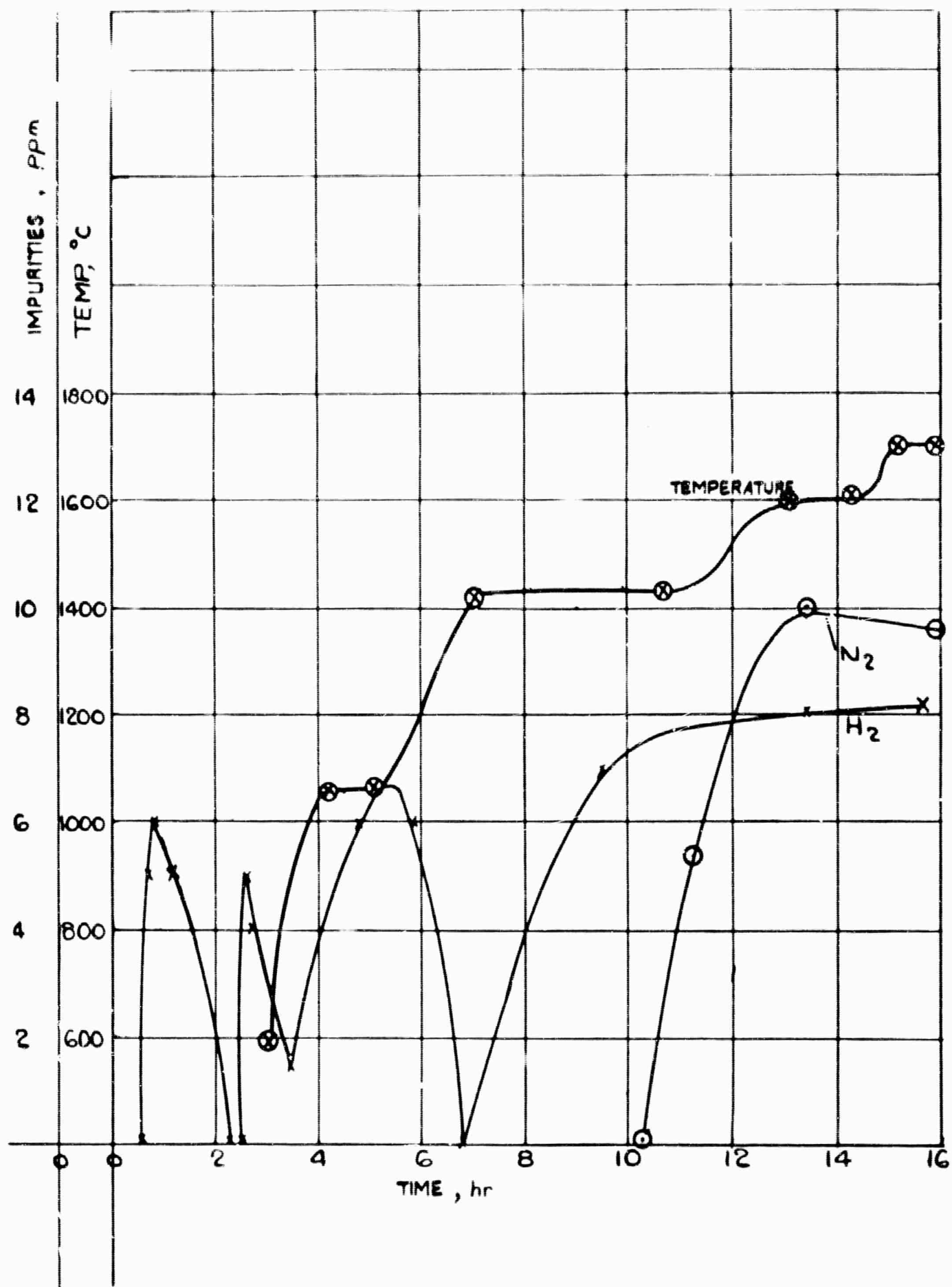
HELIUM PURITY R. H.T. 34

FIG 2.6



AXIAL DISTRIBUTION ALONG GENERATOR OF RESISTANCE BETWEEN ELECTRODE PAIRS AT 1400°K A.H.T. 34

FIG2.7



HELIUM PURITY R.H.T. 35

FIG28

**BLANK PAGE**

## CHAPTER 3

### POWER GENERATION EXPERIMENTS

by

I.R.McNab, R.Brown, V. Brown, K. Cass, J.Davidson and G.Johnson

#### 3.1 INTRODUCTION

A detailed description of the IRD MPD generator has been given<sup>1-4</sup>. On 14 July 1964 a series of power generation experiments with cesium seeding of the helium was undertaken. This series differed from the previously reported seeded runs<sup>3,4</sup> mainly in the generator and nozzle configuration and materials. To reduce end current leakage at the inlet to and exit from the generator channel, the tantalum nozzle previously employed was replaced by a boron nitride nozzle, the exit region of the generator was lengthened by about 2 in. and the interior of the first part of the diffuser plasma spray-coated with alumina. The generator duct, with dimensions of  $7\frac{3}{4}$  in.  $\times$   $1\frac{1}{2}$  in.  $\times$   $\frac{1}{2}$  in., was constructed from boron nitride. Sixteen pairs of narrow ( $\frac{1}{16}$  in.  $\times$   $\frac{1}{2}$  in.) tantalum-tungsten alloy electrodes were used in place of the five pairs of square ( $\frac{1}{2}$  in.  $\times$   $\frac{1}{2}$  in.) electrodes used in the first seeded run<sup>3,4</sup>; the gap between the electrodes was large (as with the square electrodes) to reduce the possibility of insulator and boundary layer electrical breakdown. In addition to the electrodes, five pairs of  $\frac{1}{16}$  in. diameter tantalum pins were used to monitor open circuit voltages, two pairs being in the nozzle (before and after the throat) and three pairs in the generator exit region. Four pressure stations and three thermocouples were also placed in the channel wall; Fig. 3.1 shows the relative positions of these instruments.

#### 3.2 FLOW PROPERTIES

During operation of the loop, two of the channel thermocouples failed. The temperature recorded (continuously) by the remaining channel thermocouple, together with that at the nozzle inlet, is shown in Fig. 3.2. Also shown are the pyrometer measured heater element temperatures.

The pressures observed at the four stations in the channel and at the nozzle inlet are shown in Table 3.1 in atmospheres absolute; also shown is the pressure ratio across the nozzle found from the nozzle inlet and first channel pressure station measurements. To obtain sonic velocity across a nozzle the ratio of inlet stagnation pressure to sonic pressure:

$$\frac{p_0}{p^*} = \left(\frac{\gamma+1}{2}\right)^{\gamma/\gamma-1} = 2.05 \text{ (for helium)}$$

must be exceeded. Table 3.1 also shows the corrected helium mass flow in the loop. From the quasi one dimensional equations of continuity and state, the flow velocity may be found:

$$U = 42.4 \text{ m } T/p$$

where  $m$  is the  $\text{kgm/sec}$ ,  $T$  in  $^{\circ}\text{K}$  and  $p$  in  $\text{ata}$ ; the Mach number is then obtained from

$$M^2 = 2.19 \cdot 10^{-4} U^2/T.$$

The velocity and Mach number in the channel obtained by this procedure are shown in Table 3.1. The calculated Mach number is always subsonic, contrary to the behaviour expected from the observed pressure ratio across the nozzle.

### 3.3 ELECTRICAL PROPERTIES

The cesium injection circuit was constructed to give a seeding rate of about 0.2 atomic percent: this rate, which is about one-tenth optimum, is necessitated by the low capacity of the present evaporator. In practice, while cesium was injected for only a short time (maximum 15 sec) the observed voltages in the channel lasted much longer, decaying only slowly to zero; in many cases measurable voltages were apparent several minutes after seeding stopped. In some cases, after the main seeding effects had decayed, large and apparently random voltage pulses were observed probably indicating that cesium was trapped in the injection system. Fig. 3.3 shows average open circuit voltages on pins 1, 2, 19 and 20 for the first few seconds of run 2; the average voltages vary considerably. Table 3.2 shows the voltages measured in the decay period following the main cesium flow (for several runs) together with the nominal cesium injection time and that actually observed. In view of the slow decay of voltage the observed seeding period is not well defined; however, considerable dilution of the seed occurs, generally by a factor of about two. Pin 2 consistently shows much higher voltages than pin 1, reflecting the higher flow velocity at nozzle exit. In several cases pin 2 shows step variations suggesting that the observed voltage is influenced by the different loads (and hence different currents) being switched on to the channel electrodes.

In run 10, when no magnetic field was applied, pin 2 registered a peak of 4 volts. This could occur if a residual magnetic field existed in the magnet, if the two pins were at different temperatures, or if they had different cesium coverage.

The open circuit voltage varies considerably down the channel. Fig. 3.4 illustrates this for runs 5, 10B and 11; the voltage falls appreciably down the channel, a particularly sharp drop being between electrode pairs 12 and 13. It is



likely that the change in voltage occurs as the gas velocity decreases; however, as gas temperature was measured at only one point in the channel this cannot be verified.

At low open circuit voltages, reverse voltages were occasionally observed, as illustrated in Fig. 3.5: this could arise if end current leakage occurred (see Fig. 25 McNab and Cooper<sup>5</sup>) but the observed voltages are so small that this is not certain.

The magnet coil currents for each run are given in Table 3.3; Fig. 3.6 shows the calibration curve for the magnet. This curve is obtained in the absence of the nozzle and generator channel assembly and therefore with a cold (or self-heated) magnet. When the MPD loop is operating the magnet core is considerably heated by radiation from the hot regions; no thermocouples were attached to the magnet during this run so that the extent of the heating is not known. An increase in the operating temperature of 200°C will decrease the magnetic field by about 5 percent (Bozorth<sup>6</sup>).

To obtain the electrical conductivity of the plasma in the channel on seeding, each of the sixteen electrode pairs was switched on to five load resistors (18, 68, 280, 1000, 4700 ohm) and open circuit in rapid sequence and the resulting voltage displayed on a 24 channel u.v. recorder trace. This sequence takes about 1½ sec and can be repeated continuously. From the deflections on the u.v. traces the voltages and currents for each load may be obtained and voltage-current characteristics constructed. The slope of these curves gives the conductivity of the plasma when the electrode area and path length are known. While this procedure is tedious and subject to some error due to 'hash' and overlapping of the traces, it enables a large amount of data to be obtained for a short cesium injection time. In addition a four channel u.v. recorder displays the open circuit voltage on pins 1, 2, 19 and 20.

Table 3.4 compares measured open circuit voltages with the product  $UB_d$ . In all cases the measured voltage is less than  $UB_d$ , the maximum ratio  $V_{meas}/UB_d$  being 0.60. Conducting deposits on the inner channel surfaces may be responsible, although these apparently only become significant at higher temperatures, as in run 13. In runs 6, 7 and 8 the measured open circuit voltage exhibits a saturation effect with magnetic field similar to that found previously (Lindley et al<sup>3</sup>).

Table 3.3 shows electrical conductivities calculated from the voltage-current curves. In many cases the voltage-current curves exhibit behaviour which is not interpretable; in these cases the best linear fit is employed. The slope of the voltage-current is the internal resistance ( $r$ ) of the plasma, which is related to the conductivity by  $\sigma = L/rA = 475/r$  mho/m where  $r$  is in ohm,  $L$  is the distance between the electrodes (1.5 in.) and  $A$  the electrode area. Assuming that the whole channel

volume carries current,  $A$  is the channel width ( $\frac{1}{4}$  in.) multiplied by the electrode pitch ( $\frac{1}{4}$  in.). This assumption yields the most pessimistic value of conductivity; the assumption may be tested by examining the conductivities on each side of an unloaded electrode. Table 3.3 shows that these conductivities are not appreciably higher than the channel average, indicating that the whole volume is not carrying current. The true conductivities therefore lie between the values given in Table 3.3 and values four times larger. Fig. 3.7 compares the average channel conductivities with thermal equilibrium values in the same temperature range. A seeding fraction of 0.1 atomic percent was used in calculating the equilibrium values and the two curves are for the appropriate channel inlet pressures (the lowest measured in the channel). The observed conductivities are up to fifty times larger than equilibrium at the gas temperature. To account for these values merely by incorrect temperature measurement would require, in the highest cases, errors of at least  $300^{\circ}\text{C}$ ; this is unlikely.

In several cases the voltage-current curves were as shown in Fig. 3.8. In these cases the lowest voltage points are probably in error owing to the difficulty of measuring small voltages on the u.v. trace. For a low load resistor a small uncertainty in voltage measurement causes a large error in the derived current value. If the curves are correct some form of current limitation appears to be occurring. Well defined concave voltage-current curves were also observed in several cases. If these are correct they indicate electron temperature elevation, although the same comments concerning the measurement of low voltages apply.

The expression given by Hurwitz et al<sup>7</sup> for the ratio of electron to gas temperature in a segmented-electrode generator with magnetically-induced ionization is

$$\frac{T_e}{T} = 1 + \frac{\gamma(1-K)^2 M^2 \beta_e^2}{35(1+\beta_e \beta_i)^2}$$

where  $K$  is the loading factor,  $\gamma$  the ratio of specific heats,  $M$  the Mach number and  $\beta_e$  and  $\beta_i$  the Hall parameters for electrons and ions. Neglecting ion slip and assuming a low seeding fraction, so that the electronic collision frequency depends only on electron-helium atom collisions ( $q_{e-\text{He}} = 6.1 \times 10^{-20} \text{ m}^2$  as in McNab<sup>8</sup>) solution of the resultant quadratic equation yields

$$\frac{T_e}{T} = 0.5 + 0.5 \left[ 1 + 8.88 \times 10^{-3} \frac{(1-K)^2 M^2 B^2 T}{\delta^2 p} \right]^{\frac{1}{2}}$$

For run 3b (electrode 8) a concave voltage-current curve was observed. Fitting the results to the above equation (assuming that the observed conductivities correspond to elevated electron temperatures given by Saha's equation) values of the inelastic

collision factor ( $\delta$ ) were found. For the three load resistors, 4700, 1000 and 280 ohms, the values of  $\delta$  were 8.45, 19.2 and 25.5. As the load resistance decreases the current flowing through the plasma increases; for these three cases the ratios  $\delta/I$  were 02, 3.88 and 3.96  $\text{mA}^{-1}$ , possibly indicating that as the current density increases, increased amounts of impurities enter the plasma.

In view of the uncertainty in the voltage-current curves at low voltages no attempt has been made to analyse these results in greater detail.

### 3.4 DISCUSSION

Temperatures measured by thermocouples embedded in the channel wall are in error through conduction along the leads. While these errors can in principle be calculated, in practice this is difficult unless the complete environment temperatures are known; this was not the case for this run. In addition gas flow calculations are required to relate the wall temperature to the midstream static gas temperature. Introduction of thermocouples into the gas stream has been dismissed in view of the attempts to achieve supersonic flow.

Attempts were made to estimate the generator channel wall temperature profile by measuring the change in resistance of the individual electrode strips. This procedure was carried out at five different temperatures (as recorded by the single operating thermocouple in the channel) during the operation. Assuming that the resistivity of the electrodes follows the law  $\rho = a + bT$  the difference between the measured 'hot' and 'cold' resistances gives a direct measure of the wall temperature. Fig. 3.9 shows this difference down the channel for two temperatures. The general tendency is for the temperature to fall along the channel, although the effects of conduction along the electrode leads may vary down the channel. Fig. 3.10 shows the average resistance difference against thermocouple measured temperature for five different times. The accuracy of these measurements is in grave doubt following the discovery of several cracked electrodes on disassembly of the channel.

Pressure measurements in the channel (Table 3.1) indicate a rise in pressure for the first three stations followed by a fall for the last station. In addition, the sharp drop in open circuit voltage between electrodes 12 and 13 (Fig. 3.4) occurs at the same point in the channel, and, although a pressure ratio across the nozzle of more than 2.05 was achieved, supersonic Mach numbers were never found. This behaviour could be consistent with supersonic flow where shock occurred between the third and fourth pressure station. However, Table 3.1 shows that similar pressure profiles exist when the flow is far from supersonic, for example with a pressure ratio of 1.22, and the existence of cracked electrodes could account for the sharp drop observed in open circuit voltage.

Further experiments are required to clarify the situation. The general discrepancies between predicted and observed flow properties undoubtedly follow from (amongst other factors) the operation of a nozzle with a pressure ratio more than seven times smaller than the design value. The attainment of only a low pressure ratio across the nozzle follows from the inefficiency of the compressor and the higher-than-anticipated pressure losses in the loop components. Under these circumstances the nozzle design pressure ratio should be matched to that achievable in the loop and consequently the following nozzle is now (17 August 1964) in place in the loop

inlet temperature	1430°C
inlet pressure	0.73 ata
pressure ratio	2.40
throat area	2.272 cm <sup>2</sup>
exit velocity	2288 m/sec
exit temperature	930°C
exit Mach number	1.13

The throat area above is 31% greater than that for the nozzle used here and the nozzle has been constructed merely by removing material from the present nozzle throat. The above conditions are evaluated for pure helium; the addition of cesium will affect the flow because of dissociation, but provided the seed concentration is low, this is not significant.

A further complicating effect exists in the present geometry because of the close proximity of the nozzle to the generator channel. Since the magnetic field does not cut-off sharply, flow through the nozzle may be affected by eddy currents. The simplest way to overcome this is to increase the channel length, restricting the magnetic field to the central region.

Leakage resistances were measured throughout the run and values are shown in Fig. 3.11 for electrode pair 10. The resistance decreases as temperature increases, as expected; it is only at the highest temperature that the leakage resistance becomes comparable with the highest load resistance. On dismantling the loop after operation a black conducting deposit, similar to that found in the run during March<sup>3</sup>, was found on the inside walls of the nozzle and channel. This conducting layer, together with the cracked electrodes previously mentioned, could be responsible for several anomalous effects, including the low open circuit voltages, the sharp open circuit voltage drop between electrodes 12 and 13 and the low and widely varying voltages observed in runs 13, 14 and 15. Except in isolated circumstances it is impossible to interpret these last results owing to the considerable voltage variation

on each resistance value. There is no pronounced upward or downward trend in the observed electrical conductivities along the channel (Table 3.3). Consequently, remembering the relatively low flow velocity and anomalous flow behaviour, it is unlikely that frozen flow occurred during the nozzle expansion. Any higher-than-equilibrium conductivities therefore indicate magnetically induced extra-thermal ionization.

The maximum electrode current observed during the run was about 15 mA, although extrapolated short circuit currents are higher. For the electrode area ( $2 \times 10^{-5} \text{ m}^2$ ) this yields a current density of  $750 \text{ A/m}^2$ . This is far higher than the thermionic current density obtainable from pure tantalum but less than that from pure cesium; Fig. 3.12 shows values calculated from the Richardson-Dushman equation and three experimental values. Unless arc spots are occurring, the electrodes must have a partial cesium coverage which, if power is to be provided continuously, must be continuously replenished. Different coverage factors could account for the variation in power output and conductivities along the channel.

### 3.5 CONCLUSIONS

Many complicated and interrelated factors, including flow, material and electrical effects, are at present combining to make interpretation of results from seeded runs a complex problem. Nevertheless, accounting all probable errors, electrical conductivity values higher than for thermal equilibrium ionization appear to have been observed in a segmented-electrode generator. Further experiments to clarify these observations are planned.

### REFERENCES

- 1 LINDLEY, B.C. A magnetoplasmdynamic power generation experiment using helium-cesium. Third Symposium on the Engineering Aspects of MHD University of Rochester 1962
- 2 LINDLEY, B.C. A closed cycle MPD experiment Magnetoplasmdynamic Electrical Power Generation. IEE Conference report series no. 4 1963
- 3 LINDLEY, B.C., BROWN, R., and McNAB, I.R. MPD experiments with a helium-cesium loop. International Symposium on MHD Electrical Power Generation, Paris, July 1964
- 4 Research programme on magnetoplasmdynamic power generation. Technical Summary Report 1 December 1962 to 31 March 1964. IRD 64-36
- 5 McNAB, I.R. and COOPER, N.A. Flow processes in MPD generators. IRD 63-82 October 1963

- 6 BOZORTH, R.M.M. Ferromagnetism. Bell Laboratory Series 1959
- 7 HURWITZ, H., SUTTON, G.W., and TAMOR, S. Electron heating in MHD power generators. ARS Journal vol. 32, no. 8, p1237, 1962
- 8 McNAB, I.R. The electrical properties of cesium-helium plasma. C.A. Parsons report NRC 61-12. March 1961

TABLE 3.1

LOOP PARAMETERS : SEEDED RUNS 14 JULY 1964

Time	Run No.	Nozzle inlet pressure, ata	Duct pressures, ata				Nozzle pressure ratio	Mass flow, gm/sec	Nozzle inlet temp, °K	Duct exit temp, °K	Flow velocity, m/sec	Mach No.	B, T
			1	2	3	4							
10.45		.970	.940	.940	.942	.940	1.03	7.03					
12.00		.996	.946	.950	.952	.950	1.05	7.01					
13.30		.915	.820	.825	.830	.825	1.11	6.78					
15.15	1								1313	973			1.0
16.00		.863	.708	.718	.748	.715	1.22	6.91			519	0.25	
18.00		.772	.383	.423	.504	.420	2.02	7.98			1152	0.58	
18.50		.755	.319	.372	.382	.369	2.36	7.81			1365	0.64	
19.27	2								1693	1295			1.02
20.05	3								1673	1288			1.01
20.20		.752	.322	.376	.379	.379	2.33	7.75			1315	0.63	
20.40	4								1685	1291			1.03
20.45	5								1685	1291			1.03
21.07	6								1688	1291			1.03
21.12	7								1689	1291			.92
21.17	8								1691	1291			.69
21.22	9								1693	1291			.45
21.30		.718	.299	.352	.362	.349	2.40	7.68			1408	0.67	
22.10		.628	.232	.298	.318	.302	2.70	6.28			1509	0.71	
22.20		.625	.228	.295	.308	.298	2.74	6.18			1542	0.72	
22.43	10								1883				1.03
22.47	10L								1893	1355			1.04
22.58	11								1898	1353			1.02
00.15	12								1973	1383			1.03
00.20		.608	.205	.251	.298	.278	2.97	6.03			1730	0.79	
00.22	13								1973	1383			1.03

**TABLE 3.2**

## CESIUM INJECTION PERIOD AND OBSERVED VOLTAGES ON ELECTRODE 10

[illegible]



TABLE 3.3  
MEASURED ELECTRICAL CONDUCTIVITIES IN CHANNEL

Run No.	Magnet current, amp	Conductivities, mho/m, at following electrode pair numbers																Average
		3	4	5	7	8	9	12	13	14	15	16	17	18				
1	165		VERY SMALL															
2a†	175			.75	.44	.46	.31	.74	.60	.75	.95	.86					.65	
2c†		.034	.025	.024	.028	.025	.030	.034		.033	.117	.109	.117	.080			.054	
3a†	170		.125	.143	.146	.160	.117	.112	.112	.154	.154	.132	.132	.132			.137	
3b†			.150	.144	.171	.158	.173	.125	.173	.172	.17	.180	.475*	.172			.160	
3c†			.153	.178	.196	.210	.246	.154	.180	.152	.152	.163	.163	.163			.176	
4	180		.167	.167	.150	.150	.210	.167	.169	.195	.195	.240	.592*	.195			.182	
5	180		OPEN CIRCUIT															
6	180			.243	.245	.249	.273		.476	.368	.312	.224	.225	.295			.291	
7	130		.233	.241	.266	.258	.284	.301	.330	.396	.371	.371	1.25 *	.470			.320	
8	70		.357	.393	.440	.399	.440	.352	.529	.402	.365	.365		.341			.398	
9	40																	
10B	185		.231	.231	.248	.284	.302	.286	.415	.353	.368	.332	.376	.306			.311	
11	175		OPEN CIRCUIT															
12	180													.58				
13a†	180													.58				
15a†		2.06																
15b†														.68				
15c†														.60				

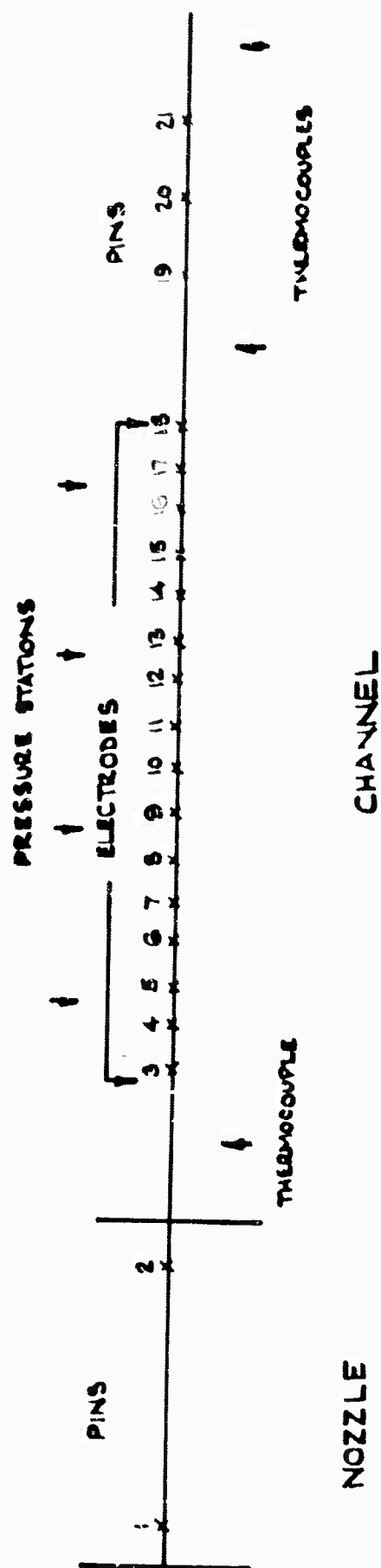
\* Values not included in average

† a,b,c refer to different regions of UV trace

TABLE 3.4

MEASURED AND CALCULATED OPEN CIRCUIT VOLTAGES

Run No.	Time	U, m/sec	$\frac{B}{T}$	UBd, volts	V <sub>meas</sub> volts	$\frac{V_{meas}}{UBd}$
1	15.15	-	1.0	-	-	-
2	19.27	1365	1.02	53.0	7.3	0.14
3	20.05	1365	1.01	52.5	24	0.46
4	20.40	1315	1.03	51.6	24	0.46
5	20.45	1315	1.03	51.6	23.4	0.45
6	21.07	1315	1.03	51.6	25.2	0.49
7	21.12	1315	0.92	46.1	23.6	0.51
8	21.17	1315	0.69	34.5	18	0.52
9	21.22	1315	0.44	22.0	-	-
10B	22.47	1542	1.04	61.8	36.9	0.60
11	22.58	1542	1.02	60.0	35.5	0.59
12	00.15	1542	1.03	60.6	-	-
13	00.22	1730	1.03	62.9	5	0.08



PRESSURE, THERMOCOUPLE AND ELECTRODE STATIONS IN THE NOZZLE AND CHANNEL

FIG 3.1

OBSERVED TEMPERATURE DURING SEEDED RUN

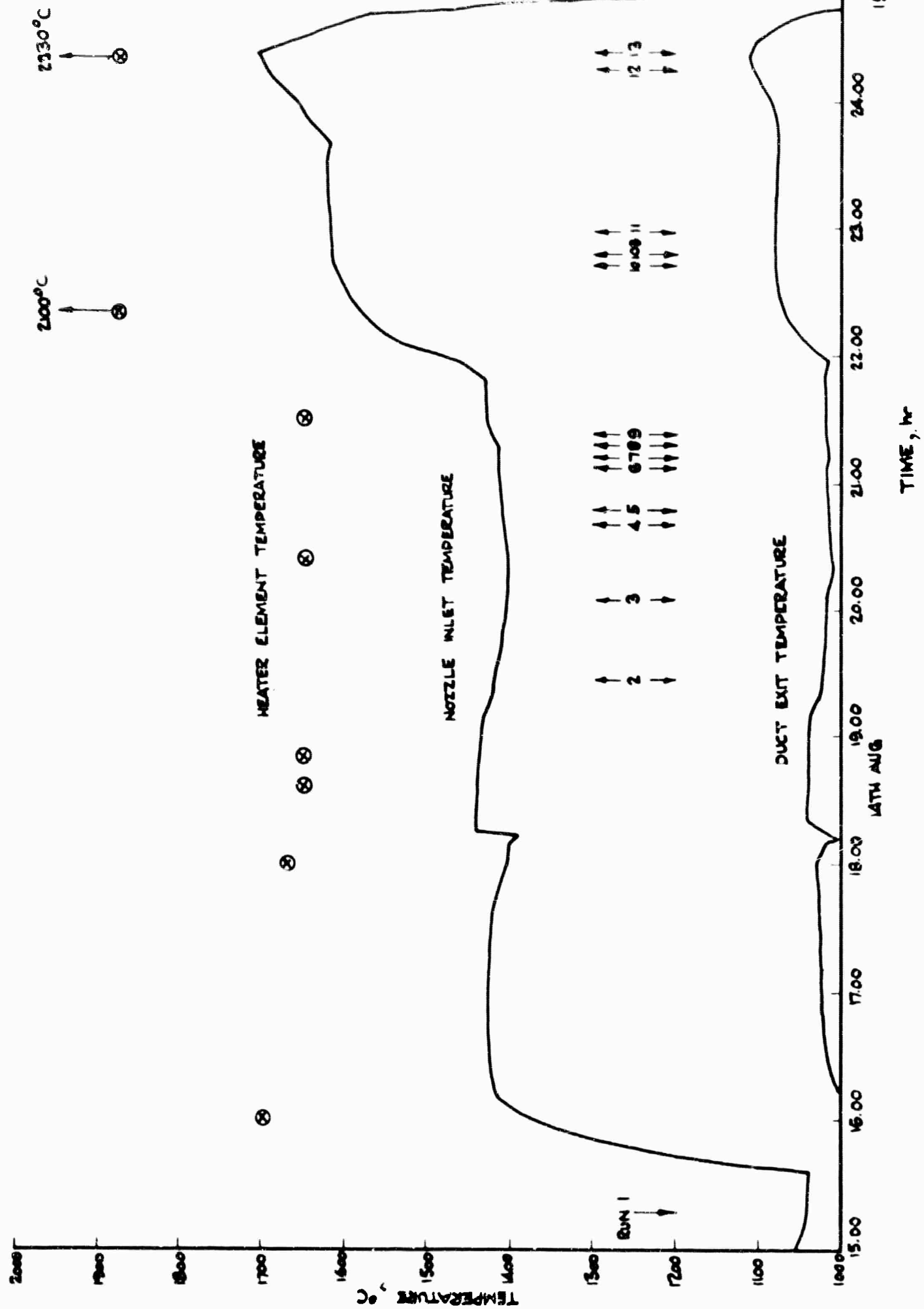


FIG 3.2

VARIATION OF PIN VOLTAGES WITH TIME

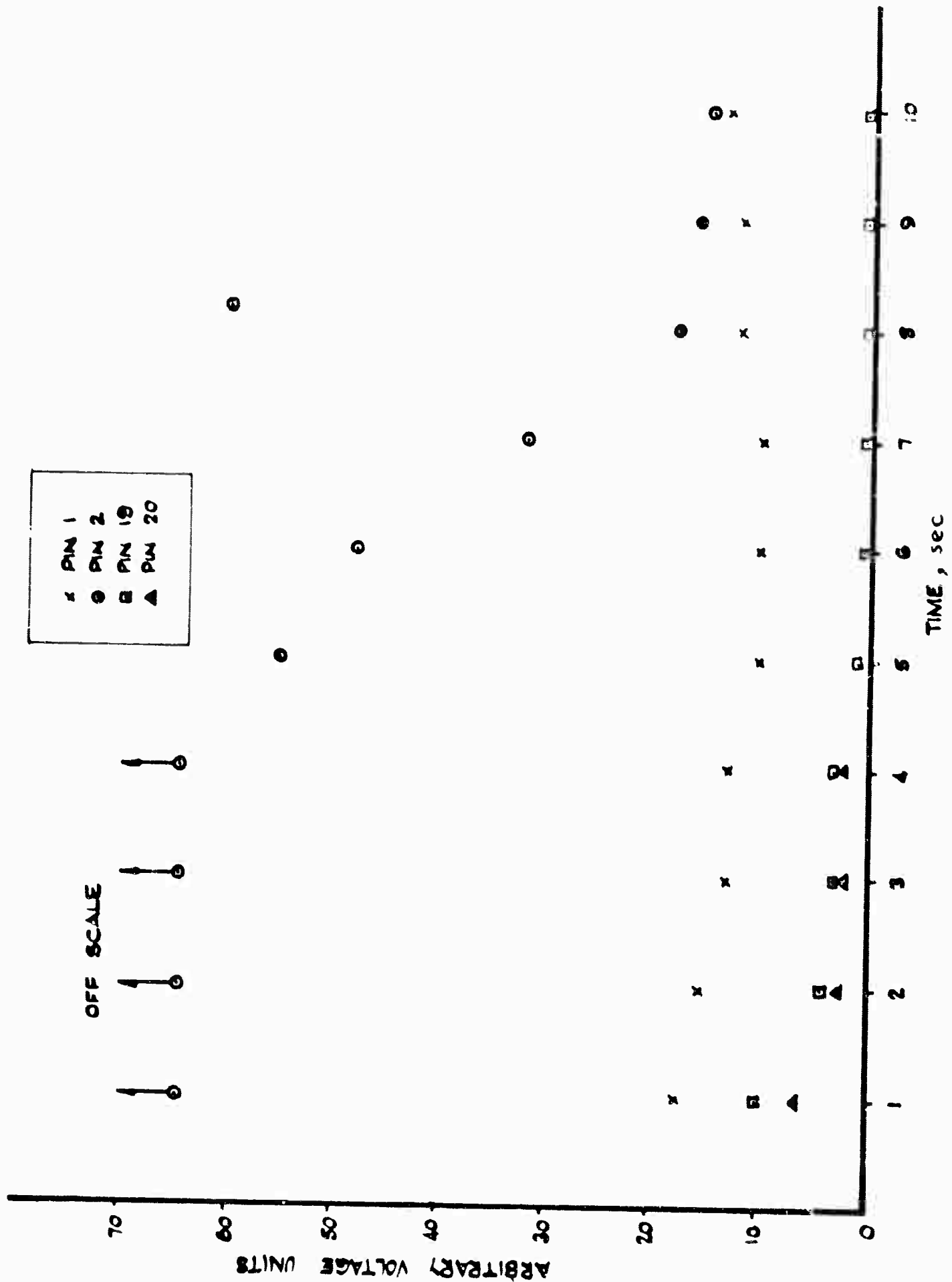


FIG 3.3

# OPEN CIRCUIT CHANNEL VOLTAGES

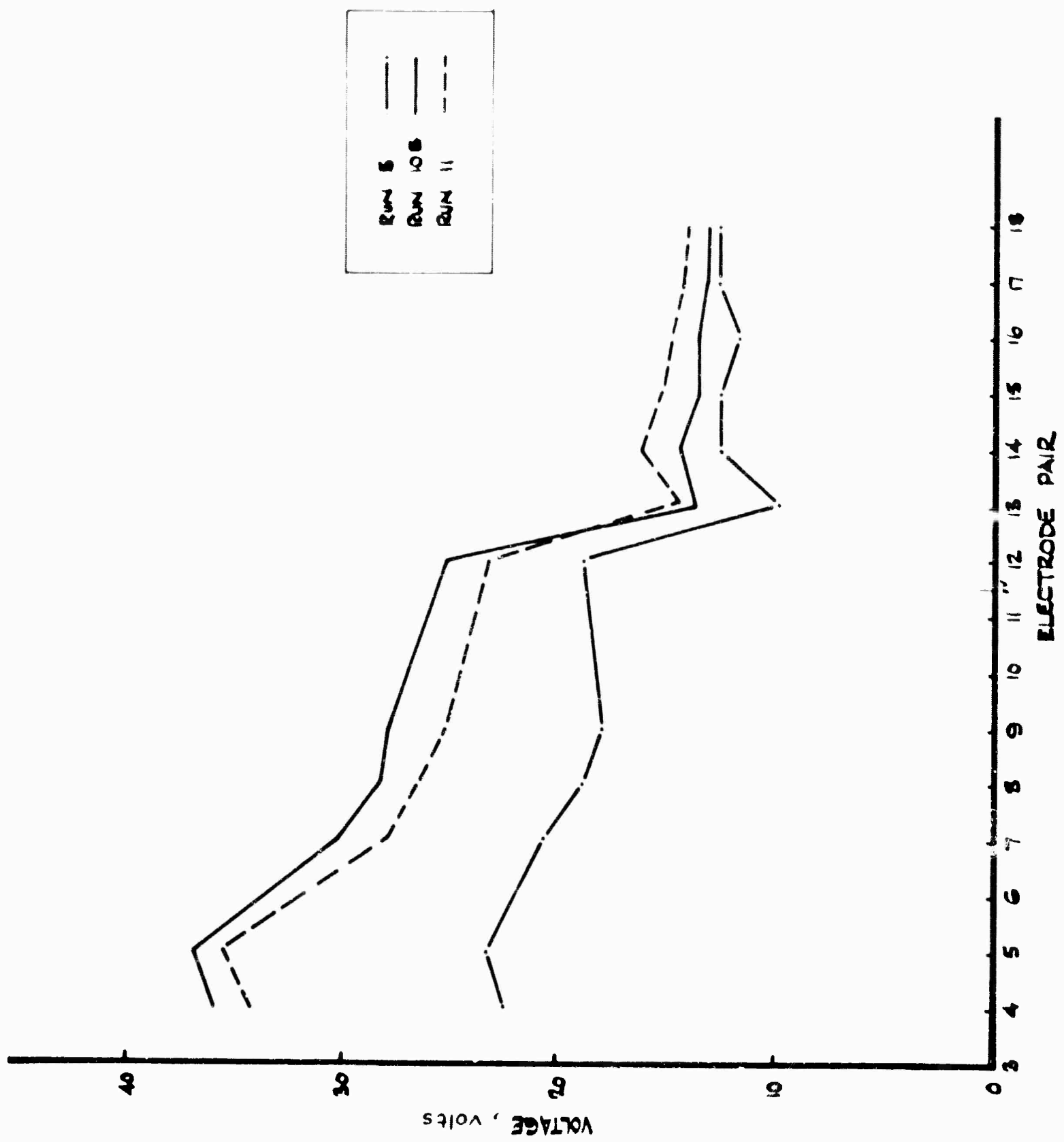
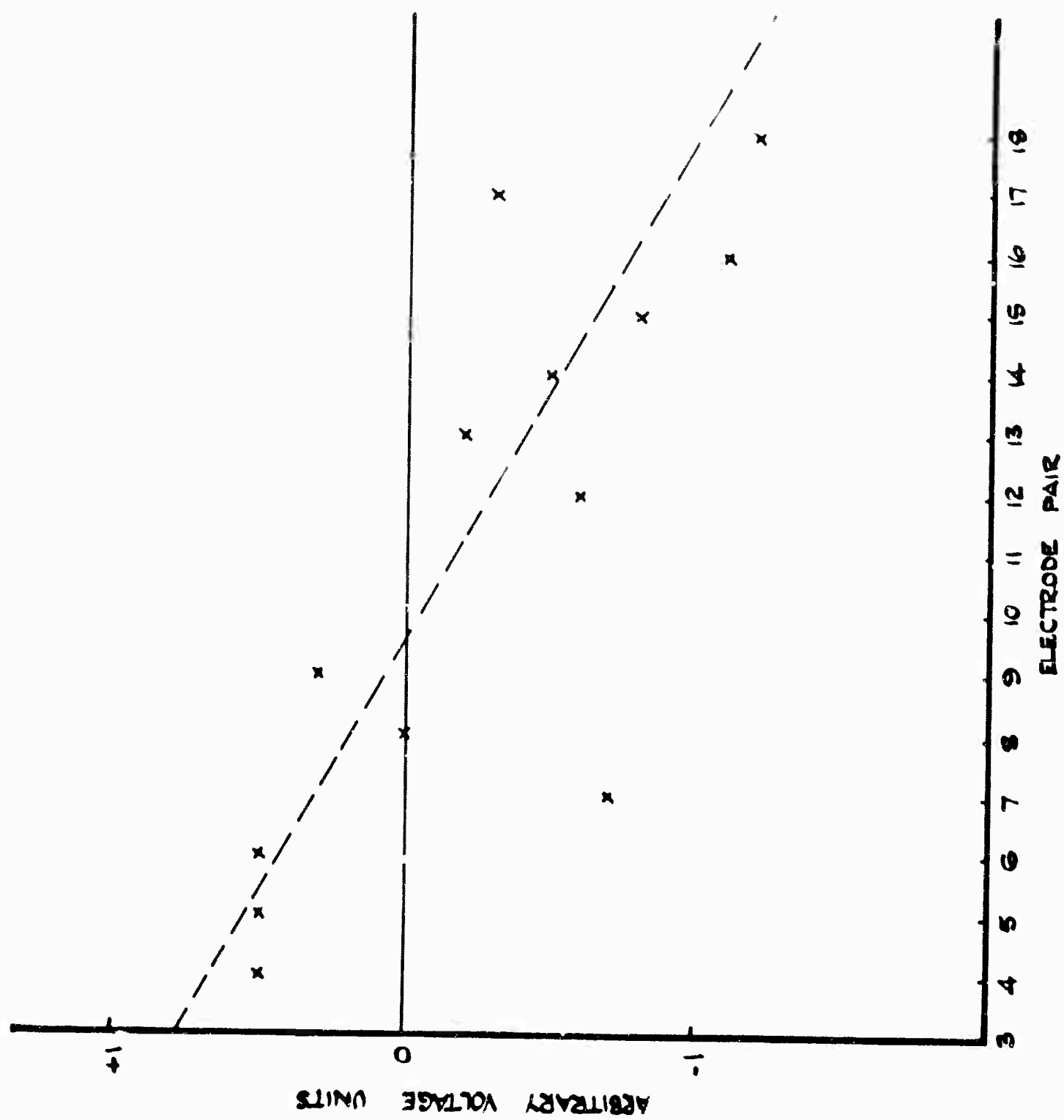


FIG 3.4



REVERSE VOLTAGES IN CHANNEL

FIG 3.5

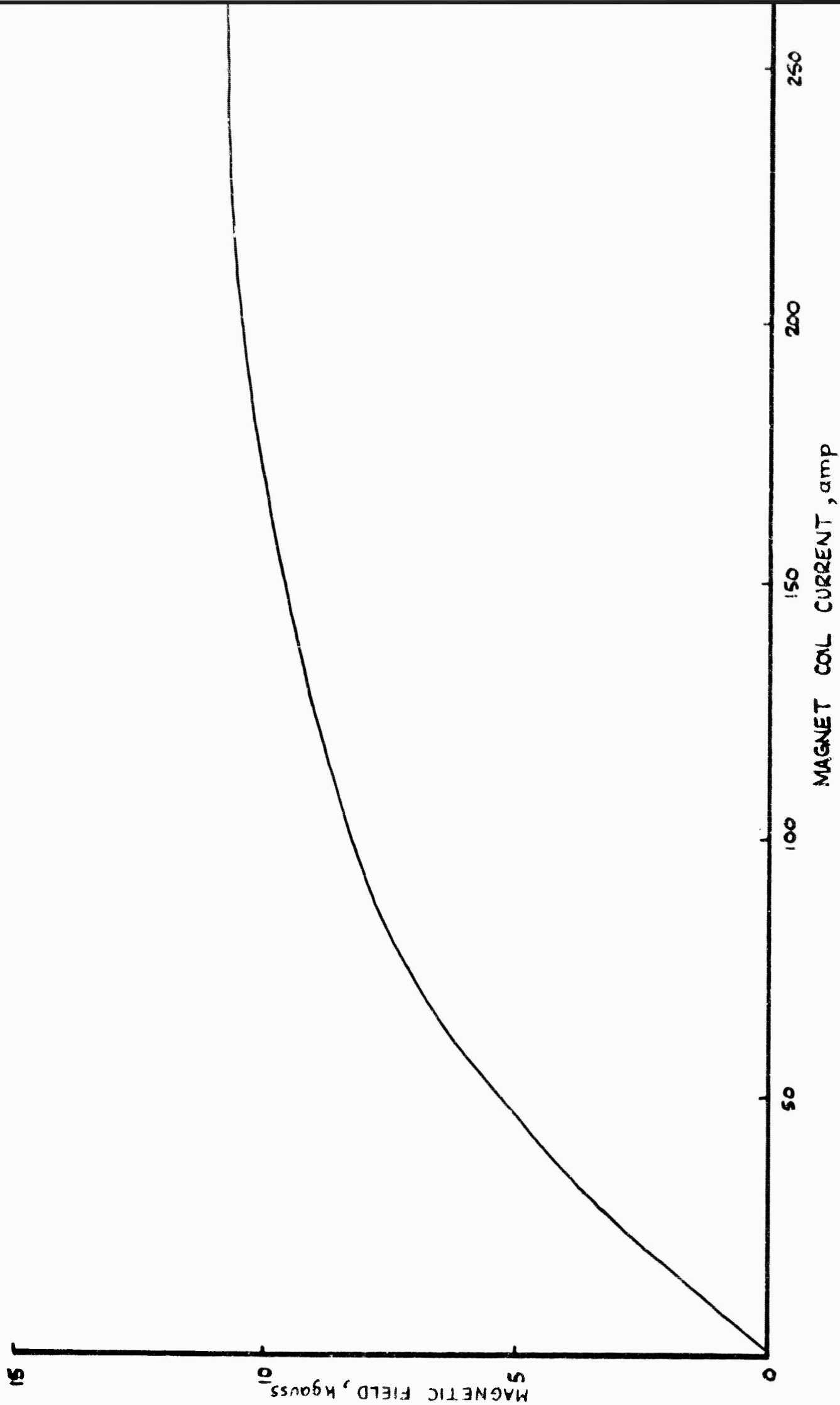
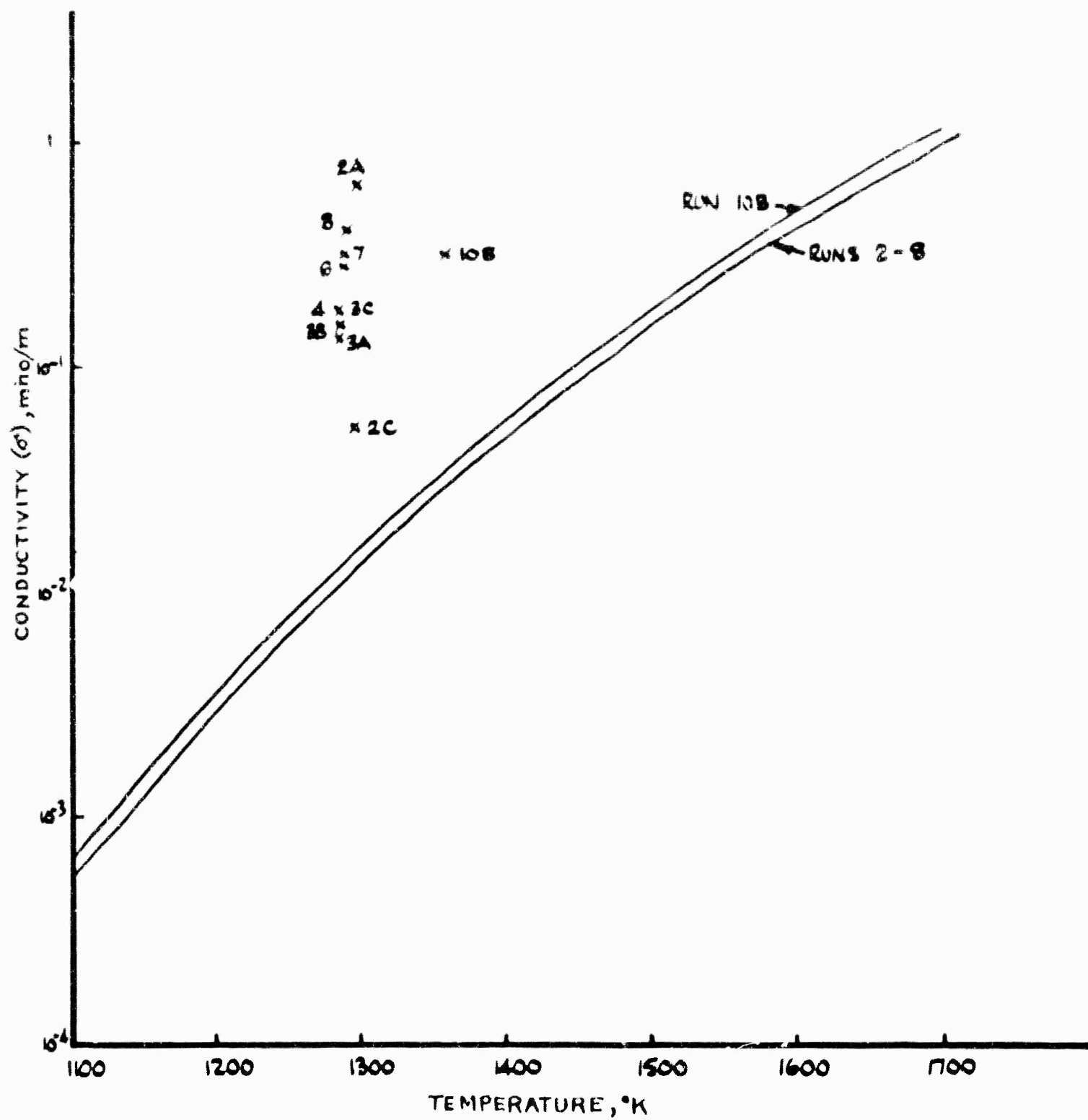


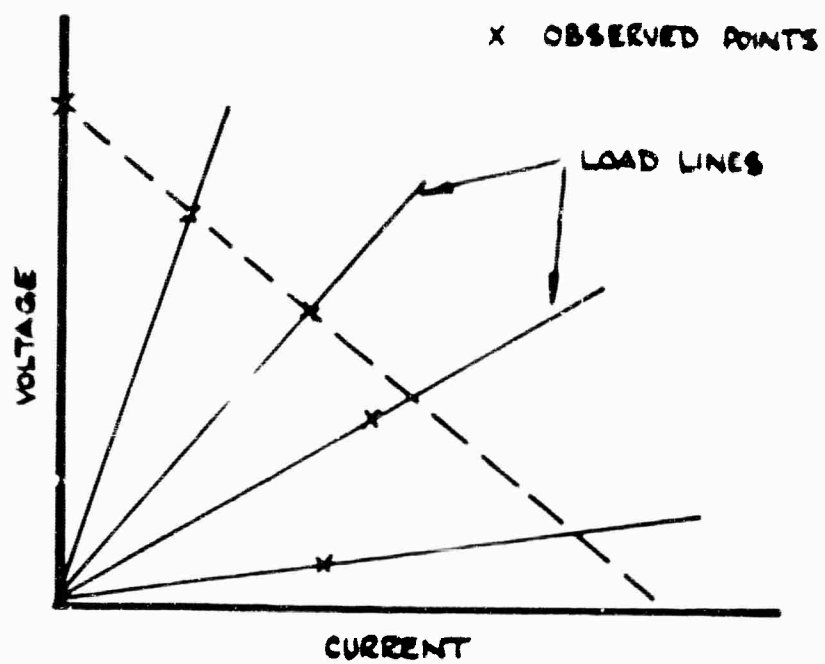
FIG 3.6





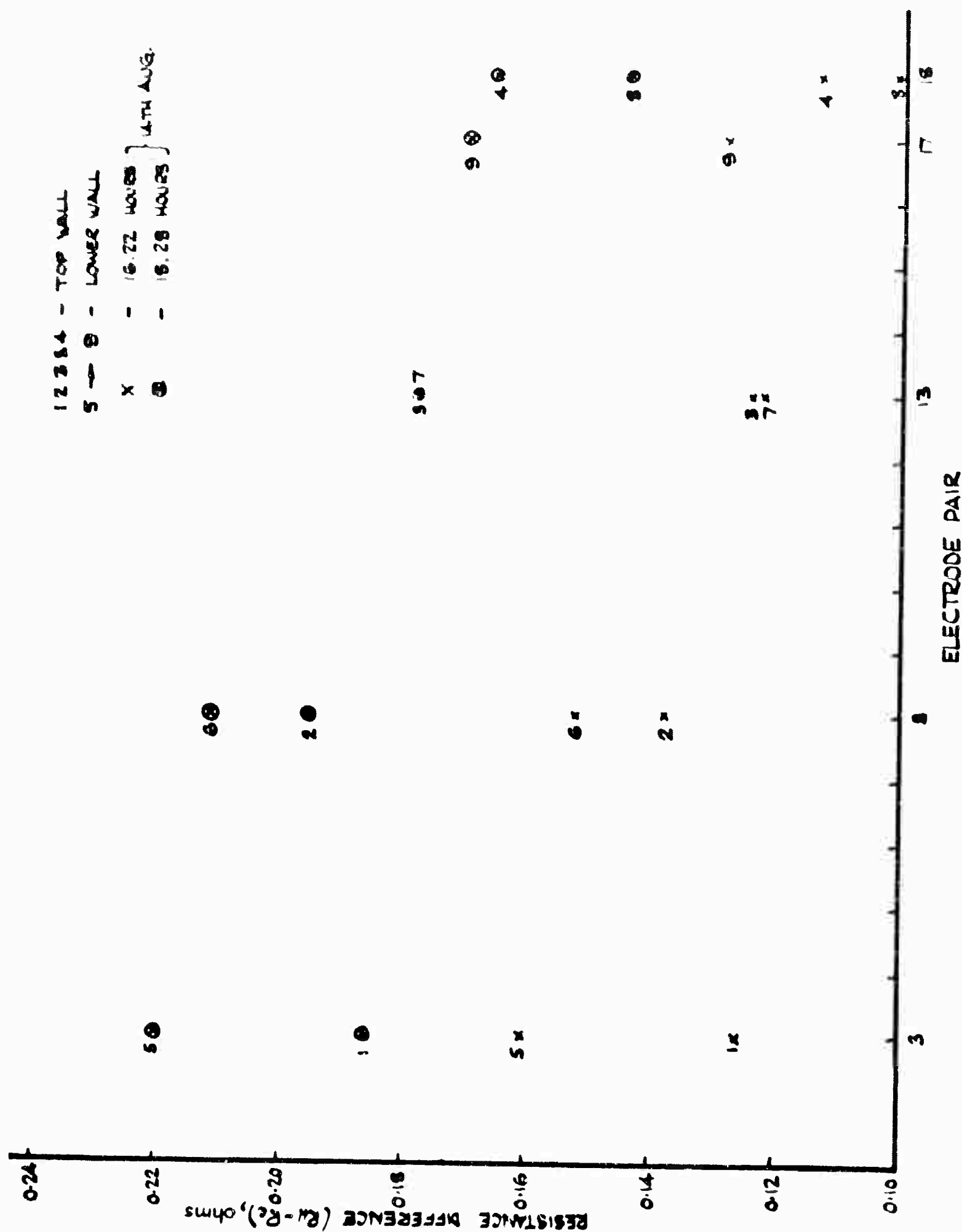
OBSERVED AND CALCULATED ELECTRICAL CONDUCTIVITIES

FIG 3.7



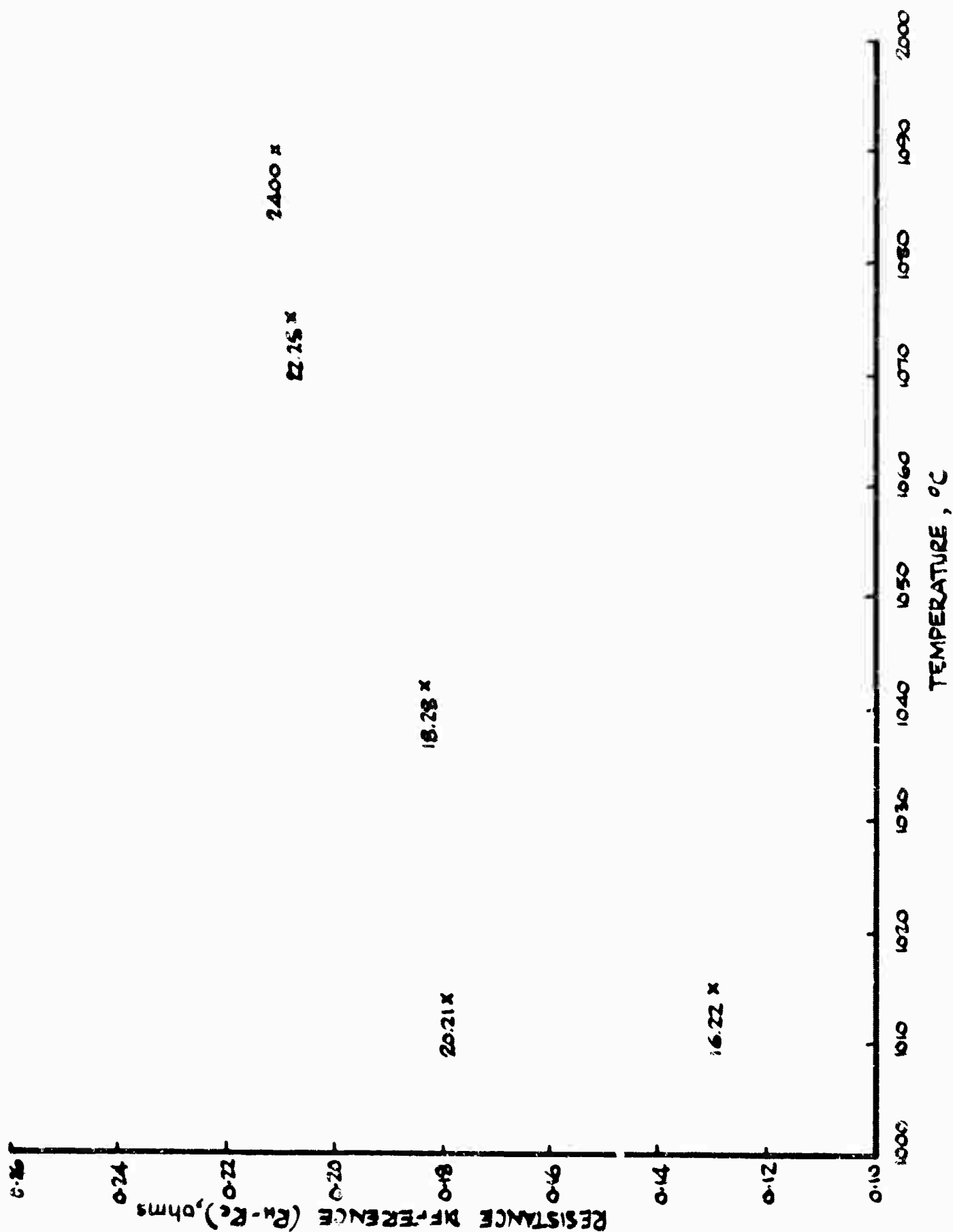
OBSERVED VOLTAGE-CURRENT CURVE

FIG 3.8



ELECTRODE RESISTANCE DIFFERENCES ALONG CHANNEL

FIG 3.9



AVERAGE ELECTRODE RESISTANCE DIFFERENCE COMPARED WITH TEMPERATURE MEASURED BY THERMOCOUPLE

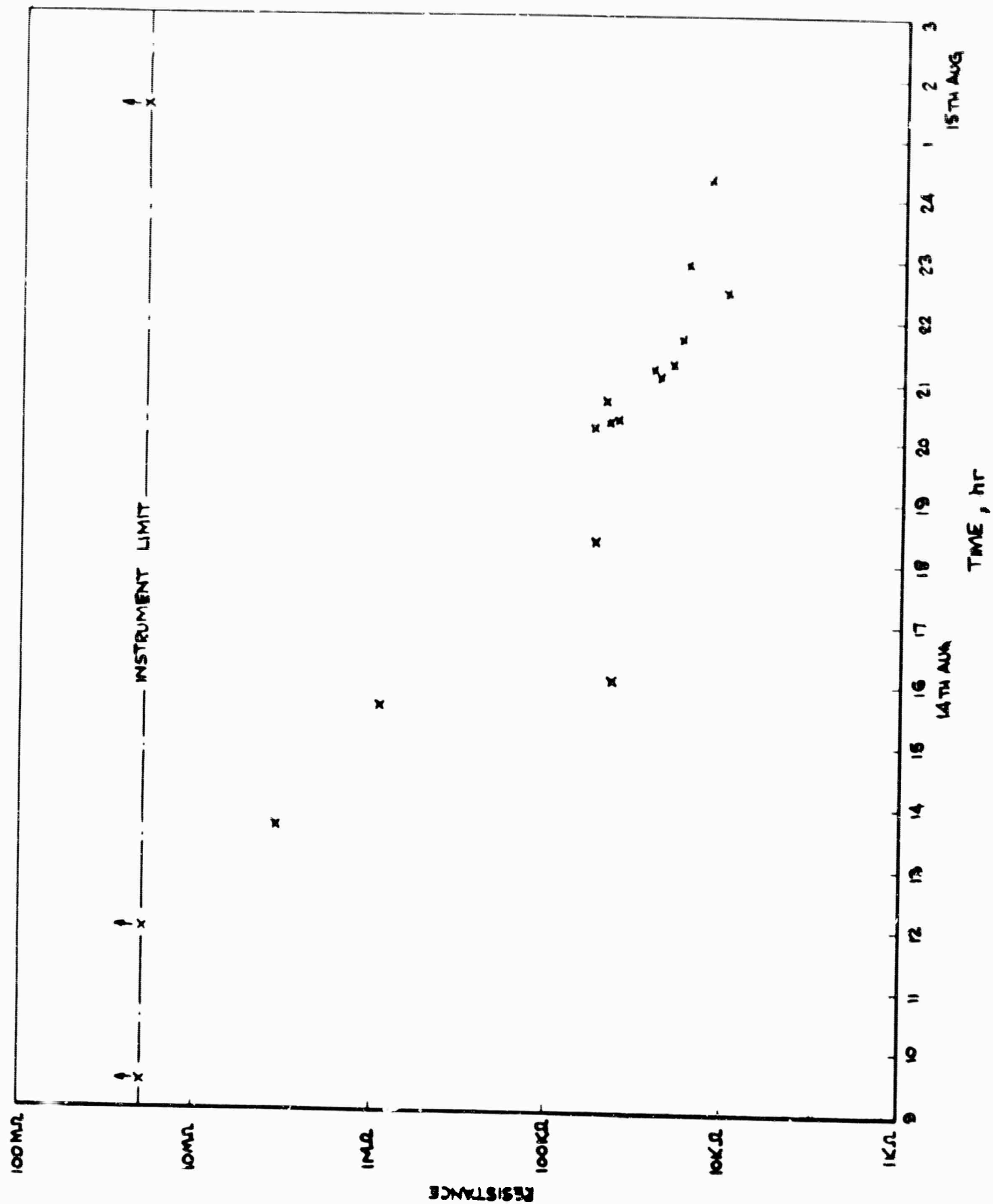
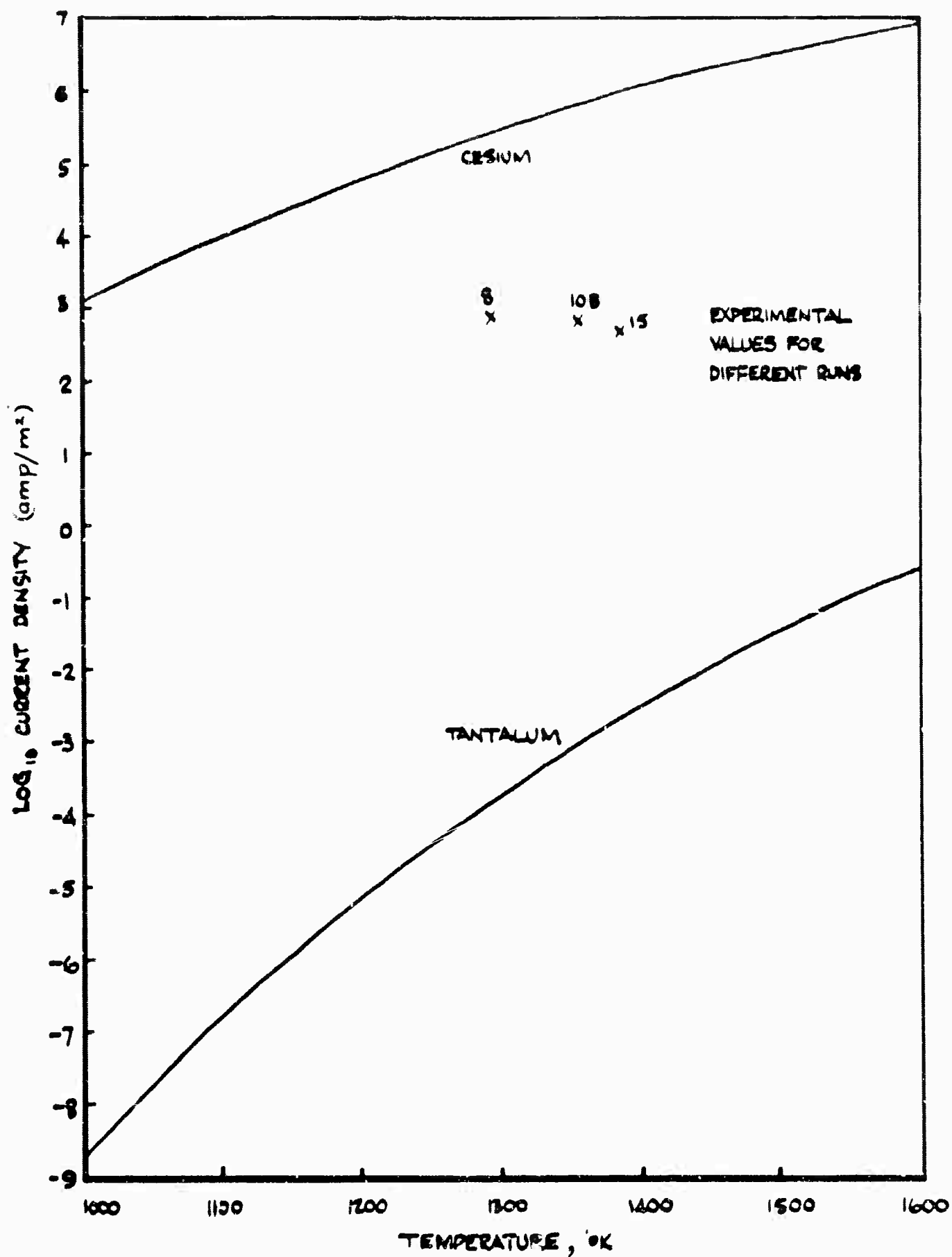


FIG 3.11



THERMIONIC EMISSION CURRENT DENSITY AND OBSERVED VALUES

FIG 3.12

## CHAPTER 4

### CESIUM INJECTION AND RECOVERY

by

R. Brown, T. Archbold, and A. Sands

#### 4.1 OPERATING PROBLEMS

The ultimate objective for the MPD closed-loop is to continuously supply and meter cesium vapour to the high temperature helium flow, and to attain the same temperature as the helium by superheating the cesium vapour before injection or through efficient mixing of the helium-cesium after injection. To date, operation of the loop with cesium seed has clearly demonstrated the inefficiency of the present vaporizing and recovery techniques.

It has been established that during injection a cloud of cesium droplets form in the diffuser-heat exchanger region. In recent operation the cloud density and duration has been monitored at the heat exchanger outlet station, where two opposite windows are arranged to accommodate a light source and photo cell respectively. The responses from the cell are continuously displayed on a u.v. recorder. The window systems are 1 in. ID  $\times$  6 in. long and have remained completely clean throughout a series of runs, including a throughput of approximately 600 gm cesium. Although the cloud monitoring system does not give an absolute measure of the cesium throughput it establishes the delay interval from the injection point to the heat exchanger outlet and gives some indication of dilution compared with the nominal rate of injection.

All seeded runs to date have been associated with low removal efficiencies and carry-through of cesium droplets to the helium circulator. The original concept of cesium removal involved cooling the helium-cesium mixture through the heat exchanger, allowing the flow to impinge at a low velocity on a cooled surface at the base of the heat exchanger and finally passing the mixture through a cooler with large water-cooled surface area. The method proved totally inadequate, with a net removal efficiency of less than 2 per cent. In the circulator, cesium forms a highly viscous complex in the lubricating oil, with subsequent overheating of the circulator. Resin impregnation was employed originally on the circulator to achieve a leak-tight unit, so that the possible ingress of cooling water through breakdown of the epoxy resin represents a hazard and limits the tolerable overheat of the circulator. Under these conditions of cesium throughput to the circulator a maximum of 20 seeded operations, each of 15 sec duration and up to 0.5 % cesium

(total approximately 300 gm), can be carried out before experiments are suspended to allow purging of the circulator. Purging with lubricating oil takes several hours of cold running with helium alone.

The positive displacement cesium injection systems employed up to the present for seeded runs are not entirely satisfactory for short injection periods. The metered cesium liquid is brought via the injection system (Fig. 4.1) stop valve through the double skin of the loop and into the internal vaporizer (Fig. 4.2). The liquid path is relatively long and on short term injection ( $\sim 15$  sec), the seeding rate is not uniform. Continuous open circuit voltage measurements taken during seeded runs exhibit pulsing effects and indicate dilution of the actual injection rate, probably caused by limited and intermittent boiling of the cesium vapour.

The problems to be resolved are therefore :

to improve the efficiency of seed removal and recovery from the present 12 to 99 percent and so facilitate continuous and steady conditions of seed injection and throughput;

to improve the efficiency and handling capacity of the cesium vaporizer and superheat system to allow for seed fractions up to 1.5 atomic percent; and

to determine the temperature of the cesium vapour (probably using spectroscopic line-reversal techniques).

## 4.2 CYCLONE SEPARATION

### 4.2.1 Introduction

After the seeded run in March 1964 (RHT 32) a cyclone separator was considered for the removal of cesium, the design conditions being as follows:

helium mass flow,  $G = 6.7$  gm/sec

heat exchanger outlet temperature =  $100^{\circ}\text{C}$

Mach number at generator exhaust = 1

The cyclone inlet pressure is determined by the conditions in the generator duct and by the subsequent expansion in the diffuser. Assuming that the kinetic energy of the gas at the heat exchanger inlet is low compared with the kinetic energy at the diffuser inlet, then

$$\frac{P_1}{P_0} = \left( \frac{\gamma-1}{2} \right) \cdot M_1^2 + 1 \Big)^{\frac{\gamma}{\gamma-1}} \quad (\text{Pankhurst and Holder}^1) \quad \dots (4.1)$$



Now  $\gamma = 1.63$  for helium

$$M_1 = 1$$

$$\epsilon = 0.85$$

so that  $\frac{P_1}{P_0} = 1.82$

From McNab and Cooper<sup>2</sup>, when  $B = 0$ , the generator duct exhaust static pressure will be 16000 newton/m<sup>2</sup>. Thus, the diffuser exhaust static pressure will be

$$P_1 = \frac{16000 \times 1.82}{10^5}$$

$$P_1 = 0.291 \text{ ata}$$

The pressure change through the shell side of the heat exchanger will be negligible (Appendix) so that the above pressure will exist at the inlet to the cyclone, that is

$$P_2 = 0.291 \text{ ata}$$

Although it is known that the cesium condenses as a mist, the droplet size is not known. According to Perry<sup>4</sup>, condensed mists and fogs range in droplet size from  $0.1\mu$  to  $20\mu$ ; it is therefore proposed to design a cyclone having the highest possible efficiency for small particles. Since both pressure loss and collecting efficiency increase as the size of a cyclone is reduced, the cyclone will be made as small as possible provided the cyclone pressure loss does not exceed 0.5 psi. The cyclone will then have the maximum efficiency. Design data are presented in Perry<sup>4</sup> for cyclones having the proportions given in Fig. 4.6.

Thus, the pressure difference between the inlet and outlet of the cyclone is given as

$$\Delta P_{23} = \left[ F_{23} - 1 + \left( \frac{4 A_c}{\pi D_o^2} \right)^2 \right] h_2 \quad \dots (4.2)$$

For cyclones of the given proportions

$$F_{23} = 8h_2 \text{ (Perry<sup>4</sup>)}$$

so that

$$\Delta P_{23} = \left[ 7 + \left( \frac{4 A_2}{\pi D_o^2} \right)^2 \right] h^2$$

Also

$$\begin{aligned} A_2 &= H_c B_o \\ &= \frac{D_c^2}{8} \end{aligned}$$

and 
$$D_c = \frac{D}{2}$$

therefore 
$$\Delta P_{23} = \left[ 7 + \left( \frac{2}{\pi} \right)^2 \right] h_2$$

$$\Delta P_{23} = 7.405 h_2$$

The inlet velocity head 
$$h_2 = \frac{1}{2} \rho_2 V_2^2 \text{ dyne/cm}^2$$

where 
$$V_2 = \frac{G}{A_2 \rho_2}$$

Now 
$$G = 6.7 \text{ gm/sec}$$

$$A_2 = \frac{D_c^2}{8} \text{ cm}^2$$

$$\rho_2 = 3.8 \times 10^{-5} \text{ gm/cm}^3$$

and, hence 
$$V_2 = \frac{1.41 \times 10^6}{D_c^2} \text{ gm/sec}$$

and 
$$h_2 = \frac{3.78 \times 10^7}{D_c^4} \text{ dyne/cm}^2$$

from which it follows that

$$\Delta P_{23} = \frac{2.8 \times 10^8}{D_c^4} \text{ dyne/cm}^2$$

As previously stated

$$\Delta P_{23} = 0.5 \text{ psi}$$

so that

$$D_c^4 = \frac{2.8 \times 10^8}{3.45 \times 10^4}$$

and 
$$D_c = 9.48 \text{ cm } (= 3.73 \text{ in.})$$

Using the proportions given in Fig. 4.6 as a guide, a cyclone was constructed as detailed in Fig. 4.7.

#### 4.2.2 Construction

The cyclone must be inserted into a six-inch bore pipe downstream of the heat exchanger shell side. A conical section changer is needed to lead the inflowing gases smoothly into the tangential entry duct. This is shown as an integral part of the assembly in Fig. 4.7. The gas leaves the cyclone through a  $1\frac{5}{8}$  in. bore pipe having a  $90^\circ$  lobster-back bend, and exhausts into a six-inch bore pipe through a  $7^\circ$  diffuser.

The lower end of the  $1\frac{5}{8}$  in. bore exhaust pipe is fitted with a 22 gauge skirt to act as a drip-point within the inlet vortex for any liquid cesium film running down the outer wall of the exhaust. Without this skirt, any such cesium film would drip off at the exhaust lip and be carried away up the tube by the outgoing helium. A collecting pot is provided at the lower end of the cyclone to receive the cesium as it flows down the core. This pot can be drained into a lower pot through a  $\frac{1}{4}$  in. bore pipe and a bellows-sealed valve.

All parts are made of EN58B stainless steel and all joints argon arc welded. Unnecessary projections and roughnesses inside the cyclone were removed to improve the cyclone collecting efficiency.

#### 4.2.3 Pressure losses

Before considering the system pressure loss it is necessary to know if the gas Mach number is significant. The maximum average velocity will occur at the cyclone inlet. The Mach number there will be

$$M_2 = \frac{G}{A_2 \sqrt{\gamma P_2 \rho_2}} \cdot$$

$$\text{Now } G = 6.7 \text{ gm/sec}$$

$$A_2 = 10.56 \text{ cm}^2$$

$$\gamma = 1.63$$

$$P_2 = 0.291 \times 1.003 \times 10^3 \times 981$$

$$= 2.95 \times 10^5 \text{ dyne/cm}^2$$

$$\rho_2 = 3.8 \times 10^{-5} \text{ gm/cm}^2,$$

$$\text{so that } M_2 = 0.148$$

This is sufficiently low to be negligible in pressure loss calculations.

The overall pressure change in the separator system can be conveniently split into the following parts; inlet section-changer, cyclone, exhaust pipe and bend, diffuser. These are considered separately.

The cyclone inlet Reynolds number is

$$Re_2 = \frac{G D_H}{A_2 \mu_2}$$

$$\text{where } G = 6.7 \text{ gm/sec}$$

$$D_H = \frac{2 B_c H_c}{H_c + B_c}$$

$$= \frac{2 \times 0.875 \times 1.875 \times 2.54}{2.75}$$

$$= 3.03 \text{ cm}$$

$$A_2 = 10.56 \text{ cm}^2$$

$$\mu_2 = 0.023 \times 10^{-2} \text{ poise}$$

Therefore

$$Re_2 = 8.3 \times 10^3$$

The inlet flow is thus turbulent. The pressure loss in the section changer can therefore be expressed<sup>5</sup> as

$$P_1 - P_2 = \frac{1}{2} \rho_{12} (V_2^2 - V_1^2 + K V_2^2)$$

$$= \frac{1}{2} \frac{G^2}{\rho_{12}} \left[ \frac{1}{A_2^2} - \frac{1}{A_1^2} + 0.05 \right]$$

$$= \frac{1}{2} \frac{G^2}{\rho_{12}} \left[ \frac{1.05}{A_2^2} - \frac{1}{A_1^2} \right] \quad \dots\dots (4.3)$$

$$G = 6.7 \text{ gm/sec}$$

$$\rho_{12} = 3.8 \times 10^{-5} \text{ gm/cm}^3$$

$$A_2 = 10.56 \text{ cm}^2$$

$$A_1 = 182 \text{ cm}^2$$

so that the inlet section pressure loss,  $P_1 - P_2 = 5.58 \times 10^3 \text{ dyne/cm}^2$

and the cyclone pressure loss,  $P_2 - P_3 = 3.45 \times 10^4 \text{ dyne/cm}^2$

In the exhaust pipe and bend Reynolds number  $Re_3 = \frac{4 G}{\pi D_e \mu}$ ,

and

$$G = 6.7 \text{ gm/sec}$$

$$D_e = 4.12 \text{ cm}$$

$$\mu = 0.023 \times 10^{-2} \text{ poise,}$$

so that

$$Re_3 = \frac{4 \times 6.7}{\pi \times 4.12 \times 0.023 \times 10^{-2}}$$

$$= 9.01 \times 10^3$$

The pressure loss in the pipe is given by

$$P_3 - P_4 = \frac{4 f L}{D_e} \cdot \frac{G^2}{2 \rho_{34} A_3^2} \text{ dyne/cm}^2 \quad \dots\dots (4.4)$$

in which

$$f = 0.008$$

$$L = L_{st} + L_b$$

$$= 30 + 32 \times 4.12$$

$$= 161.7 \text{ cm}$$

$$G = 6.7 \text{ gm/sec}$$

$$\rho_{34} = 3.8 \times 10^{-5} \text{ gm/cm}^3$$

$$A_3 = 13.3 \text{ cm}^2,$$

so that the exhaust pipe and head pressure loss,  $P_3 - P_4 = 4.72 \times 10^3 \text{ dyne/cm}^2$

For a diffuser operating at low Mach number the pressure change is given by

$$\begin{aligned} P_5 - P_4 &= \frac{\rho_{54}}{2} \left[ V_4^2 (1 - \zeta) - V_5^2 \right] \text{ dyne/cm}^2 \\ &= \frac{G^2}{2 \rho_{54}} \left[ \frac{1}{A_4^2} (1 - \zeta) - \frac{1}{A_5^2} \right] \end{aligned} \quad \text{..... (4.5)}$$

in which  $\rho_{54} = 3.8 \times 10^{-5} \text{ gm/cm}^3$

$$G = 6.7 \text{ gm/sec}$$

$$A_4 = 13.3 \text{ cm}^2$$

$$A_5 = 182 \text{ cm}^2$$

$$\zeta = 0.088, \quad (\text{de Kovats and Desmur}^6)$$

so that the diffuser pressure loss,  $P_5 - P_4 = 3.04 \times 10^3 \text{ dyne/cm}^2$ .

$$\text{Thus } P_1 - P_2 = +5.58 \times 10^3$$

$$P_2 - P_3 = +3.45 \times 10^4$$

$$P_3 - P_4 = +4.72 \times 10^3$$

$$P_4 - P_5 = -3.04 \times 10^3$$

$$\begin{aligned} \text{so that } P_1 - P_5 &= +41.76 \times 10^3 \text{ dyne/cm}^2 \\ &= 0.605 \text{ psi} \end{aligned}$$

This can be expressed generally as

$$P_1 - P_5 = 1.05 \times 10^{-5} \frac{G^2 T_2}{P_2} \text{ psi} \quad \text{..... (4.6)}$$

#### 4.2.4 Collecting efficiency

The collecting efficiency of a cyclone depends upon the cyclone geometry, velocity of the carrier fluid at inlet, the nature of the material to be extracted, and the particle size. The data used in Fig. 4.8 were abstracted from Perry<sup>4</sup> and

shows the variation of collecting efficiency with a non-dimensional particle diameter  $\frac{D_p}{D_{PC}}$  for a cyclone as defined in Fig. 4.6.  $D_{PC}$  refers to the particle size for which the cyclone has an efficiency of 0.5. Considerations of the forces acting on the particles in a cyclone show that

$$D_{PC} = \frac{3 B_c}{16 \pi N_e} \cdot \frac{C_D Re_P}{D_P V_2} \cdot \frac{\mu_f}{(\rho_P - \rho)} \quad \dots (4.7)$$

where  $Re_P$  and  $C_D$  are related by

$$C_D = \frac{8 G^2 D_P^2 (\rho_P - \rho)}{A_2^2 r_c^2 \rho \mu_f^2 Re_P^2} \quad \dots (4.8)$$

For particle systems having  $0.0001 < Re < 2.0$ , Stokes' law is valid, and the above equations reduce to

$$D_{PC} = \sqrt{\frac{9 \mu B_c}{2 \pi N_e V_2 (\rho_P - \rho)}} \quad \dots (4.9)$$

Using the given design conditions, with Fig. 4.8, it is possible to predict (see table below) the collecting efficiency of the cyclone for cesium droplets of different sizes.

Thus, since  $\mu = 0.023 \times 10^{-2}$  poise

$B_c = 2.22$  cm

$N_e = 5$  (see Perry<sup>4</sup>)

$V_2 = 1.67 \times 10^4$  cm/sec

$\rho_P = 1.8$  gm/cm<sup>3</sup>,

then  $D_{PC} = 0.695 \times 10^{-4}$  cm

$D_P$	$D_P/D_{PC}$	$\eta$
0.5	0.72	0.37
1.0	1.44	0.65
1.5	2.16	0.82
2.0	2.88	0.90
2.5	3.6	0.94
3.0	4.32	0.96
3.5	5.03	0.97
4.0	5.75	0.97
4.5	6.47	0.98
5.0	7.20	0.98

**BLANK PAGE**

It must be noted here that these predicted collecting efficiencies refer to solid spherical particles. When the particles are liquid, the secondary vortices in the upper annular section of the cyclone can induce a flow of liquid along the inner walls towards the exhaust, thus reducing the efficiency. This effect can be reduced by introducing drip points. If the liquid particles agglomerate, then the collecting efficiency will increase.

#### 4.2.5 Pressure loss tests

Before installation into the MPD closed-loop, the cyclone separator was tested in the open circuit (Fig. 4.9) for pressure loss and collecting efficiency.

Air was drawn from the laboratory by a centrifugal fan and led by 3 in. bore piping into the cyclone inlet. The 3 in. pipe was extended into the conical section changer to ensure a smooth transition from 3 in. diameter. The air exhausted into the laboratory through the diffuser. Flow variation was possible by variation of the fan speed, or by a gate valve located just downstream to the fan.

For this test the  $\frac{1}{4}$  in. bore pipe at the lower end of the cyclone collecting pot was plugged with a rubber bung. The air mass flow was measured with a plain intake orifice<sup>7</sup> of outside diameter 5.72 cm, attached to the fan inlet. A paraffin filled inclined manometer measured the pressure difference across the orifice.

The pressure difference across the cyclone system was determined by measuring the static pressure of the flowing air just upstream to the conical section changer, using a water filled manometer, and assuming the exhaust pressure to be atmospheric at the diffuser outlet.

Measurements were taken for air flows ranging from 10 to 30 gm/sec, the observed orifice heads and static pressures being recorded graphically in Fig. 4.10. From these results

$$H = 36.2 h \quad \text{where the units of } h \text{ are in. of } H_2O,$$

$$H \text{ are cm of } H_2O..$$

$$\text{For the orifice, } G = 19.8 \sqrt{\frac{h P_a}{T_a}} \text{ gm/sec where the units of } h \text{ are in. of } H_2O,$$

$$P_a \text{ are mm of Hg,}$$

$$T_a \text{ are } ^\circ K.$$

The system pressure loss is therefore

$$P_1 - P_3 = 9.24 \times 10^{-2} \left[ \frac{G G^2 T_a}{P_a} \right] \text{ dyne/cm}^2$$



During the test

$$T_a = 296^\circ\text{K}$$

$$P_a = 747.65 \text{ mm Hg,}$$

so that  $P_1 - P_2 = 35.9 \text{ G}^2 \text{ dyne/cm}^2 \text{ (for air)}$

To determine the losses introduced by the cyclone itself, it is necessary to separate the losses in the section changer, exhaust pipe, and diffuser.

From equation (4.3)

$$P_1 - P_2 = \frac{1}{2} \frac{G^2}{\rho_{12}} \left( \frac{1.05}{A_2^2} - \frac{1}{A_1^2} \right) \text{ dyne/cm}^2$$

and, for air  $\rho_{12} = 1.17 \times 10^{-3} \text{ gm/cm}^3$

$$A_1 = 45.7 \text{ cm}^2$$

$$A_2 = 10.56 \text{ cm}^2,$$

so that  $P_1 - P_2 = 3.8 \text{ G}^2 \text{ dyne/cm}^2 \text{ (for air)}$

From equation (4.4)

$$P_3 - P_4 = \frac{4 f L}{D_e} \frac{G^2}{2 \rho_{34} A_3^2}.$$

Now

$$Re_3 = \frac{4 G}{\pi D_e \mu_3}$$

$$D_e = 4.12 \text{ cm}$$

$$\mu_3 = 0.0182 \times 10^{-2} \text{ poise}$$

$$G = 10 \text{ to } 30 \text{ gm/sec}$$

therefore  $Re_3 = 1.7 \times 10^4 \text{ to } 5.1 \times 10^4$

and then  $f = 0.0065 \text{ to } 0.0053$

Taking an average value

$$f = 0.0059$$

Also  $\rho_{34} = 1.17 \times 10^{-3} \text{ gm/cm}^3$

$$A_3 = 13.3 \text{ cm}^2$$

$$L = 161.7 \text{ cm,}$$

so that  $P_3 - P_4 = 2.24 \text{ G}^2 \text{ dyne/cm}^2$

From equation (4.5)

$$P_5 - P_4 = \frac{G^2}{2 \rho_{54}} \left[ \frac{1}{A_4^2} (1 - \zeta) - \frac{1}{A_5^2} \right]$$

$$\rho_{54} = 1.17 \times 10^{-3} \text{ gm/cm}^3$$

$$A_4 = 13.3 \text{ cm}^2$$

$$A_5 = 182 \text{ cm}^2$$

$$\zeta = 0.088,$$

so that  $P_5 - P_4 = 2.57 \text{ G}^2 \text{ dyne/cm}^2$

Now the cyclone pressure loss is  $(P_2 - P_3)$  and

$$\begin{aligned} (P_2 - P_3) &= (P_1 - P_3) - (P_1 - P_2) - (P_3 - P_4) - (P_4 - P_5) \\ &= (35.9 - 3.8 - 2.24 + 2.57) \text{ G}^2 \text{ dynes/cm}^2 \end{aligned}$$

$$(P_2 - P_3) = 32.43 \text{ G}^2 \text{ dynes/cm}^2.$$

Expressed in inlet velocity heads,

$$(P_2 - P_3) = 8.45 h_2.$$

#### 4.2.6 Collection efficiency tests

To simplify the experimental techniques, the cyclone was tested with a mixture of air and carbonyl iron powder simulating cesium (manufactured by Inco Mond), the particles being spherical and of known sizes. Two grades of powder were used: MDG and MCHP of average particle sizes 2.9 and 7 micron.

The iron powder was injected into the air through the static pressure tapping upstream to the cyclone section changer in the following manner. Powder was placed in a pot fitted with a perspex lid and, by blowing dried nitrogen through a 1/16 in. bore pipe tangentially into the pot base, the powder could be fluidized and carried through an 1/8 in. bore pipe into the main air flow. To collect the powder separated by the cyclone, a weighed glass boiling tube was attached to the 1/4 in. pipe at the lower end of the cyclone by a bored rubber bung.

During a test run, a known weight of either MDG or MCHP grade powder was placed in the clean fluidizer pot and the lid sealed. The main air flow was adjusted to the required value. Then the nitrogen flow into the fluidizer was started and adjusted until the powder was seen to be thoroughly entrained in the induced vortex. Shortly after this condition was achieved, powder could be seen settling at the bottom of the glass collecting tube. From time to time during the run, the cyclone was struck with a plastic hammer to release any powder clinging to the cyclone inner walls. When the fluidizing pot was empty the air flow was increased to a maximum to clean the cyclone of collected powder. The collecting tube was detached, closed with a weighed bung, and weighed. This procedure was repeated for various air flows using each of the powders.

After completion of the measurements the cyclone and section changer were carefully removed from the circuit. Iron powder had settled on the bottom of the pipe below and downstream of the injection point in the upper wall of the pipe. Powder had also collected in the dead space between the section changer cone and the length of 3 in. pipe protruding into the section changer (Fig. 4.9). The powder was deposited in layers of light grey and brown grey, showing that both grades were present. All of this powder was collected and weighed.

The measured air flows, injected weights of powder, and collected weights of powder are recorded in the following table.

Test No.	G, gm/sec	Powder grade	D <sub>P</sub> , micron	W <sub>i</sub> ', gm	W <sub>s</sub> ', gm	W <sub>i</sub> ', gm	W <sub>c</sub> ', gm	η	D <sub>PC</sub> , micron	$\frac{D_P}{D_{PC}}$
1	9.1	MCHD	7	110	31.2	78.8	78.8	0.997	1.52	4.6
2	13.9	MDG	2.9	23.1	0.008	23.1	22.4	0.97	1.25	2.32
3	32.5	MCHD	7	69.2	5.38	63.8	75.4	1.15	0.806	8.68
4	9.2	MDG	2.9	79.5	4.2	75.3	51.5	0.686	1.46	1.98
5	5.65	MCHD	2.9	19.5	1.69	17.8	14.1	0.794	1.935	1.5
6	9.32	MCHD	7	48.2	13.7	34.5	31.2	0.92	1.415	1.95
7	33.3	MDG	2.9	23.2	0.34	22.9	23.4	1.02	0.757	1.0
8	5.65	MCHD	7	36.2	16.7	19.2	21.2	1.09	1.935	3.62

Before calculating collecting efficiencies it was necessary to correct the measured injected weights for the amount of powder lost by settling during each run. This was done by proportioning the total deposited weight according to the efficiency as a gravity settler of the 3 in. pipe downstream to the injection point for each set of test conditions. According to Perry<sup>4</sup>, a rectangular gravity settler has the efficiency:

$$\eta_s = \frac{u_t L_s}{H_s V}$$

The weight of powder lost by settling during each test was thus estimated as

$$W_s = \frac{W_i \eta_s}{\sum W_i \eta_s} \cdot \sum W_s$$

The weight of powder actually entering the cyclone was calculated as

$$W_i' = W_i - W_s$$

and the collecting efficiency as

$$\eta = \frac{W_c}{W_i'}$$

The ratio  $D_P/D_{PC}$  was evaluated for each test using equation (4.9). The appropriate values of  $C_D$  and  $Re_P$  were found from equation (4.8), in conjunction with Fig. 114 of reference 4 which shows the variations of drag coefficient with Reynolds number for spheres.

The results of these tests are presented in the above table and in Fig. 4.11. The  $D_P/D_{PC}$  characteristic recommended by Perry<sup>1</sup> is also given. The two curves do not differ significantly, so that the design is satisfactory.

On the basis of the measured characteristic, the expected collecting efficiency has been calculated for the design conditions (Fig. 4.12).

#### 4.2.7 Loop operation

The unit was fitted into the loop (Fig. 4.3) at the heat exchanger outlet; the performance from seeded runs RHT 33 and 35 (and later runs not reported) showed an actual cesium removal efficiency of ~12 per cent. A commercial Centrifix Separator has been ordered and will be installed in the loop for seeded runs planned early in December 1964. A removal efficiency better than 99 per cent is guaranteed.

### 4.3 ELECTROSTATIC PRECIPITATION

Careful consideration has been given to the feasibility of a cesium removal system employing electrostatic precipitation techniques for the cesium-helium mist. Such a system with negligible pressure loss and very high available efficiency is extremely attractive for application in the closed cycle MPD power generation facility. Whereas with a cyclone separator the separation efficiency for gas-borne particles of less than 50 micron falls off rapidly, the electrostatic precipitator maintains a high separation efficiency for small particles.

A theoretical feasibility study has been carried out and small development units built and tested. At present, stable coronas have been achieved with helium alone (Fig. 4.3) but insufficient operation has been possible with cesium-helium flows to prove performance potential.

#### 4.3.1 Principles and theory

In electrostatic precipitation unwanted charged particles drift out of the main gas flow under the influence of an electric field, the efficiency of removal depending upon the applied voltage. Particles must be electrically charged, one means of achieving this being to create a corona by applying a sufficiently strong field between the electrodes. Two types of d.c. corona can be set up, depending upon whether the corona electrode is positive or negative. Positive corona is set up at higher voltages than for negative corona in hydrogen, carbon dioxide and nitrogen; in helium, oxygen and air the critical electric field is lower for positive

than for negative corona at pressures greater than 1 cm Hg, but higher at lower pressures. However, positive corona is usually employed because of its more uniform distribution; negative corona appears as tufts or beads along the corona electrode, the presence of which complicates the precipitation mechanism and renders theoretical analysis difficult.

Charging of the particle takes place by ionic impact, either by attachment to gas ions migrating to the cathode or with ions under thermal motion (effective only for particles of less than  $\frac{1}{2}$  micron diameter).

A full analysis shows that the number ( $n$ ) of elementary charges ( $e$ ) acquired in time  $t$  by a spherical particle under migrating ion impact conditions is given by

$$n = \frac{p E_c a^2}{e} \cdot \frac{t}{t + \frac{1}{\pi N e k}} \quad \dots\dots (4.10)$$

where  $p$  is a constant depending upon the particle material,

$a$  is the radius of the particle,

$E_c$  is the field strength at corona electrode surface,

$N$  is the ion concentration, and

$k$  is the ion mobility.

As  $t \rightarrow \infty$ , then  $\frac{t}{t + \frac{1}{\pi N e k}} \rightarrow 1$

In practice maximum charge is attained in a fraction of a second, and

$$n(\text{MAX}) = \frac{p E_c a^2}{e}$$

or maximum charge  $q = n(\text{MAX})e$

so that  $q = p E_c a^2$ . \dots\dots (4.11)

The constant  $p = 3$  for conducting particles and, for non-conducting particles  $p = \frac{e \epsilon}{\epsilon + 2}$  where  $\epsilon$  is the dielectric constant.

Under conditions of thermal ion motion, the number of charges accepted by a particle is

$$n = \frac{a K T}{e^2} \log \left( 1 + \frac{\pi a s N e^2 t}{K T} \right) \quad \dots\dots (4.12)$$

where  $K$  is Boltzmann's constant,

$T$  is absolute temp,

$s$  is r.m.s ion velocity, and

$N$  is ion concentration.

For concentric cylinders it has been shown that a corona can only be produced when the ratio of outer to inner radii of electrodes exceeds a certain critical limit: the starting voltage for a corona depends upon the size and shape of the corona electrode (wire) and interspace.

The field strength  $E$  between two radii  $R_1$  and  $R_2$  can be defined by

$$V = \int_{R_2}^{R_1} E \, dr$$

where  $V$  is the potential difference between  $R_1$  and  $R_2$ .

The field strength at a radius  $r$  is given by

$$E = \frac{V}{r \log_e R_2/R_1} = \frac{c}{r} \quad \dots\dots (4.13)$$

$$\text{where } c = \frac{V}{\log_e R_2/R_1} \quad \text{constant}$$

In the presence of an ionic space charge the field is modified to

$$\frac{dE}{dr} + \frac{E}{r} - 4\pi\sigma = 0 \quad \dots\dots (4.14)$$

where  $\sigma$  is space charge per unit volume.

At radius  $r$  the ionic current  $i$  per unit length of electrode wire is given by

$$\begin{aligned} i &= 2 \pi r \sigma \cdot (\text{ion velocity}) \\ &= 2 \pi r \sigma E k \end{aligned} \quad \dots\dots (4.15)$$

where  $k$  is ion mobility.

From equations (4.14) and (4.15) the following equation may be obtained

$$E = \left( \frac{2i}{k} + \frac{c^2}{r^2} \right)^{\frac{1}{2}}$$

and, for large values of  $i$  and  $r$ ,  $\frac{c^2}{r^2}$  can be neglected

$$\text{so that } E = \left( \frac{2i}{k} \right)^{\frac{1}{2}} \quad \dots\dots (4.16)$$

When particles are present equation (4.16) is modified to

$$E = \left( \frac{2i}{k} \right)^{\frac{1}{2}} \cdot \left( 1 + \frac{1}{3} p S r \right) \quad \dots\dots (4.17)$$

where  $S$  is the surface area of particles per unit volume.

This equation shows a linear relationship between field strength and radius, which is dependent upon the nature and concentration of particles. Fig. 4.13 shows how

particles effect the field strength.

The force  $F_1$  acting on a particle with charge  $q$  in a field  $E_p$  is given by

$$F_1 = q E_p.$$

From equation (4.11)

$$F_1 = p E_c E_p a^2$$

where  $E_c = E_p$  for a high particle concentration.

The viscous drag, by Stokes' law, is

$$F_2 = 6 a \mu w \pi$$

where  $a$  is particle radius,

$\mu$  is viscosity of gas, and

$w$  is velocity.

The transverse terminal velocity  $u$  is reached fairly quickly, so that

$$F_1 = F_2$$

$$u = \frac{p E_c E_p a}{6 \pi \mu}$$

Therefore

For a conducting particle  $p = 3$  and therefore

$$u = 0.16 \frac{a E_c E_p}{\mu} \quad \dots (4.18)$$

The longitudinal velocity for laminar flow  $v$  is given by

$$v = 2V \left( 1 - \frac{y^2}{R^2} \right) \quad \dots (4.19)$$

where

$V$  = average flow of gas

$y$  = radius from centre

$R$  = outer radius of tube.

A particle close to the inner electrode will take the longest time of all to precipitate, and will give a theoretical maximum for the length of tube required.

The longitudinal velocity of such a particle =  $2V$

$$\text{at } y = 0 \quad \dots (4.20)$$

and the length of tube necessary to precipitate a particle is given by

$$L = \frac{4}{3} \cdot \frac{vR}{u}$$

and from equations (4.18), (4.20) the maximum length of tube required is given by

$$L_{(MAX)} = \frac{4}{3} \cdot \frac{2 V R \mu}{0.16 a_{MAX} E_c E_p}$$

where  $a_{(MIN)}$  is the minimum radius of particle in the system.

Therefore 
$$L_{(MAX)} = \frac{16.7 V R \mu}{E_c E_p a_{(MIN)}} \dots\dots (4.21)$$

If  $V$  is in cm/sec,  $a$  and  $R$  in cm,  $\mu$  in poise,  $E_c$  and  $E_p$  in esu/cm (300 volt/cm = 1 esu/cm) then  $L$  will be in cm.

#### Sample Calculation

Without full investigation, both theoretical and experimental, the critical voltage  $E_c$  at which the corona appears cannot be determined. The potential difference to precipitate all cesium particles can be calculated from the following equation.

$$L_{(MAX)} = \frac{16.7 V R \mu}{E_c E_p a_{(MIN)}} \dots\dots (4.22)$$

The following dimensions and flow data are used:

maximum length for precipitation	$L_{(MAX)}$	= 2 m
radius of tube	$R$	= 7 cm
mean helium flow	$V$	= 4.5 m/sec
viscosity of helium at 150°C	$\mu$	= $25.5 \times 10^{-5}$ poise
radius of smallest particle	$a_{(MIN)}$	= 1 micron

The product  $E_c E_p$  is found to be  $670 \text{ (esu/cm)}^2$ . If it is assumed that  $E_c = E_p$  then  $E_c \approx (670)^{1/2} \approx 26 \text{ esu/cm} = 7800 \text{ volt/cm}$  and the potential difference required is about 40 kilovolts.

The above calculation allows for extreme conditions; an increase in minimum particle size, or a decrease in temperature (and hence viscosity), flow rate, or radius of the tube would lower the potential difference needed to produce the corona.

#### 4.4 ULTRANSONIC CESIUM REMOVAL SYSTEMS

Ultrasonic techniques are also being considered to promote cesium droplet agglomeration and facilitate its removal from the helium flow.

For the next series of seeded runs a 500 watt power source is to be used to drive an ultrasonic transducer titanium 318A alloy probe (Fig. 4.4). Transmitted powers of up to 1 watt are expected. The probe is to be mounted at the bottom of a vertical glass column (6 in. diameter, 8 ft high) and is arranged to propagate axially in the direction of the helium-cesium flow. Stringent pre-sealing tests will be carried out to determine possible fatigue characteristics of the glass system.



Should the electrostatic precipitator and ultrasonic systems prove practically feasible, a combination of the two will give extremely high efficiency of seed removal.

#### 4.5 CESIUM VAPORIZATION AND SUPERHEAT

Until the problem of seed removal is resolved, only short duration seeded injection will be possible. For the immediate future a considerable programme is planned for investigations at nozzle inlet temperatures lower than  $1800^{\circ}\text{K}$ . A system has been designed (Fig. 4.5) (and is in the final development stage) to temporarily replace the high temperature helium heater, high temperature transfer and cesium vaporizer. The system is horizontal, axially in line with and connected directly to a subsonic nozzle and generator duct. It comprises a stainless steel mesh electrical heater connected mechanically in series with a boron nitride insulated tungsten element electrical resistance heater, the tungsten element being in three stages to allow for power balance. Cesium is to be injected through three jets and atomized with the helium flow prior to entry into the stainless steel mesh heater (available power 27 kilowatts) which takes helium-cesium to  $\approx 900^{\circ}\text{C}$  (cesium in vapour state). The second-stage tungsten heater (power 20 kilowatts) raises the helium-cesium temperature (mass flow helium 5 gm/sec at 1 ata; cesium fraction 1.5 %/o) to approximately  $1800^{\circ}\text{K}$ .

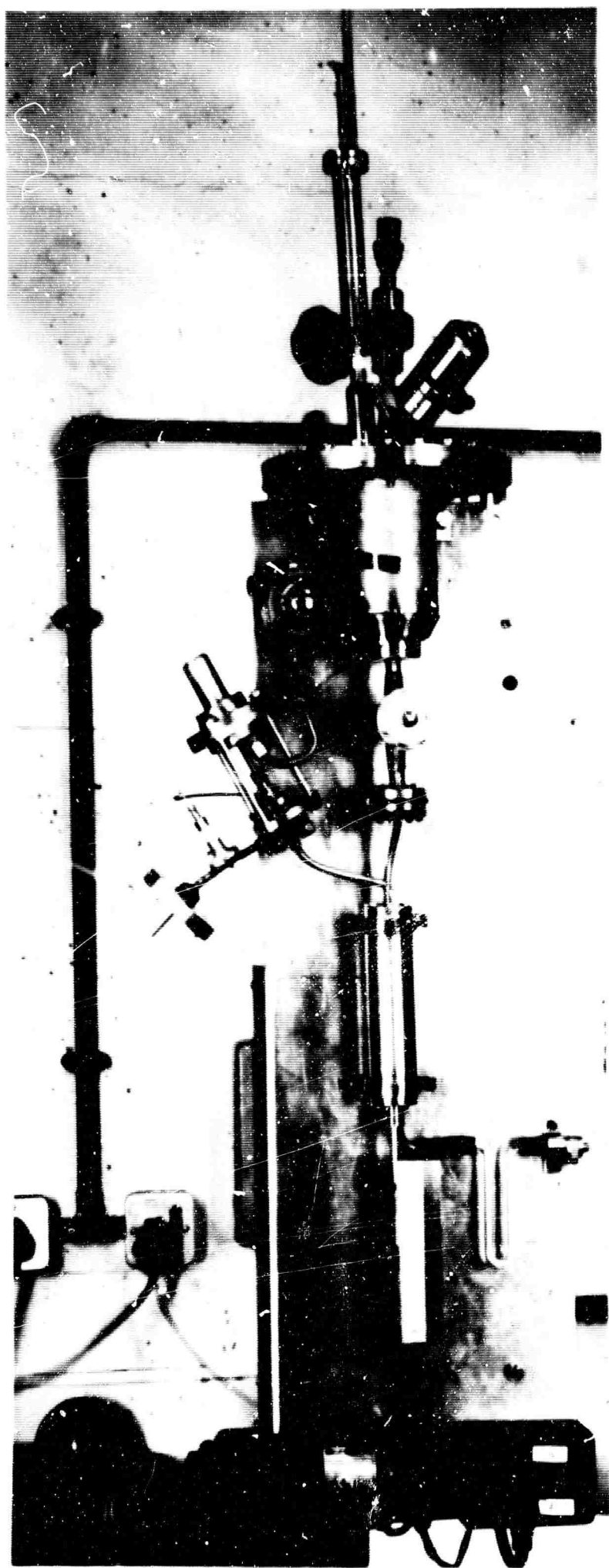
Careful consideration has been given in the design to the problems of electrical breakdown due to the presence of cesium. The unit is to be commissioned shortly and if satisfactory should give additional data on the problems of duct surface contamination.

#### REFERENCES

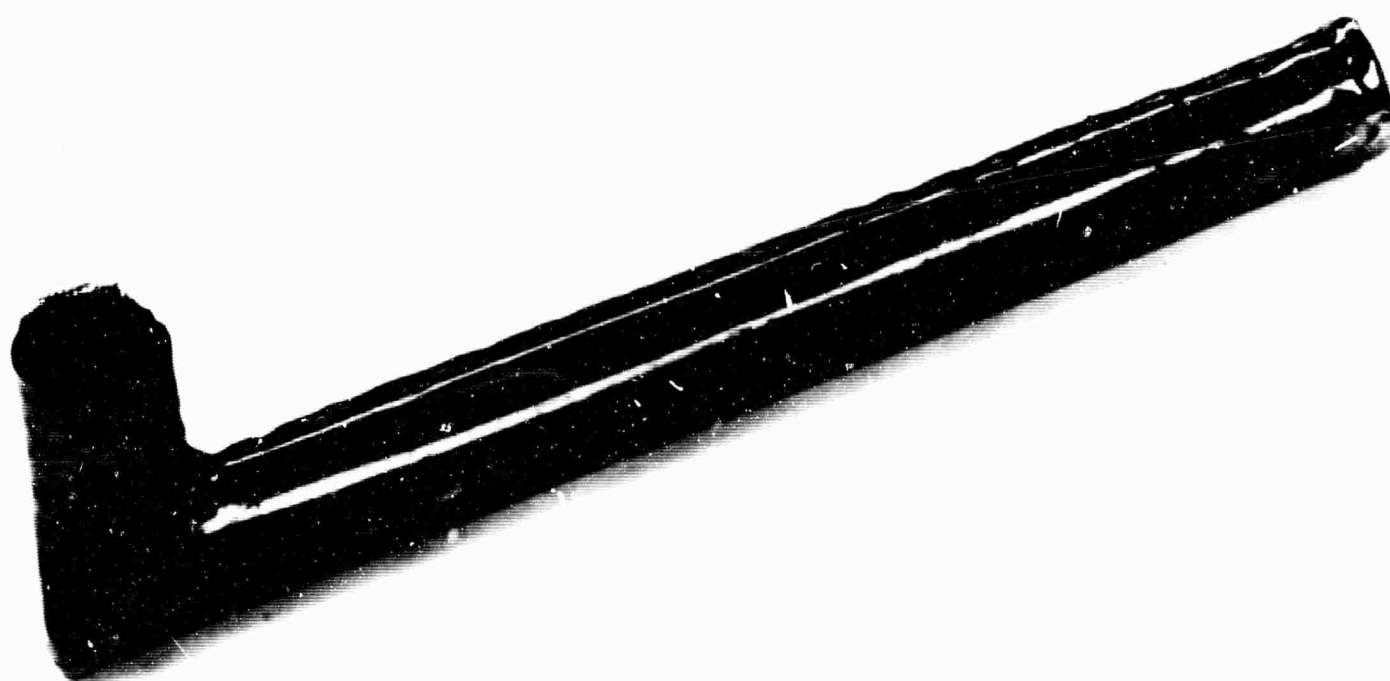
- 1 PANKHURST, R.C. and HOLDER, D.W. Wind tunnel technique. Sir Isaac Pitman and Sons Ltd. 1952
- 2 McNAB, I.F. and COOPER, N.A. Flow processes in MPD generators. IRD 63-82 1963
- 3 He-He recuperative heat exchanger for the IRD MPD circuit. IRD Tech. Memo. ref. TA/MJB, 20th June 1963
- 4 PERRY, J.H. (Editor). Chemical Engineers' Handbook. 3rd ed. 1950. McGraw-Hill Book Co. Inc.
- 5 McADAMS, W.H. Heat transmission. 3rd ed. 1954. McGraw-Hill Book Co. Inc.
- 6 DE KOVATS, A. and DESMUR, G. Pumps, fans, and compressors. Blackie 1958
- 7 LINFORD, A. Flow measurement and meters. 2nd ed. E. and F.N. Spon Ltd. 1961.

# NOMENCLATURE (Chapter 4)

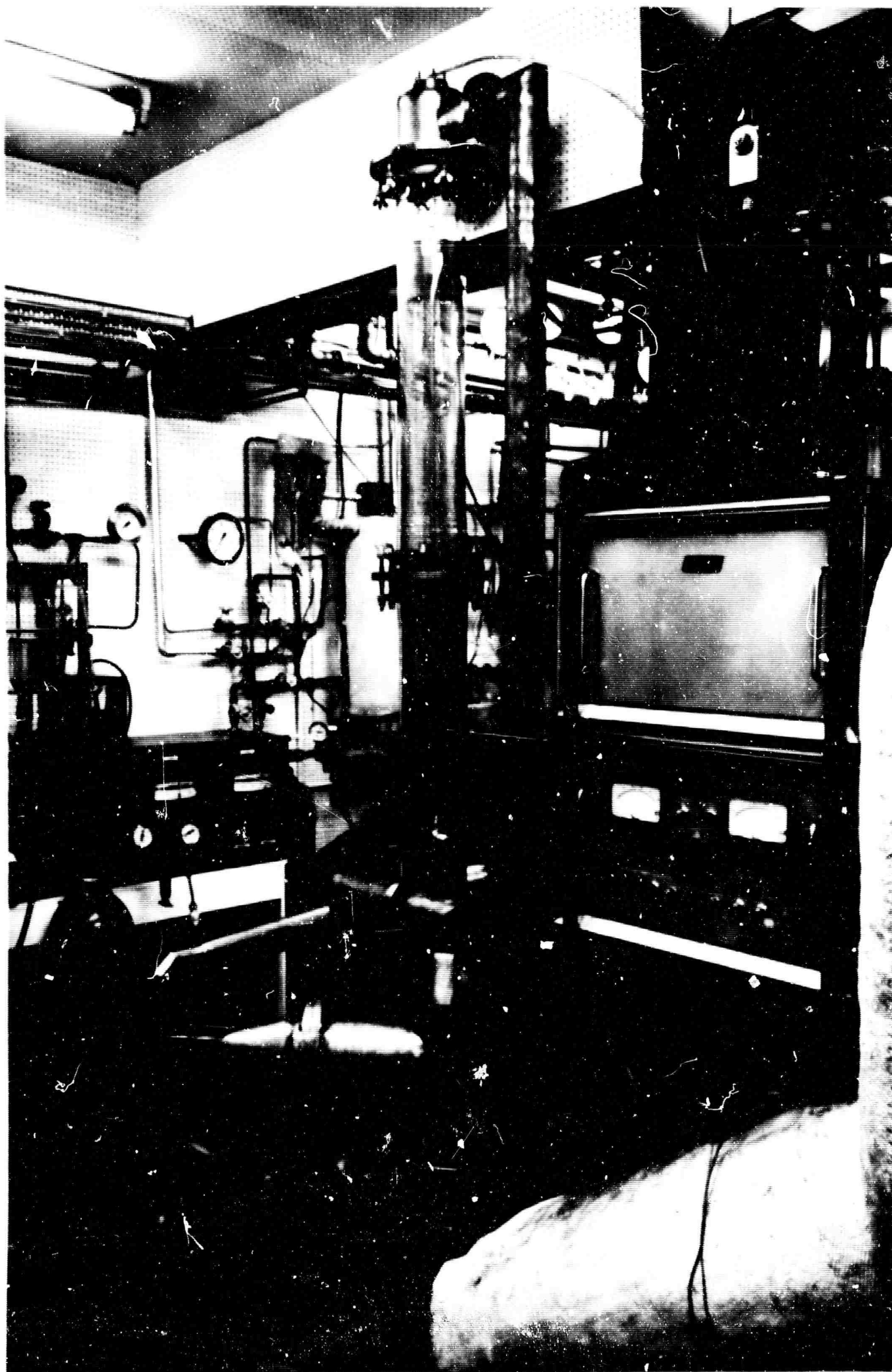
A	fluid flow area	$\mu$	viscosity
B	magnetic field	$\zeta$	diffuser losses
$B_c$	cyclone inlet width	$\rho$	density
$C_D$	drag coefficient	$\rho_p$	particle density
$D_c$	cyclone inner diameter	<u>Suffices</u>	
$D_e$	cyclone exhaust diameter	0	refers to generator duct outlet
$D_p$	particle diameter	1	refers to heat exchanger inlet
$D_{PC}$	cut particle diameter	2	refers to cyclone rectangular inlet
F	frictional losses	3	refers to cyclone outlet
f	fanning friction factor	4	refers to exhaust diffuser inlet
G	mass flow	5	refers to exhaust diffuser outlet
g	gravitational acceleration	P	refers to particle
$h_2$	cyclone inlet velocity head	f	refers to fluid
h	orifice pressure difference	a	refers to ambient conditions
H	manometer head		
$H_c$	cyclone inlet height		
$H_s$	height of gravity settler		
K	dimensionless coefficient		
L	pipe length for friction loss		
$L_{st}$	length of straight pipe		
$L_b$	equivalent length of bend		
$L_s$	length of gravity settler		
M	Mach number		
Ne	No. of turns by particle in cyclone		
P	pressure		
Re	Reynolds number		
$r_c$	radius of particle path		
T	temperature		
$u_t$	terminal velocity of particle		
V	velocity of gas		
$W_i$	injected weight of powder		
$W'_i$	corrected injected weight		
$W_s$	settled weight of powder		
$W_c$	collected weight of powder		
$\gamma$	ratio of specific heats		
$\Delta$	differential		
$\epsilon$	diffuser efficiency		
$\eta$	collecting efficiency		
$\eta_s$	gravity settler efficiency		



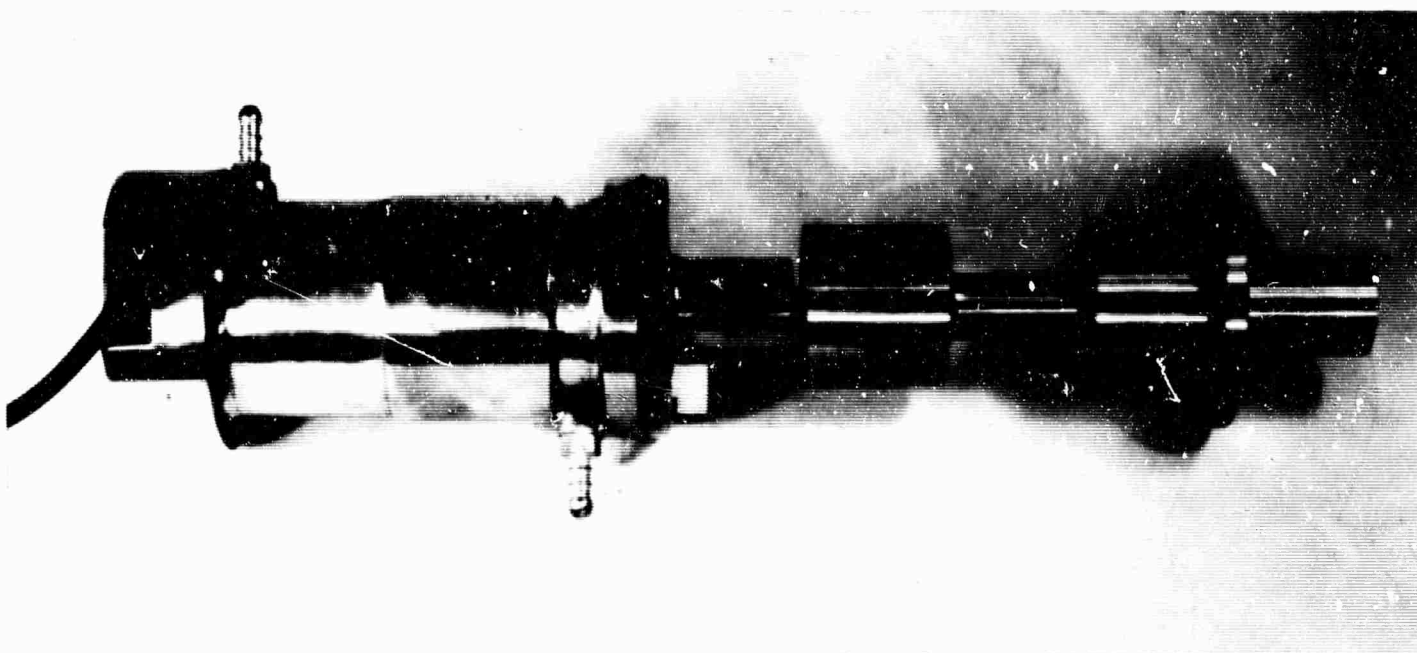
CESIUM INJECTION EQUIPMENT



CESIUM VAPORIZER

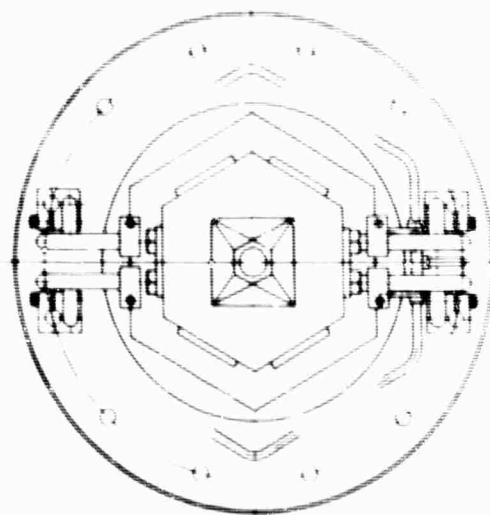
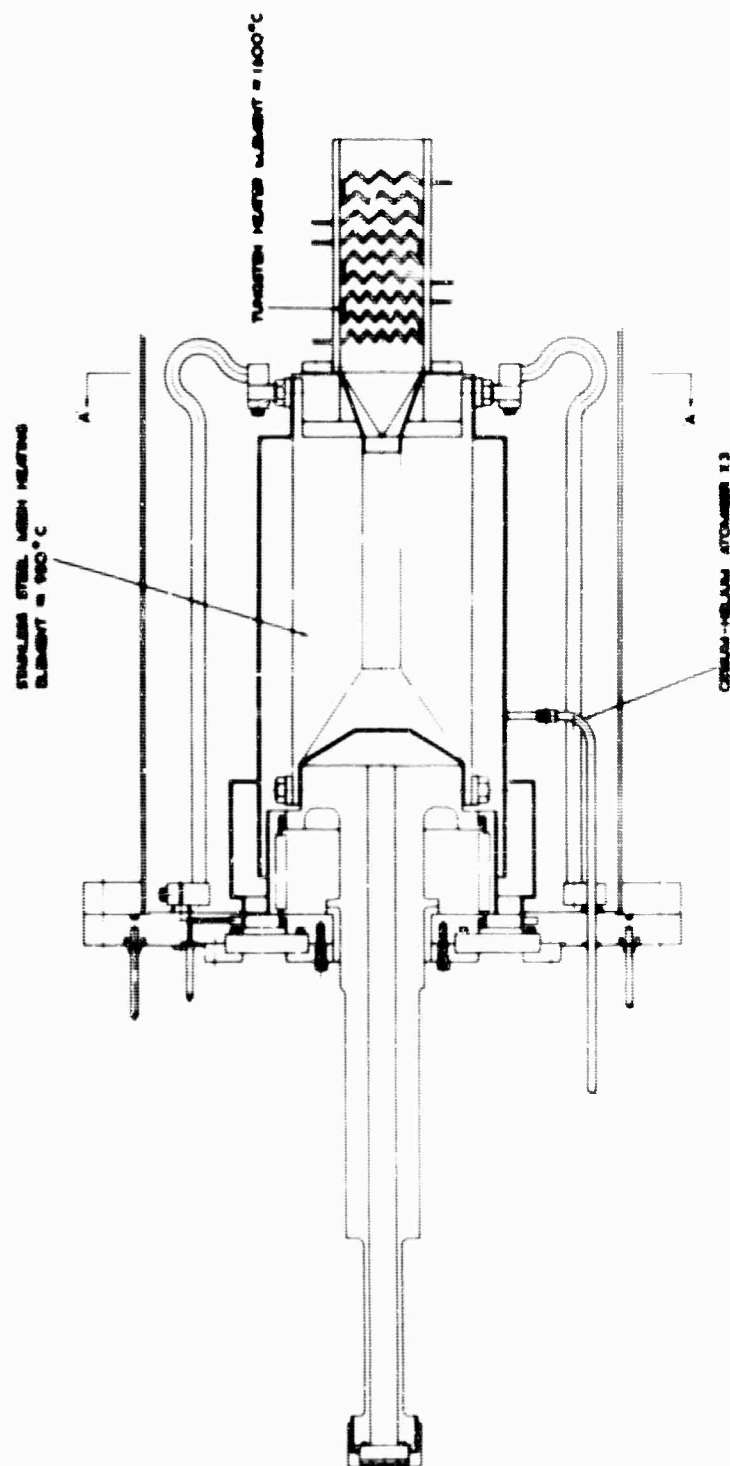


ELECTROSTATIC PRECIPITATOR AND CYCLONE SEPARATOR



ULTRASONIC TRANSDUCER WITH TITANIUM PROBE

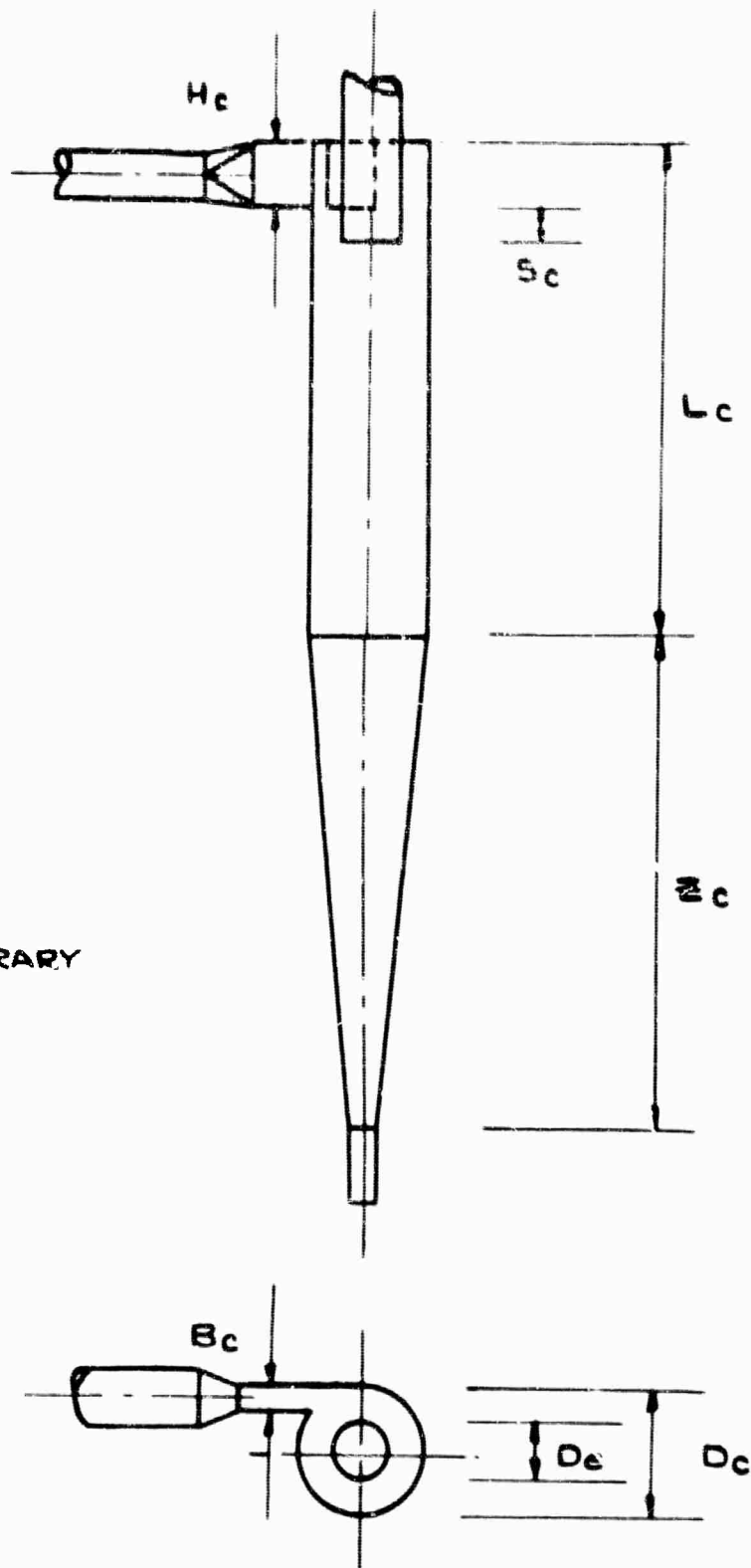
FIG 4.4



CESIUM VAPOURISATION AND SUPERHEAT SYSTEM

FIG 4.5

$$\begin{aligned}
 B_c &= D_c/4 \\
 D_e &= D_c/2 \\
 H_c &= D_c/2 \\
 L_c &= 2 D_c \\
 S_c &= D_c/8 \\
 E_c &= 2 D_c \\
 J_c &= \text{ARBITRARY}
 \end{aligned}$$

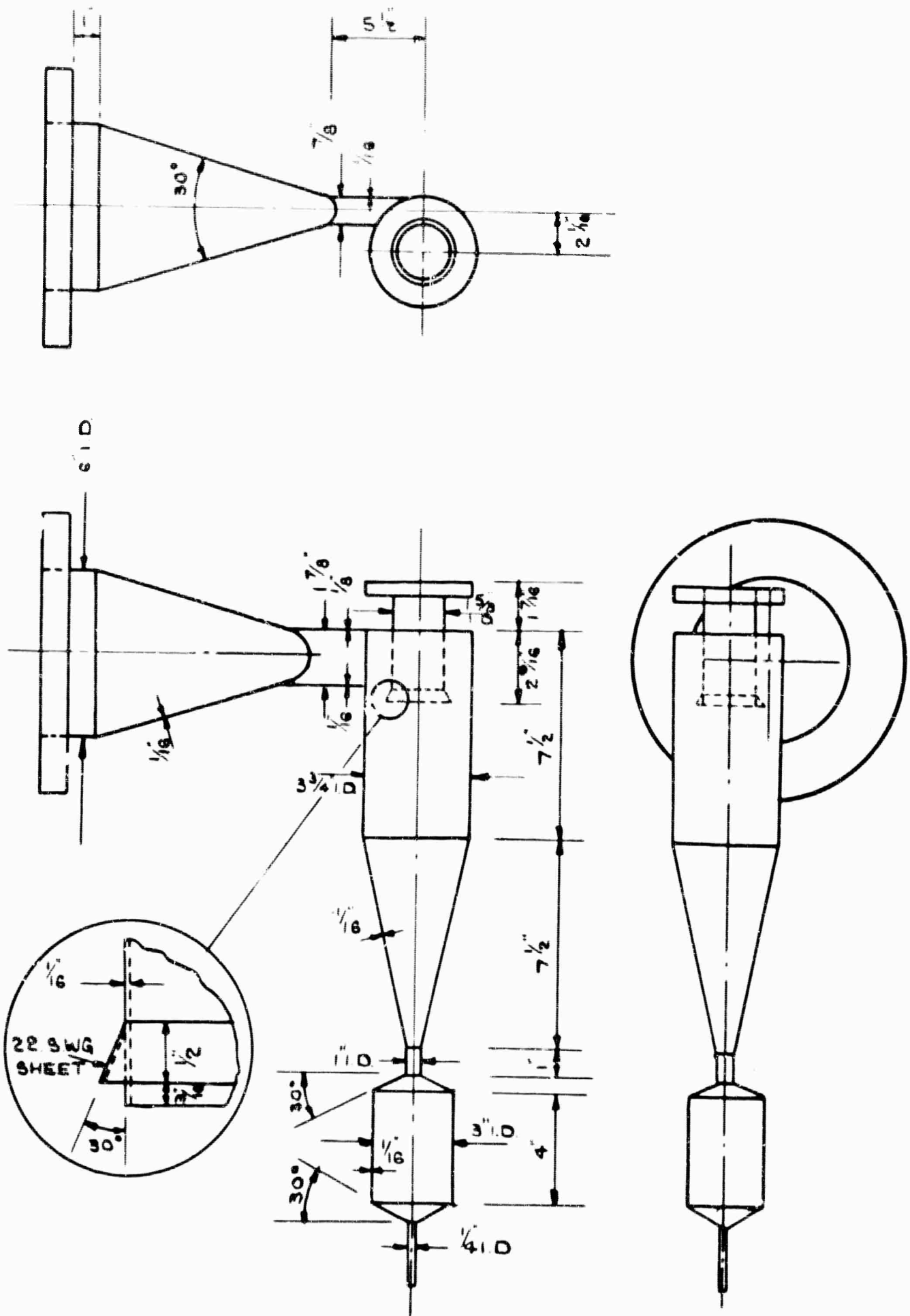


AFTER PANKHURST AND HOLDER'

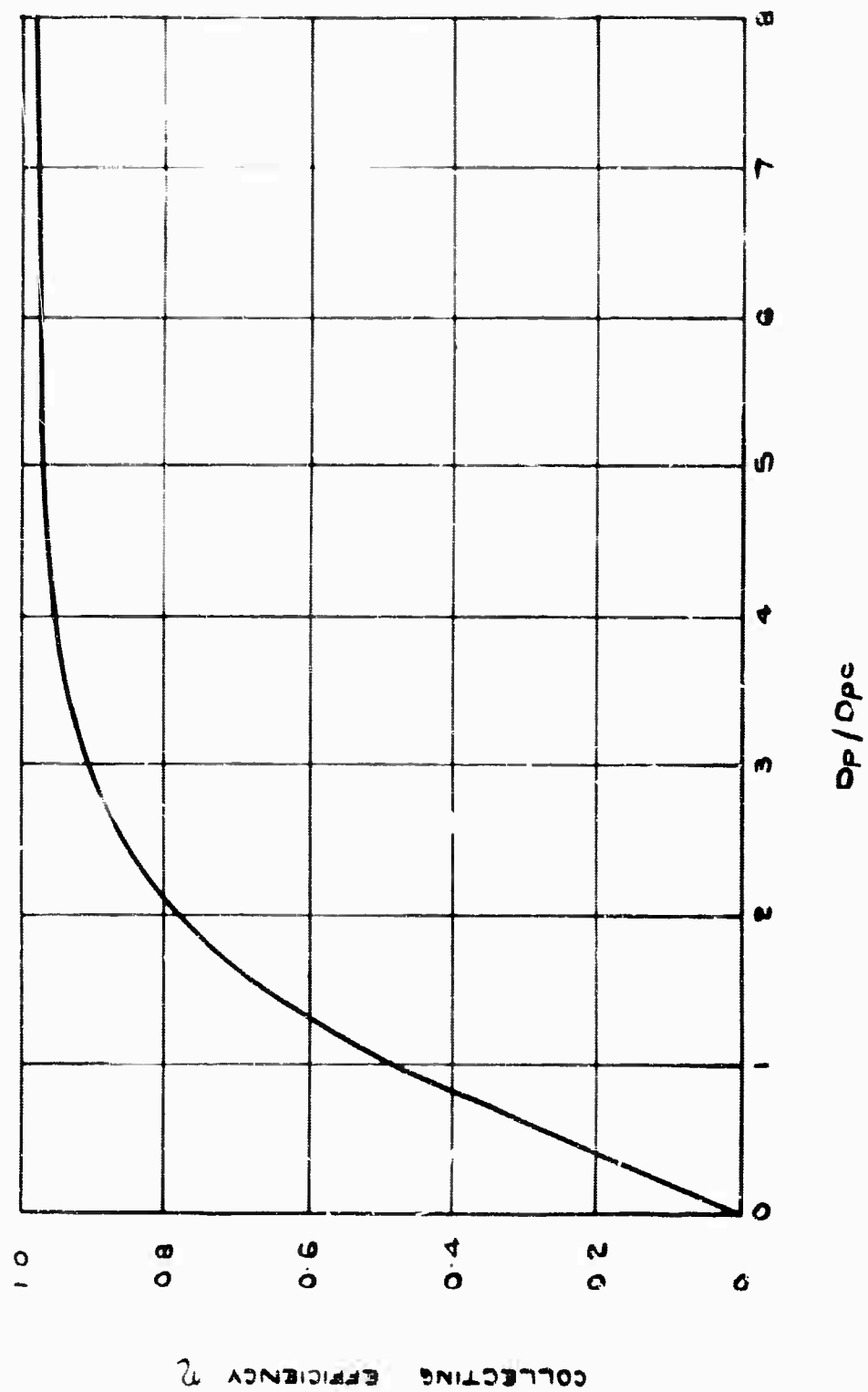
RECOMMENDED CYCLONE PORTION

FIG 4-6

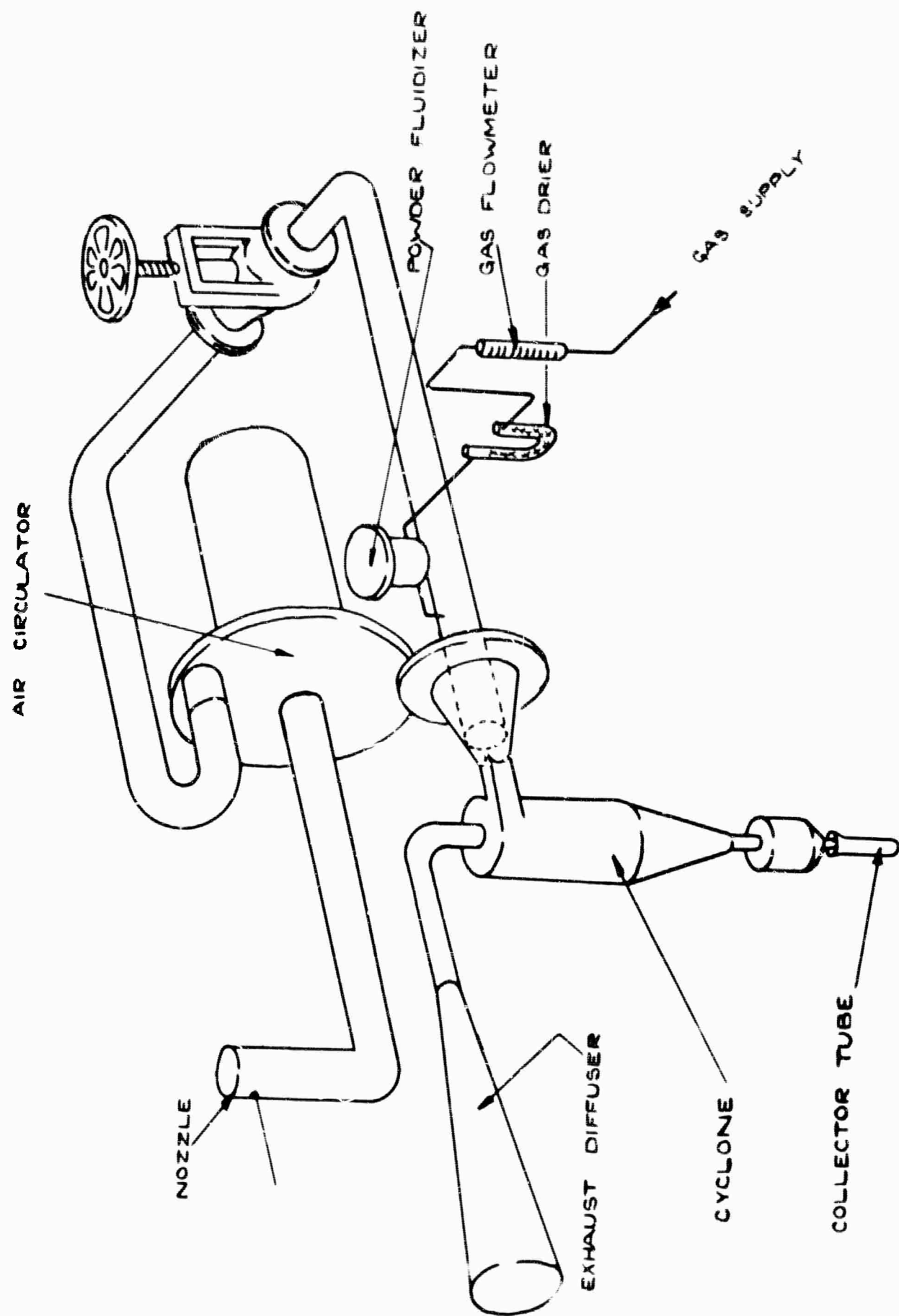




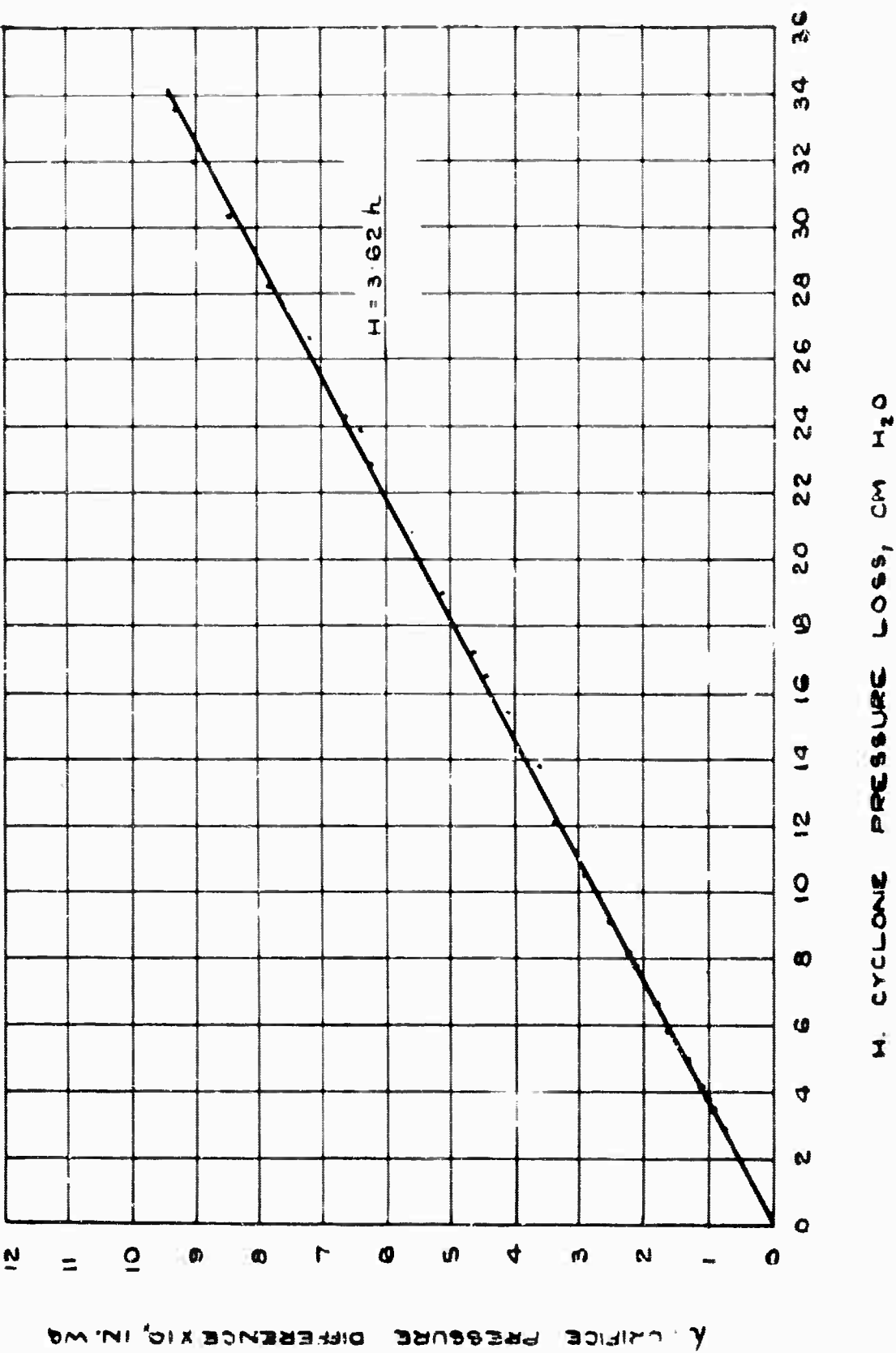
CESIUM CYCLONIC SEPERATOR FOR M.P.D. CIRCUIT



CYCLONE COLLECTING CHARACTERISTIC



CYCLONE TEST CIRCUIT



CYCLONE PRESSURE LOSS TEST RESULTS

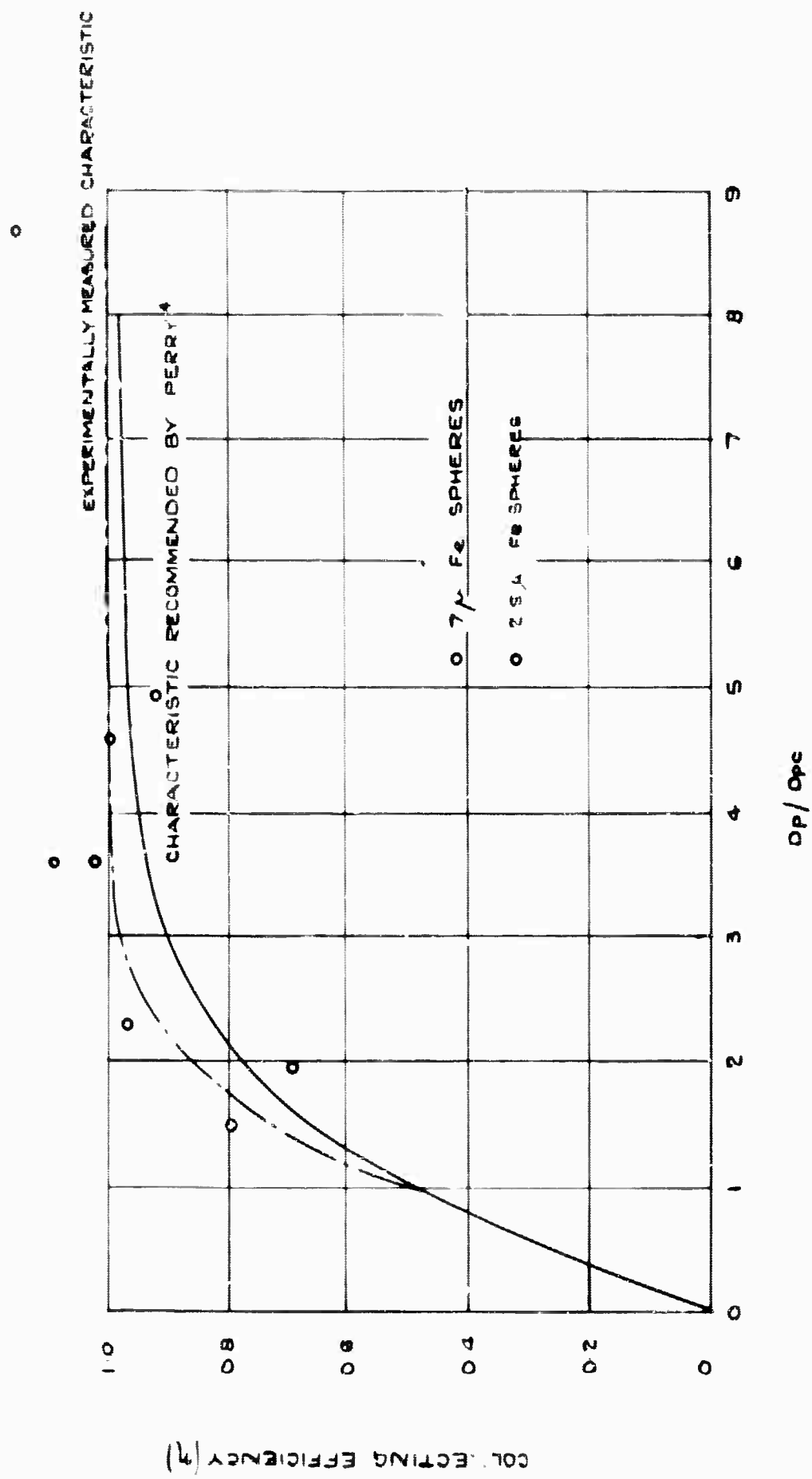
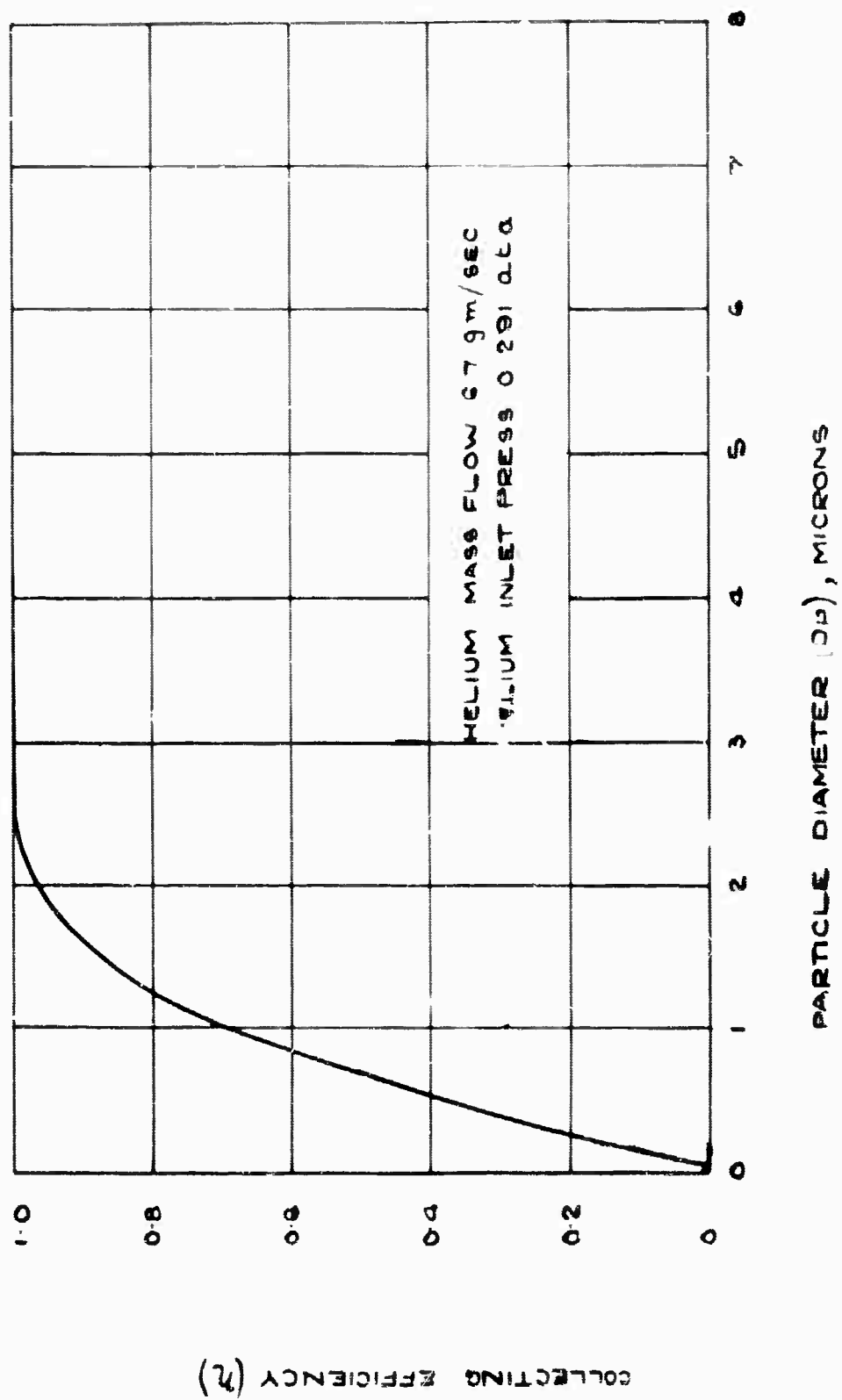
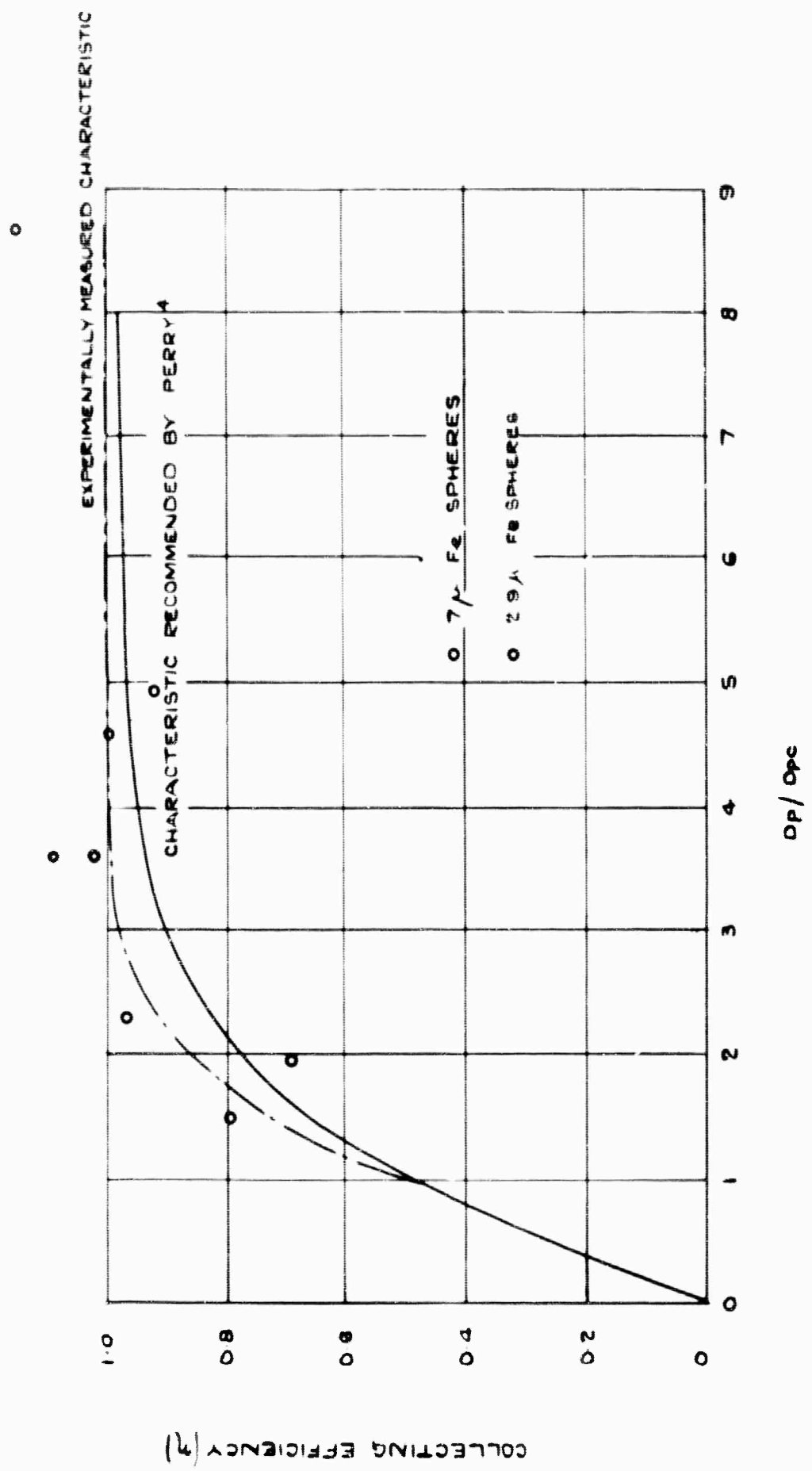


FIG 4.11



PREDICTED CESIUM COLLECTING EFFICIENCIES OF CYCLONE AT DESIGN CONDITIONS

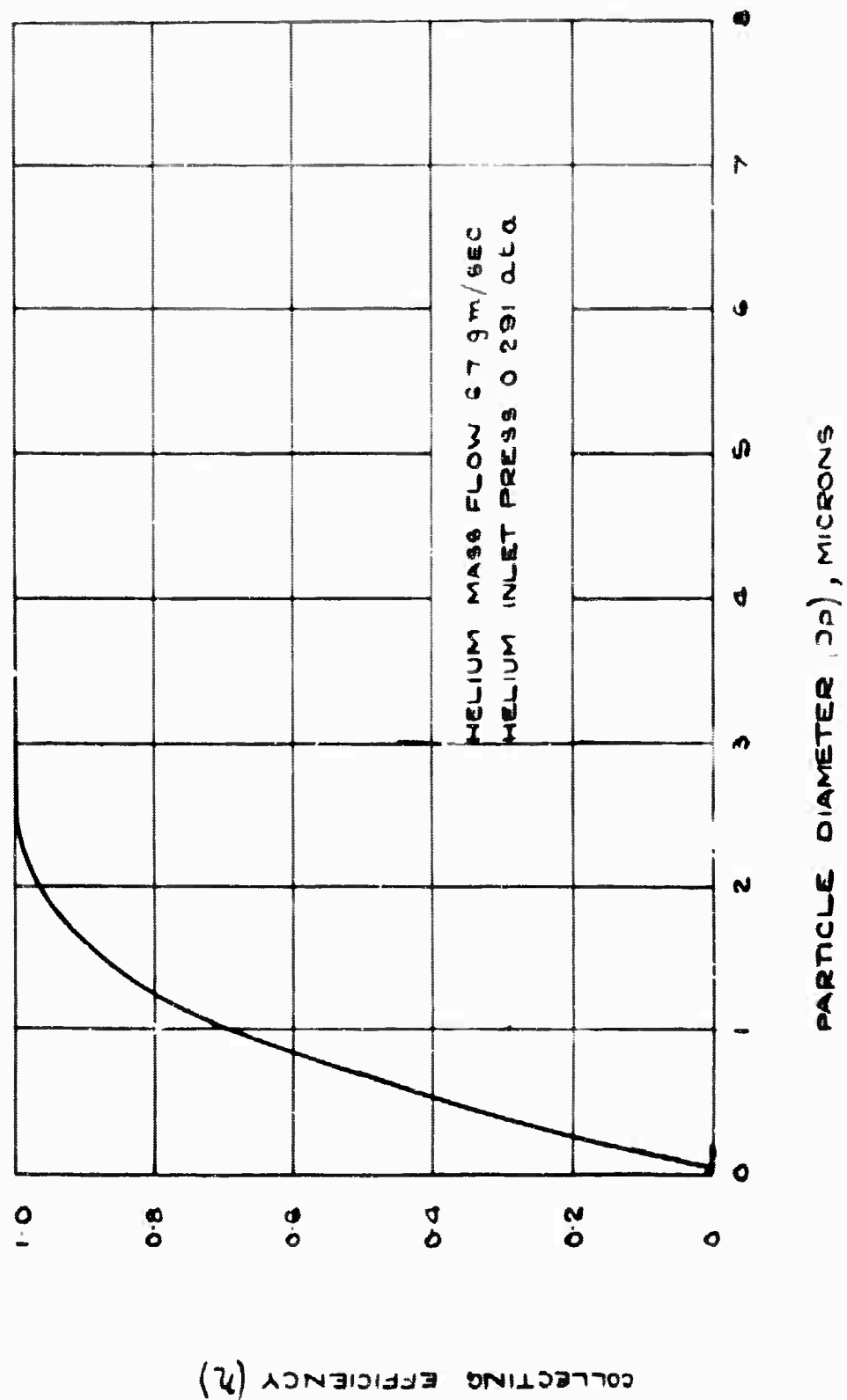
FIG 4.12



MEASURED COLLECTING CHARACTERISTIC

FIG 4.11

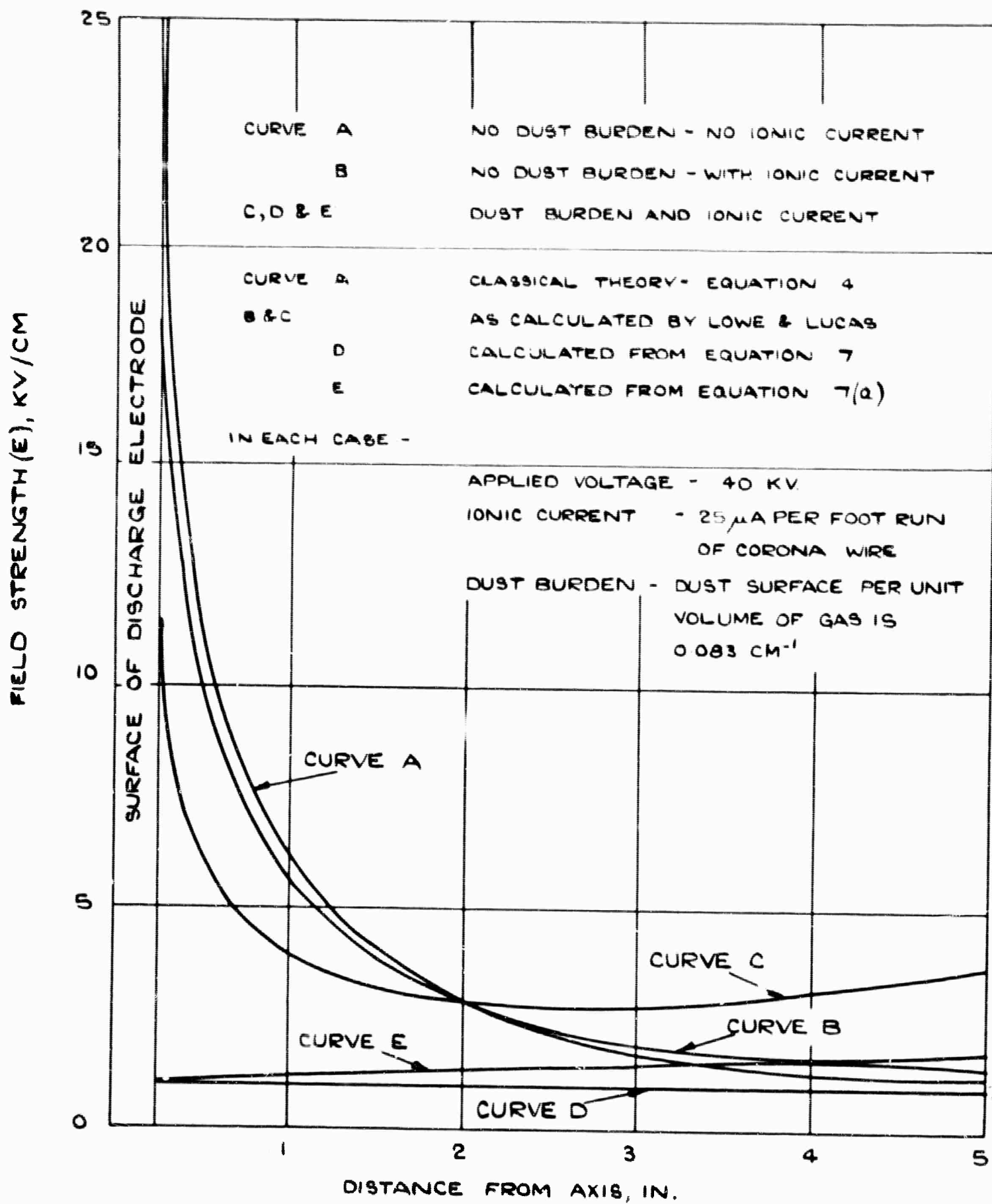
PR  
DE



PREDICTED CESIUM COLLECTING EFFICIENCIES OF CYCLONE AT  
DESIGN CONDITIONS

FIG 4.12





EFFECT OF DUST BURDEN ON FIELD STRENGTH

CHAPTER 5  
GENERATOR DUCT

by

R. Brown, W. J. Slator, V. Brown, K. Cass, J. Davidson and G. Johnson

5.1 SPECIFICATION

The generator duct system employed in the cesium-seeded runs in March 1964 (RHT 32, see IRD 64-36, Bibliography number 45) had exhibited significant electrical end leakage to earth. For the hot run (RHT 34) and the subsequent cesium-seeded runs (RHT 35) (see Chapter 3) the generator duct walls were extended axially at the subsonic diffuser end and an electrically-insulating expansion nozzle in boron nitride was fitted. Fig. 5.1 shows the tantalum (0.02 in. thick) high temperature transfer section and cesium vapourizer, with the attached boron nitride nozzle.

Duct walls	boron nitride
Duct dimensions	6 in. $\times$ $1\frac{1}{2}$ in. $\times$ $\frac{1}{2}$ in. ( $+\frac{3}{4}$ in. diverging diffuser)
Electrodes	16 pairs $\frac{1}{16}$ in. semi-circular section tungsten 10% tantalum 90% alloy (Fig. 5.2a)
Probes	$\frac{1}{16}$ in. diameter tantalum, two on each side of nozzle throat and four at diffuser end of generator
Expansion nozzle	boron nitride profiled for Mach 2.3 operation (Fig. 5.2b)
Thermal insulation	generator duct and transfer section Zirconia 'E' fibre with outer wrappings of 'Refrasil' tape
Thermocouples	$\frac{1}{16}$ in. tantalum-sheathed tungsten-tungsten 26% rhenium 1 upstream of nozzle in gas stream, 2 flush with duct wall downstream of generator

Fig. 5.3 shows the assembly (diffuser end) loaded into the generator case. Fig. 5.4a shows the generator assembly after RHT 34 and 35 in a partly disassembled state. Bonding of the boron nitride plates had occurred at the close-toleranced interface joints; this was attributed to ingress and reaction of Refrasil dust. The plates were finally forced apart mechanically.

## 5.2 ELECTRICALLY-CONDUCTING LAYERS

A fairly uniform electrically-conducting layer (less than 1 ohm/cm) was observed on all four duct inner wall surfaces and the interior surfaces of the expansion nozzle (Figs. 5.5a and 5.5b). This phenomenon has been discussed previously (IRD 64-36) and extensive analysis of electrically conducting surface layers has been carried out without determining the mechanism of layer transport or the major components contributory to the electrically conducting properties of the layer.

Tests have been conducted on small samples of electrically-conducting generator walls in both boron nitride and recrystallized alumina, heating for one hour under controlled atmospheres from vacuum ( $<10^{-4}$  torr) to 1 ata helium pressure, through a temperature range  $1450^{\circ}\text{K}$  to  $1850^{\circ}\text{K}$ . Samples taken from ducts used in runs before RHT 33 have lost the conducting layer with this procedure and recovered the initial electrical resistivity. A further test included fitting six electrically-conducting samples of recrystallized alumina, three upstream and three downstream of the cesium injection station in the MPD tantalum high temperature transfer section allowing the layered surface to be 'washed' by the hot helium and helium-cesium flow during cesium-seeded RHT 36 (not reported here). Inspection of the samples after the runs showed that the conducting layer had been removed in all cases with recovery of the surface electrical resistivity (Fig. 5.7). The generator walls (boron nitride) from RHT 33, 34 and 35 had become layered and electrically conductive (less than 1 ohm/cm). From these tests it was deduced that the conducting layer was unstable above  $1450^{\circ}\text{K}$ ; it therefore appears that the layer formation is by deposition on the cooler generator duct walls.

## 5.3 ELECTRODES

Inspection of the tantalum-tungsten strip electrodes after RHT 34 and 35 showed extensive transverse cracking (Fig. 5.6). Complete fractures were noted in 11 of the 32 strip electrodes and appeared to occur in each case at the lead-out bend where the internal stress promoted through forming would be highest. Some inconsistencies of power generation results (Chapter 3) along the axis of the generator can possibly be attributed to the high interface resistance of the fractures and in some cases intermittent open circuit.

A transverse section was taken from a cracked electrode at a position midway along the active electrode and the areas were examined metallographically. At the electrode-gas interface the layer had an even thickness of 17 microns. At the boron nitride-electrode interface, although there was no evidence of a definite layer, the electrode surface was extensively cracked both axially and transversely

(attributed to reaction between the electrode and boron nitride). At the corner connecting the boron nitride-electrode interface to the gas-electrode interface, the depth of penetration of cracks was about 250 microns. All three samples were extremely brittle.

An overall X-ray analysis of the electrode surfaces showed the presence of  $Ta_2O_3$  and TaB. The layer at the boron nitride-electrode interface was assumed to be TaB. Samples of boron nitride and boron nitride surface layers were analysed spectrographically. Unused samples of boron nitride showed major B, trace Si and minor traces Al and possibly Cu. Boron nitride from the duct wall remote from the gas interface (non-conducting electrically) showed the same analysis.

At the interface between boron nitride and the electrically conducting layer, the analysis gave major B, trace Al (higher than previous samples), Ca, and Si and minor traces Fe, Cr and possibly Cu.

#### 5.4 GENERATOR DUCT WALL HEATER DEVELOPMENT

Although efficient insulating materials have been used externally on the generator section (for example, Zirconia 'E' fibre) there is a space limitation transversely between the poles of the magnet and it has been recognized that the generator walls (and especially the electrodes) have been at significantly lower temperatures than the plasma in the generator. This has resulted in:

electrically-conducting layers on the generator wall inner surfaces, causing low inter-electrode resistance and effective short circuiting of the generator with progressive and sometimes rapid performance deterioration and uncertainty of results during seeded runs;

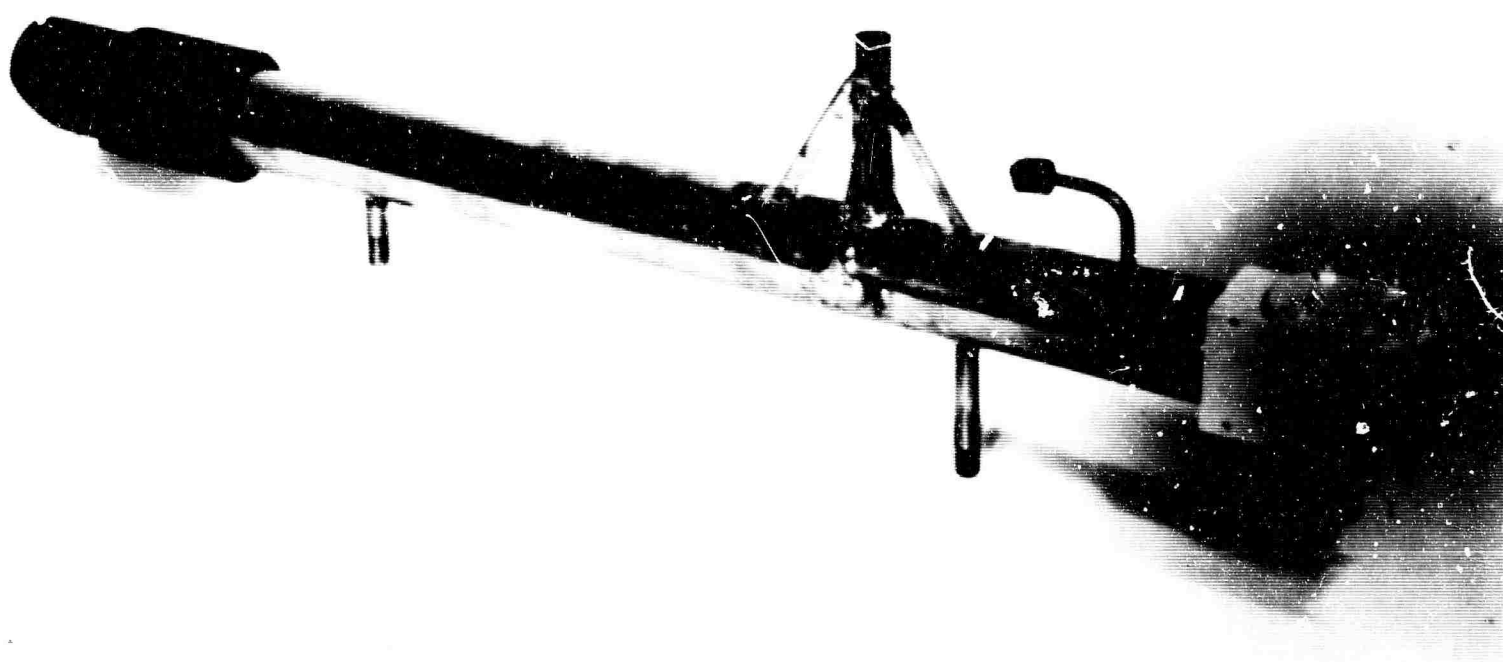
limitation of electron emission from the electrode surfaces; and  
uncertainties of gas-wall interfacial temperatures and subsequent difficulty in theoretical interpretation of results.

For these reasons a programme has been initiated for the development of externally-heated generator duct walls. Design considerations have been for a minimum useful heater life of 25 hr at up to  $1900^{\circ}K$ , uniform temperature distribution, and provision for lead-through of the required complex of electrode, pressure and thermocouple station leads. Early work was carried out using a boron nitride duct top wall ( $7\frac{3}{4}$  in.  $\times$   $1\frac{1}{4}$  in.  $\times$   $\frac{3}{8}$  in.) split and screwed to accommodate single refractory metal (0.010 to 0.020 in. W and Ta) heating elements (Figs. 5.8a and 5.8b).

A rectangular duct has been built to the cross sectional dimensions of the system used in RHT 34 and 35, but with the length reduced to 4 in. Internal tantalum (0.020 in. thick) heaters were fitted in each wall and series-connected. The system was insulated externally with zirconia fibre and thermally cycled to 1750°K under high vacuum conditions; the temperature was held at 1750°K for 25 hr (Figs. 5.9a, b and c). Inspection showed no deterioration of the system other than embrittlement of the element due to reaction with the boron nitride.

The tests are now being extended to study generator wall heater performance under conditions of helium flow and at the time of writing a complete heated generator system is being built for power generation runs in the closed loop.

he  
ed.  
o  
hr  
r  
nce



TANTALUM HIGH TEMPERATURE TRANSFER SECTION WITH BORON  
NITRIDE NOZZLE

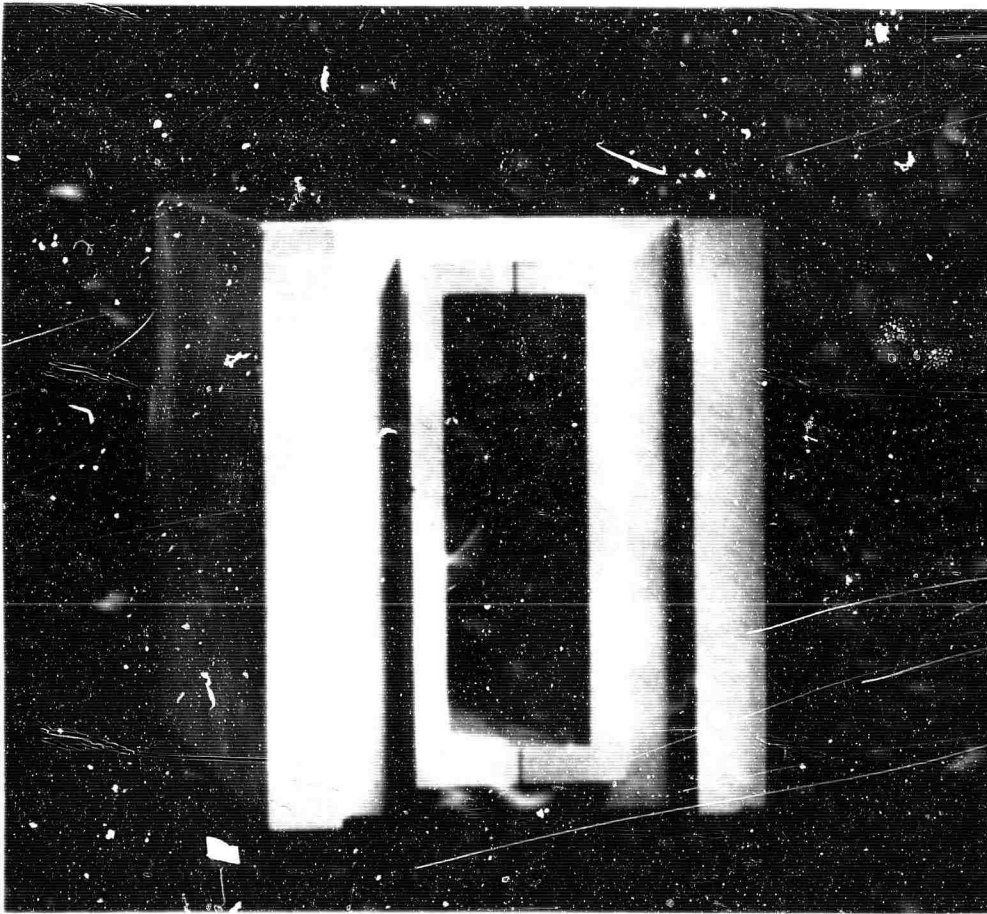
FIG 5.1



16 ELECTRODE PAIR BORON NITRIDE GENERATOR WALL BEFORE ASSEMBLY

BORO

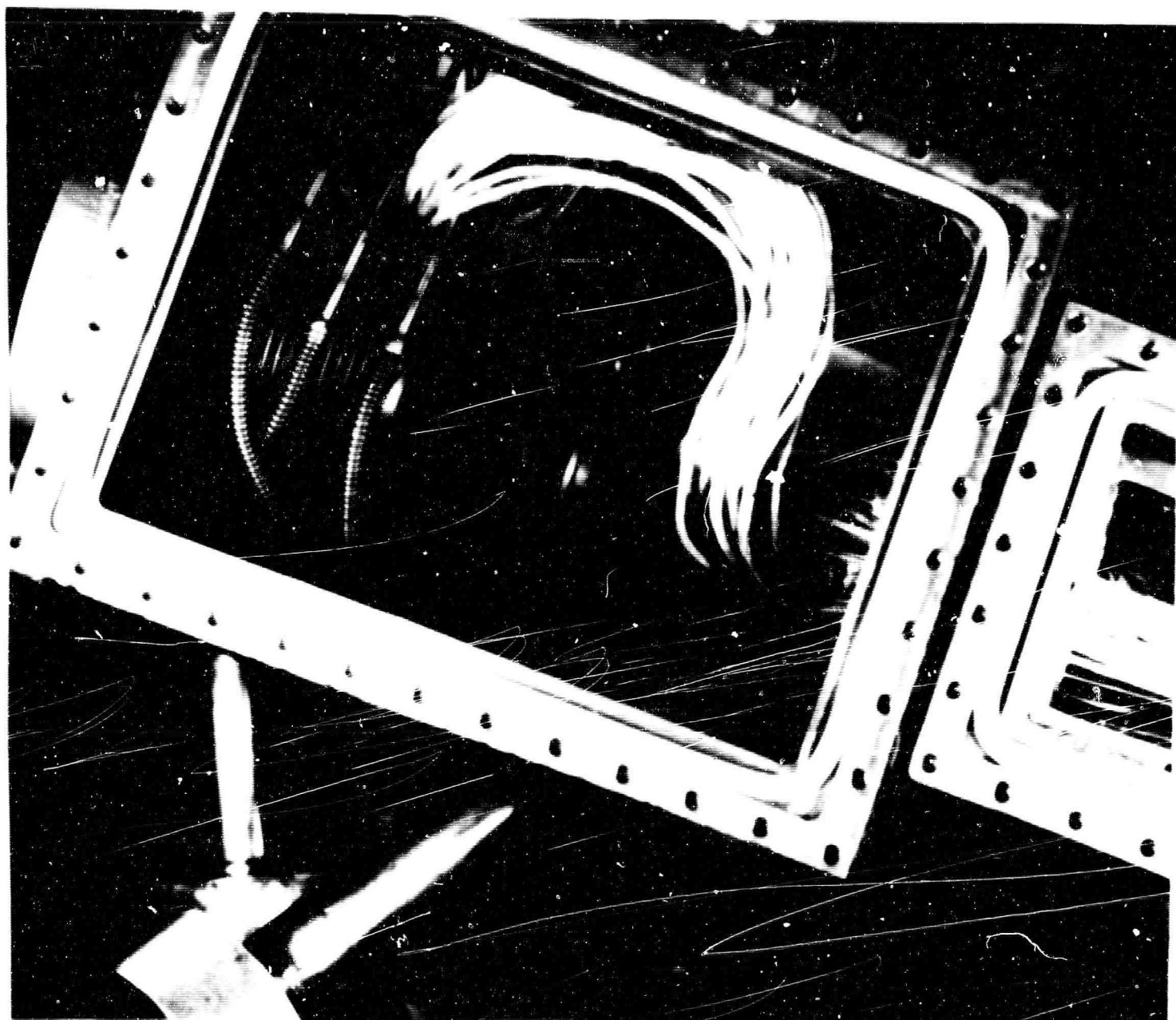
FIG5.2a



BORON NITRIDE SUPERSONIC NOZZLE

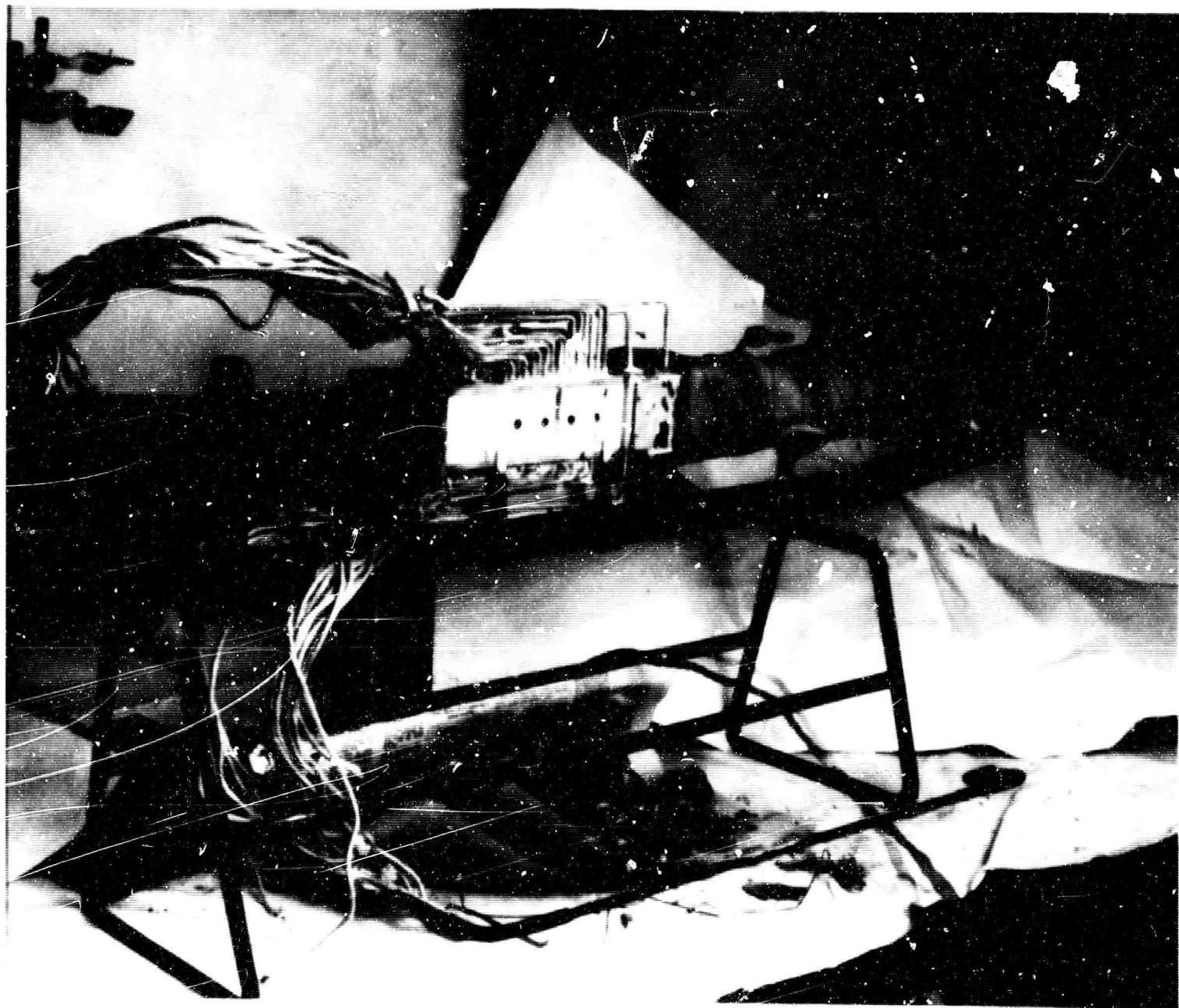
FIG 5.2 b





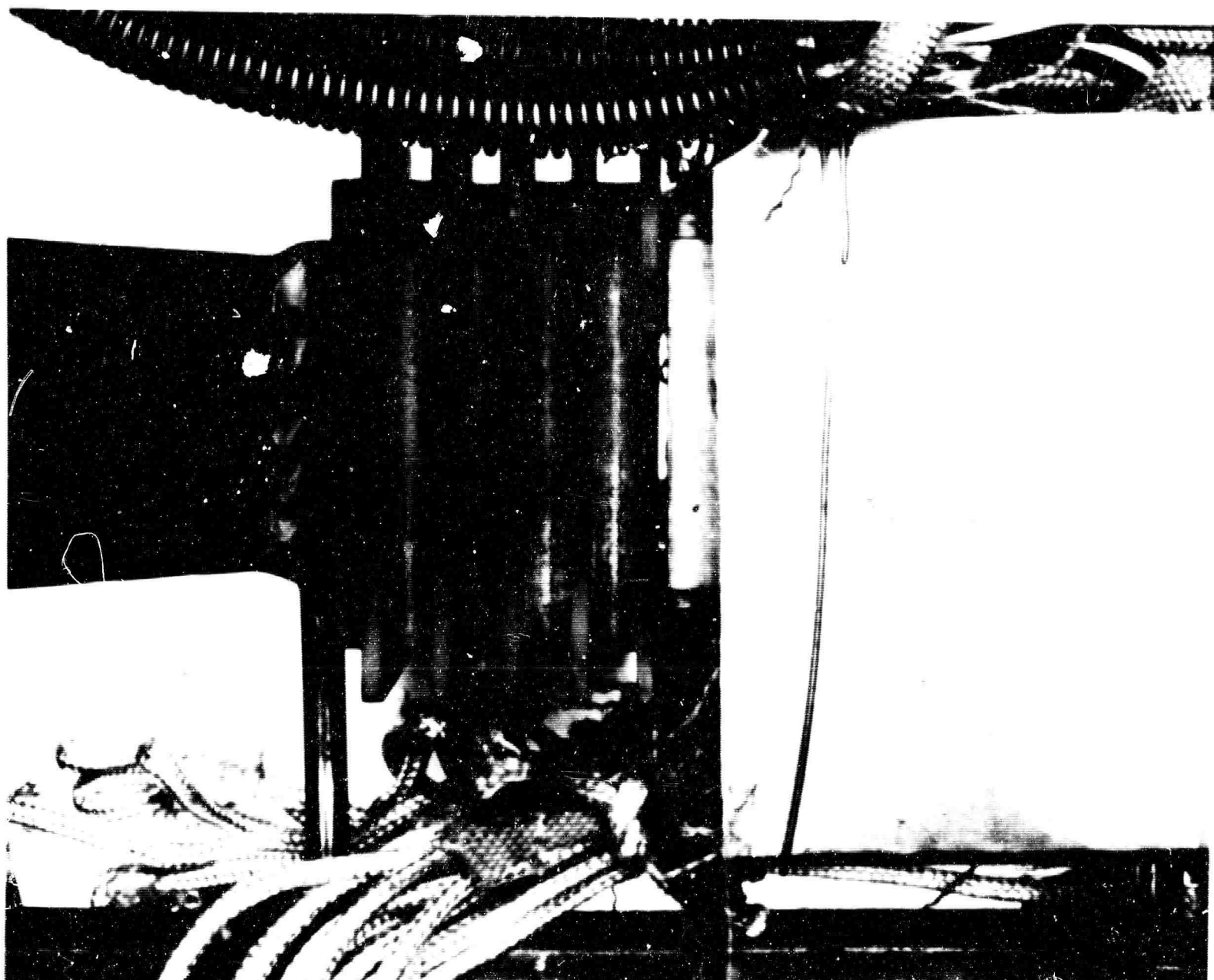
ASSEMBLY IN GENERATOR CASE

FIG 53



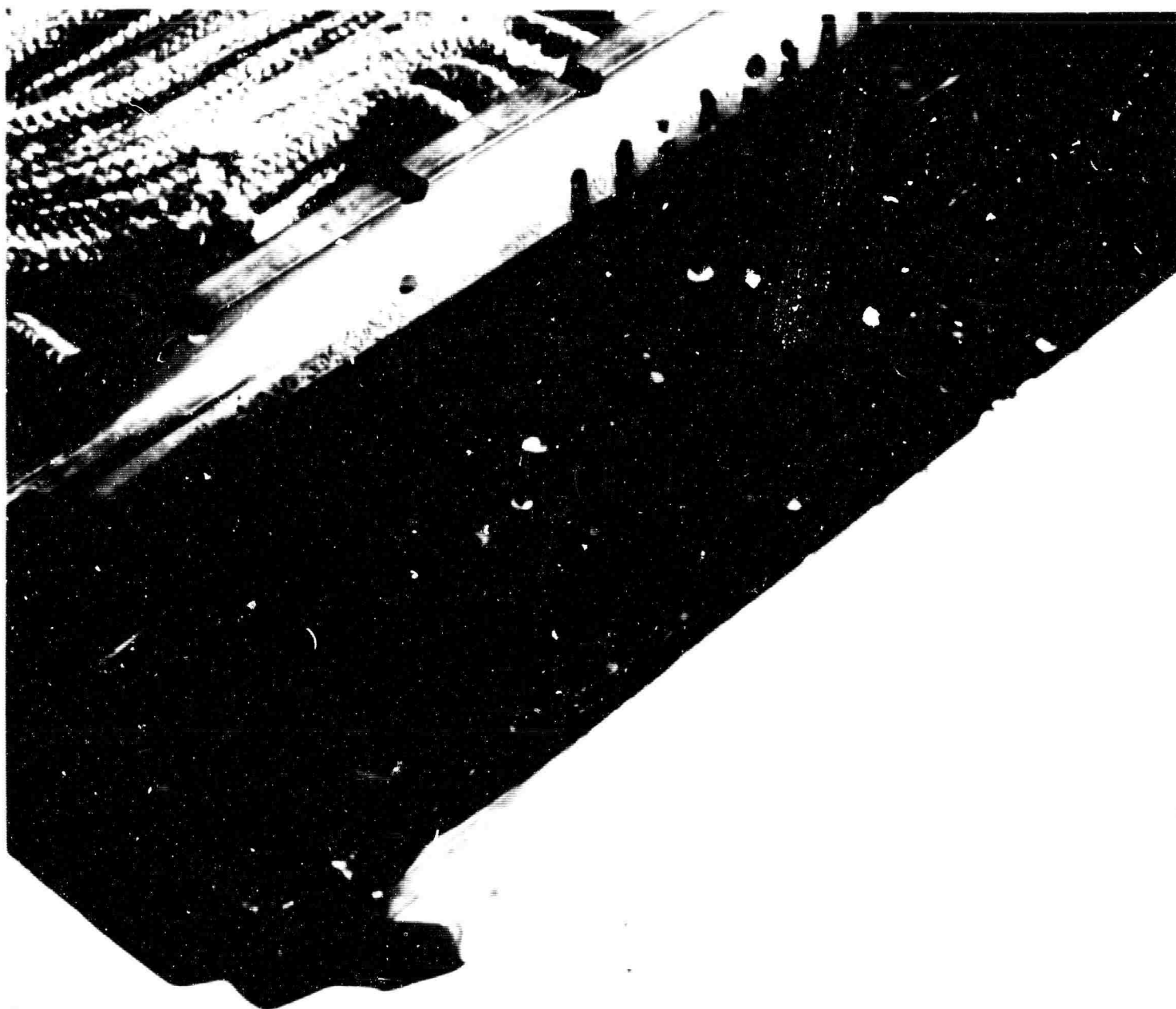
GENERATOR ASSEMBLY AFTER RUN

FIG 5.4a



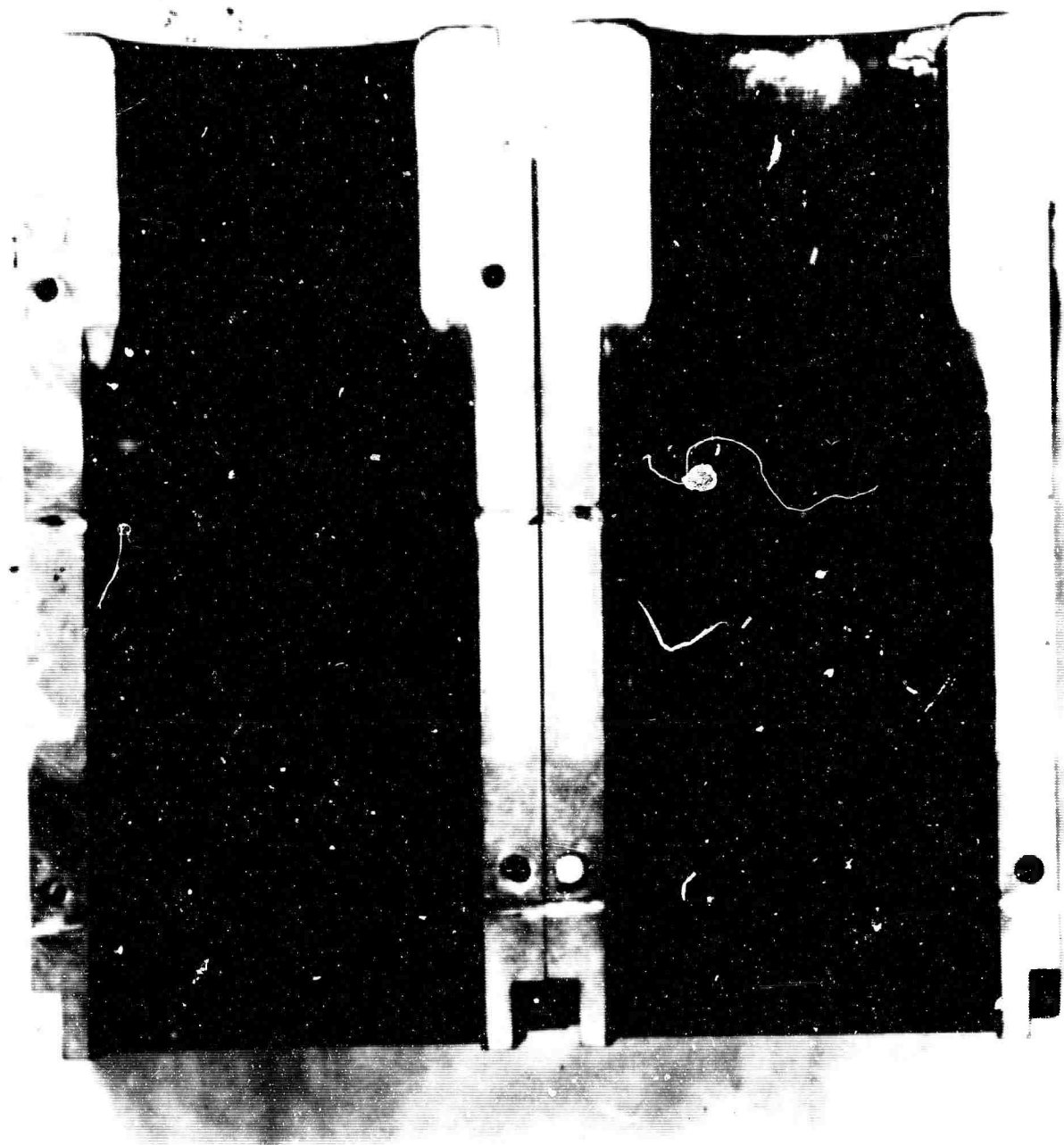
HELIUM LEAKAGE PATH BETWEEN DUCT END AND DIFFUSER

FIG 5.4b



SPLIT GENERATOR DUCT SHOWING ELECTRICALLY CONDUCTING LAYERS AND  
PITTING OF BORON NITRIDE SURFACE

FIG 5.5a



SPLIT BORON NITRIDE NOZZLE SHOWING ELECTRICALLY CONDUCTING LAYERS

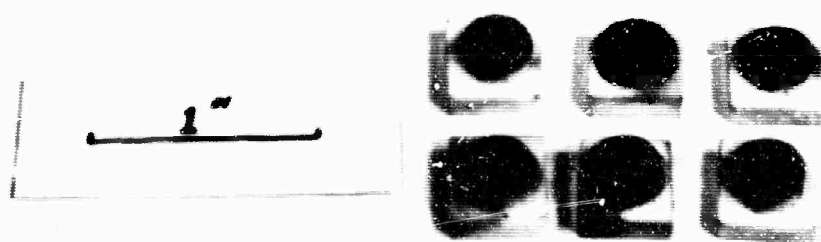
FIG 5.5b



CRACKING OF 90% TANTALUM 10% TUNGSTEN ELECTRODES

b

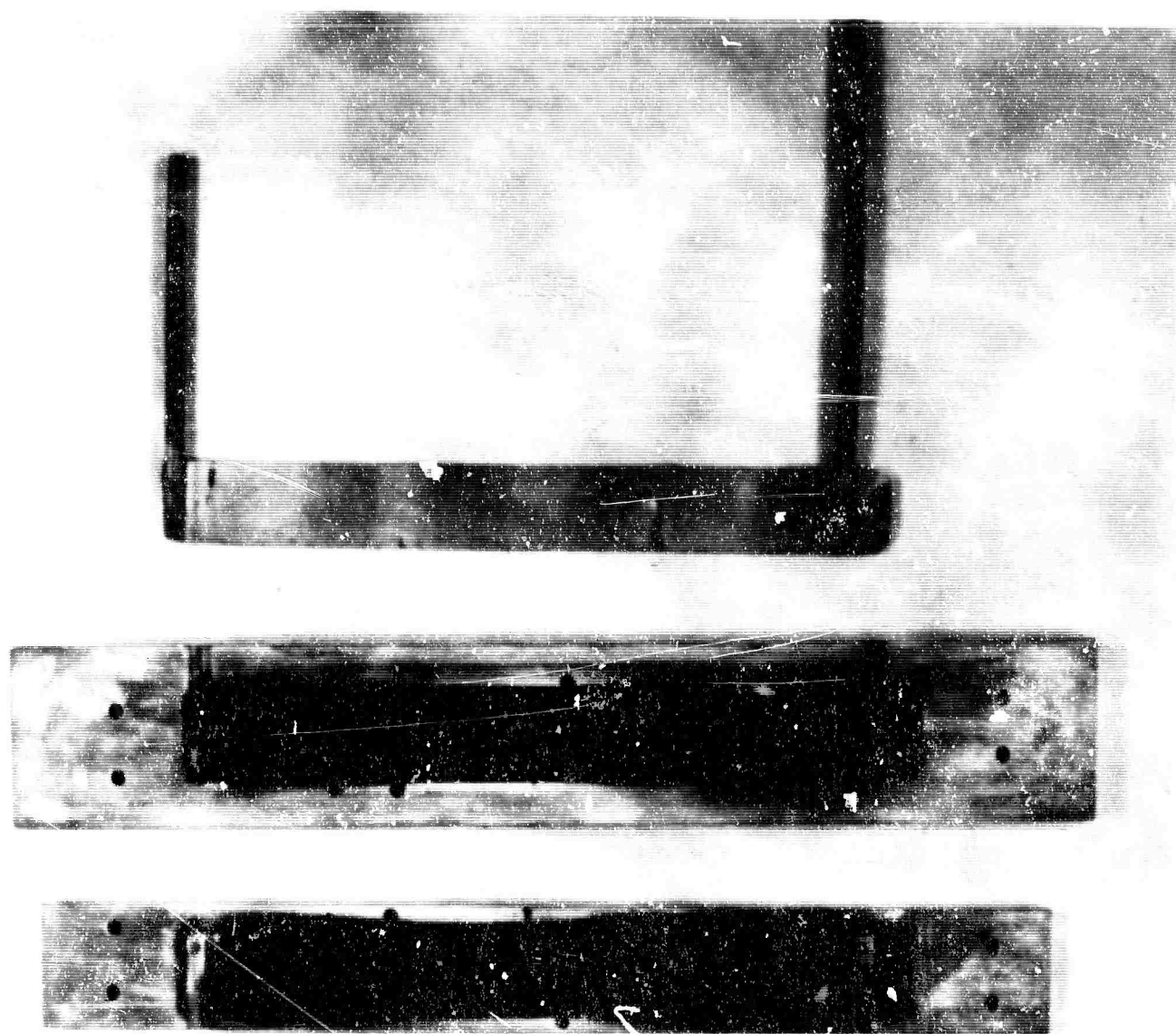
FIG 5.6



ALUMINA SAMPLES SHOWING REMOVAL OF ELECTRICALLY CONDUCTING LAYER

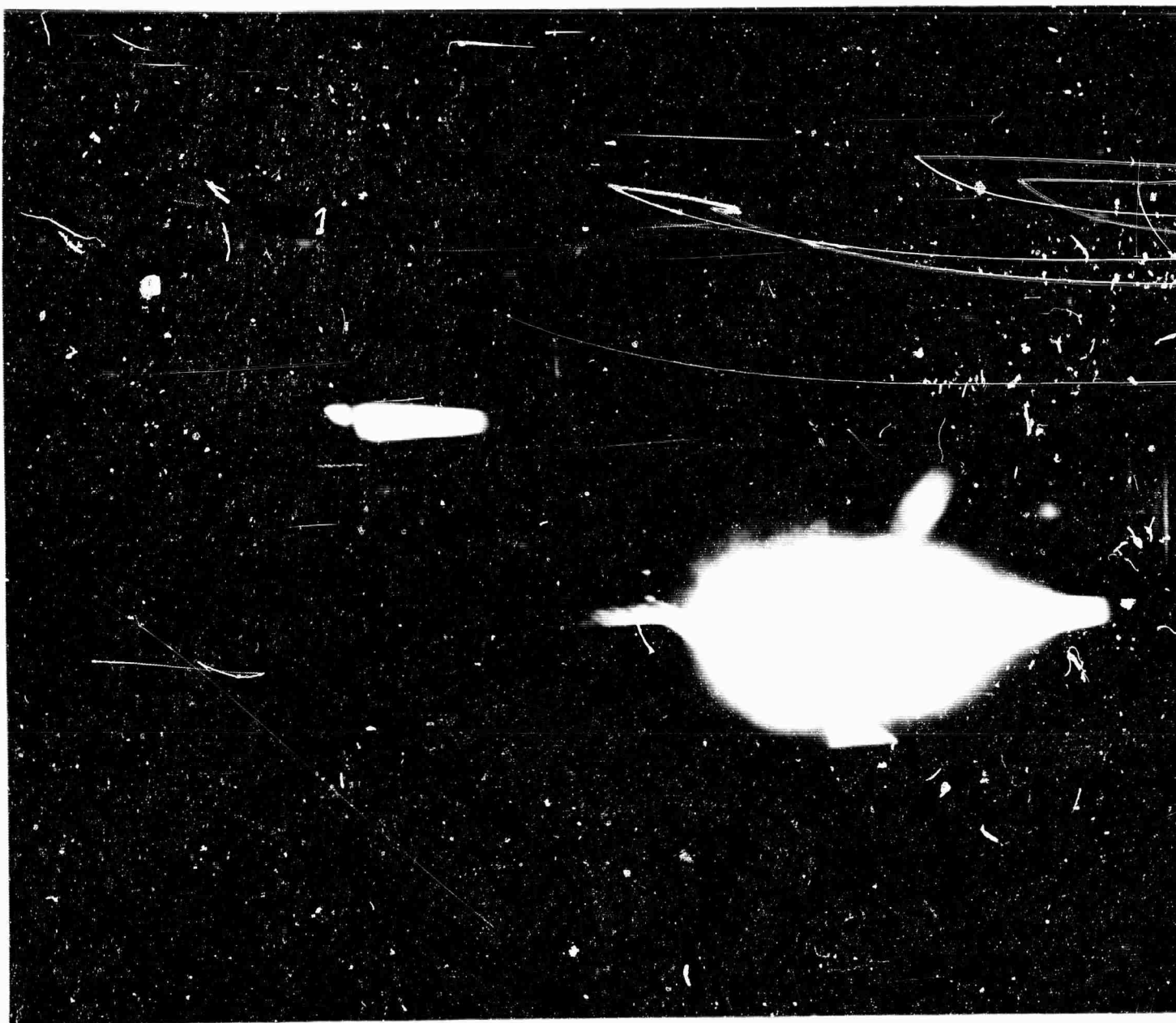
FIG 5.7





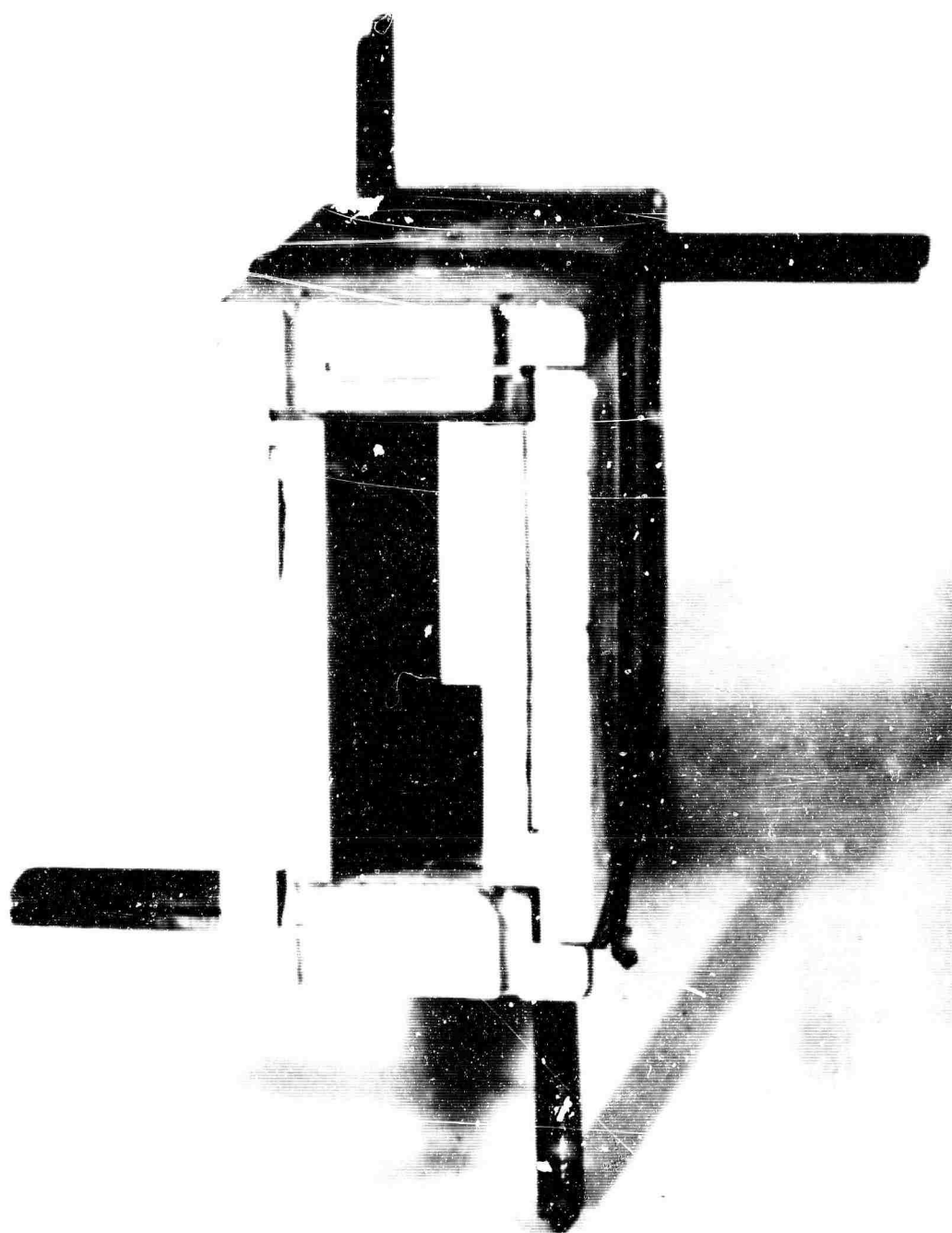
HIGH TEMPERATURE (1600°C) DUCT WALL HEATER MK I





DUCT WALL HEATER DEVELOPMENT AT 1400°C

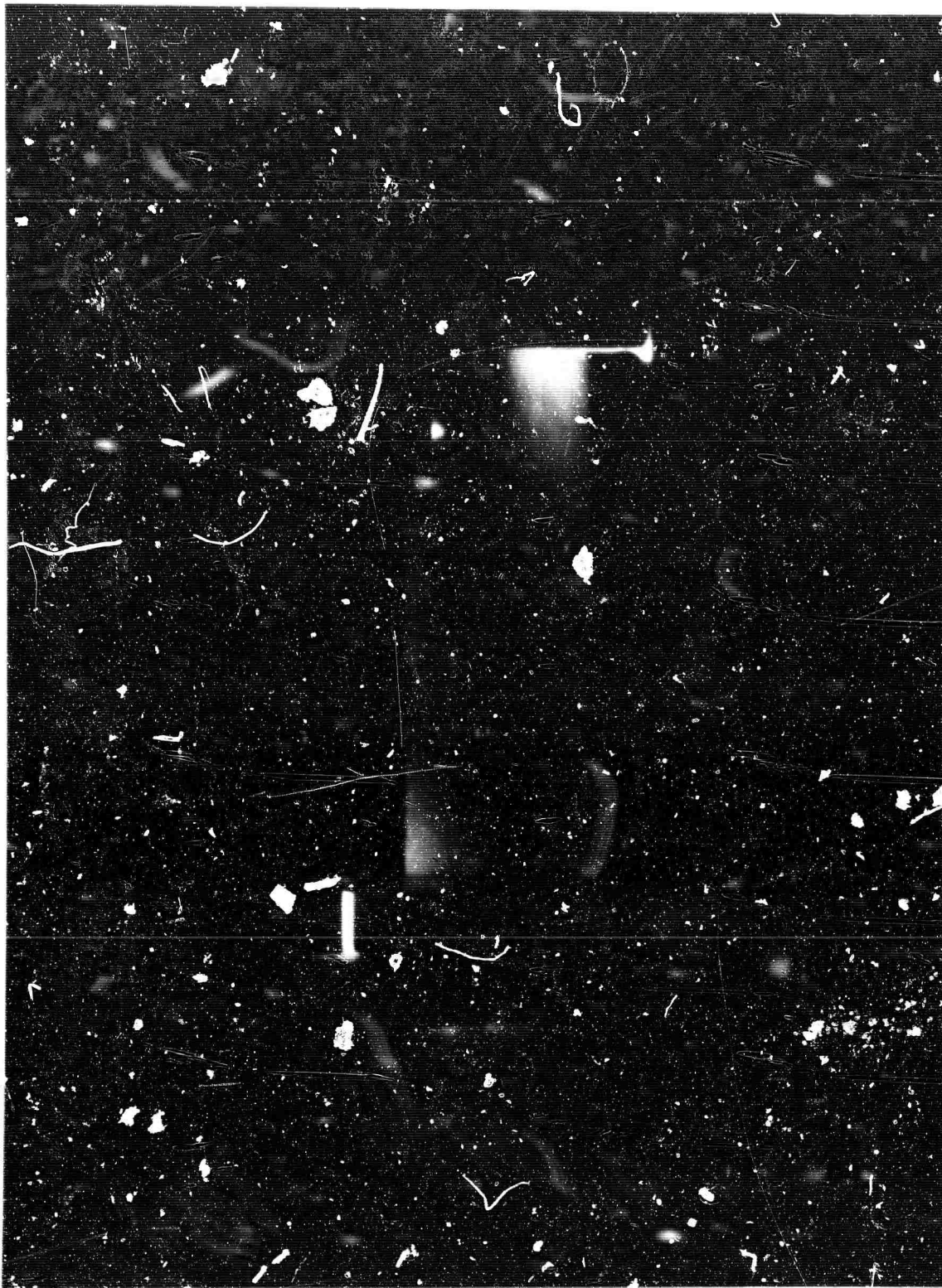
FIG5.8 b



ASSEMBLED DUCT WITH TANTALUM WALL HEATERS

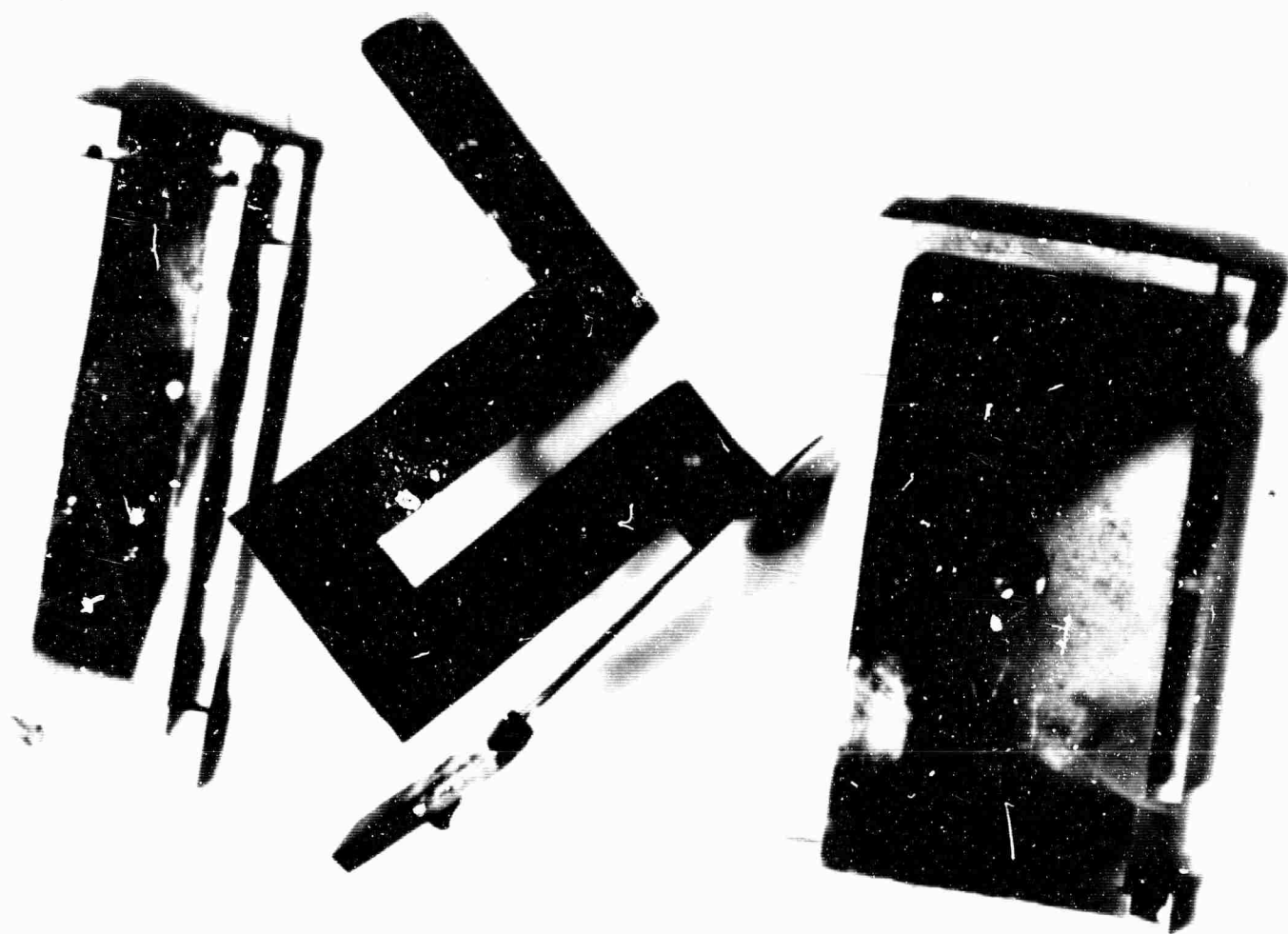
b

FIG 5.9a



DUCT ON 25 hr LIFE TEST AT 1500°C WALL TEMPERATURE

FIG 5.9b



DUCT STRIPPED SHOWING ONE WALL HEATER

FIG 5-9c

**BLANK PAGE**

INSTRUMENTATION

by

F.B. Jones, M. Watson, I. Wilson, R. Brown and I.R. McNab

6.1 INTRODUCTION

As indicated in the previous Technical Summary Report (IRD 64-36, Chapter 10) much effort has been devoted to accurate measurement of the plasma flow parameters in the MPD generator duct itself. Of particular importance is the problem of temperature measurement for which no satisfactory solution has been resolved although the method described in Section 6.4 is of some interest; consequently for this and other reasons, heated duct walls are to be used so as to operate under as nearly isothermal conditions as possible.

The system for generator output parameters (described in Section 6.2) has proved satisfactory and is currently being modified for more sophisticated measurements of generator characteristics.

6.2 GENERATOR CHARACTERISTICS

During cesium-seeded operation it is essential to extract the maximum information in the available time. Cesium may only be injected for 5 sec periods, and in the early runs, the instantaneous concentration fluctuated rapidly; ideally, the MPD generator loading would be cycled faster than these fluctuations.

The following information was required:

V-I characteristic of each electrode pair under power generation conditions;

voltages on 5 probe pairs outside main MPD duct;

Hall-effect emf's and short circuit currents;

interelectrode leakage resistance;

plasma passive V-I characteristics;

electrode resistance as an index of electrode temperature distribution along the duct;

cesium injection period; and

flow of cesium at heat exchanger exit.

### 6.2.1 V-I power characteristics

A typical 18-electrode pair (A, B, C...R) channel (designated X) is shown at the top of the circuit (Fig. 6.1). The electrodes (shown diagrammatically on the extreme top left are connected to the temperature-scanning uniselector and current loop (described later) and one lead from each electrode is taken to the patch panel. This has leads fitted with stacking plugs to allow parallel connection (any plug will fit into the top of any other); at present, electrode pairs are each connected to one loading and measuring channel by linking X11 to X13 and X12 to X14.

This links the electrode pairs to a level on one of two 25-way 11-level uniselectors (USA and USB) which, on the first five positions, step through five load resistors (R6 - R10) repeated on all 18 channels. At this stage the groups of relays (A and B) are not energized and a galvanometer in the 25-channel recorder, connected as a voltmeter, is connected across the electrode pair. As in Fig. 6.2a, a shunt resistor (R4 plus R5) is provided, also a series resistor selected from the chain R1-3 by a range switch. The diodes across the galvanometer have a high resistance at 0.1 V, but would shunt the galvanometer and protect it under overload. On their sixth step the uniselectors disconnect all loads so that open circuit voltage is recorded in all channels.

Thus for each electrode pair the voltage at various known loads is recorded, the current in each load can be calculated and the V-I characteristic derived.

### 6.2.2 Probe voltages

The probe pairs outside the main duct are connected to galvanometers in the 6-channel recorder with range resistors and shunts as in Fig. 6.2a. The open circuit voltage is monitored continuously in this way; no loads are connected to the probes.

### 6.2.3 Hall effect

On the seventh and eighth steps the electrodes of each pair are shorted to each other. Alternatively, by moving flying leads, any of the load resistors can be connected in at this stage. On the seventh step, the B group of relays come in and transfer one side of the galvanometer-as-voltmeter to earth, so that the voltage to earth is recorded. On the eighth step the A group of relays is also brought in and reconnects the galvanometers as ammeters. R4 becomes the shunt shown in Fig. 6.2b, but for heavier current R5 can be reconnected via a 39 and a 10 ohm resistor to pick up  $1/5$  of the voltage across R4.

#### 6.2.4 Cycling arrangements

All the uniselectors in this system are driven from a transistor multivibrator which switches a power transistor via an intermediate transistor. A master switch transfers the current pulses to temperature scan, leakage scan (described below) or power scan. The temperature scan unisector is started by a press button and then cycles to its homing position and stops. The leakage scan (USE), which has single ended wipers, is started by pressing a button and cycles through 48 positions; on its 49th step it starts USD, which cycles through 49 positions and on the 50th step pulses USD so that both reach a homing position. From the load scan during the power run (already described) USA and USB are started by pressing a button and scan through the eight positions three times over before stopping on a homing position. These uniselectors can be run continuously by closing a switch.

#### 6.2.5 Cesium injection

At the start of cesium injection a button is pressed which energises RL2, giving event marks on both ultraviolet recorders and on a recorder used for arrival of cesium at the lower end of the heat exchanger. This also gives a common point in time on all three charts.

#### 6.2.6 Cesium flow

The optical transmission of the cesium vapour at the heat exchanger exit is monitored by a simple circuit. The large window at this part is blacked out and use is made of the two small windows in line with each other. A 150 W bulb is placed outside one, while the other carries a photocell. An OCP 71 phototransistor was found unacceptable owing to dark current drift. Next a CdS cell (NSL-33 by National semiconductors of Canada) was tried. This is a specially stable type for measurement, but its response to falling intensity is slow and it is being replaced by type 36-P. The cell is connected in a bridge circuit energised by a 1.5 V cell and the output taken to a 10 mV recorder. Ranges of sensitivity can be provided by adding resistors in series with the battery.

#### 6.2.7 Galvanometer switching

All the recorder galvanometers are liable to be used for power measurements, and panel switches are fitted to direct galvanometers for use in other tests, either with only a shunt resistor (S3X, S4X) or as a fixed range voltmeter (S1X, S2X). These switches are only fitted to a few channels; they could be incorporated in the master switch.



### 6.2.8 Duct Leakages

The electrical leakage of the insulating material of the duct is important and, to take all necessary measurements in the shortest time, a galvanometer is used in a conventional ohmmeter circuit (Fig. 6.2c). R is given switched values of 10, 100, 3300 and 100,000 ohms, while the output leads are switched via uniselectors USD and USE. The readings obtained are on a non-linear scale, and it is intended to fit a variable shunt on the galvanometer to set FSD, and to produce a calibrated scale in transparent plastic for reading resistance values directly off the chart. When this system is in use, a mask is used to black out all other galvanometer beams, except one used for registering unisector drive pulses, which are picked up by a mutual inductor T1. At first an 18V battery was used, but the results did not correspond with Avo readings across the same points; it was pointed out that plasma breakdown was occurring. Accordingly, the battery voltage was changed to 1.5 V and a more sensitive galvanometer used.

### 6.2.9 Plasma passive electrical characteristics

Using the same unisector switching, 110 V a.c. can be applied through a 1 kilohm series resistor; voltage and current are displayed on separate galvanometers. This method gives a very indirect picture of the actual V-I curve, and it is intended to substitute a low-impedance sawtooth generator for the 110 V supply. If current is monitored on the recorder the linear voltage rise will make the time axis of the chart correspond to a voltage axis.

### 6.2.10 Electrode resistance

Each of the 36 electrodes consists of a U-shaped loop, and provision is made for connecting both ends of each loop to the rig. When the master switch is set to 'Temperature' contacts are closed on a bank of relays which pass a current of about 1A through all the loops in service and also through a 0.2 ohm calibrating resistor. Pressing the 'Temperature Start' button causes a unisector to scan the voltages across all the loops, connecting the upper electrodes in turn to one galvanometer and the lower electrodes to a second. For such low resistances four-terminal connections would be preferable, but the arrangement gives some indication of temperature distribution by recording resistance changes.

## 6.3 SPECTROSCOPIC TECHNIQUES

Spectroscopic methods of temperature measurement seem to be attractive in the range 1500°K to 2300°K. Preliminary investigations into the spectrum obtained from cesium suggest that it may be possible to use cesium line reversal for measuring temperature in the duct. Should this be feasible it is proposed to adopt the optical arrangement used by Hurle, Russo and Hall<sup>1</sup> which enables the

simultaneous emission and absorption of the spectral lines to be determined using a system of matched filters and photomultipliers. The temperature which will be measured will probably be the average electron temperature of the cesium plasma in the duct.

Spectrograms of cesium from a standard discharge tube and a cesium-seeded flame have already been obtained and compared. The temperature of the flame was about  $1400^{\circ}\text{K}$  which is below the level normally studied in the duct. The spectrum showed three lines of interest: one in the green and two in the blue at 4555 and 4593 $\text{\AA}$ . The intensity of the blue lines was much greater than that of the green, as expected from the cesium line intensities obtained by Schneider et al<sup>2</sup>. In the next cesium-seeded operation of the MPD loop it is proposed to examine the duct plasma spectroscopically to assess the effects of impurities. An axial view will be taken through the window in the head of the high temperature heater.

#### 6.4 TEMPERATURE MEASUREMENT DEVELOPMENT

During the operation of the MPD system errors were being introduced in the temperature measurements due to losses in the thermocouples. The losses were mainly attributed to conduction and radiation in the thermocouple, but some error was probably caused by thermocouple recovery in the high velocity gas stream. This recovery error was caused by the thermocouple being unable to follow the high frequency temperature changes in the gas stream, the effect being to indicate a temperature between the static and total temperature. A further error was caused by noise introduced in the thermocouple emf by the same fast temperature changes, but this may be eliminated by the use of suitable low pass filters.

An investigation was begun to find alternative methods of temperature measurement, or to develop new thermocouple techniques. Two systems based on pulsed operation of thermocouples were studied. The advantage of using a pulse system was that the thermocouple never reached temperatures where conduction and radiation losses become important. This was brought about by either inserting and withdrawing the thermocouple from the hot gas at high rate, or by operation with alternate heating and cooling. The disadvantages of using this type of thermocouple are less than for a conventional high temperature thermocouple, although the pulse thermocouple tends to read low with the rise in specific heat of the thermocouple material and the recovery error affects the thermocouple in the same way as a conventional type.

The first method (the 'intermittent' pulsed thermocouple<sup>3</sup>) was based on a standard thermocouple which was passed through a solenoid supplied with a rectangular waveform. A solenoid supplied with a rectangular waveform vibrated

the thermocouple so that it was not immersed in the hot gas long enough to reach the temperatures associated with high conduction and radiation losses. The actual temperature was then derived from the heat transfer between the gas and the thermocouple. The physical size of the system and the difficulty in determining the heat transfer data made it impractical for use in the MPD loop.

The second system was made up from a chromel-alumel thermocouple fitted into a coaxial tube through which the coolant flowed. The cooling-heating cycle was controlled by a motorized cam and microswitch. When the cooling was stopped, the thermocouple output rose exponentially (Fig. 6.3). Cooling was applied before radiation and conduction losses became significant. The exponential output was fed to a thermocouple amplifier and computer circuit which predicted the final temperature. The limiting factor for the pulsed thermocouple was the signal-to-noise ratio of the thermocouple emf; when reduced to a certain level instabilities occur in the computer network.

Wormser and Pfunter<sup>4</sup> developed a practical system of pulse thermometry upon which the present study was based. Wormser and Pfunter reported that their system was used to measure temperatures up to 2900°C in an oxy-hydrogen flame with an accuracy within 1% of the theoretical temperature. The gas coolant flowed through a water-cooled jacket directly on to the thermocouple tip. The construction originally proposed was modified in the present development to the arrangement shown in Fig. 6.4.

This construction tended to increase the time constant of the thermocouple, creating a problem with the computer circuit components particularly when static gas temperatures were being measured.

The computer circuit was composed of six Solatron Operational amplifiers (Fig. 6.5). The first amplifier,  $A_1$ , raised the thermocouple emf to a value suitable to operate the second amplifier,  $A_2$ , which was connected as a differentiator. Amplifier  $A_1$  output had to have a large signal-to-noise ratio, as noise fed into  $A_2$  resulted in instabilities in this amplifier.  $A_2$  differentiated the exponential rise and added the input, giving a steep output equal to the actual temperature.

The theoretical evaluation of computer operation assumed that the thermocouple emf was of the form

$$V_T = V_0 + V_A (1 - e^{-t/\tau}); \quad \text{..... (6.1)}$$

immediately after cooling was stopped at time  $t = 0$ .

$T_0$ ,  $T_A$  and  $T_T$  (Fig. 6.6) were represented by  $V_0$ ,  $V_A$  and  $V_T$  respectively, where

$V_0$  = the cooled thermocouple emf at  $t = 0$ ,

$V_A$  = the final value of the exponential emf rise,

$V_T$  = the final thermocouple emf, i.e.  $V_0 + V_A$  at  $t = \infty$ ,

$t$  = time from  $t = 0$ , and

$\tau$  = the thermocouple time constant, defined as the time taken for the thermocouple exponential emf rise to reach  $0.632 V_A$ .

The transient response of the amplifier  $A_2$  resulted in an output

$$V_{out} = V_{in} \frac{R_4}{R_3} + \frac{dV_{in}}{dt} C_1 R_4 \quad \dots\dots (6.2)$$

Substitution of equation (6.1) into (6.2) gives

$$V_{out} \left[ V_0 + V_A (1 - e^{-t/\tau}) \right] \frac{R_4}{R_3} + \frac{d[V_0 + V_A (1 - e^{-t/\tau})]}{dt} C_1 R_4 \quad \dots\dots (6.3)$$

Solving:

$$V_{out} = V_0 \frac{R_4}{R_3} + V_A \frac{R_4}{R_3} - V_A \frac{R_4}{R_3} e^{-t/\tau} + V_A \frac{C_1 R_4}{\tau} e^{-t/\tau} \quad \dots\dots (6.4)$$

It was arranged that:

$$\frac{R_4}{R_3} = 1 \quad \dots\dots (6.5)$$

$$\text{and } C_1 R_4 = \tau \quad \dots\dots (6.6)$$

Therefore

$$V_{out} = V_0 + V_A - V_A e^{-t/\tau} + V_A e^{-t/\tau} \quad \dots\dots (6.7)$$

$$V_{out} = V_0 + V_A \quad \dots\dots (6.8)$$

This was the output of amplifier  $A_3$  and was equal to the thermocouple output at  $t = \infty$

$$\text{Equation (6.1) stated } V_T = V_0 + V_A (1 - e^{-t/\tau})$$

$$\text{Let } t = \infty, \text{ then } V_T = V_0 + V_A (1 - e^{-\infty})$$

$$V_T = V_0 + V_A$$

This signal, in terms of voltages, was fed into the input of the third amplifier  $A_3$ . A large capacitor,  $C_2$ , was placed across the input and charged up by amplifier  $A_2$  to a voltage  $(V_0 + V_A)$ . At the end of the heating cycle the circuit between amplifiers  $A_2$  and  $A_3$  was broken by  $RL_{1/2}$  with this voltage still across  $C_2$ . This voltage was retained at the input of amplifier  $A_3$  by having a large resistance,  $R_5$ , in series with the first grid of the amplifier so making the discharge time of  $C_2$  large.

Dick<sup>5</sup> and McKensie<sup>6</sup> stated that  $\tau$  was dependent on the physical size of the thermocouple, the velocity or flow rate of the hot gas, and the magnitude of the step increase a thermocouple was responding to. The effect of  $R_4C_1$  being larger or smaller than  $\tau$ , equation 6.6, was to give an output at amplifier  $A_2$  larger or smaller than  $V_0 + V_A$ . This error tended towards  $V_0 + V_A$  with time (Fig. 6.7). To enable the  $R_4C_1$  value to be changed and the  $R_4 = R_3$  relationship, equation 6.5, to be maintained, two 'ganged' variable potentiometers were used. To obtain the optimum conditions automatically, the output of amplifier  $A_2$  was differentiated by amplifier  $A_4$ . The second differential of the thermocouple emf gave the rate of change of the slope and so the change in  $\tau$ .

$$\text{For amplifier } A_4, \quad V_{\text{out}} = \frac{dV_1}{dt} C_3R_8$$

where  $V_{\text{out}}$  was given by equation 6.4 and  $R_4 = R_3$

$$V_{\text{out}} = \frac{d}{dt} \left[ V_0 + V_A - V_A e^{-t/\tau} \left( 1 - \frac{C_1R_4}{\tau} \right) \right] C_3R_8$$

$$V_{\text{out}} = \frac{C_1R_4}{\tau} V_A e^{-t/\tau} \left( 1 - \frac{C_1R_4}{\tau} \right)$$

$$\text{When } C_1R_4 > \tau, \quad V_{\text{out}} > V_A$$

$$C_1R_4 < \tau, \quad V_{\text{out}} < V_A$$

$$C_1R_4 = \tau, \quad V_{\text{out}} = 0$$

The output of amplifier  $A_4$  was fed to a servo-amplifier unit  $A_6$  which drove the two variable potentiometers  $R_3$  and  $R_4$  to a position where  $R_3 = R_4$  and  $C_1R_4 = \tau$ . Under these conditions the second differential of the thermocouple emf was zero. By a system of relays (Fig. 6.8) this operation was timed to take place during the cooling cycle, as movement of  $R_3$  and  $R_4$  during the heating cycle introduced instabilities. The servo-amplifier unit  $A_6$  introduced a great deal of noise into the system and so an integrator  $A_5$  was connected between amplifiers  $A_4$  and  $A_6$ .

Amplifier  $A_3$  was suitably switched to operate during the heating cycle.

Up to the present time, only amplifiers  $A_1$ ,  $A_2$  and  $A_3$  have been successfully used as it has not been possible to eliminate all the instabilities in amplifiers  $A_4$ ,  $A_5$  and  $A_6$ . The circuit used was sufficient to measure temperatures when  $\tau$  did not change rapidly and this was done, although some inaccuracy probably occurred.

Two sizes of thermocouple were investigated (Fig. 6.9); the larger is 0.062 in. diameter mineral insulated wire type and the smaller a 0.04 in. diameter mineral insulated wire type.

Under static gas conditions,  $\tau$  varied considerably with temperature, Fig. 6.10. The value at  $\tau$  was large for the 0.062 in. thermocouple, i.e.  $\approx 0.110$  sec at  $300^\circ\text{C}$ . This large value of  $\tau$  required large  $C_1R_4$  values for amplifier  $A_2$ . The type of amplifier used was not suited for very large component values such as these. With a value of  $R_4 > 5$  Mohm, without noise, the amplifier was unstable, and even with this value a large  $C_1$  was required i.e.  $22\mu\text{F}$  which created overloading problems in the amplifiers. The system was calibrated up to  $800^\circ\text{C}$ , using manual adjustment for  $\tau = C_1R_4$  conditions. The repeatability was good, but the instabilities in amplifier  $A_2$  created oscillation about the  $V_0 + V_A$  output, making accurate calibration difficult.

The use of the 0.04 in. thermocouple reduced  $\tau$  by a factor of two at  $300^\circ\text{C}$ , and at  $800^\circ\text{C}$   $\tau$  was approximately 20 sec.

From Fig. 6.10 it was seen that  $\tau$  fell with increasing temperature and from this trend the required  $C_1R_4$  should be of realistic values at temperatures above  $1000^\circ\text{C}$ .

Only preliminary tests have been carried out with flowing gas to determine the magnitude of  $\tau$ . Using an ordinary gas torch,  $\tau$  was 50 sec at  $500^\circ\text{C}$  and 12 sec at  $1100^\circ\text{C}$  (Fig. 6.11) for the 0.062 in. thermocouple. Again it was assumed that as the temperature rose above  $1000^\circ\text{C}$  the value of  $\tau$  would reduce even further. This reduction of  $\tau$  and  $C_1R_4$  would give increased stability and reduce the tendency for amplifier  $A_2$  to overload.

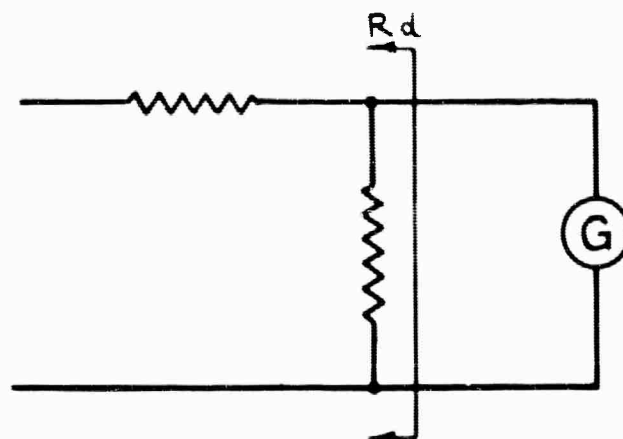
A more stable system should be developed, perhaps by using servo-differentiators if they were found to have any advantages. It is proposed to extend the range of measurement to at least  $2000^\circ\text{C}$  under flow conditions, and also with static gas if feasible. The high value of  $\tau$  was still troublesome and therefore a new design of coolant tube, to reduce  $\tau$ , is to be considered; with this reduction in  $\tau$  achieved, the instabilities in amplifier  $A_2$  would probably be eliminated. The feasibility of using one computer system for several thermocouples is also to be studied.

## REFERENCES

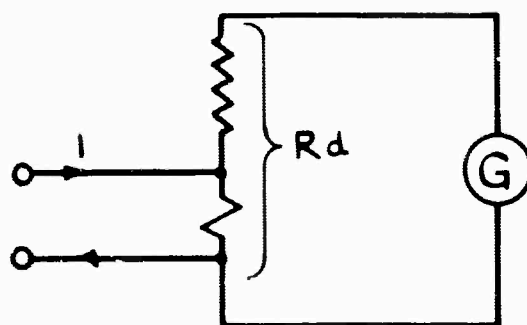
- 1 HURLE, I.R., RUSSO, A.L. and HALL, Gordon, J. 'Spectroscopic studies of vibrational nonequilibrium in supersonic nozzle flows' Cornell Aeronautical Laboratory. 1963
- 2 SCHNEIDER, R.T., WILHELM, H.E. and TIPTON, D.L. 'Measurement of fluid properties for magnetoplasmadynamic power generators'. Allison Division, General Motors Corporation. First Quarterly Technical Summary Report, 1963
- 3 Intermittent pulse thermometer. Temperature, its measurement and control. Science and Industry. Editor A.I. Dahl, Reinhold Publishing Corporation, vol. III, part 2, p901
- 4 WORMSER, A.F. and PFUNTER, R.A. Pulse technique extends range of chromel-alumel to 7000°F. Society of Aut. Eng. Inc. National Aeronautic Meeting, New York, April 3rd-6th, 1962
- 5 DICK, A. Thermal response of a pyrotenax thermocouple with insulated hot junction. Nuclear Power Plant Co. Ltd., NPPC Report No. IGC/NPPC/FEWF/P395.
- 6 MCKENSIE, W.H. Response rates of thermocouple suitable for measurements of the reactor channel exit gas temperature. English Electric Co. Ltd., Atomic Power - Report A.C.E.D. ref. No. NPCC/FEWF/P306



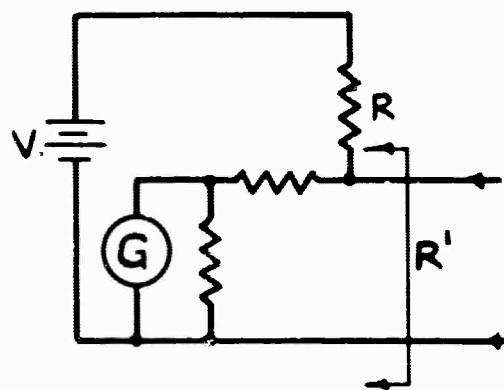




(a) GALVANOMETER AS VOLTMETER.

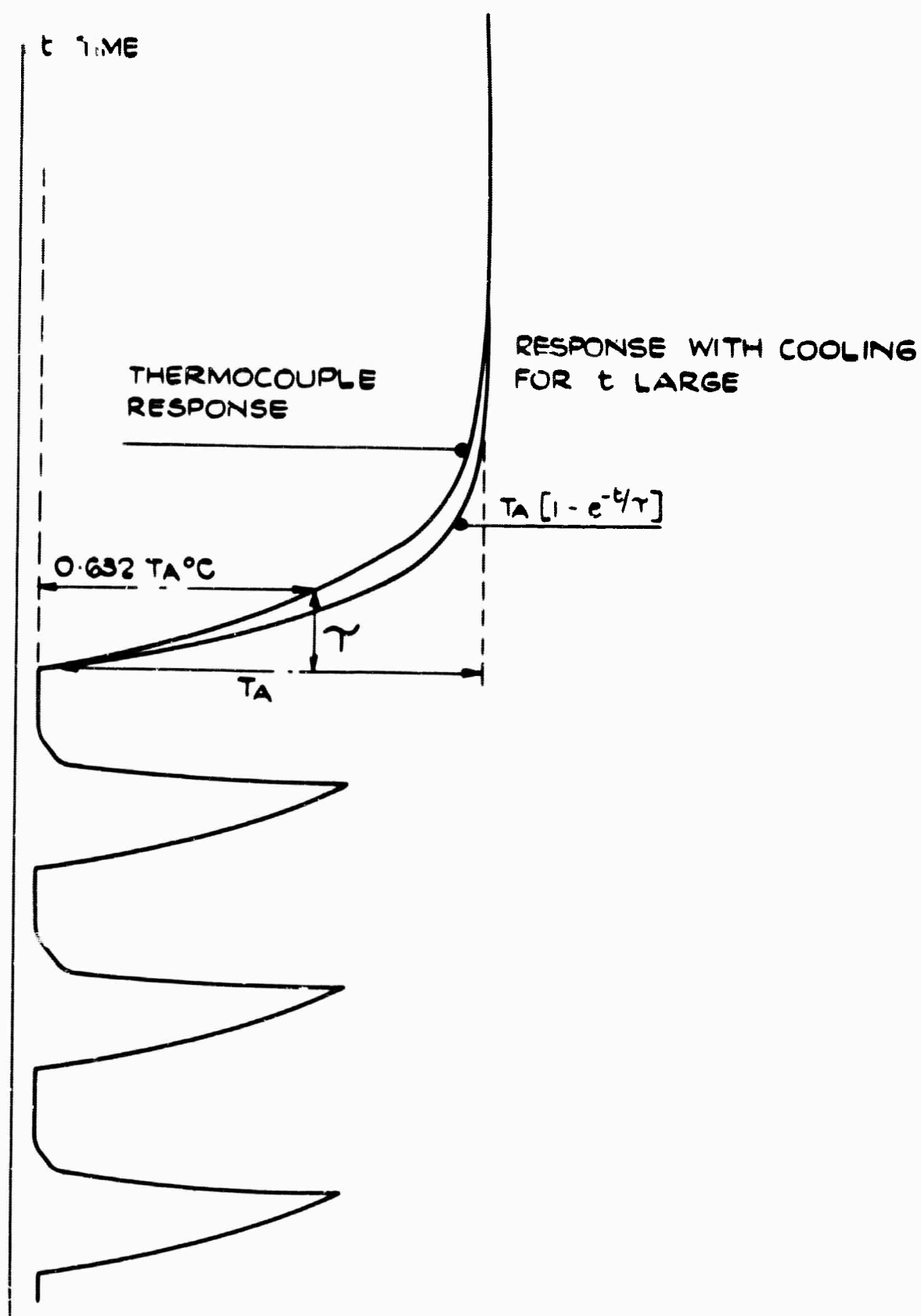


(b) GALVANOMETER AS AMMETER.

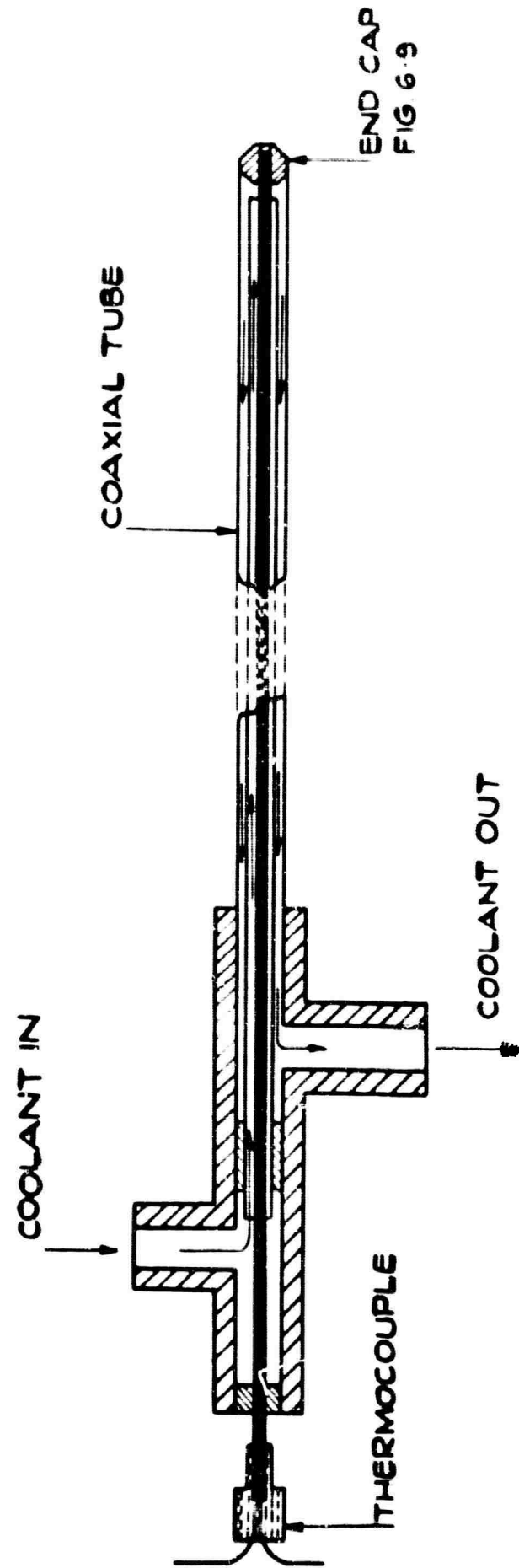


(c) GALVANOMETER AS OHMMETER.

# GALVANOMETER CONNECTIONS



THERMOCOUPLE RESPONSE WHEN COOLED  
AUTOMATICALLY AT SET TIME INTERVALS



THERMOCOUPLE COOLANT TUBE

PULSE THERMOCOUPLE COMPUTER SYSTEM

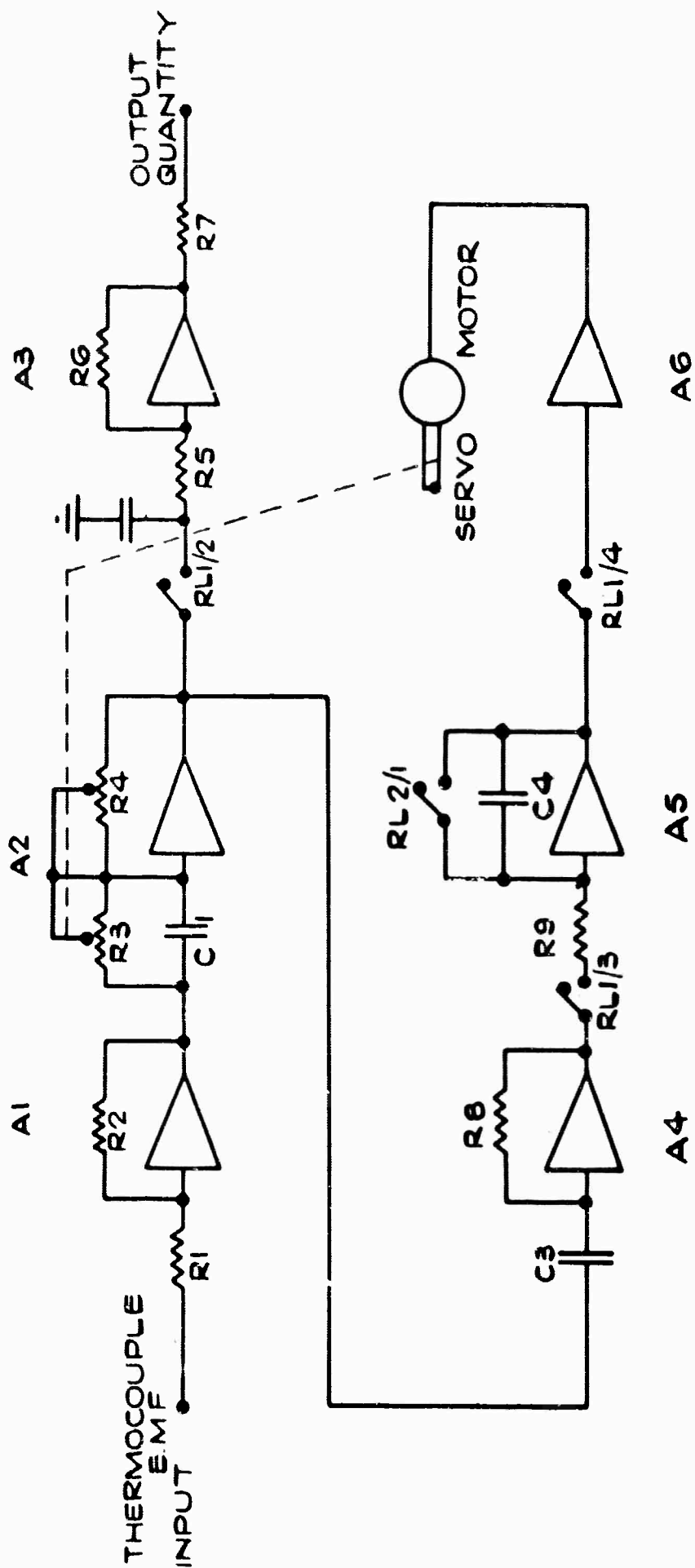
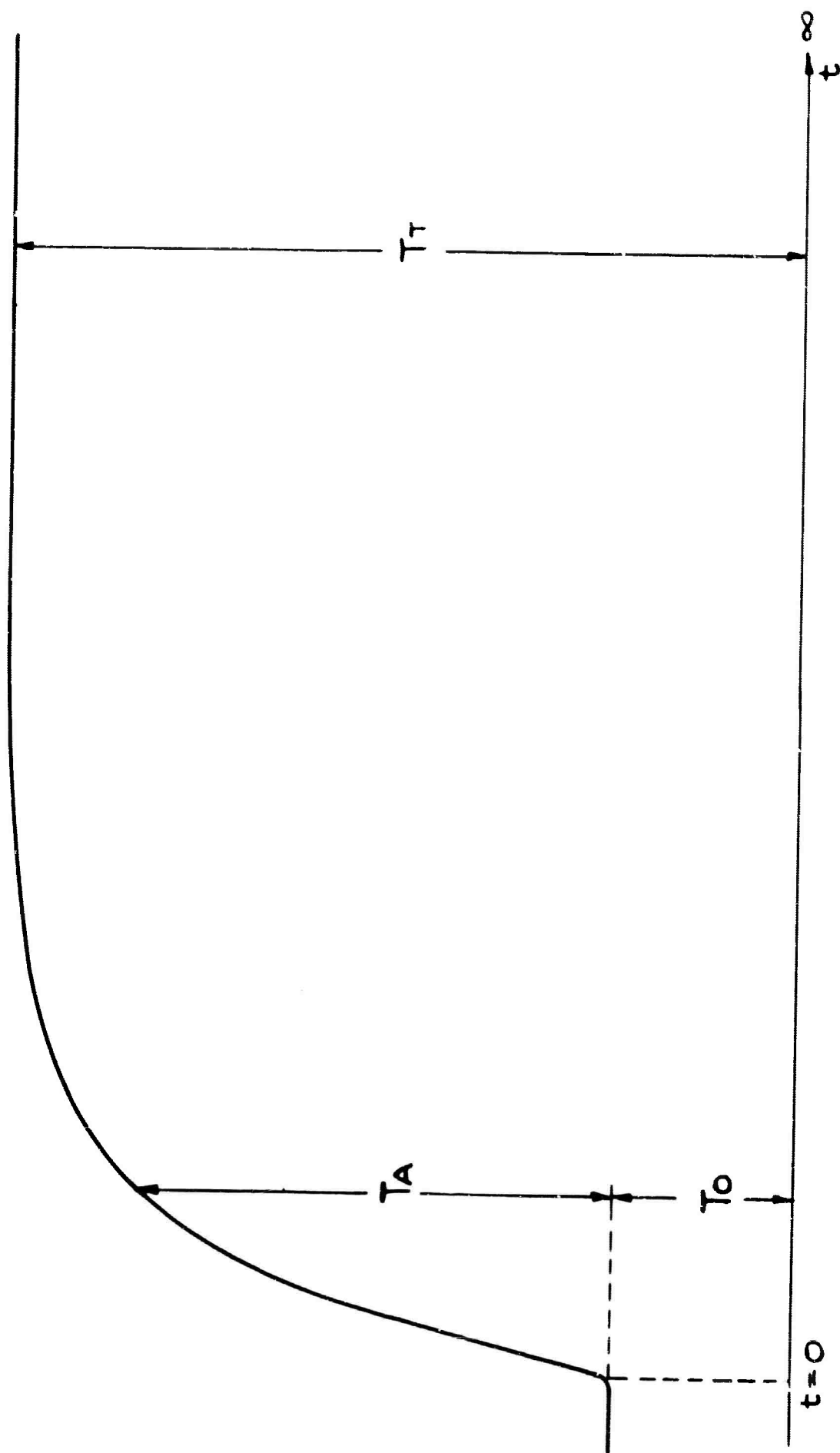
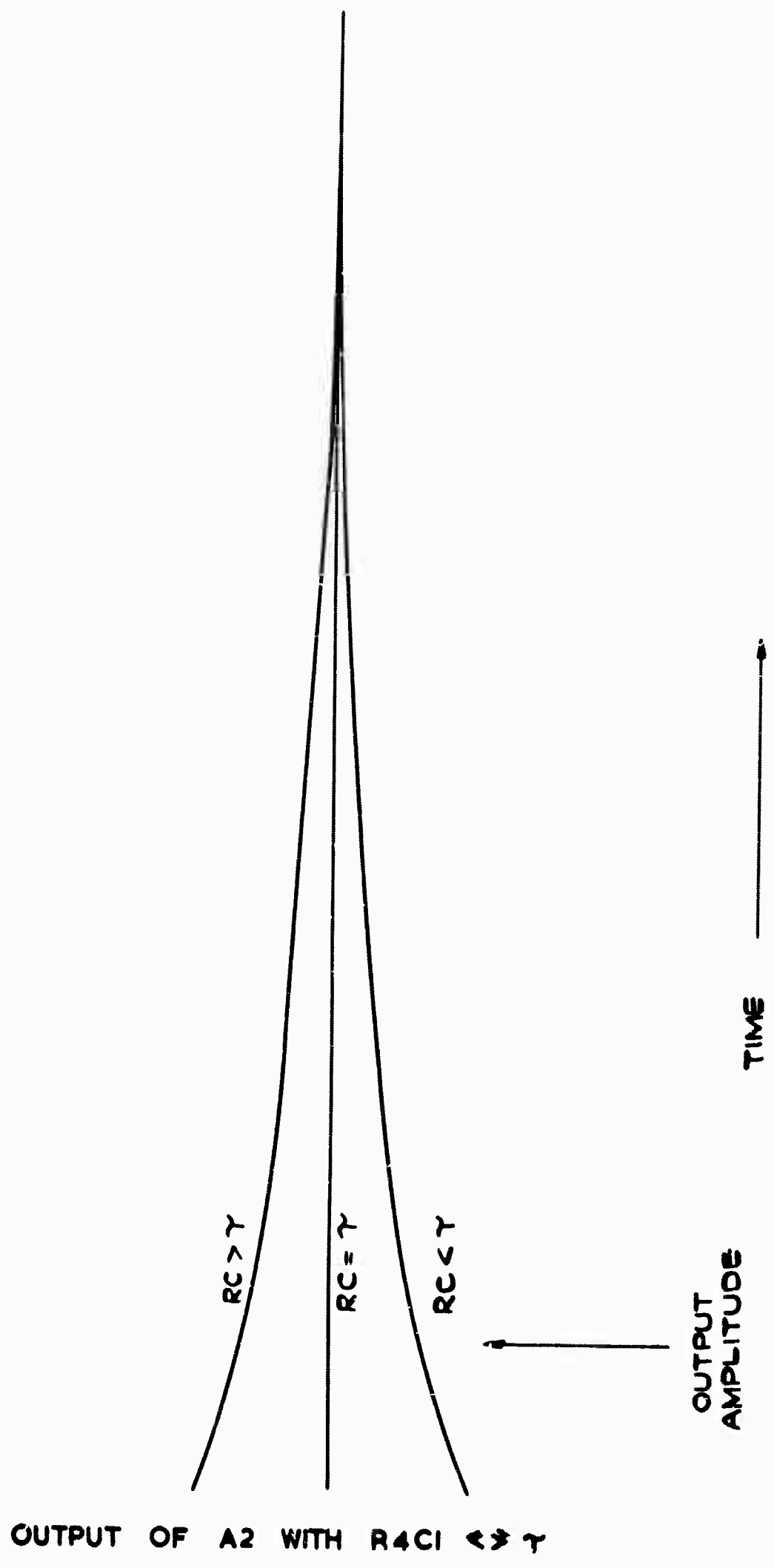


FIG6-5



TYPICAL THERMOCOUPLE RESPONSE TO A  
STEP CHANGE IN TEMPERATURE



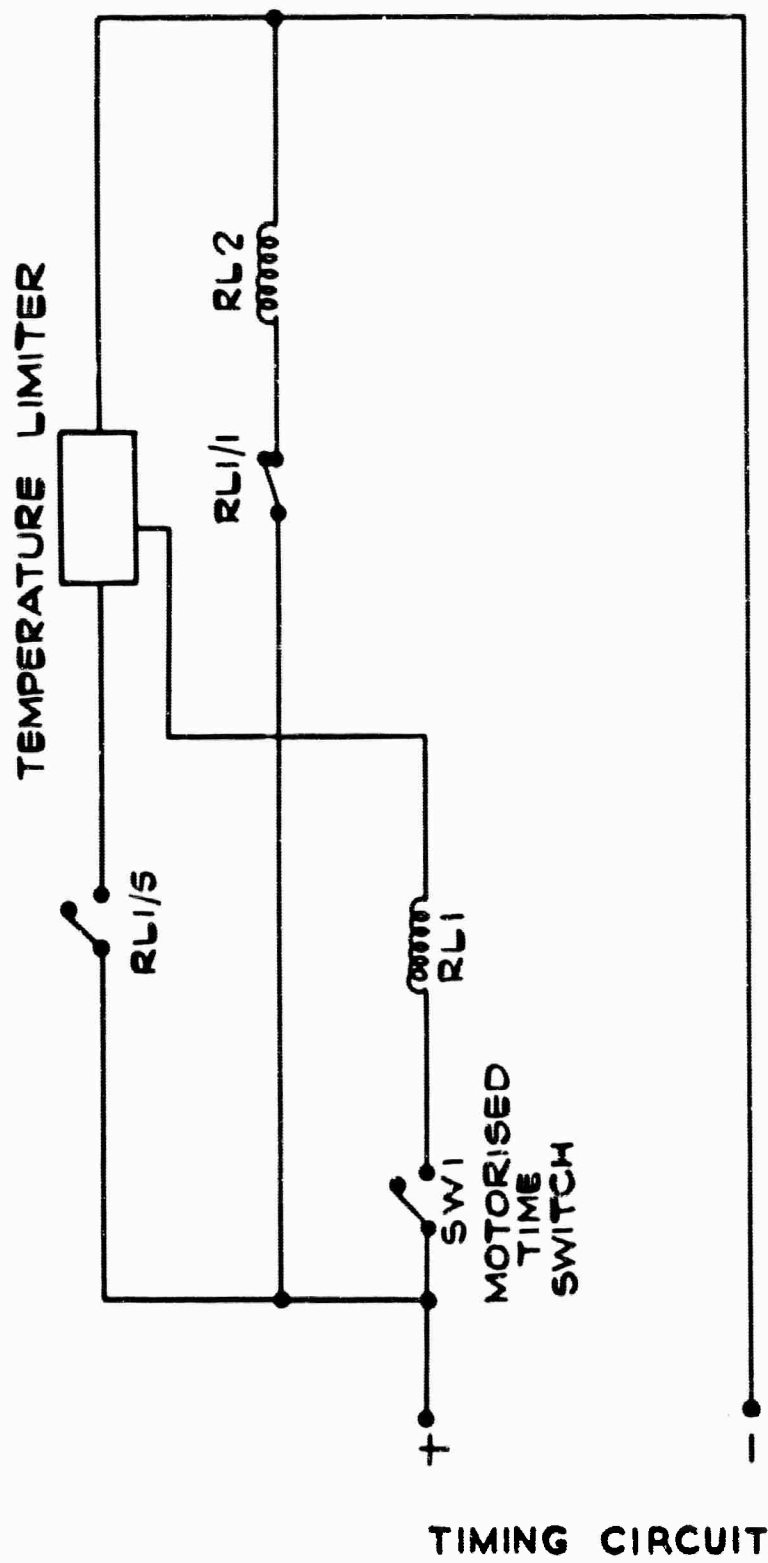
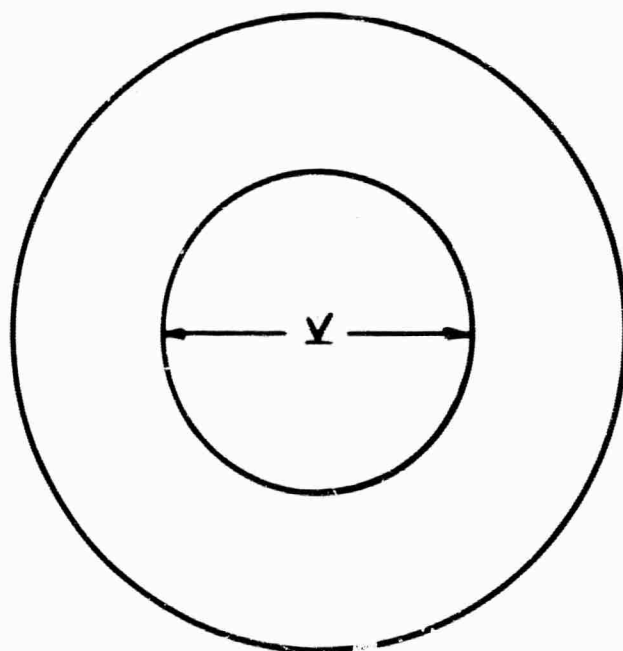
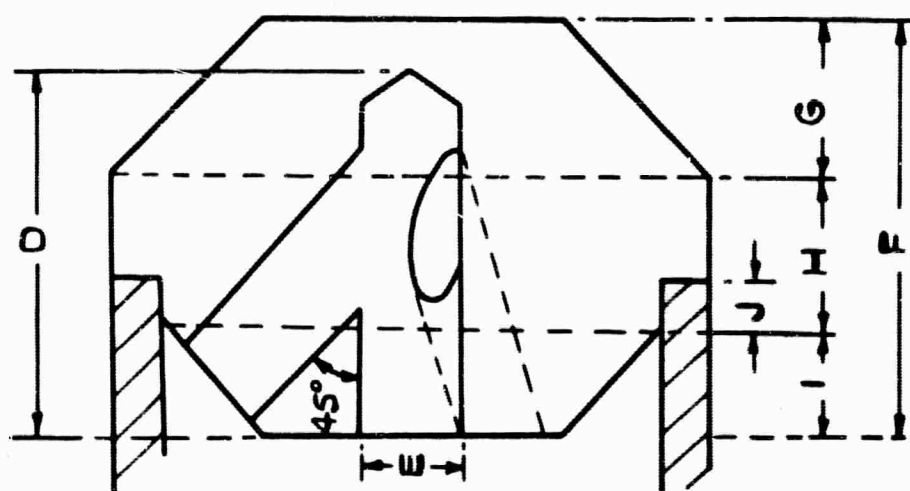
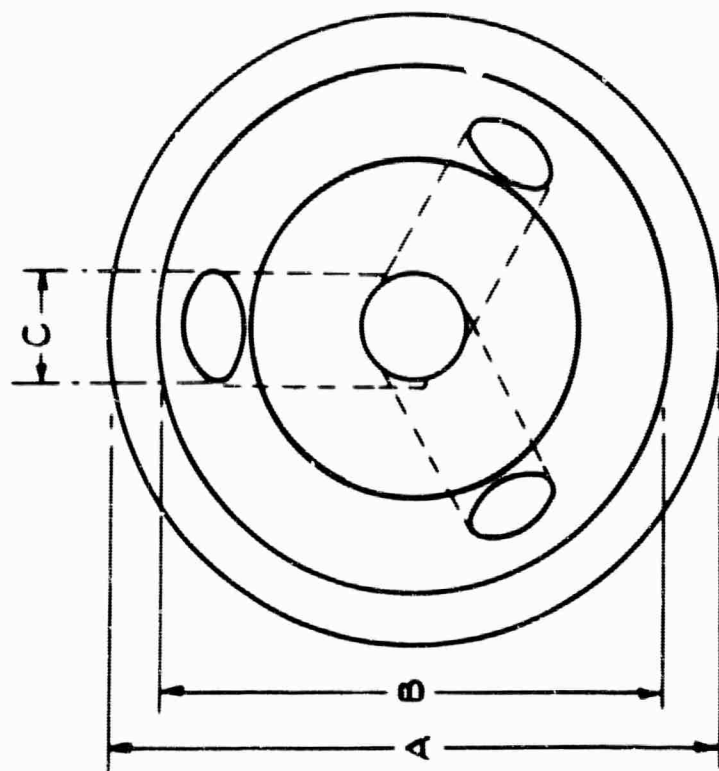


FIG 6.8

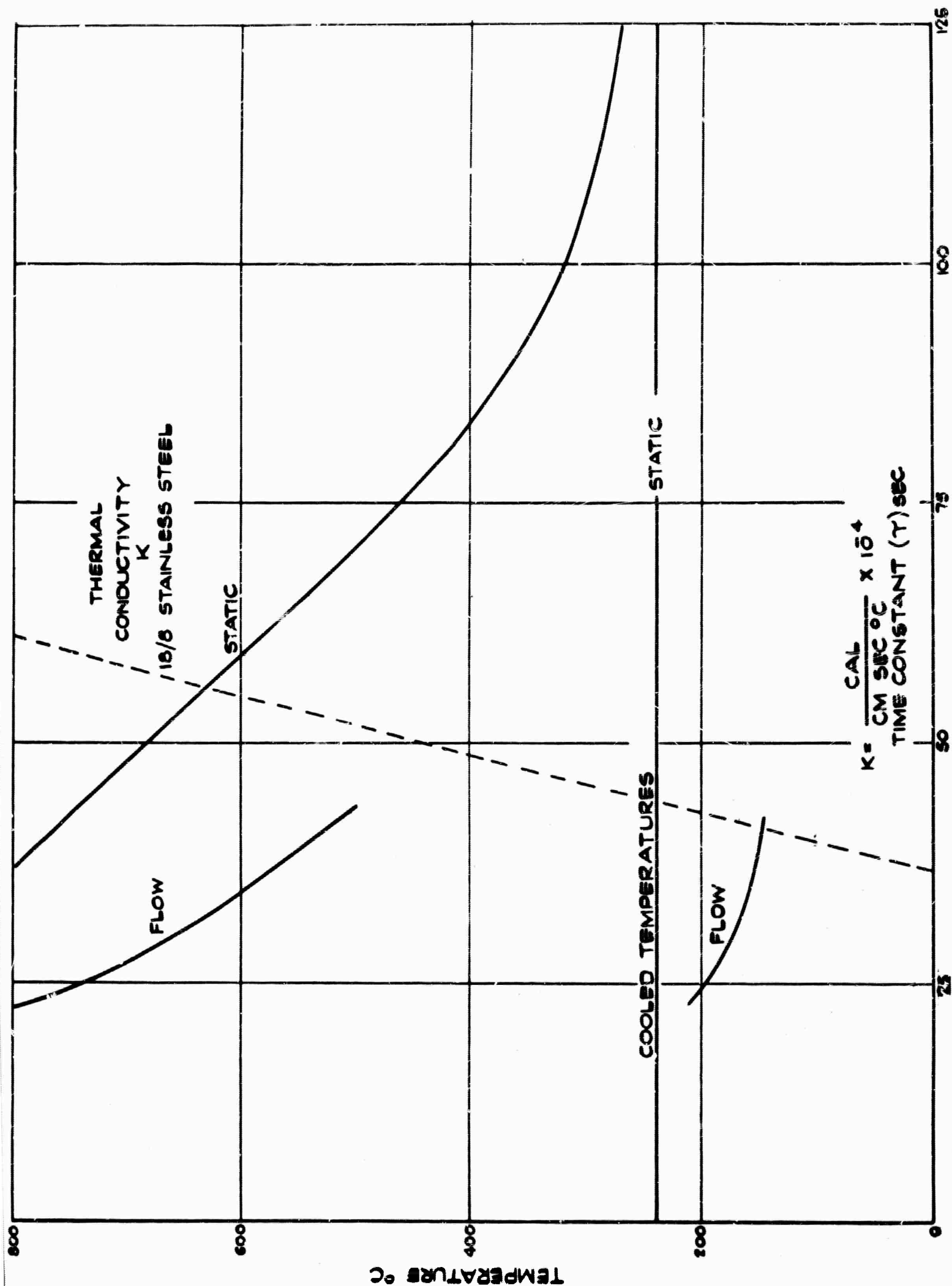


DIMENSION	A	B	C	D	E	F	G	H	I	J	K
.062" T/C	3/8	5/16	1/16	7/16	1/16	1/4	3/32	9/32	1/16	1/32	3/16
.04" T/C	1/4	3/16	3/64	1/4	3/64	3/16	3/32	1/16	1/16	1/32	1/16

THERMOCOUPLE COOLANT TUBE END CAP

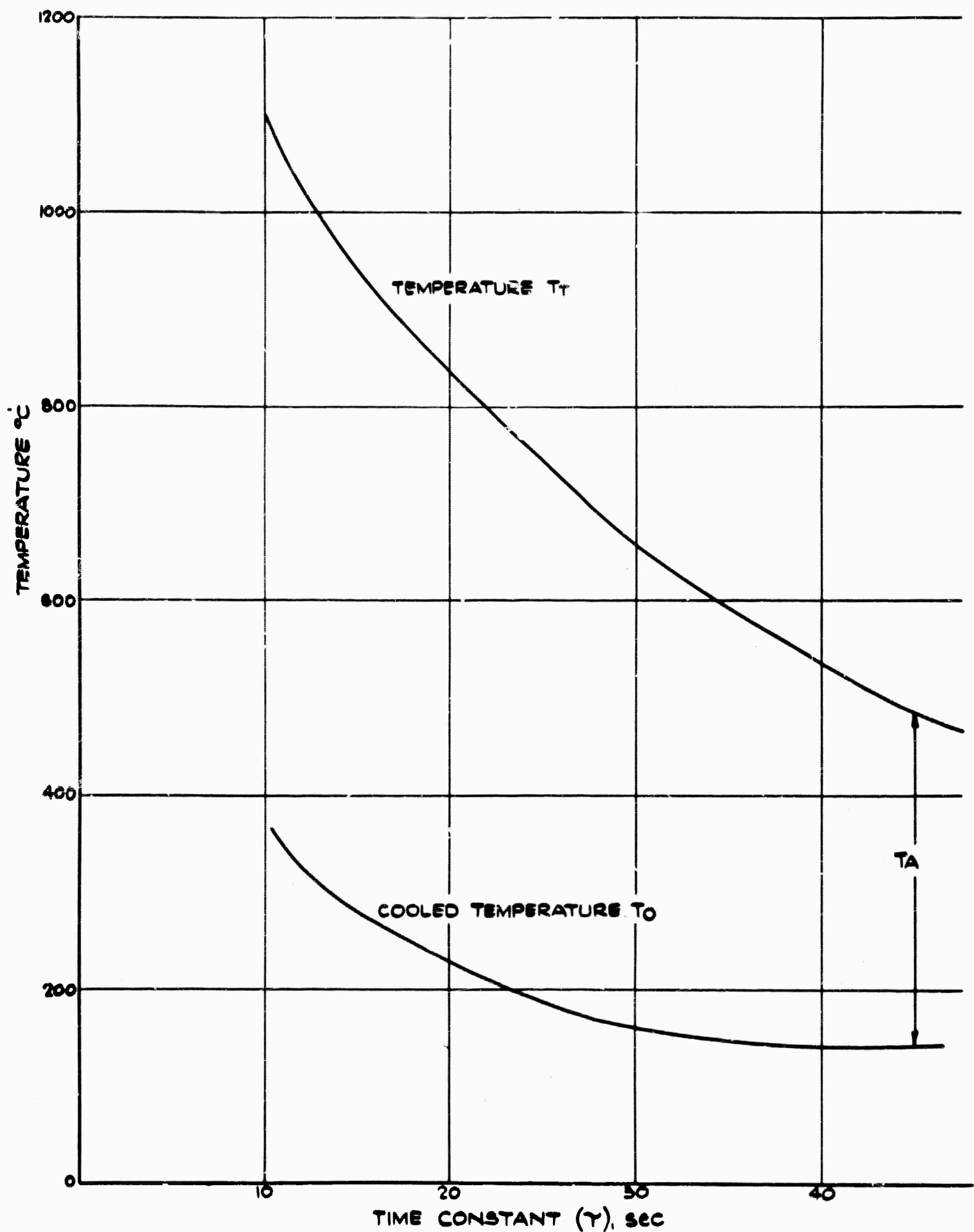
FIG 6-9





0.062 in THERMOCOUPLE VARIATION OF THE TIME CONSTANT  $\tau$  WITH TEMPERATURE FOR STATIC GAS AND FLOW

FIG 6.10



0.062 in THERMOCOUPLE VARIATION OF TIME CONSTANT  $\gamma$  WITH INCREASING HEAT FLOW AND TEMPERATURE

FIG 6.11

CHAPTER 7  
FUTURE PROGRAMME

by

B.C. Lindley

As intimated in the previous Technical Summary Report (IRD 64-36), a continuing two-year programme of research is envisaged, following the successful technological development which led to the first cesium-seeded operation in March 1964. Much of the value of the data obtainable in subsequent operations depends upon ability to obtain the flow parameters with reliable accuracy and to eliminate the leakage currents due to electrically-conducting layers on the MPD duct walls. Convenience of operation of the facility will depend on success in developing methods of separating cesium from helium, a problem which is important in a number of practical concepts of MPD generator.

Details of the range of parameters over which data on plasma behaviour and MPD power extraction are to be obtained were given in Section 1.2 of IRD 64-36. A somewhat greater emphasis will be placed on electrode processes since it is believed that these represent an ultimate limitation on specific power: current densities measured to date have been up to a few hundred amp/m<sup>2</sup> and in large-scale systems two orders of magnitude increase may be necessary.

PART 2 : PLASMA PHYSICS

## CHAPTER 8

### MICROWAVE STUDIES OF NON-EQUILIBRIUM PLASMA

by

J.H. Harris and D. Balfour

#### 8.1 GENERAL

The microwave cavity experiment was originally suggested as a means of studying photoionization and recombination in cesium and cesium-helium mixtures in relation to the possibility of increasing the efficiency of MPD generators by using ultra violet radiation to induce non-equilibrium ionization. This remains the long-term objective but in testing this experiment, in understanding the behaviour of the microwave bridge and in calibrating the response of the bridge it was advantageous to use electrical discharge pulses to create the ionization. Using a discharge tube it was possible to cut off the electric field in a few microseconds and then study the loss processes occurring in the afterglow of the discharge.

The information which this experiment can yield on the decay processes in cesium-helium mixtures is of very great importance to MPD generation in that the degree of ionization, and hence the electrical conductivity attainable in an MHD generator under non equilibrium conditions, is limited by the rate of loss of ionization. The loss processes include diffusion, recombination and attachment. The diffusion loss may be small in a generator, and, while attachment to cesium and helium may be negligible, attachment to impurity atoms may be significant. A small quantity of oxygen for example could make attachment the dominant loss mechanism. Most theoretical papers on generator performance have considered recombination as the only loss process and in particular have used values of recombination coefficient of  $\sim 10^{-13}$  cm<sup>3</sup>/ion sec appropriate to a three-body process. However, at lower temperature, dissociative recombination may be more important and the value of  $10^{-6}$  cm<sup>3</sup>/ion sec measured by Riondi and Brown<sup>1</sup> was ascribed to this process. The uncertainty of the recombination mechanism and the very sensitive dependence of three-body recombination on temperature call for accurate measurements of the recombination coefficient.

All of these loss processes can be studied in the existing experiment. So far the pressure and degree of ionization have shown diffusion to be the essential loss process; measurements have been made of the mobility of cesium ions in cesium vapour. The ionization and pressure can be adjusted to enable recombination to

be more important and the measurement of recombination of cesium will be the next stage in the experimental programme. A further stage will be the introduction of impurities to measure attachment probabilities.

## 8.2 MICROWAVE BRIDGE

The previous Technical Summary Reports (TRD 63-1 and 64-36) describe how a steel cavity was designed and constructed to operate in the  $TM_{020}$  mode at a resonant frequency of approximately 9000 mc/sec with a quartz tube inserted along its axis. The cavity was incorporated in a microwave bridge circuit (Fig. 8.1) or frequency discriminator, where a change in resonant frequency of the cavity results in an out-of-balance signal.

Tests on this bridge were made using the ionization produced in an electrical discharge in air between tungsten electrodes sealed in the ends of the plasma tube. The first type of discharge to be used was produced by half-wave rectified alternating high voltage supply. This gave results of the type illustrated in Fig. 8.2 where the top trace shows part of one cycle of the current flowing through the discharge tube, and the bottom trace gives the out-of-balance signal. A square-wave modulation of 1000c/sec was applied to the klystron signal in this early set of measurements and both traces are displayed with time plotted horizontally. The interesting feature of Fig. 8.2 is that over the region where the current is increasing, the bridge signal first grows rapidly, passes through a maximum and then slowly decreases.

## 8.3 BRIDGE THEORY AND CALIBRATION

A theory of the action of the bridge (Fig. 8.1) was developed to explain these features, where the bridge has been adjusted initially so that in arm A the signal C reflected from the cavity leads the signal P reflected from the short-circuit plunger by  $90^\circ$  but in arm B the signal C lags  $90^\circ$  behind the signal P. This is illustrated in Fig. 8.3.

$$\begin{aligned} \text{Bridge out of balance signal} &= B^2 - A^2, \text{ since square law detectors are used,} \\ &= 4PC' \sin \Delta\phi \end{aligned}$$

where  $C'$  is the signal reflected from the cavity and  $\Delta\phi$  is the shift in phase of the reflected signal when free electrons are present in the plasma tube.

If  $V$  is the voltage amplitude falling on the cavity and  $S$  is the VSWR of the cavity, then

$$\text{Bridge signal} = 4FV \left( \frac{1-S}{1+S} \right) \sin \Delta\phi \quad \dots (8.1)$$

The reactance,  $X$ , of the cavity is given by

$$X = 2Q_u R \frac{\Delta f}{f_0} \quad \dots (8.2)$$

where  $R$  is the cavity resistance,

$Q_u$  is the unloaded selectivity of the cavity,

and  $\Delta f$  is the shift of frequency from the resonant frequency  $f_0$ .

With a new quartz plasma tube inserted in the cavity, the precision attenuator and slotted-guide standing wave indicator were used to obtain values of  $S$  over a range of frequencies with the results shown in Fig. 8.4. The graph yields the following values:

VSWR at resonance	= 0.50
loaded selectivity ( $Q_L$ )	= 5700
unloaded selectivity ( $Q_u$ )	= 8000 and
coupling factor ( $\beta$ )	= 0.40

The value of  $S$  at resonance specified the impedance contour to be used on a Smith Chart. A value of  $\Delta f$  was chosen and substituted in equation (8.2) to obtain the corresponding  $X$  value. The intersection of this value of  $X$  with the impedance contour gives the corresponding values of both  $\Delta\phi$  and  $S$  to be substituted in equation (8.1) to calculate the bridge signal. This procedure is illustrated in Fig. 8.5. Results were compared with two independent sets of experimental results. One method involved keeping the klystron frequency constant and varying the resonant frequency of the cavity by varying its diameter (through change of temperature over a range of  $40^\circ\text{C}$ ). This gave the results shown in Fig. 8.6. In the other method the resonant frequency of the cavity was kept constant and the klystron frequency was varied; this gave an identical set of results. Fig. 8.6 shows the agreement between the theoretical and experimental results. The variation of out-of-balance signal with frequency shift is called the calibration curve.

In some experimental cases, the calibration curve was observed to be asymmetrical. This may possibly have been due to inaccurate setting of the short circuit plunger, and to check on this, the effect on the theoretical curve of an inaccuracy of setting of 1mm was evaluated by modifying equation (8.1) to become:

$$\text{Bridge signal} = 4PV \left( \frac{1-S}{1+S} \right) \sin(\Delta\phi + \alpha) \quad \dots\dots (8.3)$$

where  $\alpha$  is the phase change introduced by a plunger movement of 1 mm. The resulting calibration curve is shown in Fig. 8.7.

The decay of ionization on suddenly removing the voltage applied to an electrical discharge in air was recorded using different sections of the calibration curve. The bottom trace of Fig. 8.8 shows a plasma decay taking the cavity over the range A to D, Fig. 8.8b from B to E and Fig. 8.8c from C to F (for the significance of the letters, A, B, C, D, E and F, see Fig. 8.9). In each

case the top trace shows the current through the discharge. Fig. 8.10 shows the electron concentration decay curves calculated from Figs. 8.8a, b, c and since these exhibit the same form the interpretation of the calibration curve was considered valid.

#### 8.4 IDENTIFICATION OF TM<sub>020</sub> MODE

It was observed experimentally that on inserting the plasma tube through the cavity the frequency of the TM<sub>020</sub> mode was shifted by 800 Mc/s and that with the tube in position this resonance was within 60 Mc/s of another mode (see IRD 64-36 Fig. 16.1). Initially there was difficulty in identifying the TM<sub>020</sub> mode. Inconclusive attempts to distinguish the TM<sub>020</sub> mode were made firstly by heating the cavity and secondly by introducing shims to increase the cavity length, but the resonant frequencies of both modes were independent of the length of the cavity. However, by inserting a steel wire along the axis of the cavity one mode exhibited a continuous decrease in Q value as the wire was introduced and finally disappeared completely, whereas the other mode was unaffected. The affected mode was the TM<sub>020</sub> with its strong axial electric field.

#### 8.5 ELECTRON CONCENTRATION MEASUREMENTS IN ARGON AFTERGLOW

Having established the working characteristics of the bridge and its ability to follow a rapid decay in electron concentration, attention was turned toward decay conditions in argon to obtain a comparison with results reported by other workers. The air in the discharge tube was replaced with commercial cylinder argon and the decay of ionization on suddenly removing the applied voltage was recorded over a range of argon pressures.

Fig. 8.11 shows a typical oscilloscope trace, where the argon pressure was 2.7 torr: the graticule squares each represent 20  $\mu$ sec on the horizontal time scale. The top trace shows the bridge signal, line 1 gives the level of the upper turning point of the calibration curve and line 2 gives the lower turning point; the balance point of the bridge in this trace was on the lower turning point. The variation of electron concentration with time calculated from Fig. 8.11 is shown in Fig. 8.12 (the calculation made to obtain electron concentration from frequency shift assumes that the collision frequency is small compared with the radian frequency of the applied signal).

Electron loss processes in the decaying plasma are ambipolar diffusion, ion-electron recombination and electron attachment, and the loss rate may be written as

$$\frac{dn_e}{dt} = D_a \nabla^2 n_e - \alpha n_e^2 - \nu_a n_e \quad \dots (8.4)$$



where  $n_0$  is the electron concentration,  
 $D_a$  is the ambipolar diffusion coefficient,  
 $\alpha$  is the recombination coefficient,  
 $h$  is the attachment coefficient, and  
 $\nu_0$  is the electron collision frequency.

A study of equation (8.4) shows that the diffusion and attachment processes yield an exponential decay of electron concentration with time, but the recombination process leads to a linear relationship between the inverse of electron concentration and time.

In Fig. 8.13 the logarithm of frequency shift is plotted against time. Since frequency shift is proportional to electron concentration the straight line form of these curves indicates that, as an electron loss process, recombination is negligible at the gas pressure and electron concentration used in the present experiments. Furthermore, the rate of loss of electrons varies approximately as the inverse of the gas pressure and this suggests that the loss process is essentially diffusion: the pressure dependence of an attachment process would be either linear in the case of a two-body mechanism or quadratic in a three-body mechanism. A theoretical treatment of ambipolar diffusion leads to the following expressions for the ambipolar diffusion coefficient  $D_a$  and the reduced mobility  $\mu_0$  (reduced to NTP)

$$D_a = \frac{A^2}{\tau} = \left(\frac{r}{2.405}\right)^2 \frac{1}{\tau} \quad (\text{for first order diffusion}) \quad \dots (8.5)$$

$$\mu_0 = \frac{4.17 \times 10^3}{1 + \frac{T_e}{T_g}} \frac{p}{T_g} \frac{A^2}{\tau} \quad \text{cm}^2/\text{volt sec} \quad \dots (8.6)$$

where  $r$  is the radius of the discharge tube,  
 $p$  is the gas pressure in torr,  
 $A$  is the characteristic diffusion length of the plasma enclosure,  
 $\tau$  is the time constant of the electron concentration decay, and  
 $T_g$  is the gas temperature and  $T_e$  the electron temperature.

In the results quoted here, the electron temperature was assumed to be equal to the gas temperature. When the applied voltage is removed the electron temperature is likely to be much larger than the gas temperature but it has been estimated that thermal equilibrium will be approached in a period of approximately 50  $\mu\text{sec}$ . The zero of time in Figs. 8.11, 8.12 and 8.13 correspond to at least 50  $\mu\text{sec}$  after the removal of the ionising voltage.

Biondi and Brown have shown that for ambipolar diffusion under conditions of thermal equilibrium  $p_0 D_a = \text{constant}$ , where  $p_0$  is the pressure reduced to normal temperature. Values of  $\mu_0$  and  $p_0 D_a$  for argon over the range of pressures studied were calculated from the curves of Fig. 8.13 and are given in the following table.

p, torr	0.1	1.5	2.7	6.0	8.2	10
$\mu_0$ , cm <sup>2</sup> /volt-sec	7.9	9.4	4.9	6.4	7.5	8.3
$p_0 D_a$ , torr cm <sup>2</sup> /sec	350	420	220	280	330	370

The values of  $p_0$  and  $D_a$  are sufficiently constant to be consistent with electron loss due to ambipolar diffusion as deduced independently from the variation of the loss rate with pressure. The values of  $\mu_0$  shown in the above table are higher by a factor of at least 2 than the values reported by Biondi and Chanin<sup>2</sup>. However, the impurity in the argon in these experiments may have been appreciable. Higher values of electron concentration are required before recombination becomes the dominant process.

## 8.6 ELECTRON MEASUREMENTS IN CESIUM AFTERGLOW

The decay process in cesium vapour was studied in the same way as for argon. The electrical discharge tube was connected to a cesium-capsule container and bath, pumped down to a very low pressure, sealed off and enclosed in ovens. The capsule was broken; the plasma tube, connecting line and cavity were raised to a constant temperature in the region of 700°K, and the cesium vapour pressure was controlled and estimated using the temperature of the cesium bath. High voltage pulses were applied to the cesium vapour and cut off sharply using the method described in the previous report (IRD 64-36).

The initial experiments were aimed at studying the effect of the power of the probing signal on the decay of electron concentration, since the microwave signal might tend to heat the electrons. The effect of varying the length of the ionization pulse so that uniform breakdown might be produced in the discharge tube was also studied.

### 8.6.1 Effect of varying microwave power

Decay curves were recorded first with the full klystron power (approximately 0.15 watt) supplied to the bridge, then with 6 db attenuation between klystron and bridge, and finally with 13 db inserted. The trace with 6 db inserted is shown in Fig. 8.14 together with starting level, top and bottom levels of the calibration curve and the discharge current trace.

The graphs of the logarithm of resonant frequency shift of the cavity against time are given in Fig. 8.15. The relative displacements of the parallel lines are due only to different times of triggering and the straight line form shows that the process responsible for decay of electron concentration is ambipolar diffusion. The graphs also show a diffusion rate independent of power level.

The effect of introducing large microwave power into the discharge would be to raise the electron temperature and since

$$D_a = \frac{D_+}{1 + \frac{T_e}{T_g}} \quad \dots (8.7)$$

the ambipolar diffusion coefficient would be correspondingly affected. The measurements indicate that for the values of microwave power used in the experiments the heating of the electrons was not significant. However, under conditions where recombination is the dominant loss process the dependence on electron temperature may be much more sensitive. Under these circumstances a further check on the effect of microwave power will be necessary.

#### 8.6.2 Effect of varying the length of the ionization pulse

Various authors have reported that the rate of loss of electrons from afterglows is dependent on the duration of the ionizing pulse. In certain cases where the ionization pulse is short the distribution of ionization in the discharge tube is inhomogeneous; Oskam and Mittelstadt<sup>3</sup>, for example, have reported asymmetrical light distribution for ionization pulses shorter than 15  $\mu$ sec. Where the ionization is limited to a filament within the discharge tube the assumption that the ionization fills the discharge tube will lead to overestimates of diffusion coefficients and of recombination coefficients. By increasing the width of the ionization pulse a more uniform distribution of the ionization can be achieved and more reliable values of diffusion and recombination coefficients can be deduced.

An experiment was carried out to make certain that the results deduced from the afterglow measurements were not affected by the duration of the ionisation pulse. Cesium vapour was contained in the discharge tube at 600°K and 0.6 torr as determined by the temperature of the vapour bath. The duration of the ionisation pulse was varied between 100 and 300  $\mu$ sec and for each case the decay in electron concentration after cutting off the ionizing pulse was monitored by recording the out-of-balance signal of the microwave bridge.

As in the earlier experiments the electron loss process was dominated by ambipolar diffusion and since the frequency shift of the cavity due to ionization in the discharge tube is proportional to electron concentration a linear dependence was

found between the logarithm of the frequency shift and time (Fig. 8.16). Points are shown for the two extreme values of ionization pulse width and, within experimental error, all points can be related to the same straight line.

The conclusion from this experimental result is that ionization pulses of only 100  $\mu\text{sec}$  are sufficient to produce homogeneous breakdown.

## 8.7 CESIUM ION MOBILITY

The mobility of the cesium atoms can be deduced from the measured diffusion coefficient. The Einstein relationship between the mobility and diffusion coefficients of a particle can be written as

$$\frac{\mu}{D} = \frac{e}{kT} \quad \text{..... (8.8)}$$

where  $\mu$  is the mobility of the particle

$D$  is the diffusion coefficient of the particle

$T$  is the temperature of the particles

$e$  is the electronic charge and

$k$  is Boltzmann's constant

For ions:

$$\frac{\mu_+}{D_+} = \frac{e}{kT_+} \quad \text{..... (8.9)}$$

and the ion diffusion coefficient  $D_+$  can be expressed in terms of the ambipolar diffusion coefficient,  $D_a$ , by the equation

$$D_a = D_+ \left( 1 + \frac{T_e}{T_+} \right), \quad \text{..... (8.10)}$$

where  $T_e$  and  $T_+$  are the electron and ion temperatures.

Hence

$$\mu_+ = \frac{e}{kT_+} \cdot \frac{D_a}{1 + \frac{T_e}{T_+}} \quad \text{..... (8.11)}$$

In practice, mobilities are reduced to normal temperature and pressure so that the reduced mobility  $\mu_0$  is given by

$$\mu_0 = \frac{e}{kT_+} \cdot \frac{D_a}{1 + \frac{T_e}{T_+}} \cdot \frac{p}{760} \cdot \frac{273}{T_g} \quad \text{..... (8.12)}$$

where  $p$  is the gas pressure in torr and  $T_g$  is the gas temperature.

To deduce the ambipolar diffusion coefficient the diffusion equation must be solved for the cylindrical geometry of the discharge tube.

$$\begin{aligned}\frac{dn}{dt} &= -\text{div}(nv) \\ &= D_a \nabla^2 n\end{aligned}\quad \text{..... (8.13)}$$

If the electron concentration decays with a time constant  $\tau$ , then  $n = n_0 e^{-t/\tau}$  where  $n_0$  is the initial electron concentration, and the diffusion equation can be written as

$$\nabla^2 n_0 + \frac{n_0}{D_a \tau} = 0 \quad \text{..... (8.14)}$$

For a cylinder of radius  $r_0$  and height  $h$  a solution of this equation is

$$n(r, z, t) = \sum_{i=1}^{\infty} \sum_{j=1}^{\infty} G_{ij} J_0(\alpha_i, r) \cos \frac{(2j-1)\pi z}{h} \exp \left[ -\frac{t}{\tau_{ij}} \right]$$

with

$$\frac{1}{D_a \tau_{ij}} = \alpha_i^2 + \left[ \frac{(2j-1)\pi}{h} \right]^2$$

where  $\alpha_i r_0$  is the  $i^{\text{th}}$  root of the Bessel function  $J_0$ . Assuming that the first diffusion mode dominates the loss process, then  $i = j = 0$  and

$$\frac{1}{D_a \tau} = \left( \frac{2.405}{r_0} \right)^2 + \frac{\pi^2}{h^2}$$

For the discharge used in the experiment  $h \gg r_0$  so that, assuming that the ion temperature  $T_+$  is equal to the gas temperature  $T_g$ , the reduced mobility can be written as

$$\mu_0 = \frac{4.17 \times 10^3}{1 + \frac{T_e}{T_g}} \frac{p}{T_g} \left( \frac{r_0}{2.405} \right)^2 \frac{1}{\tau} \text{ cm}^2/\text{volt sec} \quad \text{..... (8.15)}$$

From the slopes of the  $\log \Delta f$  vs  $t$  plots, values of  $1/\tau$  were deduced for the experiments described earlier in which the microwave power was varied and in which the width of the ionization pulse was changed. The calculated values of  $\mu_0$  deduced from these results are given below.

	p, torr	$T_g, ^\circ\text{K}$	$\frac{1}{\tau}, \text{sec}^{-1}$	$\mu_0, \text{cm}^2/\text{volt sec}$
Experiment 1	1.1	630	$460 \times 10^3$	0.26
Experiment 2	0.6	600	$4.84 \times 10^3$	0.17

Earlier measurements of the mobility of cesium ions in cesium vapour are as follows.

	ion	$\mu_0$ , cm <sup>2</sup> /volt sec	Method
Dandurand and Holt <sup>4</sup>	Cs <sub>2</sub> <sup>+</sup>	0.065	Diffusion : microwave cavity
Chen and Raether <sup>5</sup>	Cs <sup>+</sup>	0.4(revised to 0.2)	Diffusion : microwave transmission (assumes Blancs Law for mobility in mixtures)
Chanin and Steen <sup>6</sup>	Cs <sub>2</sub> <sup>+</sup>	0.21	Time of flight
	Cs <sup>+</sup>	0.075	

The values of reduced mobility determined in the present experiment are close to the revised value of Chen and Raether and the faster ion detected by Chanin and Steen. There is no experimental evidence whereby the ions dominating the diffusion loss in the present experiment may be identified but the values measured are close to the theoretical value of 0.2 deduced by Chanin and Steen from the Langevin classical theory of mobility for Cs<sub>2</sub><sup>+</sup>.

It is interesting to note that Oskam and Mittelstadt<sup>3</sup> measured values of mobility for rare gas ions in the parent gas which increased with increasing pressure before reaching a constant value at pressures above a few torr; this low pressure behaviour was explained in terms of diffusion cooling. A similar behaviour might be expected in cesium vapour and so it is proposed to measure  $\mu_0$  as a function of pressure in the near future.

Brown<sup>7</sup> has shown that in a d.c. electric field the mobility of an ion can be written as

$$\mu = \frac{e}{m_i \nu_m} \quad \dots (8.16)$$

where  $m_i$  is the mass of the ion and  $\nu_m$  is the frequency of collision for momentum transfer.

$$\nu_m = \nu_0 \overline{(1 - \cos \theta)} \quad \dots (8.17)$$

where  $\nu_0$  is the collision frequency and  $\overline{1 - \cos \theta}$  is averaged over all values of  $\theta$ , the angle through which a particle is scattered with respect to the electric field direction.

The total collision cross section for the ion may be expressed in terms of the collision frequency as

$$Q = \left( \frac{\pi m_+}{8kT_+} \right)^{1/2} \frac{\nu_0}{m_+}$$

$$= \left( \frac{\pi}{8kTm_+} \right)^{\frac{1}{2}} \cdot \frac{e}{\mu m} \cdot \frac{1}{1 - \cos\theta} \quad \dots (8.18)$$

and

$$\mu = \left( \frac{r_0}{2.405} \right)^2 \cdot \frac{1}{\tau} \cdot \frac{e}{kT_+} \cdot \frac{1}{1 + \frac{T_-}{T_+}} \quad \dots (8.19)$$

An accurate assessment of  $1 - \cos\theta$  is difficult to determine but if the value 1 be used then a lower limit of  $500 \times 10^{-16} \text{ cm}^2$  is obtained for the total cross section for scattering of cesium ions by cesium atoms.

### 8.8 DIFFUSION, RECOMBINATION AND ATTACHMENT

In all of the experiments reported, the loss of electrons in the afterglow has been due to ambipolar diffusion. To measure recombination coefficients it will be necessary to modify conditions so that the rate of volume recombination becomes greater than the rate of diffusion loss. Gray and Kerr<sup>8</sup>, using a TM<sub>010</sub> microwave cavity, have studied the decay of ionization in which diffusion and volume recombination are both significant. They define a parameter which is the ratio of the initial volume recombination rate in the absence of diffusion to the rate of diffusion in the fundamental mode, and for reliable estimates of recombination to be deduced from  $\frac{1}{n}$  vs  $t$  plots they have shown that

$$\beta \gg 15$$

$$\text{where } \beta = \frac{\alpha n_e^2(t_0)}{D_a \frac{n_e(t_0)}{\Lambda^2}}$$

and  $\Lambda$  is the characteristic diffusion length ( $\Lambda = 2.405$  for the discharge tube used in the present experiment).

Thus it may be possible in the present apparatus to measure loss due to volume recombination by increasing the electron concentration and by working at higher pressures where  $D_a$  is smaller (because  $p D_a = \text{constant}$ ). Some increase in electron concentration can be achieved by decreasing the value of the current limiting resistor and the cesium vapour pressure can be increased to about 10 torr in the present apparatus. The diffusion loss could also be reduced by applying a longitudinal magnetic field and the dimensions of the tube could be increased if necessary. Thus, by choosing suitable conditions it should be possible to enable recombination coefficients to be measured in pure cesium. Subsequently the recombination processes occurring in cesium-helium mixtures will be studied and, by introducing impurities into the plasma tube, it will also be possible to evaluate attachment coefficients.

The experiment is inherently capable of studying all the loss processes that will limit the level of ionization and plasma electrical conductivity attainable in an MPD generator.

#### 8.9 PRELIMINARY EXPERIMENTAL STUDIES OF PHOTOIONIZATION

Fig. 8.17 shows a plasma tube with quartz end windows which was used to detect photoionization in cesium vapour produced by a mercury vapour lamp. The cesium vapour pressure was determined by controlling the temperature of the cesium bath and the plasma tube was heated to approximately  $600^{\circ}\text{K}$ . The variation of electron density in the cesium vapour is shown in Fig. 8.18 for a vapour pressure of approximately 10 torr and with the lamp mounted so that an ultra violet beam was directed along the axis of the plasma tube. The lamp was operated from 50 c/s mains supply and the electron density reveals the anticipated 100 c/s variation superimposed on a much lower frequency which was due to a mechanical vibration. This lower frequency is also displayed in the absence of any illumination from the lamp.

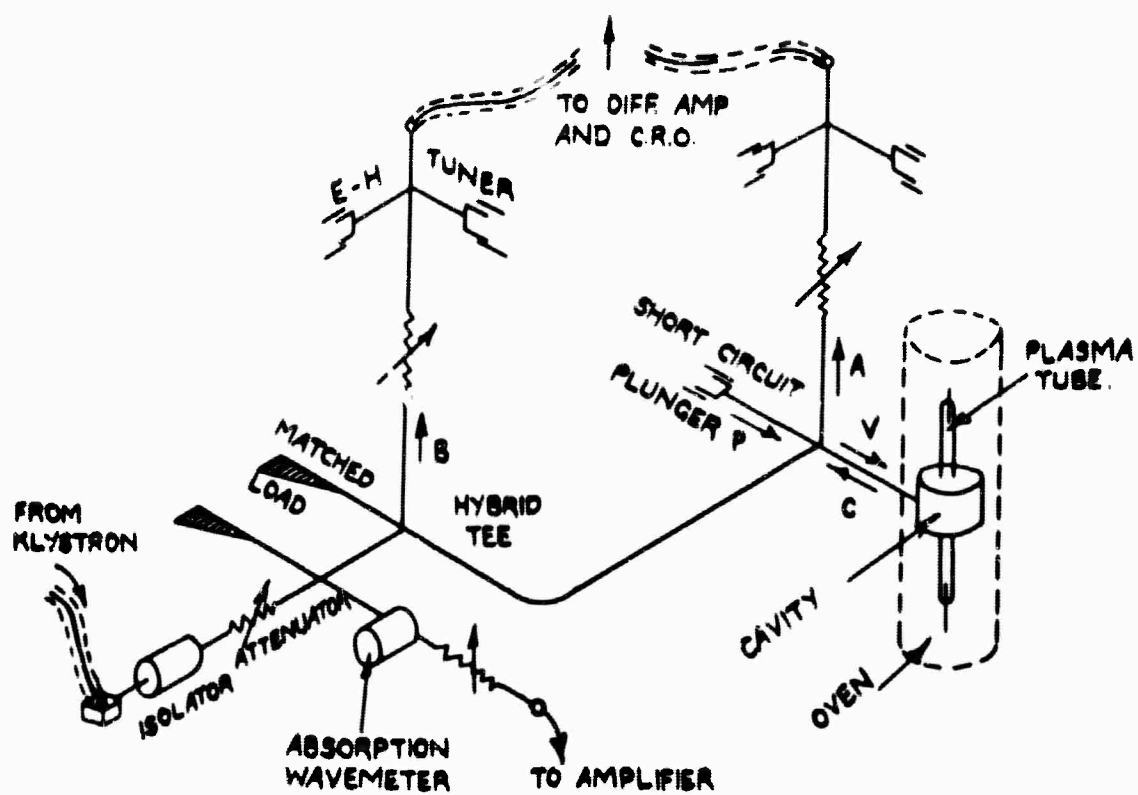
The microwave bridge was tuned to maximum sensitivity to record this photoionization and the maximum electron density detected was approximately  $10^8 \text{ cm}^{-3}$ . The variation of peak electron concentration as a function of vapour pressure is shown in Fig. 8.19. The difference between the results for heating and cooling is due to a lag between the cesium vapour pressure variation and the bath temperature variation.

These measurements are a satisfactory preliminary step in the study of photoionization but for measurements of photoionization cross section and for recombination a more powerful source of ultra violet radiation will be required.

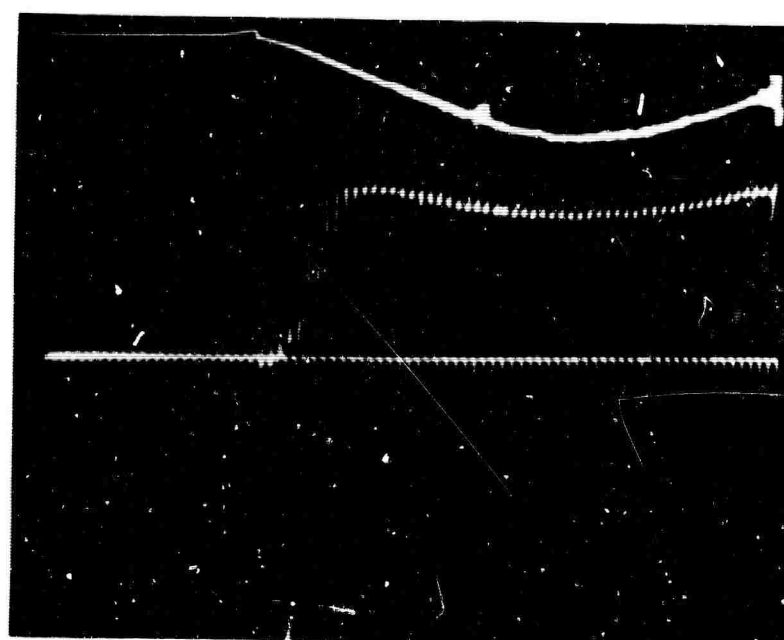
#### REFERENCES

- 1 BIONDI, M.A. and BROWN, S.C. Phys. Rev. vol.75, p1700 (1949)
- 2 BIONDI, M.A. and CHANIN, L.M. Phys. Rev. vol.94, p910 (1954)
- 3 OSKAM, H.J. and MITTELSTADT, V.R. Phys. Rev. vol.132, p1435 (1963)
- 4 DANDURAND, P. and HOLT, R.B. Phys. Rev. vol.82, p278 (1951)
- 5 CHEN, C.L. and RAETHER, M. Phys. Rev. vol.128, p2679 (1962)
- 6 CHANIN, L.M. and STEEN, R.D. Phys. Rev. vol.132, p2554 (1963)
- 7 BROWN, S.C. 'Basic data of plasma physics' p50. (John Wiley and Sons Ins. New York 1959.)
- 8 GRAY, E.P. and KERR, D.E. Fourth International Conference on Ionisation Phenomena in Gases. Uppsala, Sweden. (North Holland Publishing Company, Amsterdam (1960)



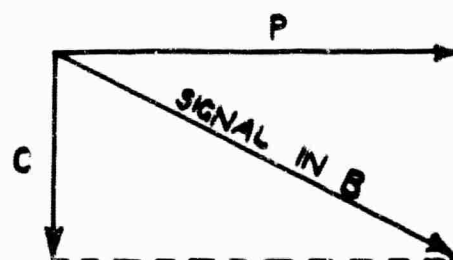
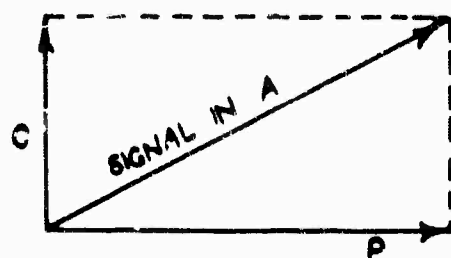


MICROWAVE BRIDGE OR FREQUENCY DISCRIMINATOR

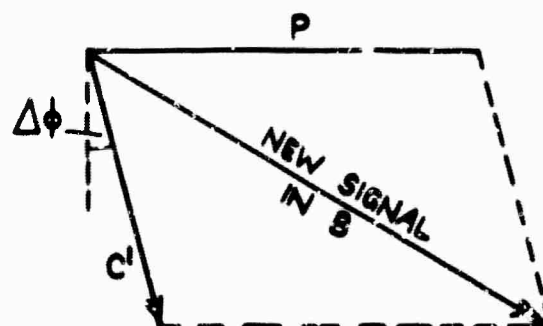
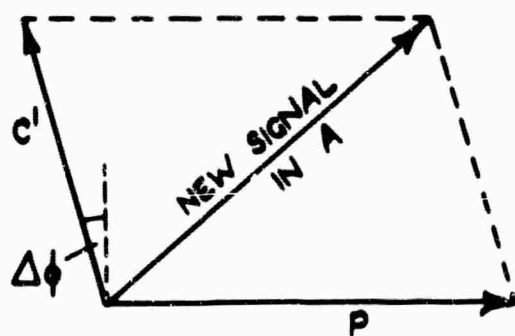


CURRENT THROUGH DISCHARGE TUBE AND CORRESPONDING OUT OF BALANCE  
SIGNAL ON MODULATED MICROWAVE BRIDGE

INITIALLY, ON RESONANCE

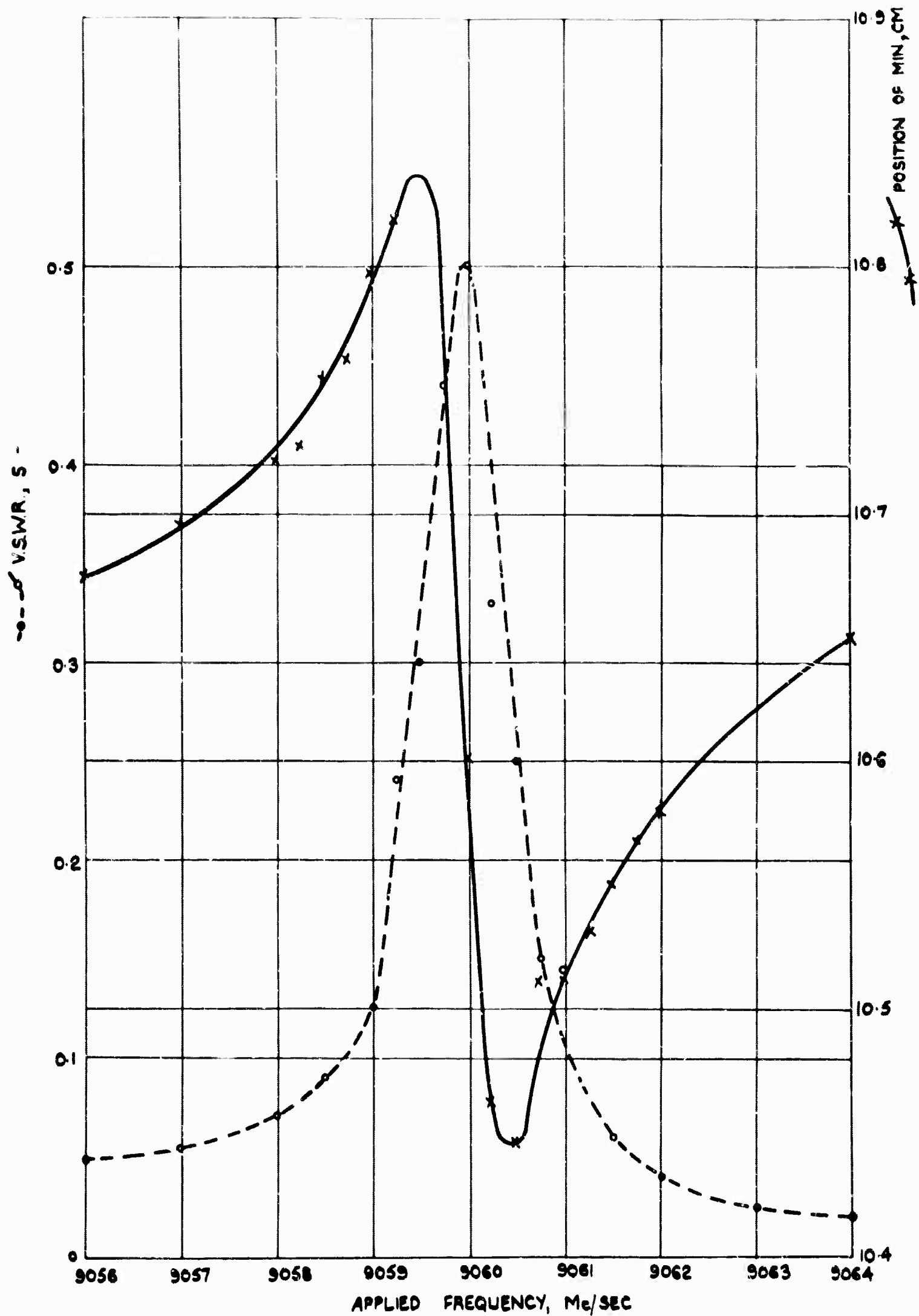


AFTER FREQUENCY SHIFT  $\Delta f$



VECTOR REPRESENTATION OF SIGNALS AT DETECTORS OF MICROWAVE BRIDGE

FIG 8.3



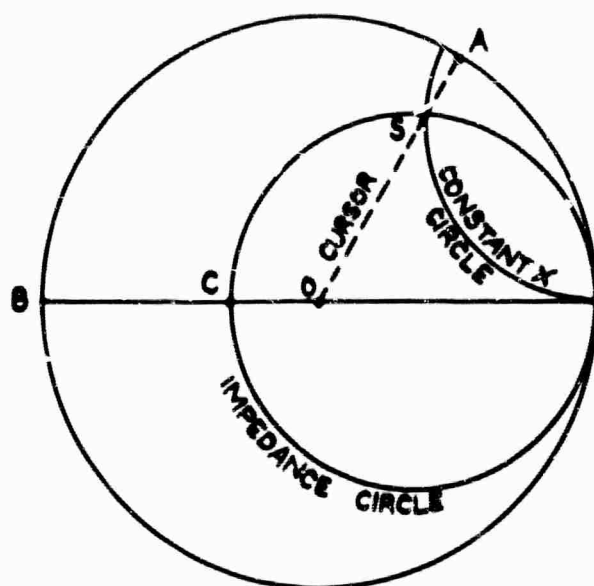
NOTE

- ①
- ②
- ③
- ④

USE

CURVES USED IN CALCULATION OF CAVITY PARAMETERS

FIG8.4

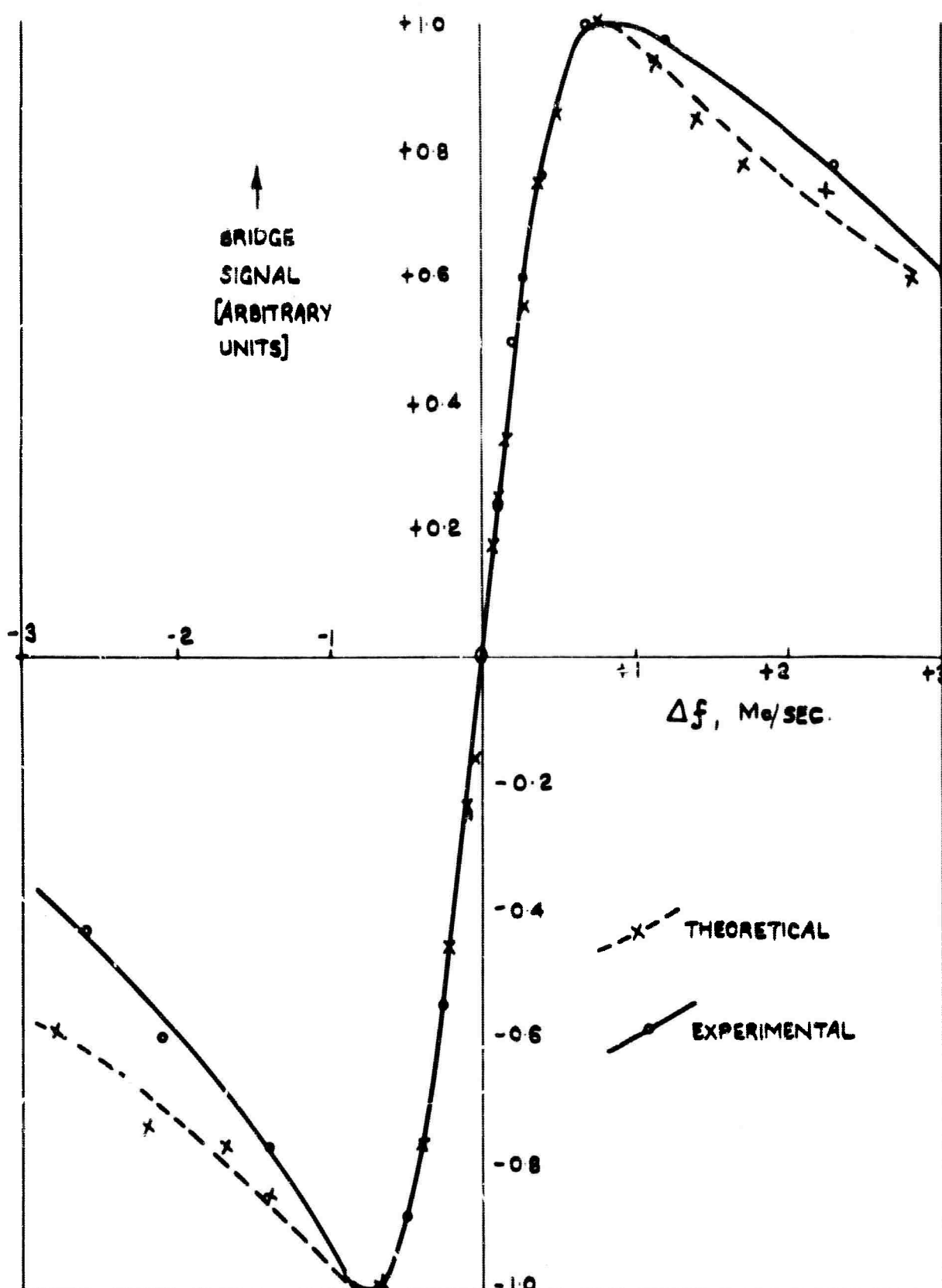


**NOTES:-**

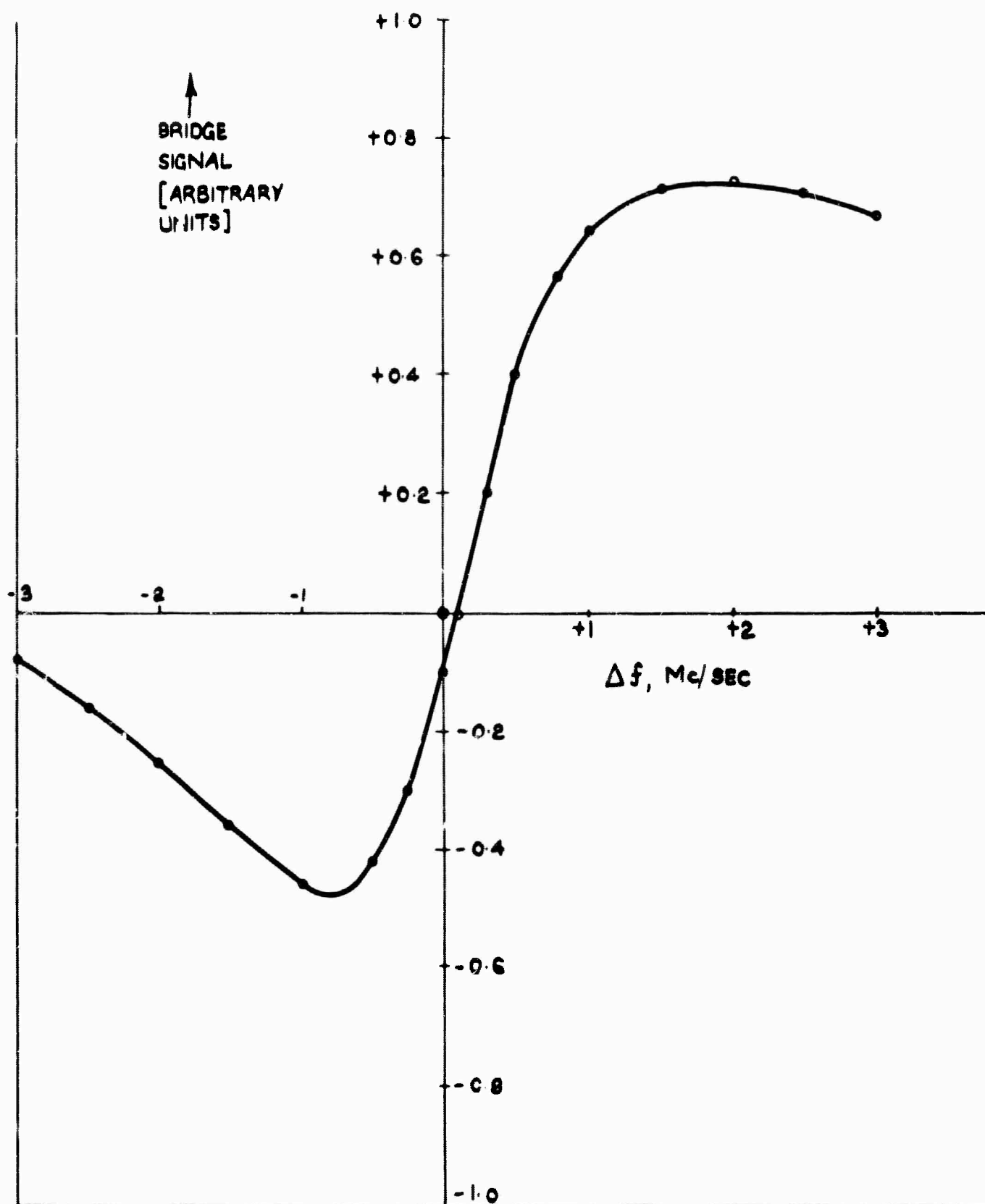
- ① DISTANCE OS ALONG CURSOR GIVES VSWR CORRESPONDING TO  $\Delta f$
- ② DISTANCE BA AROUND OUTSIDE CIRCLE GIVES  $\Delta\phi$  CORRESPONDING TO  $\Delta f$
- ③ POSITION OF POINT C IS SET BY VSWR AT RESONANCE  
AND GOVERNS SIZE OF IMPEDANCE CIRCLE
- ④ INTERSECTION OF IMPEDANCE CIRCLE AND CONSTANT X CIRCLE GIVES  
POSITION OF POINT S, AND CONSEQUENTLY POSITION OF CURSOR

USE OF SMITH CHART IN ANALYSIS OF BRIDGE

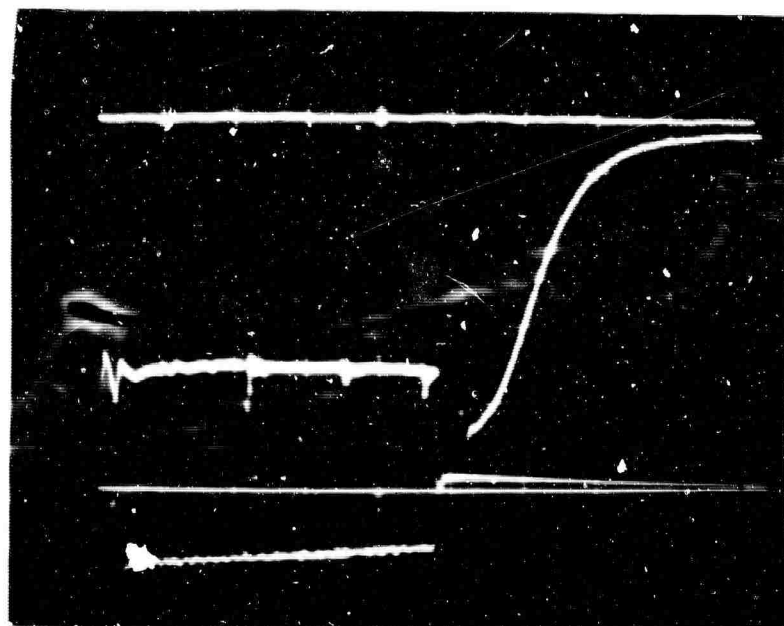
**FIG 8.5**



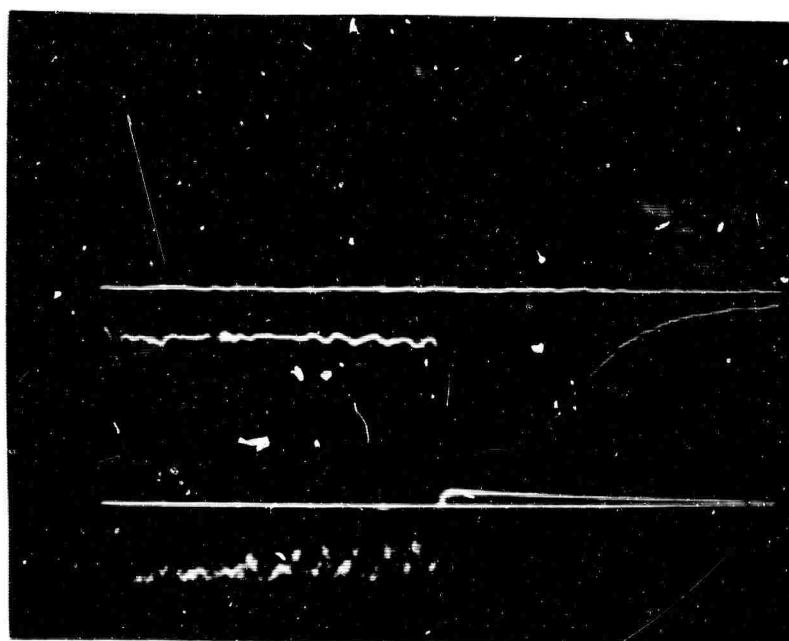
COMPARISON OF THEORETICAL AND EXPERIMENTAL CURVES FOR BRIDGE RESPONSE



EFFECT OF INACCURACY IN SHORT-CIRCUIT SETTING ON  
BRIDGE CHARACTERISTIC



(a) RANGE A-D



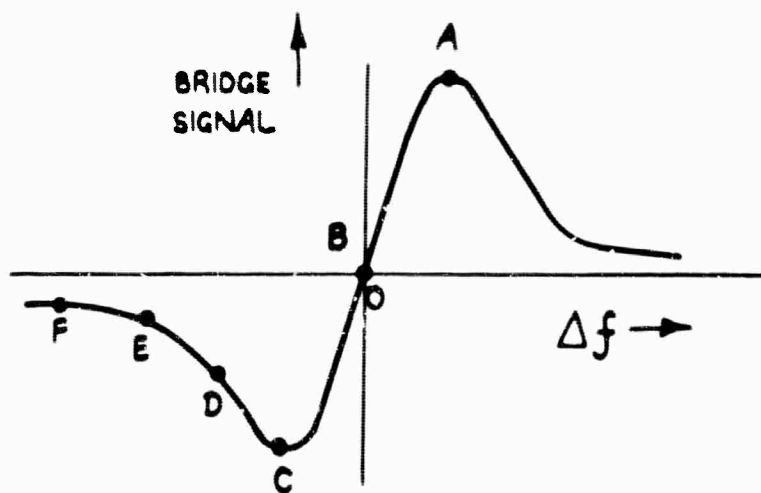
(b) RANGE B-E



(c) RANGE C-F

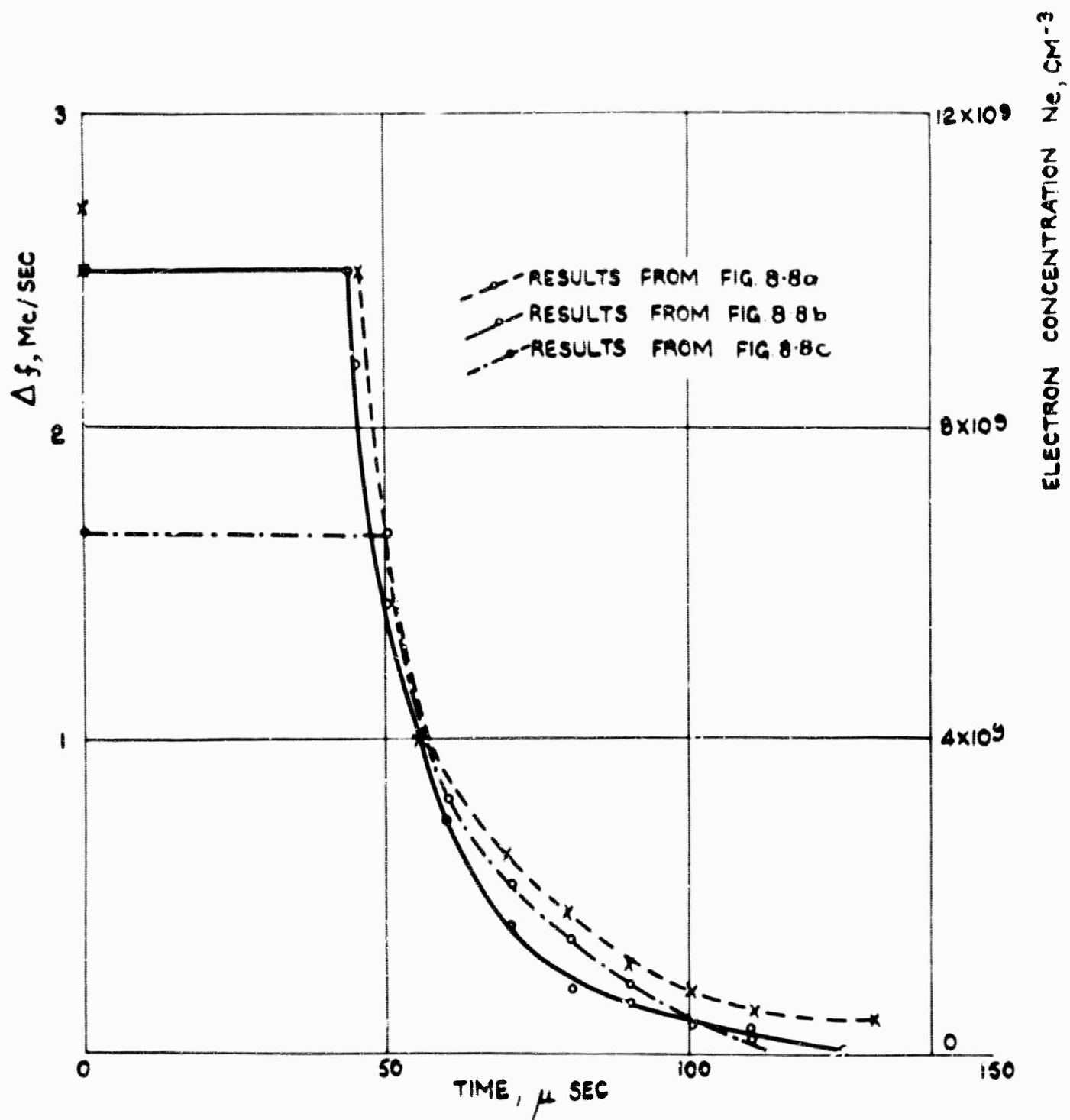
TRACES OF DECAY OF IONIZATION USING DIFFERENT RANGES OF CALIBRATION CURVE (SEE FIG 8.9)





FORM OF CALIBRATION CURVE

FIG 8.9



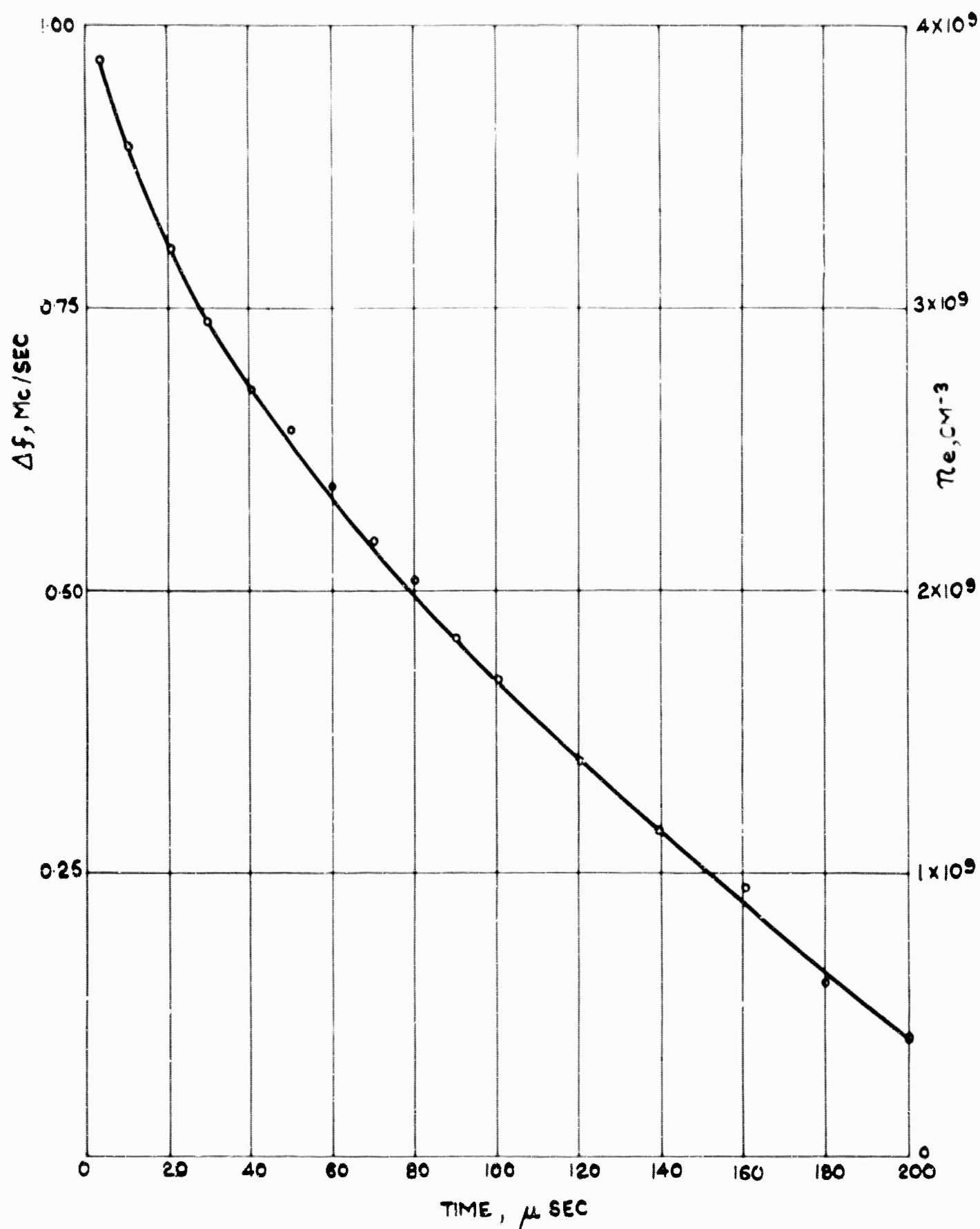
DECAY OF ELECTRON CONCENTRATION IN AIR AT 0.2 TORR

FIG 8-10



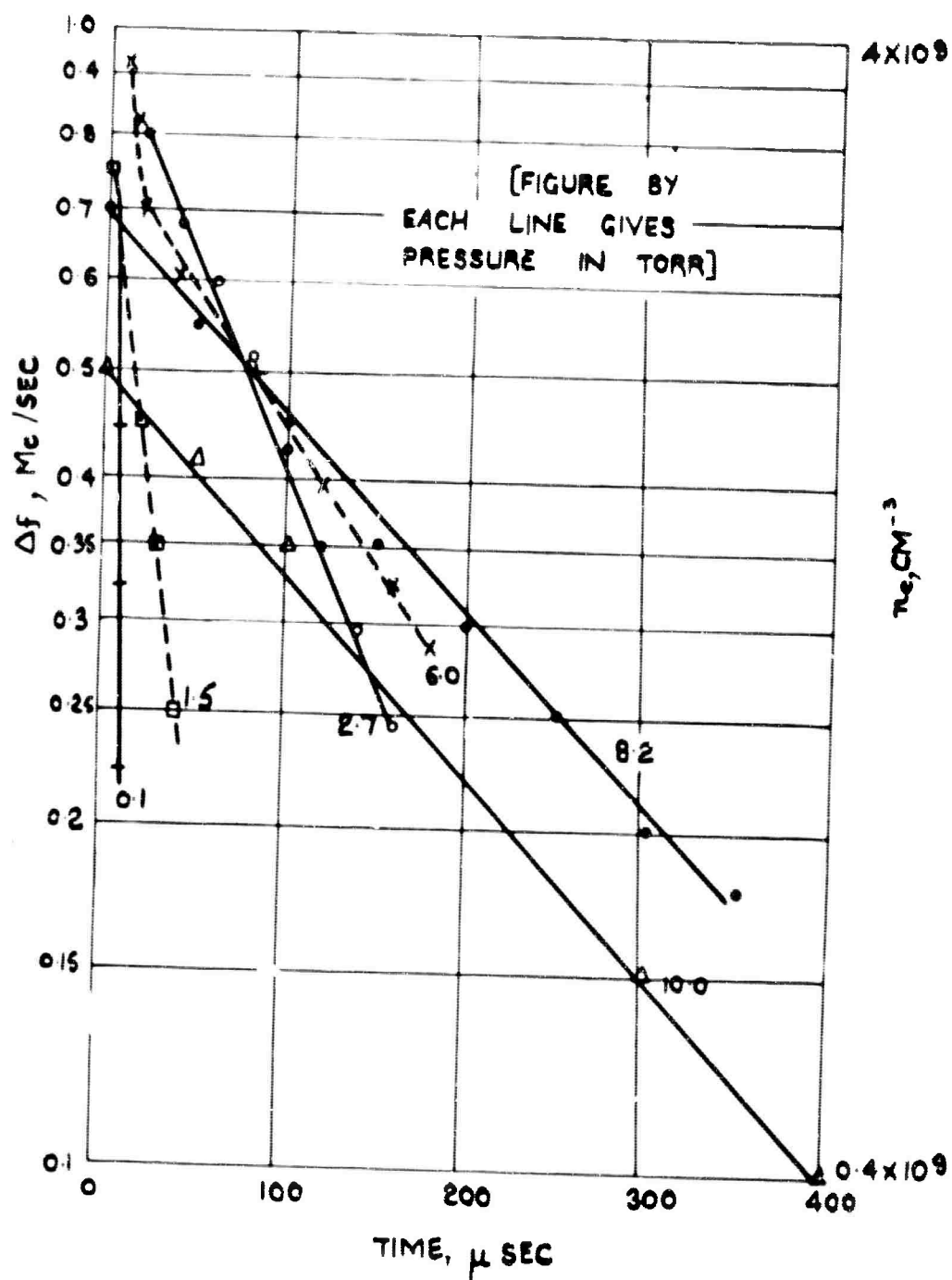
TRACE OF DECAY OF IONIZATION IN ARGON

FIG 8.11



DECAY OF ELECTRON CONCENTRATION IN ARGON AT 2.7 TORR

FIG 8-12

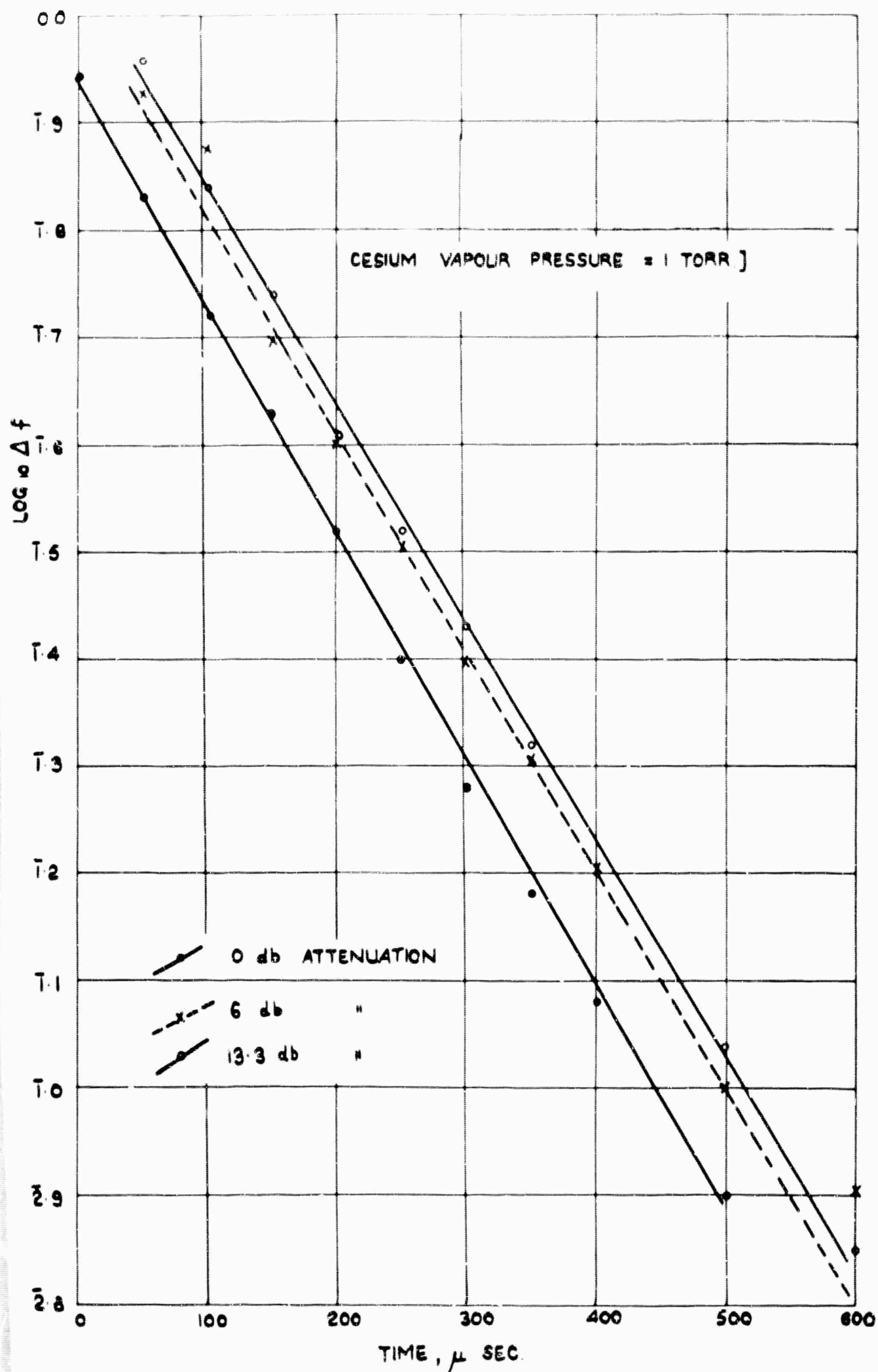


DECAY OF ELECTRON CONCENTRATION IN ARGON

FIG8-13

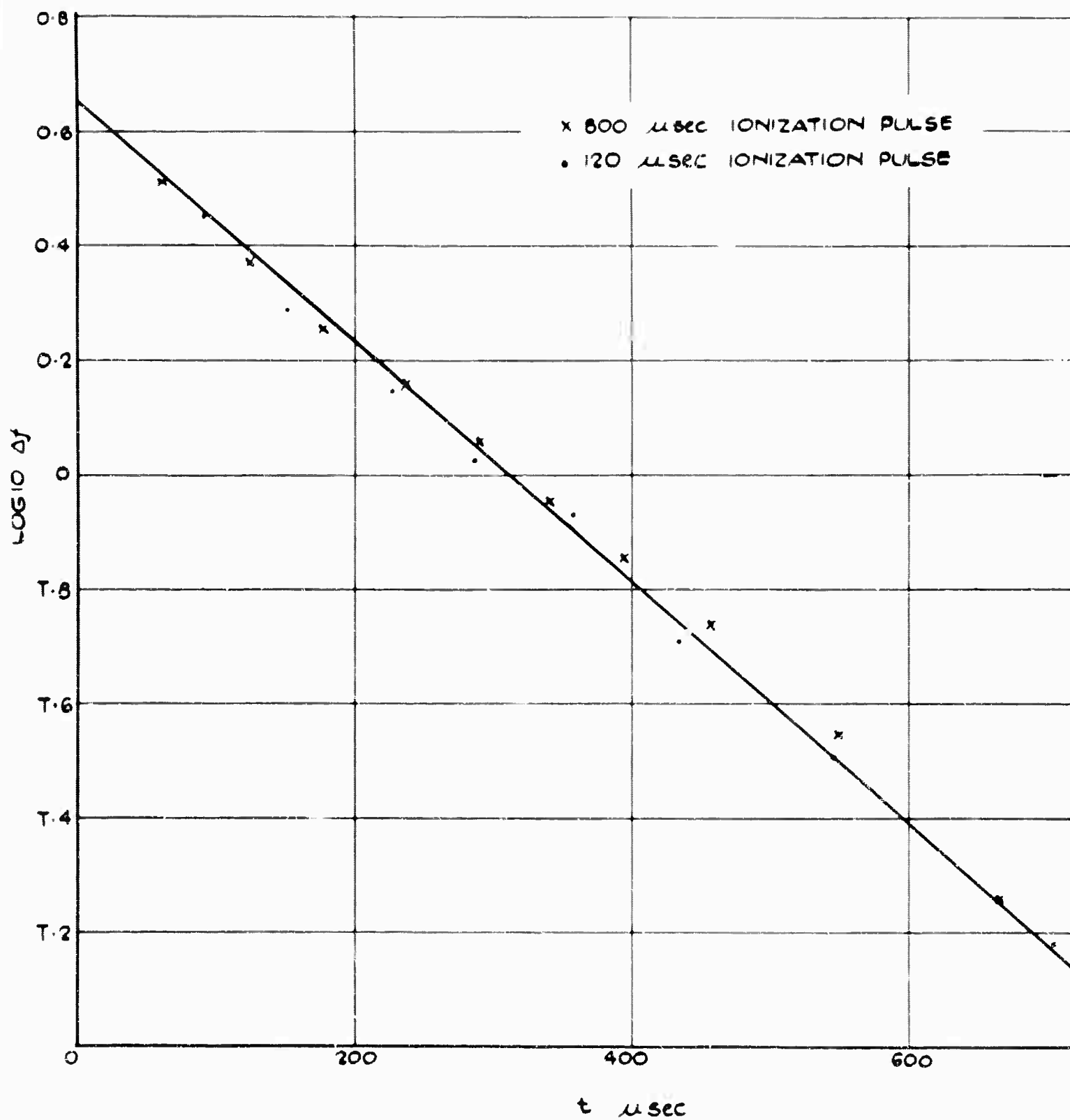


DECAY OF IONIZATION IN CESIUM VAPOUR



DECAY OF ELECTRON CONCENTRATION IN CESIUM VAPOUR FOR DIFFERENT POWERS OF MICROWAVE PROBING SIGNAL

FIG 8.15



DECAY OF ELECTRON CONCENTRATION IN CESIUM VAPOUR





G 8-17 PLASMA TUBE CAPSULE BREAKER AND CESIUM BATH

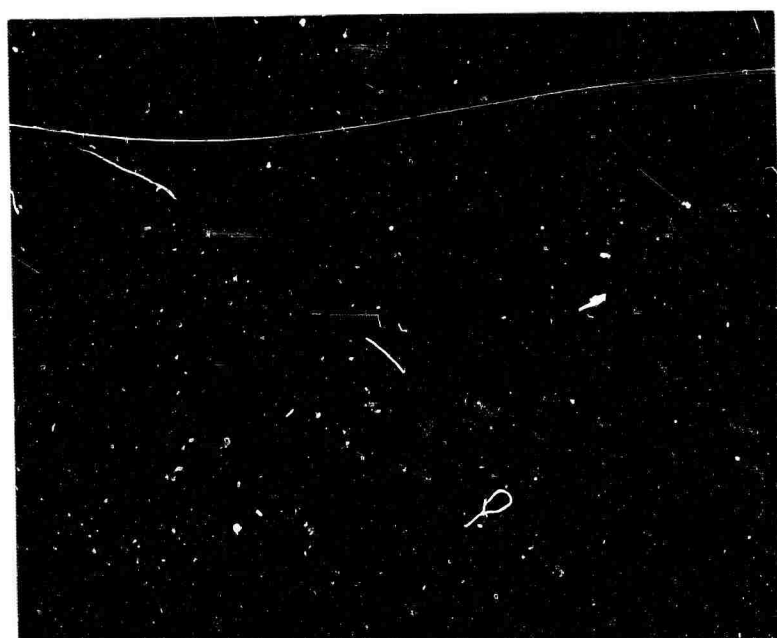
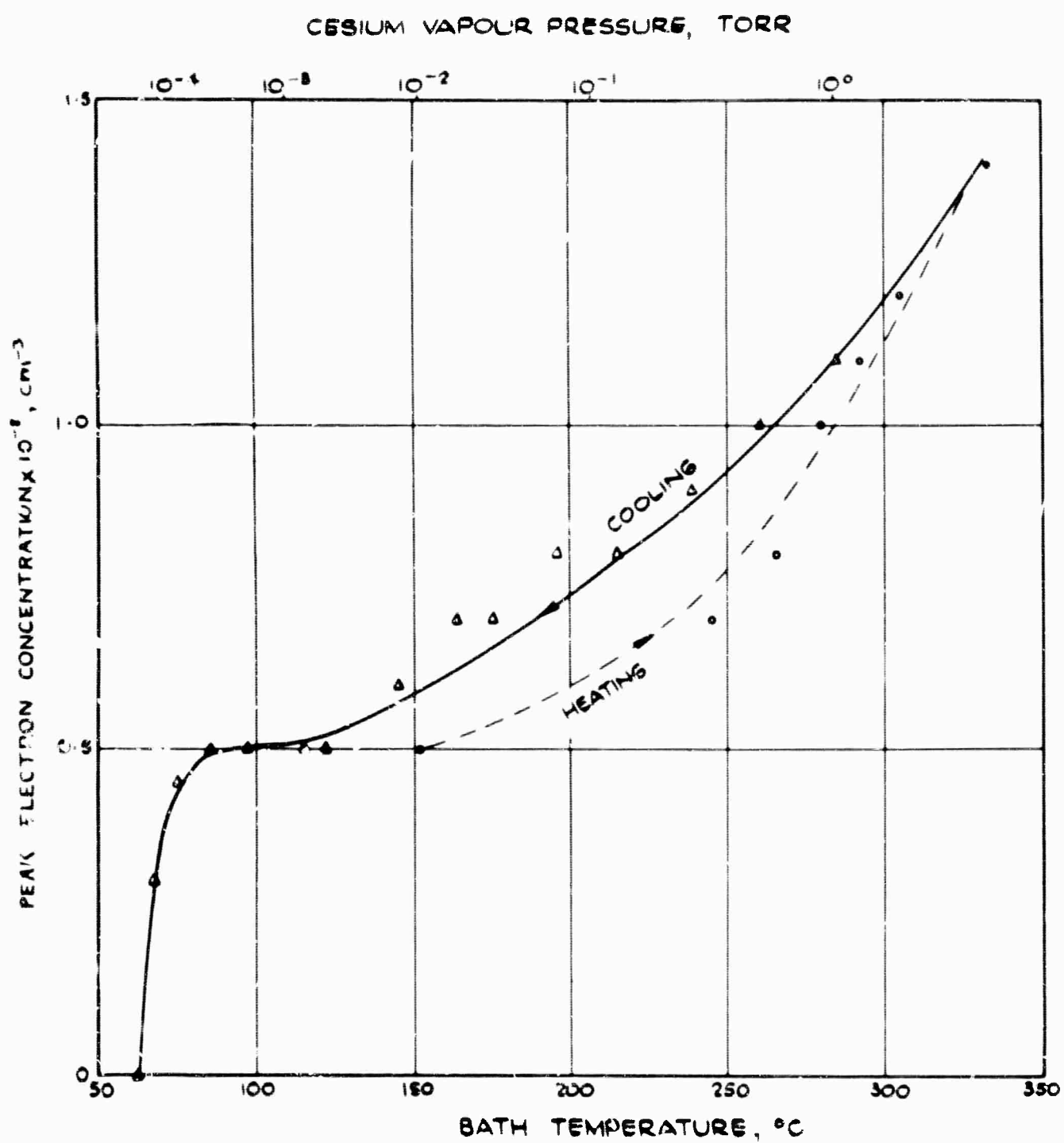


FIG 8-18 PHOTOIONIZATION IN CESIUM  
VAPOUR



EFFECT OF CESIUM VAPOUR PRESSURE ON PHOTOELECTRON CONCENTRATION

FIG8.19

## CHAPTER 9

### ATOMIC BEAM EXPERIMENT

by

A.B.Jolly, T.Bell and D.Balfour

#### 9.1 GENERAL

The objective of the atomic beam experiment is to measure the total collision cross section of cesium atoms with helium and to extend these measurements into the high temperature region ( $1500^{\circ}\text{K}$  to  $2000^{\circ}\text{K}$ ) relevant to the MPD power generation experiment. Results at low temperatures have been described in earlier reports. To make measurements at higher temperatures a Mk II apparatus was designed which incorporates high temperature heaters both on the atomic beam source and gas scattering chambers, has increased resolution due to its increased size, and is capable of being pumped down to lower base pressures. This apparatus is now complete and during the last four months the initial vacuum troubles and cold spots have been overcome so that stable beams of atomic cesium are now produced regularly, with an automatic temperature control of  $\pm 0.5^{\circ}\text{C}$  on the source. By varying the temperature of the nozzle up to  $1000^{\circ}\text{K}$  the mean velocity of the atoms effusing from the nozzle may be varied within the range 200 to 400 m/sec.

To measure the intensity of the cesium atomic beam hot wire detectors relying on surface ionization of the cesium atoms have been used. Platinum, niobium and tungsten wires have been tested and different diameters of wire have been evaluated. In general the platinum and niobium detectors, owing to the greater purity of these materials, give lower background current than tungsten and were used in the subsequent experimental programme.

Electron bombardment was considered as a possible means of heating the source to temperatures in excess of  $1000^{\circ}\text{K}$  and tests were carried out but persistent breakdown of the high voltage leads at high temperature and irregular heating of the source chamber have impeded this development. The alternative of using r.f. heating is being considered but meanwhile temperatures up to  $1000^{\circ}\text{K}$  are being achieved using only a 'Pyrotenax' heating coil.

The Mk II apparatus is equipped with a moveable rack which can support two detector filaments and using this facility a survey of beam profiles has been carried out enabling alignment and detector size to be optimized. The experience obtained in this way was then used in experiments to measure the total collision

cross section of cesium in helium. A conclusion from these experiments is that the accuracy of results is limited by the base pressure obtainable in the scattering chamber. Outgassing from the scattering chamber may be particularly disturbing when the chamber is heated to high temperature and present work is directed towards eliminating this source of error.

The initial measurement of the variation of cross section with the velocity of the atomic beam produced the  $v^{-2}$  trend that was anticipated for cesium atoms in air at  $5 \times 10^{-6}$  torr. However, on increasing the pressure of the scattering gas, the results were not reproducible and a similar measurement in helium suggested that the cross section was constant within the velocity range 200 to 400 m/sec. These problems are still under investigation and must be understood before extending the range of Cs-He cross section measurements to higher temperatures.

## 9.2 EXPERIMENTAL EQUIPMENT

### 9.2.1 General arrangement

The Mk II atomic beam experiment is basically the same as the Mk I experiment which was described in the earlier Technical Summary Reports (IRD 63-1 and 64-36) and consists of a vacuum chamber containing an atomic source with a slit from which the alkali atoms effuse as a beam, a scattering chamber with entrance and exit slits aligned so that the atomic beam can pass through the scattering gas and a hot-wire detector to measure the strength of the atomic beam after it has passed through the scattering chamber. The Mk II apparatus is an improvement on the Mk I: it has improved resolving power due to the greater separation between source and detector, is capable of being pumped to lower base pressures, and can accommodate high temperature heaters both on the exit nozzle of the source and on the scattering chamber, thereby enabling the cross-section measurements to be extended to much higher temperatures. Fig. 9.1 shows a general view of the apparatus with the source in the foreground, the gas bottles (above) connected to the scattering chamber and the differential screw for the detector mount at the far end.

The general arrangement of the atomic beam oven and superheater is shown in Fig. 9.2. A glass ampoule containing the alkali metal is housed in the flexible bellows and can be broken by compression of the bellows, allowing the alkali metal to drop down into the reservoir. The reservoir may be isolated from the main enclosure and from the nozzle by means of a stainless steel valve. This facilitates removal of the reservoir for cleaning and recharging without disturbing the vacuum condition existing in the main enclosure. The reservoir, ampoule breaker and valve are attached to the end flange of the main enclosure,

the flange seal being effected by compression of either a silicone rubber 'O' ring or fine gold wire.

The alkali vapour pressure is maintained above the liquid metal by controlling the temperature of the stainless steel reservoir which has large thermal capacity to counteract the small variations in temperature due to fluctuations of the input current. The vapour generated in the reservoir then passes to the nozzle through a 1 in. bore stainless steel bakeable valve.

#### 9.2.2 Source

A rectangular slit is cut vertically in the end of the nozzle and has dimensions of 0.015 cm x 0.5 cm. Care was taken during the welding operation to ensure that the nozzle slit was not displaced from the axis of the main enclosure.

A water cooled tube encircling the nozzle absorbs practically all of the radiated heat, thereby ensuring that the enclosure walls are kept at a reasonable temperature. It also prevents oxides forming on the enclosure walls.

The mean energy or velocity of the atoms effusing through the slit in the nozzle is controlled by the temperature of the nozzle: the beam intensity is determined by the vapour pressure in the source chamber, i.e. by the temperature of the reservoir.

The number of molecules which emerge from the slit travelling in a solid angle  $d\omega$  at an angle  $\theta$  relative to the normal of the plane at the slit is

$$dQ = \frac{d\omega}{4\pi} n \bar{v} \cos\theta A_s \quad \dots\dots (9.1)$$

where  $n$  is number density of molecules,  $\bar{v}$  is the mean molecular velocity in the source and  $A_s$  is the area of the slit.

#### 9.2.3 Scattering chamber

For measurements of scattering cross-section the scattering chamber (Fig. 9.3) is aligned with the nozzle and detector, the slits of the scattering chamber defining the beam width. The pressure in the chamber is maintained by adjusting the needle valve of the gas supply to balance the rate of loss through the slits. The scattering chamber consists of a stepped section (thermal choke) tantalum cylinder, having one end closed and the other end welded to a stainless steel tube of 1.5 in. OD (0.374 in. diameter). Holes are drilled through the tantalum cylinder near the closed end to locate the tantalum slit mountings which are used for adjustment of the slit width.

A centrally mounted 0.25 in. bore thin-walled stainless steel tube is used for sampling the gas pressure, which is measured by an ionization gauge. Various spectroscopically pure inert gases may be introduced to the system from glass bottles attached to a 5 litre gas reservoir. The gas reservoir is thoroughly outgassed to attain a pressure of  $10^{-8}$  torr before introduction of the scattering gas. The design also provides for the introduction of alkali metals so that scattering cross sections can be obtained for alkali vapours and inert gas mixtures.

#### 9.2.4 Surface ionization detector

A full description of the surface ionization detector was given in an earlier report (IRD 64-36), but for convenience, the diagram is again shown in Fig. 9.4. The principal parts of the detector are a thin filament heated to approximately  $1000^{\circ}\text{K}$ , ensircled by an electrode having a slot cut in line with the filament for admission of the beam. The electrode is held at a potential of -50 volts with respect to the filament. For a detector filament presenting an area  $A_d$  to the beam at a distance  $r$  from the slit, the number of atoms intercepted per second is

$$\begin{aligned} dQ_{\text{det}} &= \frac{A_s A_d}{4\pi r^2} n \bar{v} \\ &= 1.12 \times 10^{22} \frac{p A_s A_d}{r^2 \sqrt{MT}} \text{ atom/sec} \quad \dots (9.2) \end{aligned}$$

where  $p$  is the vapour pressure in the source expressed in torr,  $M$  is the molecular weight in grams of the beam particles and  $T$  is the temperature of the nozzle.

If every particle incident on the detector is registered as a unit charge then the maximum current attainable can be calculated. Thus for cesium at  $364^{\circ}\text{K}$  and a corresponding vapour pressure of  $3 \times 10^{-4}$  torr the maximum current acceptable in the Mk II apparatus by a niobium wire of 0.010 in. diameter is only  $2 \times 10^{-11}$  amp.

Neutral atoms colliding with the filament will normally be reflected, but under certain conditions may be re-evaporated as positive ions after a statistical time interval. This so called 'residence time' is a function of the surface temperature and work function of the filament material, and the ionization potential  $I$  of the incident atoms. The ratio of the number of re-evaporated ions  $n_+$  to the number of re-evaporated neutral atoms  $n$  is given by

$$\frac{n_+}{n} = \exp\left(\frac{\phi - I}{kT}\right) \quad \dots (9.3)$$

where  $k$  is Boltzmanns constant ( $8.5 \times 10^{-4} \text{ eV}/^{\circ}\text{K}$ ) and  $T$  is the surface temperature in  $^{\circ}\text{K}$ . It is therefore desirable that  $(\phi - I) \gg kT$  to ensure that virtually all neutral atoms colliding with the detector filament are re-evaporated and collected

as an ion current.

In general it is necessary to heat the filament to  $\sim 1000^{\circ}\text{K}$  ( $\sim 0.1$  eV) for re-emission to take place, so that the work function of the filament material should exceed the ionization potential of the incident atoms by  $\geq 0.5$  eV for efficient surface ionization detection. Cesium has an ionization potential of 3.9 eV so that any metal having a work function of  $\geq 4.4$  eV would be a possible filament material for a surface ionization detector. The majority of such metals contain traces of alkali metals (usually sodium and potassium) which give troublesome background signals; niobium and platinum, however, give low background and noise levels even when heated to  $1200^{\circ}\text{K}$ . Initially a tungsten filament was used but with limited success because of the presence of thorium oxides leading to high thermionic emission at the working temperature of approximately  $1200^{\circ}\text{K}$ . For the detection of sodium ( $I = 5.13$  eV), it is necessary to use oxygenized tungsten wire whose effective work function is raised to about 6 eV.

Two detectors are provided in the equipment to compare various filament materials and to test the resolution of the apparatus. These are mounted adjacent to each other on a vertical plate which may be accurately moved transversely across the axis of symmetry of the apparatus by means of a differential screw, sliding vacuum seals and a clock gauge (0.001 in./division).

Typical ion currents are  $10^{-11}$  A; because of the high input impedance of the current amplifier ( $10^{16}\Omega$ ) the collector insulation must exceed  $10^{12}\Omega$  if a potential of 1 mV is to be developed across a resistance of 100 M $\Omega$ . The use of a Vibron vibrating capacitor modulator in the ion current amplifier gives excellent zero stability (not more than 0.1 mV drift in 12 hr) coupled with high input impedance. Simplified diagrams of the collector and filament circuits are shown in Figs. 9.5 and 9.6.

### 9.3 EXPERIMENTAL RESULTS

#### 9.3.1 Beam profiles

The movable detector mount in the Mk II apparatus has made it possible to study beam profile and the provision of two separate detectors enables different filament materials and wire diameters to be compared. Typical beam profiles are shown in Fig. 9.7 where different materials and different diameters of filament were used in the detector. The intensity scale has been normalized to illustrate the effect of resolution on the beam profile; the slight asymmetry is due to imperfect alignment of the collimator slits. The ideal profile is shown for a detector of infinite resolving power. As the diameter of the detector filament is decreased and hence the resolution increased the profile tends towards the ideal

shape.

Fig. 9.8 shows profiles for an unattenuated beam and for a beam that has been attenuated by gas in the scattering chamber. Collisions with gas molecules result in broadening and attenuation of the scattered intensity profile. When the scattering chamber is evacuated the degree of broadening of the beam profile  $\Delta b$  is a measure of the scattering occurring with the residual gas within the vacuum enclosure. For cross section determinations the value of  $\Delta b$  at half maximum intensity was not allowed to exceed two filament diameters and the detector position was adjusted to record the maximum intensity.

### 9.3.2 Cross section measurements

The method of measuring total collision cross sections using the present experimental arrangement has been described in earlier reports. Essentially, the method consists of measuring the unattenuated beam intensity and then the attenuated intensity of the beam after it has passed through the scattering gas at known pressure and temperature. If  $I_0$  and  $I$  are the intensities of the unattenuated and attenuated beams respectively then

$$\frac{I}{I_0} = \left\langle \exp - \frac{l}{\lambda} \right\rangle \approx \exp \left\langle \frac{-l}{\lambda} \right\rangle \quad \text{..... (9.4)}$$

where the brackets imply a mean value,  $l$  is the effective scattering length and  $\lambda$  is the mean free path for a beam atom in the scattering gas. Then as shown by Ramsey<sup>1</sup>:

$$\ln I = \ln I_0 = - \left\langle \frac{l}{\lambda} \right\rangle = \frac{- \frac{1}{2} \sigma p}{2\pi^2 k T_g g(Z)} \quad \text{..... (9.5)}$$

where  $\sigma$  is the mean effective collision cross section,  $p$  is the gas pressure in dynes/cm<sup>2</sup>,  $k$  is the Boltzmann constant,  $T_g$  is the gas temperature in °K and the values of  $g(Z)$  where  $Z = \frac{T_g M_b}{T_b M_g}$  have been tabulated by Rosin and Rabi<sup>2</sup> ( $T_b$  is the beam temperature,  $M_b$  and  $M_g$  are the masses of the beam and gas atoms respectively).

In practice beam attenuation is measured for different values of scattering gas pressure and the cross section is then deduced from the slope of  $\log I$  versus  $p$  plots. Fig. 9.9 shows a plot of  $\log I$  versus  $p$  for a cesium beam scattered by xenon for a beam temperature of 500°K. In this experiment a niobium wire detector of 0.010 in. diameter was used with a resolution of ~ 1 minute of arc. The value of collision cross section deduced from the slope of this graph is  $2850 \times 10^{-16}$  cm<sup>2</sup>. Later measurements of this cross section gave lower values similar to that obtained in the previous apparatus but for these the gas was less pure. The result for cesium-xenon is likely to be realistic since the errors due to low angle scattering are considerably less than for the case of cesium-helium (described below).



A similar measurement of the cesium-helium scattering cross section resulted in the linear plot of  $\log I p$  shown in Fig. 9.10. The value of collision cross section deduced from these results was  $178 \times 10^{-16} \text{ cm}^2$  at a resolution of 0.9 minutes of arc. This compares with total collision cross section of  $162 \times 10^{-16} \text{ cm}^2$  measured by Robin and Rabi<sup>2</sup> using a resolution of 1 minute of arc. However, previous measurements in the Mk I apparatus and also by Foner<sup>3</sup> at higher resolving powers yielded much larger values. These results imply that the resolving power must be increased to yield a realistic value of total collision cross section. It is therefore intended to repeat the experiments using detector wires of smaller diameter.

### 9.3.3 Velocity dependence of collision cross section

If the nozzle temperature be increased from  $150^\circ\text{C}$  to  $750^\circ\text{C}$  the beam atoms effuse out of the slit with an energy distribution determined by the temperature of the nozzle and the mean velocity may be varied within the range 200 to 400 m/sec. Since in general the collision cross section decreases as the energy of the incident particles increases the total number of particles reaching the detector increases with beam temperature. Fig. 9.11 shows the variation of beam intensity at the detector as a function of beam temperature. In this experiment air at a pressure of  $5 \times 10^{-6}$  torr was the scattering gas and a niobium detector (0.010 in. diameter) was used. From this curve it is possible to deduce the velocity dependence of the cross section according to the argument which follows.

The attenuation ( $I/I_0$ ) of a well defined molecular beam in passing through a scattering path ( $l$ ) is related to the effective mean free path of the average beam molecule (velocity  $V$ ) in a Maxwellian gas by

$$I = I_0 \exp \left[ -\frac{l}{\lambda} \right] \quad \text{..... (9.6)}$$

and 
$$\lambda = \frac{1}{N\sigma} \quad \text{..... (9.7)}$$

where  $\sigma$  is the total effective cross section.

Put 
$$\sigma = k_1 V^{-x} \quad \text{..... (9.8)}$$

where  $x$  denotes the velocity dependence of cross-section. Assuming attractive potentials

$$\lambda = k_2 V^x \quad \text{..... (9.9)}$$

so that 
$$I = I_0 \exp \left[ -\frac{l}{k_2 V^x} \right] \quad \text{..... (9.10)}$$

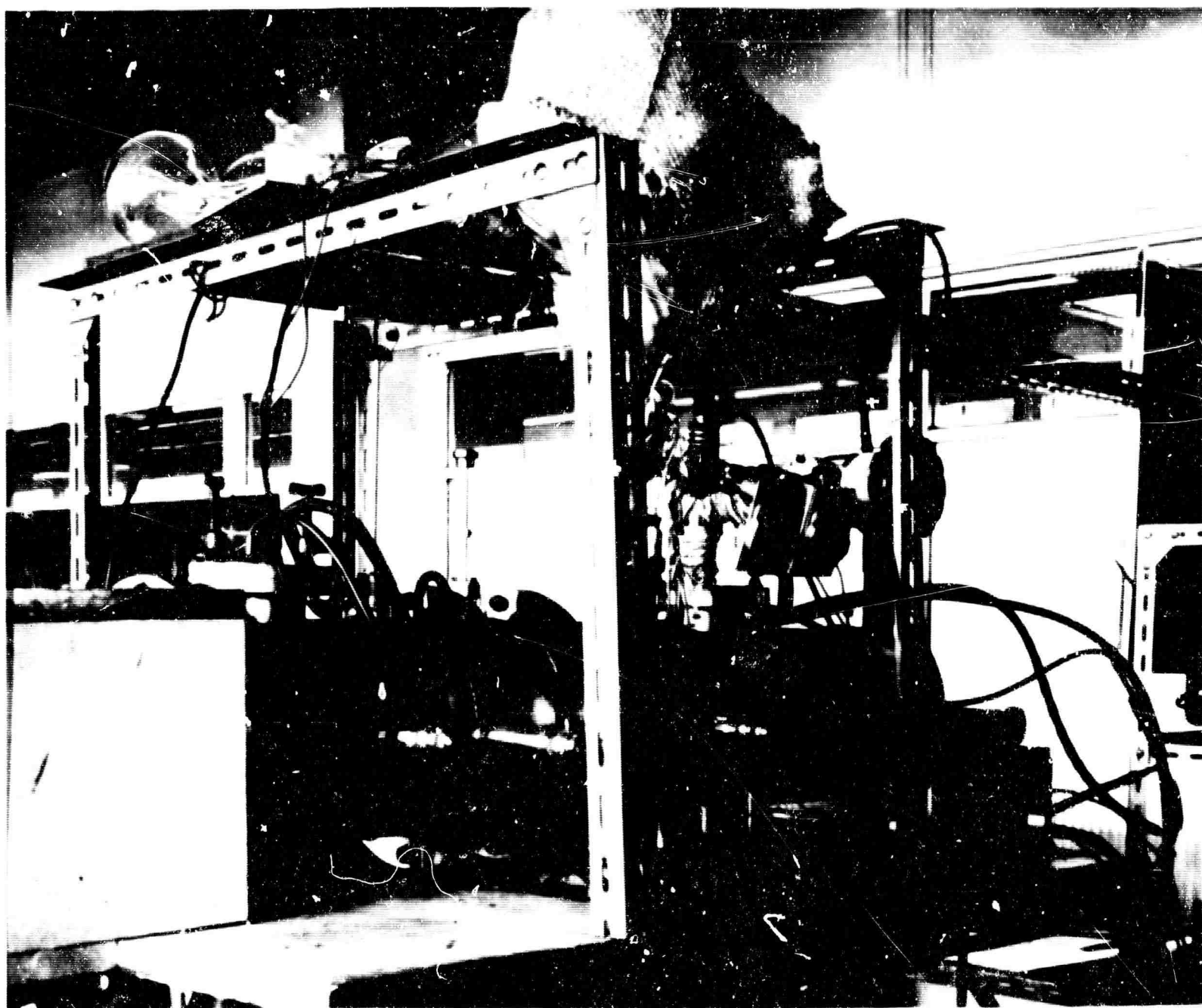
$$\text{and } \log \frac{I}{I_0} = -\frac{1}{k_2 V^x} \quad \text{or } -\left[\frac{1}{k_2}\right] \sqrt{T^x} \quad \dots (9.11)$$

If the value of  $x$  is unknown then a plot of  $\log (\log I) \sim \log V$  will give a straight line with a slope  $x$ . The value of  $\log I_0$  is constant and so may be disregarded. Hence the velocity dependence of cross-section may be directly determined from experiment, if the scattering process is entirely influenced by the long range Van der Waal attractive potential. When the results of Fig. 9.11 were plotted in the above manner (Fig. 9.12) they showed an inverse 0.37 power velocity dependence. This is consistent with the  $V^{-\frac{2}{5}}$  dependence deduced from the attractive potential term in the Lennard-Jones model.

Subsequent measurements in helium have not shown such a strong velocity dependence in this temperature range. However, these are preliminary results and further experiments are being undertaken to clarify this problem.

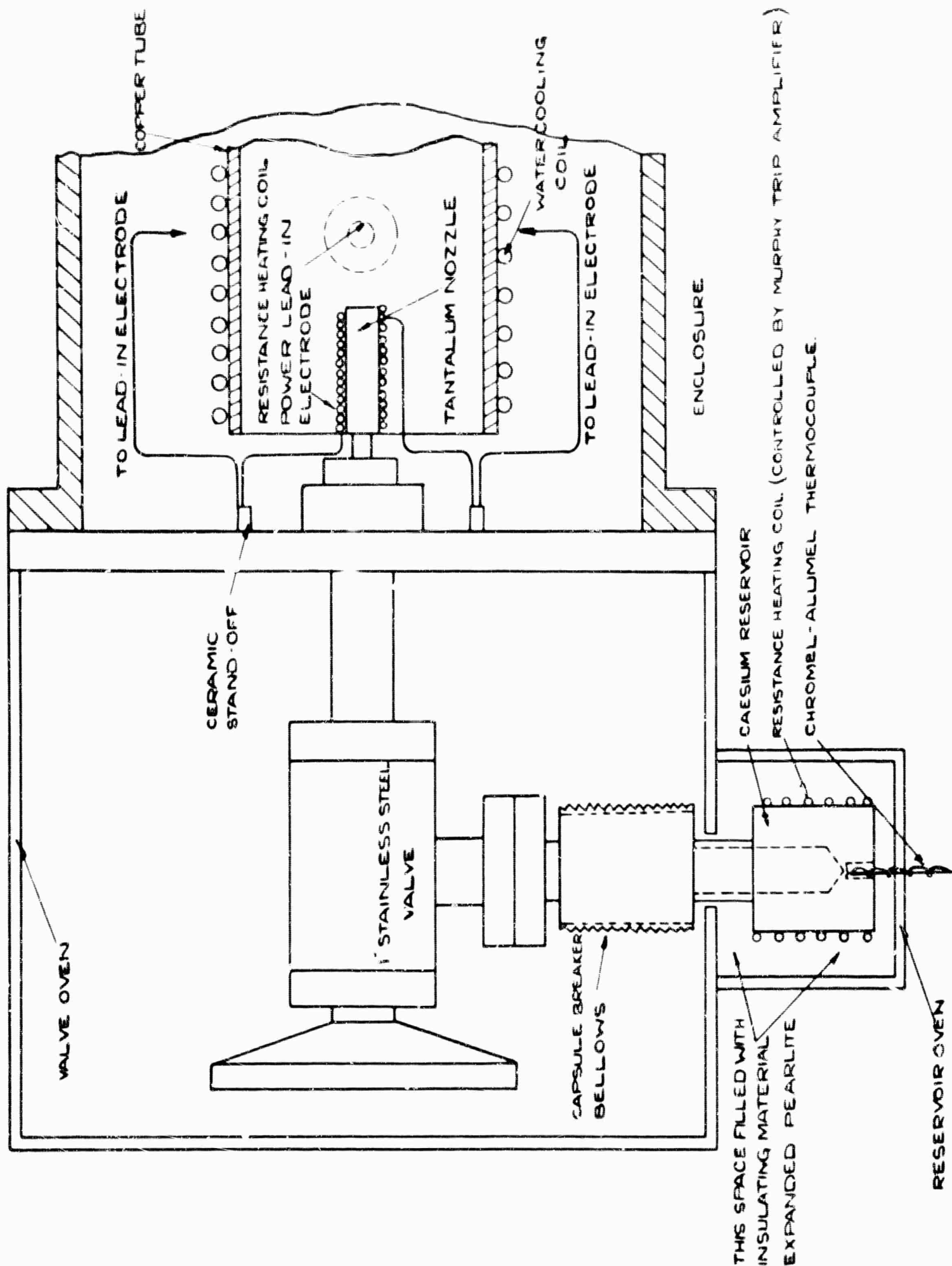
#### REFERENCES

- 1 RAMSEY, N.F. 'Molecular Beams' Clarendon Press (1956)
- 2 ROSIN, S. and RABI, I.I. Phys. Rev, vol.48, p373 (1935)
- 3 FONER, S.N. Phys. Rev, vol.71, p250 (1947)



GENERAL VIEW OF ATOMIC BEAM APPARATUS

FIG 9-1



ARRANGEMENT OF BEAM OVEN AND SUPERHEATER

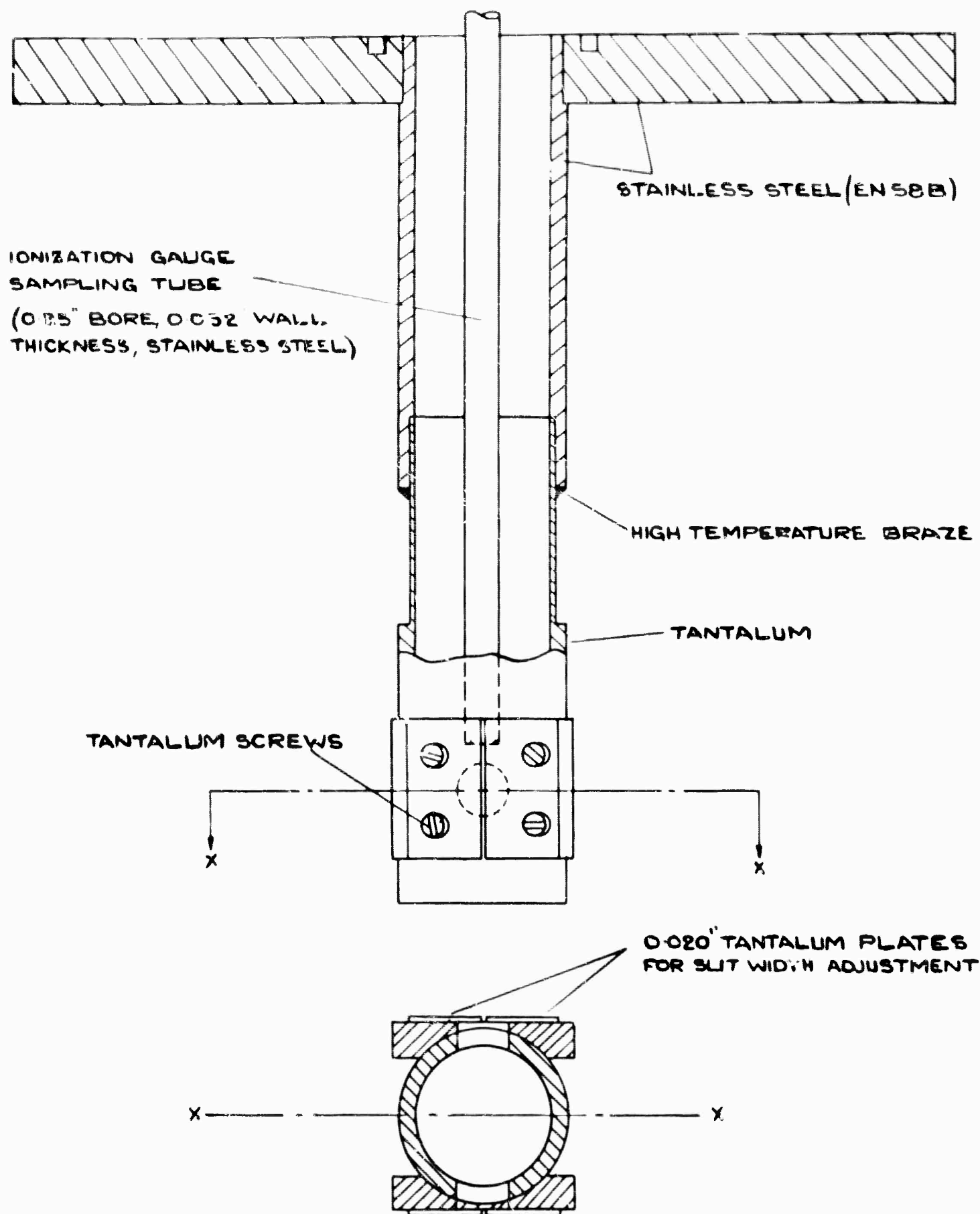
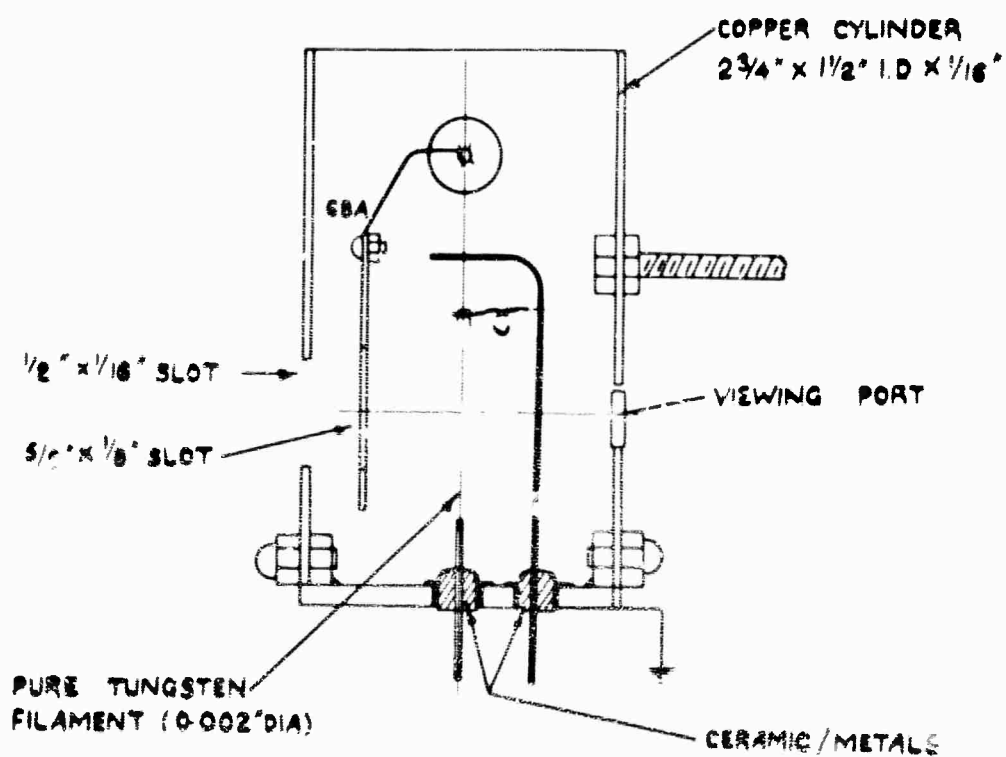
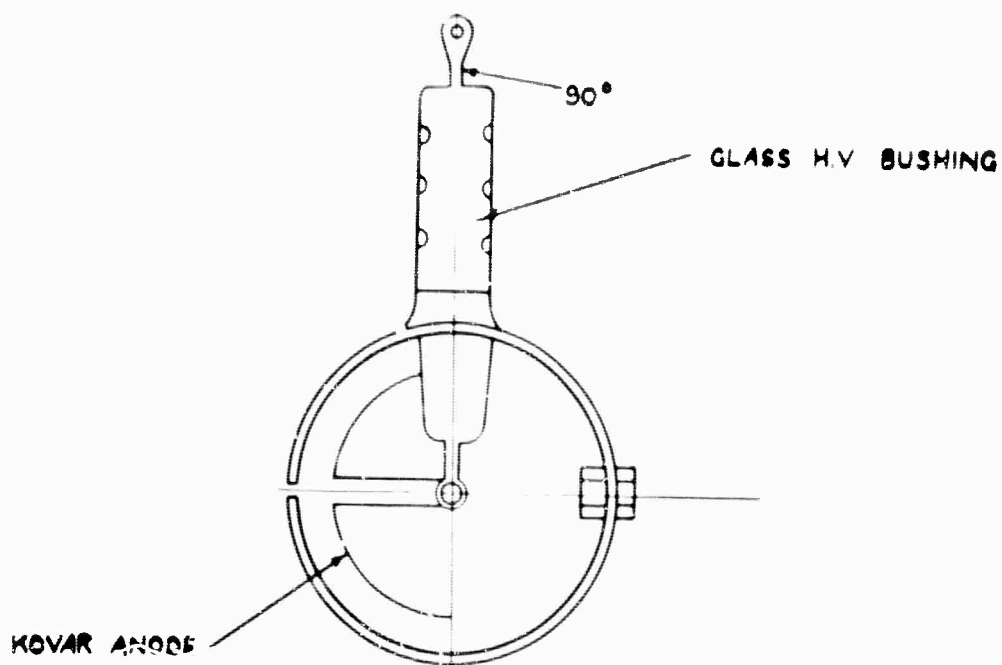
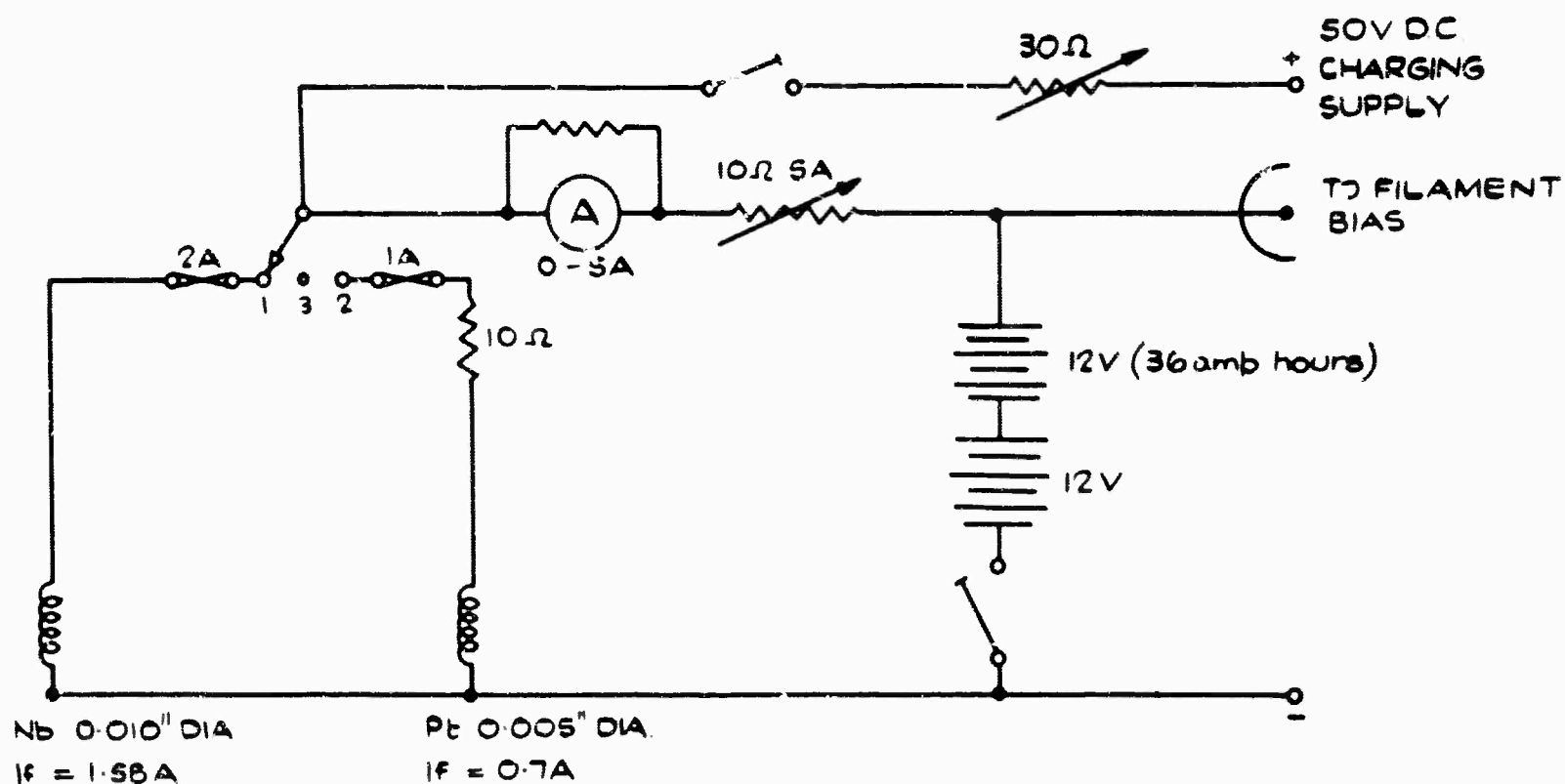
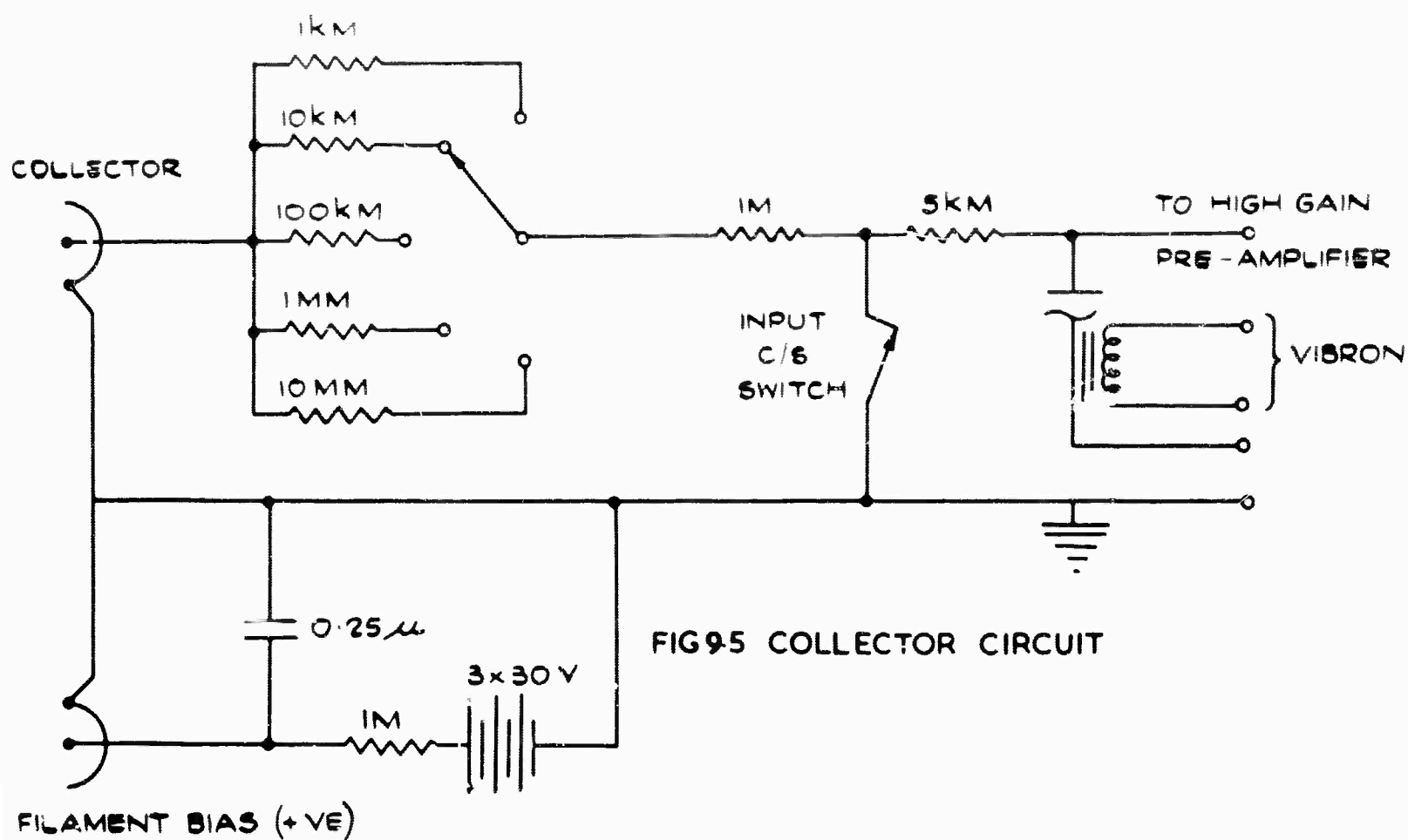
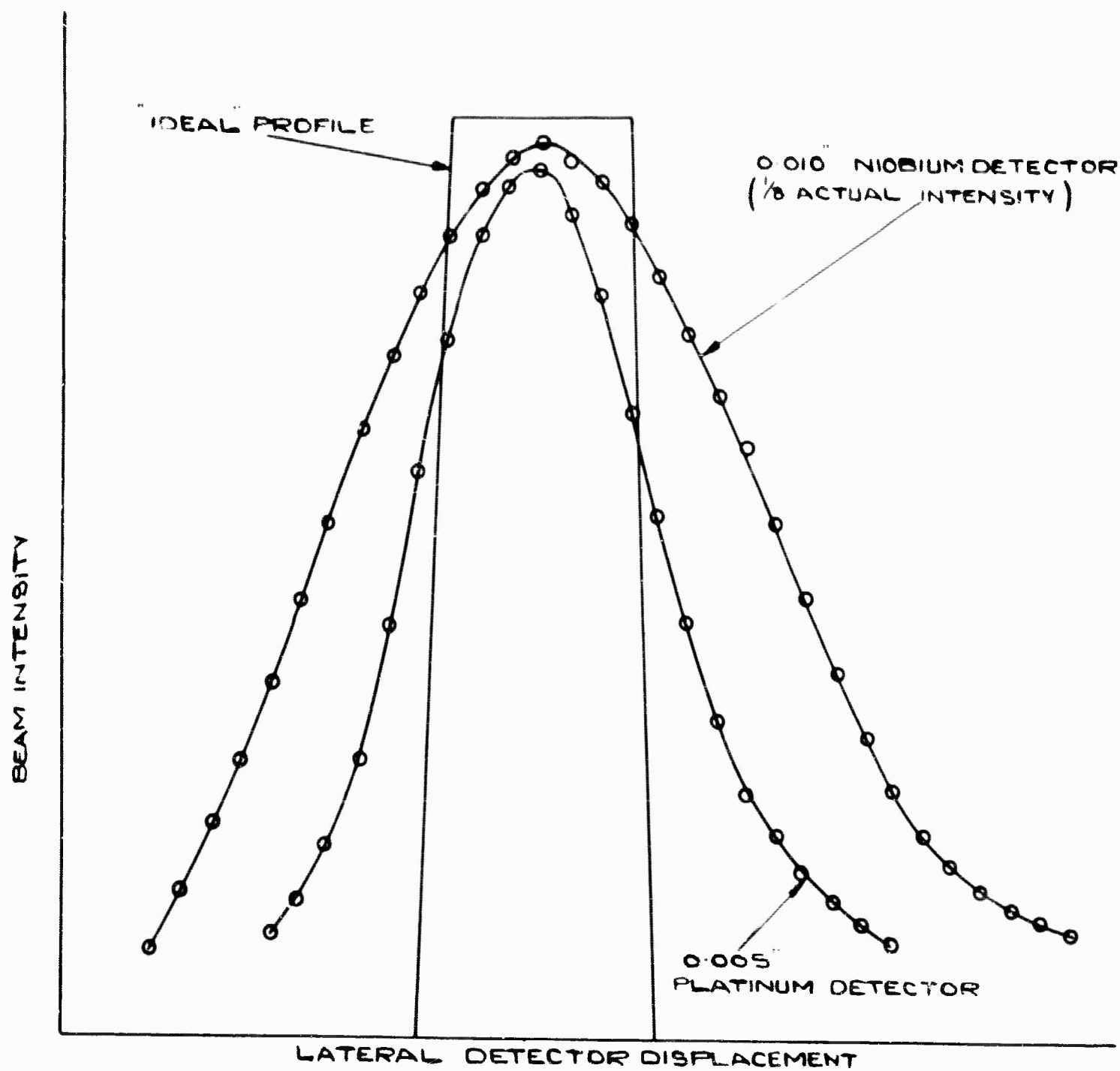


FIG. 9.3



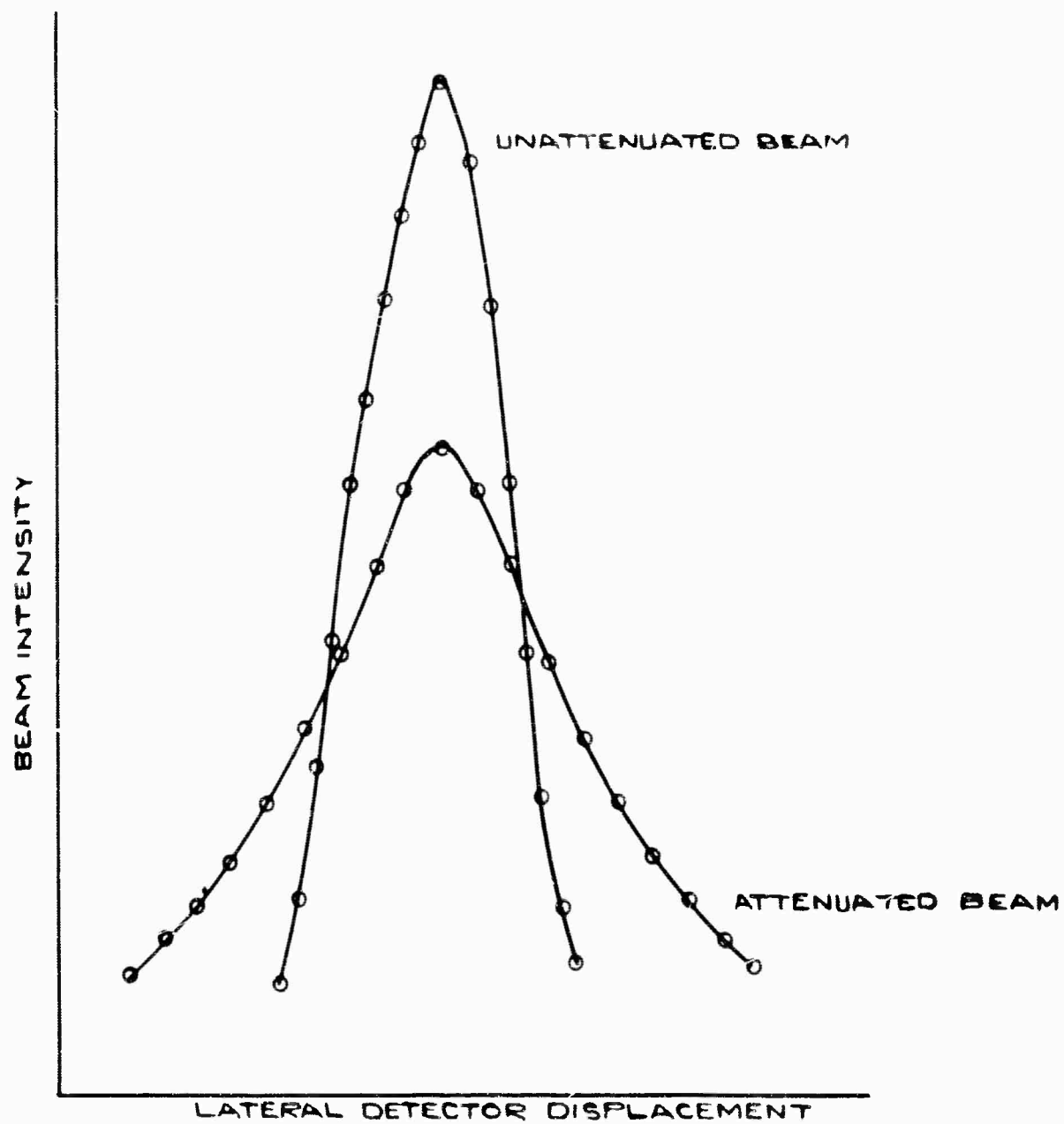
SURFACE IONIZATION DETECTOR



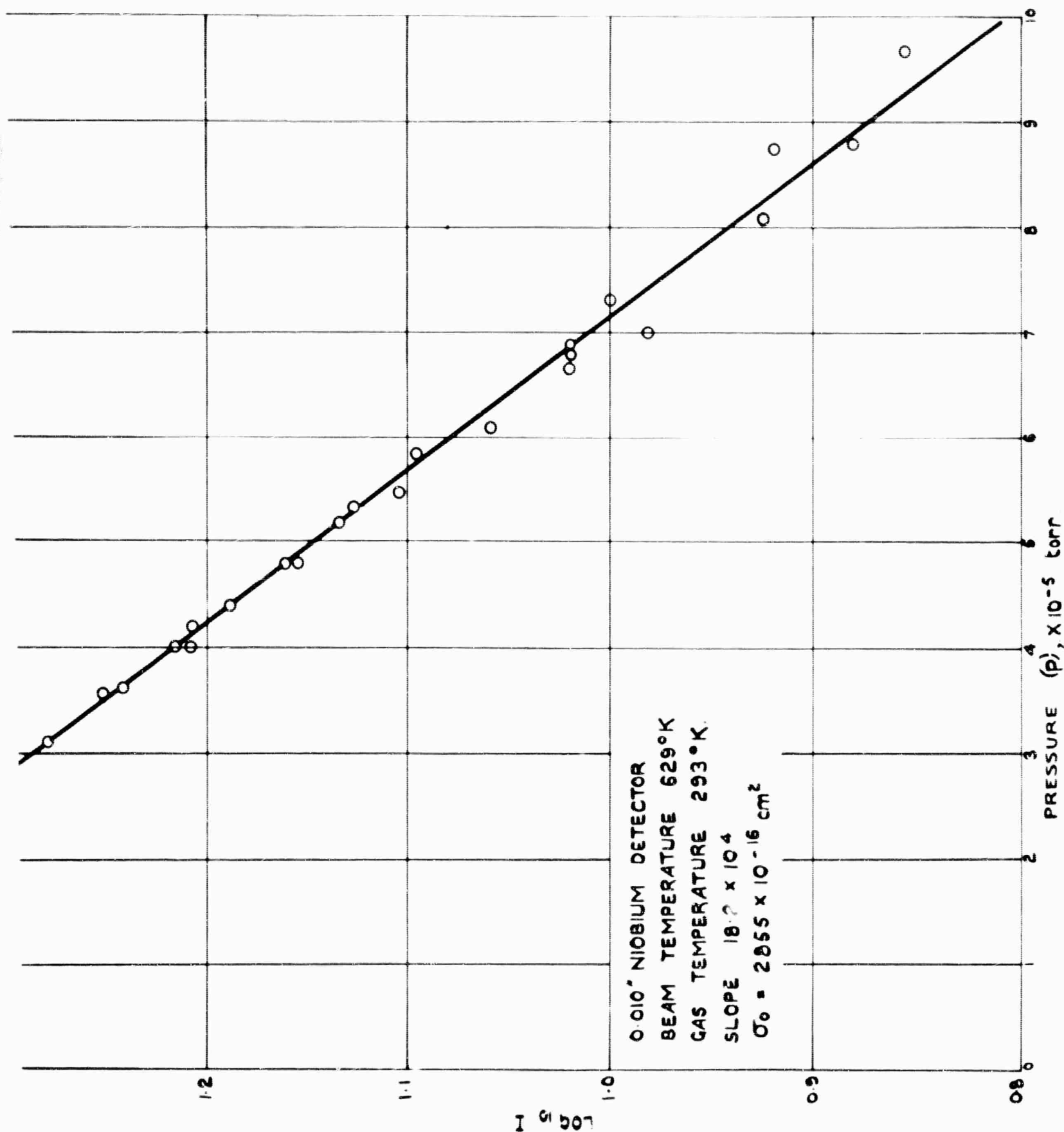


VACUUM BEAM PROFILES

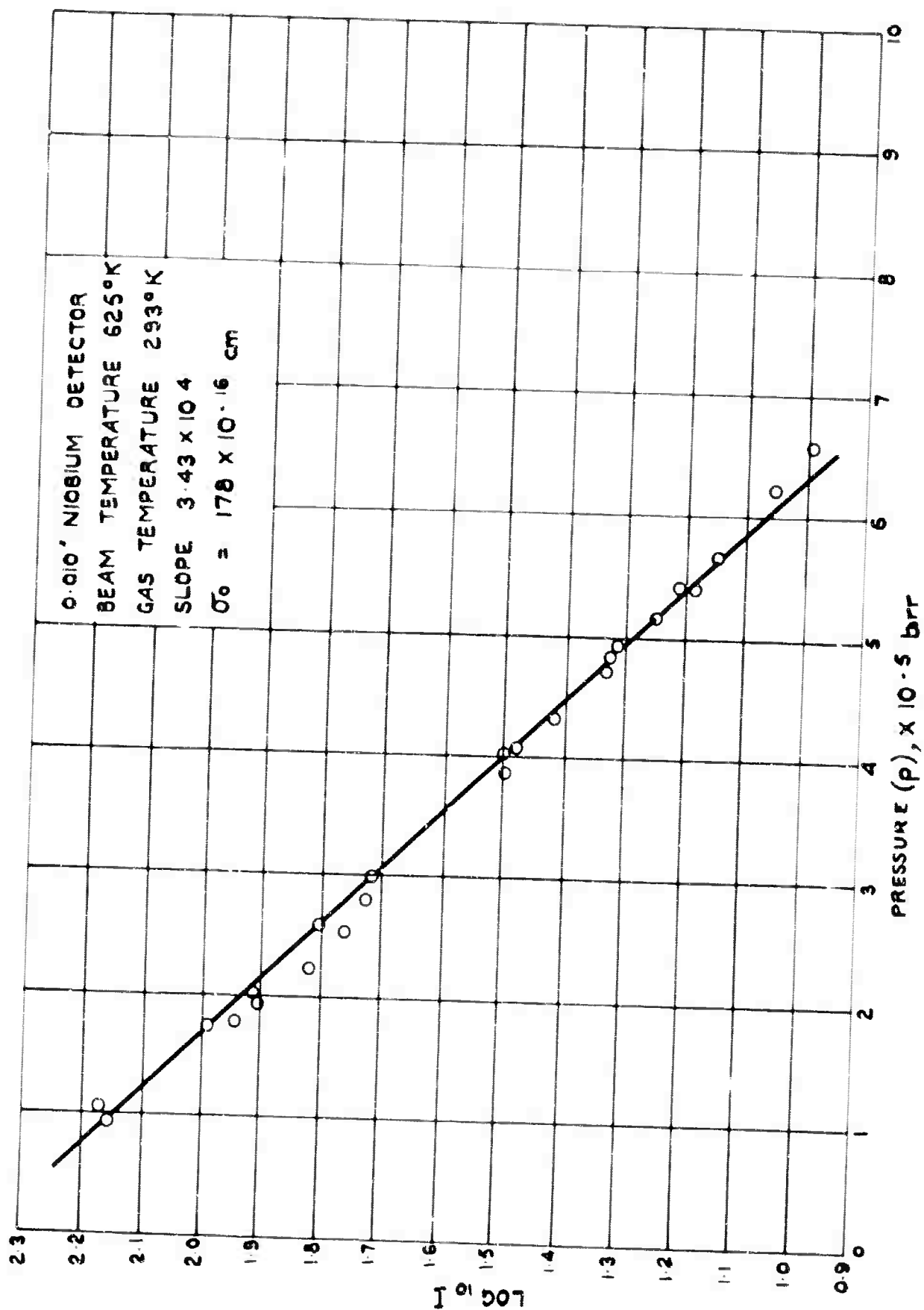




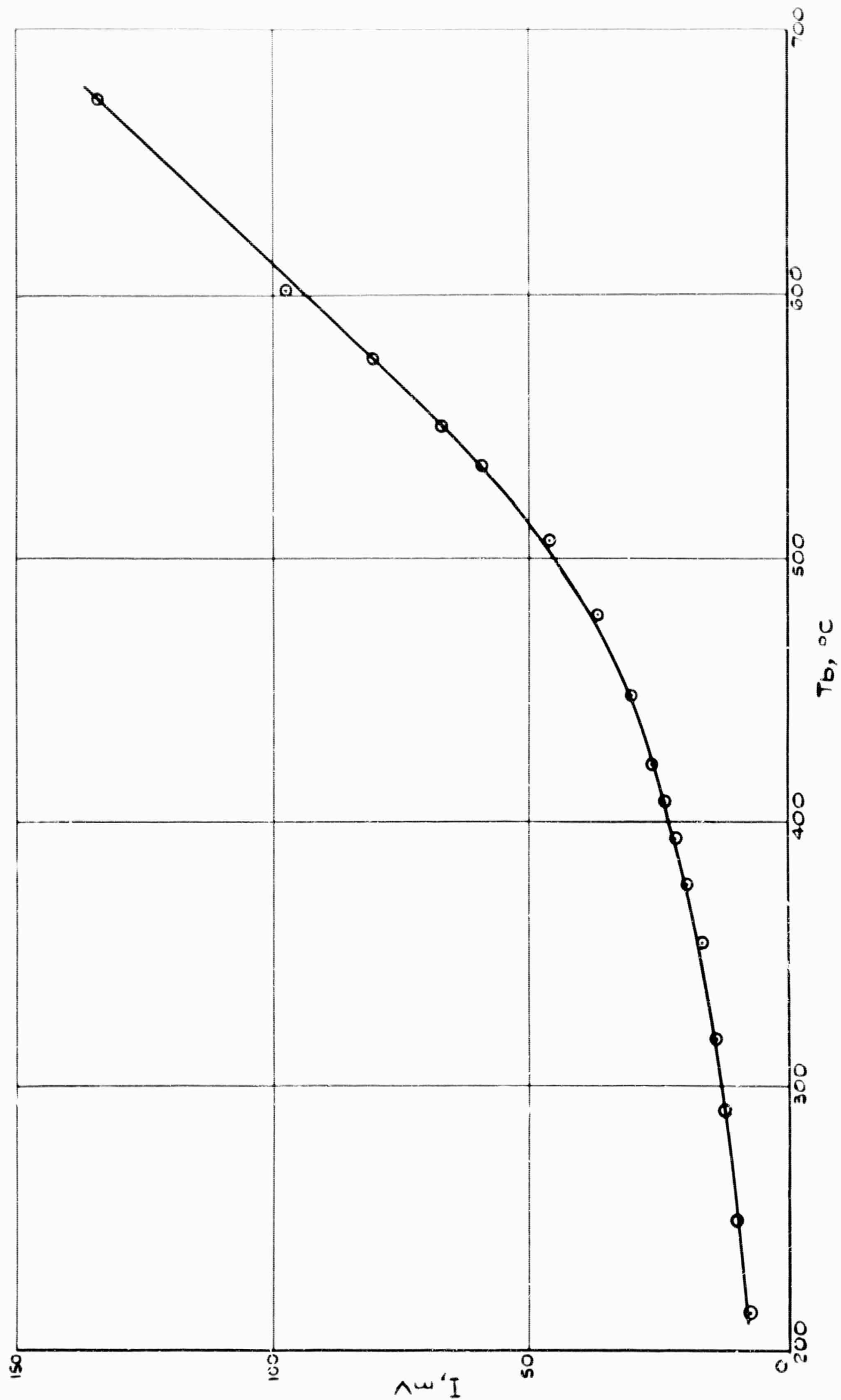
VACUUM AND ATTENUATED BEAMS PROFILES (TUNGSTEN DETECTOR)



VARIATION OF  $\text{LOG}_{10} I$  WITH PRESSURE OF SCATTERING GAS FOR A CESIUM BEAM IN XENON

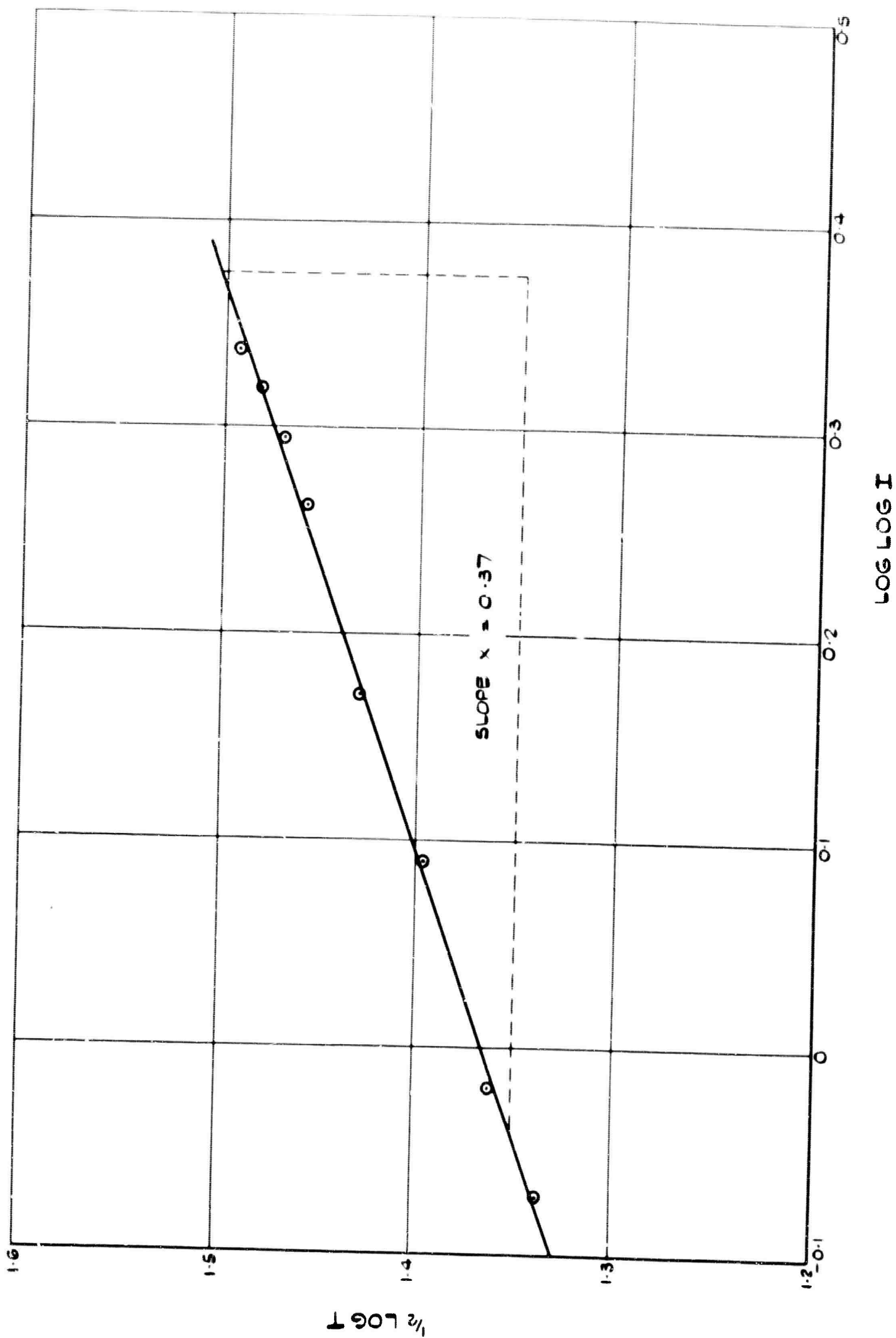


VARIATION OF  $\text{LOG}_{10} I$  WITH PRESSURE OF SCATTERING GAS FOR A CESIUM BEAM IN HELIUM



VARIATION OF BEAM INTENSITY WITH BEAM TEMPERATURE  
(NIOBIUM DETECTOR)

FIG 9.11



VELOCITY DEPENDENCE OF CROSS - SECTION

FIG 9.12

MICROWAVE STUDIES OF THERMALLY-EXCITED PLASMAS

by

J. A. Haines

10.1 THERMAL IONIZATION EXPERIMENT

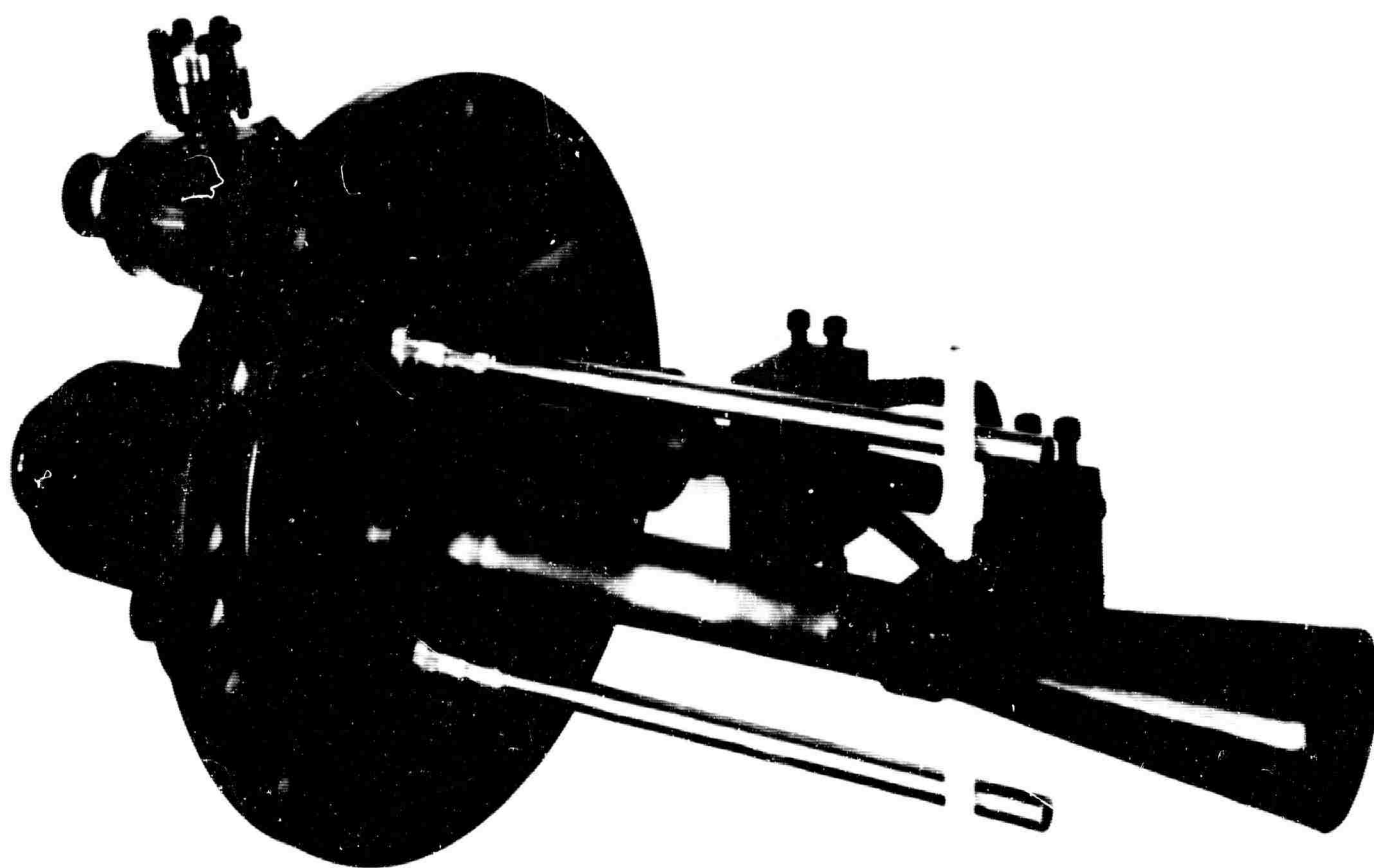
The object of the thermal ionization experiment is to produce helium-cesium mixtures in a heated tantalum tube at temperatures in the range  $2500^{\circ}$  to  $2000^{\circ}\text{K}$  and to measure by microwave transmission the resulting electron concentration (and hence degree of ionization) and electron collision frequency. The experiment is also regarded as a laboratory facility on which to test the microwave diagnostic technique which will eventually be used for measurements on the MPD closed-loop.

In the previous Technical Summary Report (IRD 64-36) an experiment was described in which the cesium-helium mixture was heated in a tantalum tube to  $2000^{\circ}\text{K}$  and the shift in phase of microwaves propagated through the tube was measured as a function of temperature in the range  $1500^{\circ}$  to  $2000^{\circ}\text{K}$ . From those measurements the average electron concentration was deduced using the relationship

$$n_e = \frac{c}{\omega} \Delta\phi \left( \frac{m_e \omega^2}{2\pi e^2} \right) \quad \text{..... (10.1)}$$

where  $\omega$  is the radian frequency of the microwaves,  $\Delta\phi$  is the phase shift in radians,  $m_e$  the mass of an electron,  $e$  the electronic charge and  $c$  the velocity of light. The maximum electron concentration detected was approximately  $5 \times 10^{10}/\text{cm}^3$ : this level of ionization is a factor of 100 less than the value calculated from the Saha Equation on the assumption that the gas pressure in the tantalum tube is determined by the vapour density in the cesium bath. However, in this experiment the apparatus was first filled with helium and the cesium bath was then heated to raise the cesium vapour pressure. In practice, diffusion of cesium through the helium and through the connection between bath and chamber is so slow that the time for the cesium pressure to become constant throughout the apparatus is very large; this condition may not have been fulfilled in the experiment. In the next experiments the cesium vapour pressure will be established before helium is introduced.

On opening up the apparatus after the cesium-helium experiment, it was found that the walls of the container were coated with an oily black substance and it was not again possible to obtain a good vacuum even on baking to  $400^{\circ}\text{C}$ , until the



MODIFIED ASSEMBLY TO SUPPORT THE TANTALUM TUBE

apparatus had been stripped completely and scrubbed with water and detergent. It is believed that this black coating is cesium hydroxide formed when the cesium coating on the walls is exposed to moist air.

A more serious consequence of this experiment was that the 0.25 in. diameter tantalum tube (0.010 in. wall thickness) fractured on cooling. The apparatus had been tested using a more robust 1.25 in. diameter tantalum tube which permitted two modes of microwave propagation. To obtain interpretable results in which only one mode was dominant it was necessary to use a tube of less than 0.25 in. diameter. At high temperature this smaller tube was strained through inadequate provision for differential expansion forces. Originally the tube conductor was supported rigidly on tantalum supports attached to a copper conductor rod, with the differential expansion between the tube and rod supposedly taken by a bellows joint at the end of the rod. In practice, the tantalum tube (embrittled by temperature cycling and very weak at  $2000^{\circ}\text{K}$ ) was incapable of supporting the stress developed across the bellows and fractured in consequence.

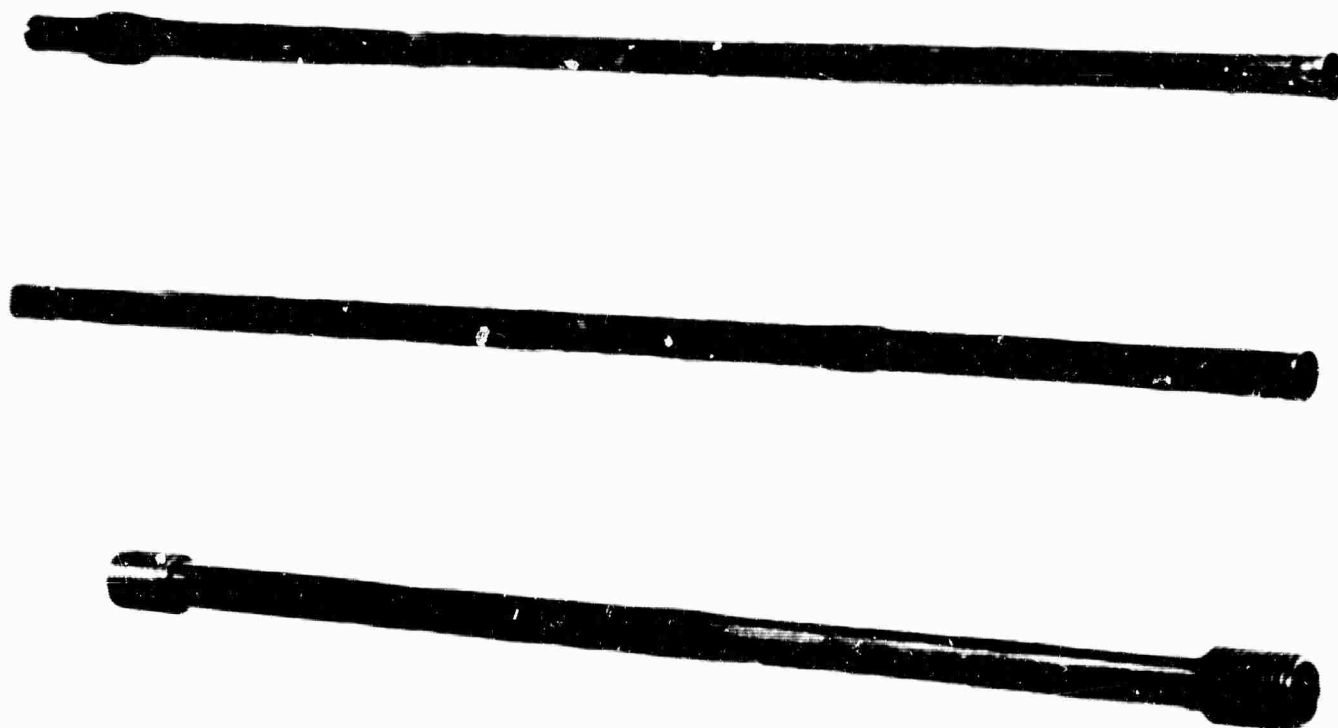
## 10.2 NEW DESIGN OF EQUIPMENT

To eliminate these troubles the apparatus has been completely redesigned. The bellows have been removed and flexible copper leads carry the heating current to one end of the tantalum tube, the opposite end being clamped to the end flange. Fig. 10.1 shows the modified structure. At the free end of the tantalum tube two stainless steel pegs have been fixed to the tantalum blocks with insulating ceramic sleeves fitted as shown. These sleeves rest on stainless steel support rods so that they can move laterally to take up the differential expansion between the supporting structure and the tantalum tube.

The assembly was tested by placing it in a glove box and heating it to  $1800^{\circ}\text{K}$  in an atmosphere of helium to simulate the experimental working conditions. The tube expanded laterally without any twisting or bowing and the complete apparatus is again being assembled in preparation for further thermal ionization experiments.

There was some difficulty in obtaining a replacement tantalum tube of less than 0.25 in. internal diameter and with 0.020 in. wall thickness. For a 9 in. tube Accles and Pollock quoted 15 weeks delivery time and a cost of £150. The Tungsten Manufacturing Company produced two seam-welded tubes fabricated from 0.020 in. sheet tantalum but these did not have a circular section. Murex Ltd finally produced a suitable tube by drilling out the bore as specified and then machining away the walls to 0.020 in. diameter (Fig. 10.2). This particular tube has had the ends threaded so that it can be screwed into the end blocks. In this new design the microwave horns will be welded directly to the tantalum blocks.





UPPER SEAM WELDED BY ELECTRON BEAM AT IRD. MIDDLE SEAM  
WELDED BY TUNGSTEN MANUFACTURING CO. LOWER DRILLED  
FROM SOLID ROD GROUND TO CORRECT WALL THICKNESS  
AND THREADED BY MUREX LTD.

TANTALUM TUBES OF 0.020 in. WALL THICKNESS AND 0.23 in. BORE

**BLANK PAGE**

## APPENDIX

### HEAT TRANSFER AND PRESSURE LOSS CALCULATIONS FOR He-He RECUPERATIVE HEAT-EXCHANGER

by

T. Archbold

#### A1 DESIGN DATA

Shell side	He inlet temperature	1690°K
	He outlet temperature	550°K
	He mass flow	5.75 gm/sec
	He average pressure	1 atm
Tube side	He inlet temperature	298°K
	He outlet temperature	1438°K
	He mass flow	5.75 gm/sec

#### A2 GEOMETRY

The heat exchanger is of the cross-counterflow multi-start helical coil type. The shell side fluid flow through an annular space containing the coiled tube bundle. Fig. A.1 shows the bundle details (excluding bundle length). The coil diameters and number of starts per coil have been chosen to give equal lengths for every tube, and the same helix angle.

#### A3 HEAT TRANSFER

##### A3.1 Shell side

The angle of the coiled tubes to the overall direction of gas flow is given by:

$$\tan \theta = \frac{\pi D_n}{n P_x}$$

where the symbols are explained in the Nomenclature at the end of the Appendix. The coil diameter  $D_n$  is defined as

$$\begin{aligned} D_n &= 2n \cdot P_t \\ \text{so that } \tan \theta &= \frac{\pi \cdot 2n P_t}{n P_x} \quad (P_t = P_x) \\ &= 2\pi \\ &= 6.28 \end{aligned}$$

$$\text{Hence } \theta = 81^\circ$$

Thus it is justifiable to consider the shell side flow as normal cross-flow. is also reasonable to treat the coiled bundle as if it were a bank of straight the curvature being perpendicular to the line of flow.

Because adjacent tube layers are wound in opposite senses, all forms of in-line tube arrays with  $P_n = P_t$  exist in the bundle. The probable effect of will be to generate heat transfer rates greater than that for a square in-line array, however, the bundle will be designed using the available data for an equivalent square in-line array (Fig. A.2).

Minimum flow area  $A_{\min}$  has been expressed by Smith<sup>1</sup> as follows:

$$A_{\min} = \frac{\pi}{4t} (D_o^2 - D_i^2) \left[ \frac{t}{2} \sqrt{\left(\frac{P}{2t}\right)^2 + 1} + \frac{t^2}{P} \cdot \ln \left( \frac{P}{2t} + \sqrt{\frac{P^2}{2t^2} + 1} - d \right) \right]$$

where  $t = P_t$  and  $P = P_x$

$$D_o = 11.1 \text{ in.} = 28.2 \text{ cm}$$

$$D_i = 4.26 \text{ in.} = 10.82 \text{ cm}$$

$$d = 0.682 \text{ in.} = 1.73 \text{ cm}$$

$$t = p = 2.16 \text{ cm}$$

Hence

$$A_{\min} = 127.4 \text{ cm}^2$$

Equivalent diameter  $D_e$  is defined as

$$D_e = \frac{4 (\text{min. flow area}) N \cdot P_x}{(\text{Heat transferring area})}$$

$$= \frac{4 \times 127.4 \times 2.16}{1330} \cdot \frac{N}{N}$$

$$= 0.828 \text{ cm}$$

$$\overline{Re}_s = \frac{G D_e}{A_{\min} \mu} \quad (\overline{T} = 84.7^\circ\text{C})$$

$$= \frac{5.75 \times 0.828 \times 10^2}{127.4 \times 0.0483}$$

$$= 77.3$$

Using the data of Fig. A.2 it is clear that the known Re range must be considerably extrapolated to reach the necessary values of Re. As explained in Kays and London<sup>2</sup> these data were obtained using a transient technique that is reliable only in the turbulent region. This means that the transient range, indicated by a broken curve, is not accurate. Consequently, the chain dotted extrapolated curve can only serve as an indication of the heat transfer data. Nevertheless, it is considered that a pessimistic value will be so obtained, probably resulting in an oversized tube bundle.

The poor quality of this data excludes the possibility of calculating the tube bundle as a sequence of short sections with different temperatures.

From Fig. A.2, when  $Re = 77.3$

$$St. Pr^{2/3} = 0.031$$

$$\text{at } \bar{T} = 847^\circ\text{C}, Pr = 0.74$$

$$\therefore St = 0.0385$$

$$Nn \quad St = \frac{hA_{min}}{G C_p}$$

$$\therefore h_s = \frac{0.0385 \times 5.75 \times 1.242}{127.4}$$

$$= 2.16 \times 10^{-3} \text{ cal/sec cm}^2 \text{ }^\circ\text{C}$$

### A3.2 Tube side

The tube bundle contains 18 tubes, so that each carries a helium flow of

$$\frac{5.75}{18} = 0.319 \text{ gm/sec}$$

This will be at an approximate pressure of 1 atm and have a maximum temperature of  $1165^\circ\text{C}$ .

$$\text{For He, } \rho_{1165^\circ\text{C}} = \frac{1.785 \times 10^{-4} \times 273}{1438} \text{ gm/cm}^3$$

So the maximum velocity in the pipes will be

$$V_{max} = \frac{0.319 \times 4 \times 1438}{1.785 \times 10^{-4} \times \pi \times (1.26)^2 \times 273} \text{ cm/sec}$$

$$= 75.3 \text{ M/sec}$$

The velocity of sound in He at 1 atm and  $1438^\circ\text{K}$  is

$$C = \sqrt{\frac{\gamma P}{\rho}}$$

$$\gamma = 1.63$$

$$P = \frac{14.7}{1.45 \times 10^{-5}} \text{ dynes/cm}^2$$

$$\rho = \frac{1.785 \times 10^{-4} \times 273}{1438} \text{ gm/cm}^3$$

$$C = \frac{1}{100} \sqrt{\frac{1.63 \times 14.7 \times 10^5 \times 10^4 \times 1438}{1.45 \times 1.785 \times 273}} \text{ m/sec}$$

$$C = 2.2 \times 10^3 \text{ m/sec}$$

Thus Mach No. in tubes =  $M_{\max} = \frac{75.3}{2.2 \times 10^3} = 0.0342$  it is therefore possible to neglect the effect of  $M$ .

Reynolds No. for a circular pipe is

$$Re = \frac{4 G}{\pi D \mu}$$

where  $G = 0.319 \text{ gm/sec}$

$$D = 1.26 \text{ cm}$$

$$\bar{\mu} = 0.042 \times 10^{-2} \text{ poise}$$

$$\therefore \bar{Re} = \frac{4 \times 0.319 \times 10^2}{\pi \times 1.26 \times 0.042}$$

$$\bar{Re} = 768$$

Thus the helium flow lies well within the laminar region.

For the laminar flow of fluids in straight smooth pipes, Hausen<sup>3</sup> recommends the relation

$$Nu = \left[ 3.65 + \frac{0.0668 \frac{Pe D}{L}}{1 + 0.045 \left\{ \frac{Pe D}{L} \right\}^{\frac{2}{3}}} \right] \left\{ \frac{\mu_{f1}}{\mu_w} \right\}^{0.14}$$

For laminar flow in coiled pipes, no data are known. It is therefore proposed to use the Hausen form, modified by the Jeschke factor to include in some degree, the effect of the tube coiling. It should be noted that the Jeschke factor has been demonstrated only for the turbulent region.

Then  $Nu_T = Nu \left[ 1 + 3.5 \frac{D}{D_H} \right]$

Previous calculations indicate that  $L$  has a value of about 11 feet, and  $\bar{T}_w \sim 994^\circ K$

Hence

$$Pe = Re.Pr.$$

$$\overline{Pr}_t = 0.76 \quad (\overline{T}_t = 593^\circ\text{C})$$

$$Re_t = 768$$

$$\therefore Re = 768 \times 0.76 = 583$$

$$D = 1.26 \text{ cm}$$

$$L \sim 11 \text{ ft.} = 335 \text{ cm}$$

$$\mu_{f1} = 0.042 \times 10^{-2} \text{ poise, } \overline{T}_{f1} = 593^\circ\text{C}$$

$$\mu_w = 0.0443 \times 10^{-2} \text{ poise, } \overline{T}_w = 721^\circ\text{C}$$

$$\overline{D}_H = 20.8 \text{ cm}$$

$$\begin{aligned} \therefore Nu &= \left[ 3.65 + \frac{0.0668 \times 583 \times 1.26/335}{1 + 0.045 \left\{ \frac{583 \times 1.26}{335} \right\}^{2/3}} \right] \left\{ \frac{0.042}{0.044} \right\}^{0.14} \\ &= \left[ 3.65 + 0.136 \right] \frac{1}{1.0067} \end{aligned}$$

$$Nu = 3.76$$

$$\therefore Nu_T = 3.76 \left[ 1 + \frac{3.5 \times 1.26}{20.8} \right] = 4.58$$

$$Nu = h D_e/K$$

$$\therefore \overline{h}_T = \frac{4.58 \times 6.85 \times 10^{-4}}{1.26}$$

$$\overline{h}_T = 2.49 \times 10^{-3} \text{ cal/sec cm}^2 \text{ } ^\circ\text{C}$$

### A3.3 Heat transfer coefficient

The overall heat transfer coefficient  $U$  is given by

$$\frac{1}{U} = \frac{1}{\overline{h}_s} + \frac{1}{\overline{h}_t} + \frac{t}{K_w}$$

where  $t$  is the tube wall thickness, and  $K_w$  is the thermal conductivity of Nimonic 75.

$$\overline{h}_s = 2.16 \times 10^{-3} \text{ cal/sec cm}^2 \text{ } ^\circ\text{C}$$

$$\overline{h}_t = 2.49 \times 10^{-3} \text{ cal/sec cm}^2 \text{ } ^\circ\text{C}$$

$$t = 0.234 \text{ cm}$$

$$K_w = 0.0622 \text{ cal/sec cm}^2 \text{ } ^\circ\text{C}$$

$$\therefore \frac{1}{U} = \frac{1}{2.16 \times 10^{-3}} + \frac{1}{2.49 \times 10^{-3}} + \frac{0.234}{0.0622}$$

$$= 463 + 402 + 3.76$$

$$\frac{1}{U} = 869 \text{ sec cm}^2 \text{ } ^\circ\text{C/cal}$$

Also,  $\frac{1}{U} = \frac{S \cdot T}{Q}$

S = total heat transfer area

$$= 18 \times \pi \times 1.49 \text{ L cm}^2$$

T =  $252^\circ\text{C}$  (constant in recuperator)

Q = Heat exchanger power

$$= 5.75 \times 1.242 \times 1140 \text{ cal/sec}$$

$$\therefore \frac{18 \times \pi \times 1.49 \text{ L} \times 252}{5.75 \times 1.242 \times 1140} = 869$$

$$\therefore L = 333 \text{ cm}$$

$$L = 10.9 \text{ ft}$$

Considering the inner coil, the length of each pipe is

$$L = m \sqrt{(\pi D_n)^2 + n^2 p^2}$$

$$D_n = 12.96 \text{ cm}$$

$$n = 3$$

$$p = 2.16 \text{ cm}$$

m = no. of turns per pipe in layer

$$m = 333 / \sqrt{(\pi \times 12.96)^2 + 9 \times 2.16^2}$$

$$m = 8.05$$

$\therefore$  Core bundle length  $y = m \cdot n \cdot p$

$$= 8.05 \times 3 \times 1.16 \text{ cm}$$

$$y = 52 \text{ cm}$$

Considering the highly inaccurate data used in this calculation, it is recommended that the coil bundle should be built at least 25% longer.



Thus the coil will be at least 65 cm long.

#### A4. PRESSURE LOSSES

##### A4.1 Shell side

From Kays and London<sup>2</sup>, the total shell side pressure losses, including the inlet, outlet and case friction effects are:

$$\Delta P_s = \frac{G^2}{2 A_{\min}^2 \rho_1} \left\{ \left[ 1 + \left( \frac{A_{\min}}{A_f} \right)^2 \right] \left[ \frac{\rho_1}{\rho_2} - 1 \right] + 4 f \frac{y}{D_e} \frac{\rho_1}{\bar{\rho}} \right\}$$

$$G = 5.75 \text{ gm/sec}$$

$$A_{\min} = 127.4 \text{ cm}^2$$

$$\rho_1 = 1.785 \times 10^{-4} \times \frac{273}{1690} = 2.88 \times 10^{-5} \text{ gm/cm}^2$$

$$A_{fr} = 533 \text{ cm}^2$$

$$\rho_2 = 1.785 \times 10^{-4} \times \frac{273}{550} = 9.83 \times 10^{-5} \text{ gm/cm}^2$$

$$f \sim 0.045 \text{ (see Fig. A.2)}$$

$$y = 65 \text{ cm}$$

$$D_e = 0.828 \text{ cm}$$

$$\bar{\rho} = 5.85 \times 10^{-5} \text{ gm/cm}^2$$

NB. All densities are calculated for 1 atm

$$\Delta P_s = 220 \text{ dynes/cm}^2$$

$$\therefore \Delta P_s = 0.0032 \text{ psi}$$

##### A4.2 Tube side

Pressure loss in a tube with inlet fluid temperature  $T_1 K$  and outlet  $T_2 K$ , with uniform heat flux is given by

$$\Delta P = \frac{1}{\rho_t} \left( \frac{G}{A_t} \right)^2 \left[ \frac{2 f L}{D} + \frac{T_2 - T_1}{\bar{T}} \right]$$

For streamline flow, in curved pipes, the normal friction factor derived for straight pipes must be increased by a factor developed by Drew (in McAdams<sup>4</sup>).

The average of this factor, weighted according to the number of pipes per layer = 1.84

$$f = 1.84 \times 16/Re$$

$$Re_t = 768$$

$$\therefore f = 1.84 \times 16/768$$

$$f = 0.0383$$

$$G = 0.319 \text{ gm/sec}$$

$$\bar{\rho}_t = 1.785 \times 10^{-4} \times \frac{273}{866} = 5.62 \times 10^{-5} \text{ gm/cm}^3$$

$$A_t = 1.245 \text{ cm}^2$$

$$L = 333 \text{ cm}$$

$$\left. \begin{array}{l} T_2 = 1438^\circ K \\ T_1 = 298^\circ K \end{array} \right\} \bar{T} = 866^\circ K$$

$$\therefore \Delta P = 2.52 \times 10^4 \text{ dynes/cm}^2$$

$$\Delta P_t = 0.365 \text{ psi}$$

#### A5 PHYSICAL PROPERTIES OF He

$$C_p = 1.242 \text{ cal/gm}^\circ C$$

$$\gamma = 1.63$$

$$\rho = 1.785 \times 10^{-4} \text{ gm/cm}^3 \text{ (273}^\circ K \text{ and 1 Atmos)}$$

$$\mu = \text{McAdams}^4 \text{ (pp 468-469 Table A-19 and Fig. A-6)}$$

$$K = \text{Eckert}^5 \text{ (up to 675}^\circ C \text{)}.$$

#### REFERENCES

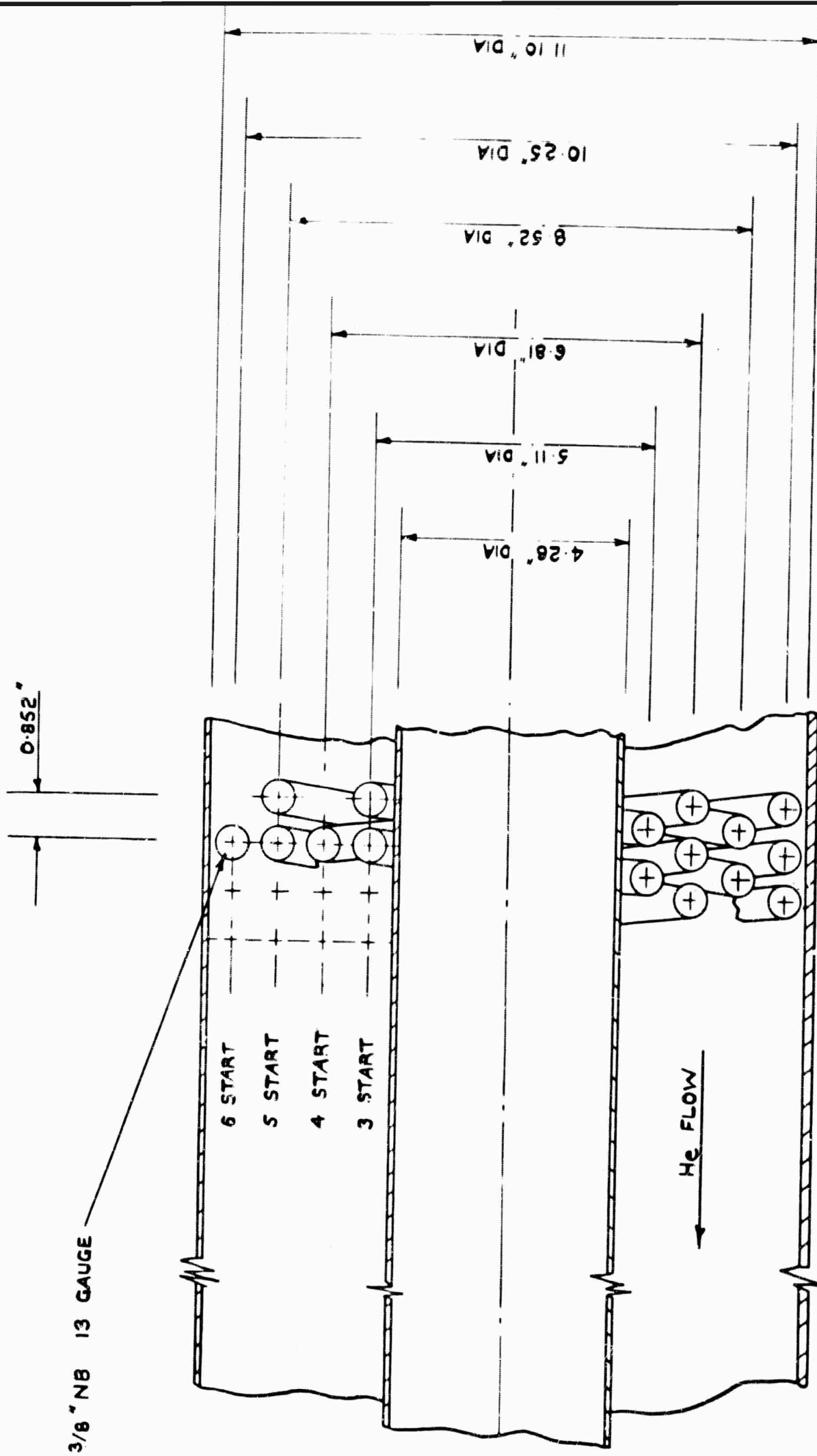
- 1 SMITH, E.M. The geometry of helical tube multi-start coil heat exchangers. (Published later at Leopoldshafen 29) January 1962
- 2 KAYS, W.M. and LONDON, A.L. Compact heat exchangers, Fig. 54, p94. 1958
- 3 HAUSEN, H. Wärmeübertragung im Gegenstrom, Gleichstrom und Kreuzstrom. Springer-Verlag
- 4 McADAMS, W.H. Heat transmission, 3rd Edition, Fig. 6-6, p151. McGraw-Hill 1954
- 5 ECKERT, E.R.G. Introduction to the transfer of heat and mass: with an appendix on property values by Robert M. Drake, 1950

# NOMENCLATURE (APPENDIX)

$A_{\min}$	minimum flow area	<u>Greek symbols</u>	
$A_{fr}$	shell side frictional area	$\gamma$	ratio of specific heats
$C$	velocity of sound	$\Delta P$	pressure differences
$C_p$	spec heat at constant press	$\Delta T$	temperature differences
$D_e$	equivalent diameter	$\rho$	density
$D_H$	helix diameter	$\theta$	angle of tube to gas flow direction
$D_N$	diameter of $n^{\text{th}}$ layer	$\mu$	viscosity
$D_o$	shell outer diameter (inside)	$\mu_w$	viscosity at wall temperature
$D_i$	shell inner diameter	$\mu_{fl}$	viscosity at mean bulk temp. of fluid
$d$	tube outside diameter		
$f$	fanning friction factor		
$G$	mass flow		
$h$	heat transfer coefficient		
$K$	thermal conductivity		
$L$	tube length		
$m$	no. of pipes in layer		
$M$	Mach number		
$n$	no. of layers		
$Nu$	Nusselt numbers		
$P_t$	transverse pitching of tubes		
$P_x$	axial pitching of tubes		
$P$	pressure		
$Pr$	Prandtl number		
$Pe$	Peclet number		
$Q$	heat exchanger power		
$Re$	Reynolds number		
$St$	Stanton number		
$S$	total heat transfer area		
$T$	temperature		
$t$	tube wall thickness		
$U$	overall heat transfer coefficient		
$V$	velocity		
$y$	bundle length		

## Suffixes

$S$	shell side
$t$	tube side
$w$	wall
$-$	mean value



TUBE BUNDLE GEOMETRY

FIG A-1

# HEAT TRANSFER AND FRICTION FACTOR DATA

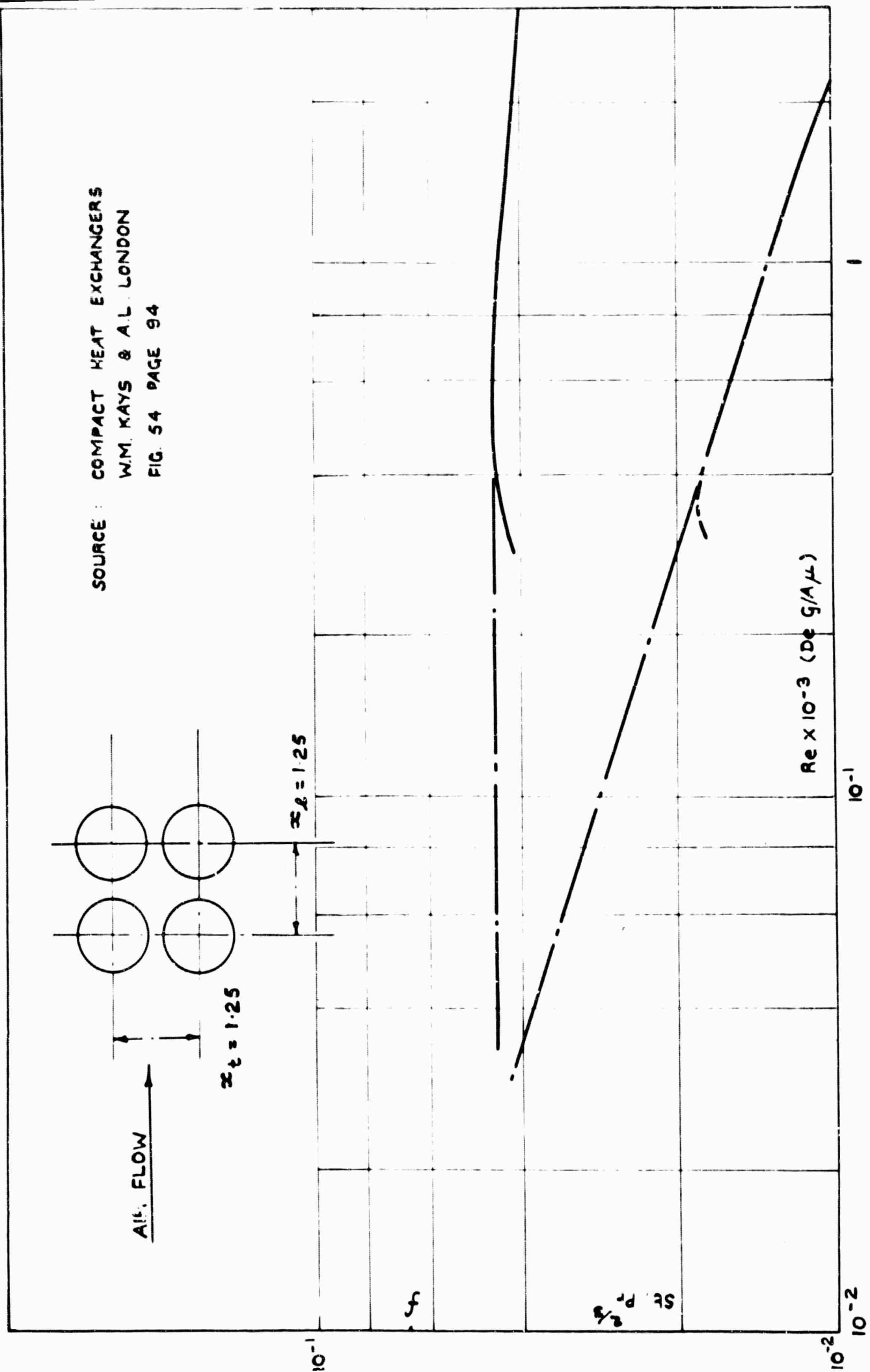


FIG A-2

EXTERNAL DISTRIBUTION

Director, Advanced Research Projects Agency The Pentagon Washington, D.C. 20301	(2)	Defense Documentation Center Camerson Street Alexandria, Virginia 22314	(20)
Office of Naval Research Power Branch (Code 429) Washington, D.C. 20360 Attn: John A. Satkowski	(6)	U.S. Army Research & Development Laboratory Fort Belvoir, Virginia Attn: Frank Shields (ERD-EP)	(1)
Commanding Officer Office of Naval Research Branch Office Box 39 Navy / 100 Fleet Post Office New York, New York	(1)	NASA, Lewis Research Center 21,000 Brookpark Road Cleveland 35, Ohio Attn: Wolfgang Moeckel Dr. B. Lubarsky Dr. M. Kosmahl	(1) (1) (1)
Commander John E. Raymond Office of Naval Research Keysign House London W.1.	(1)	U.S. Atomic Energy Commission Division of Reactor Development Direct Energy Conversion Section, RD: AED Germantown, Maryland Attn: Dr. R. Grossman (E301)	(1) (1)
Dr. J.H. Huth Department of the Navy Bureau of Ships, Washington 25, D.C.		Mr. T. Brogan AVCO - Everett Research Laboratory 2385 Revere Beach Parkway Everett, Massachusetts	(1)
U.S. Naval Research Laboratory Washington 25, D.C. Attn: Technical Information Division	(6)		
Wright-Patterson Air Force Base Aeronautical Systems Division Ohio Attn: Lt. Robert Barthelemy (AFAPL)	(1)	Dr. J. Cole Department of Aeronautics California Institute of Technology Pasadena, California	(1)
Air Force Office of Scientific Research Washington 25, D.C. Attn: Dr. Milton M. Slawsky	(1)	Mr. Arthur Sherman General Electric - Valley Forge Valley Forge Space Technical Center Philadelphia 1, Pennsylvania	(1)
U.S. Naval Ordnance Test Station Propulsion Applied Research Group China Lake, California Attn: Leroy J. Krzycki (Code 4506)	(1)	Dr. W.D. Jackson Electrical Engineering Department Massachusetts Institute of Technology Cambridge 39, Massachusetts	(1)
Rome Development Center Rome, New York Attn: Mr. Frank J. Mellura	(1)	Dr. Vernon H. Blackman MHD Research Incorporated 1535 Monrovia Street Newport Beach, California	(1)
U.S. Naval Ordnance Laboratory NA Division White Oak, Maryland Attn: Wallace Knutsen Library	(1) (2)		

Dr. Robert Eustis  
Thermosciences Division  
Stanford University  
Stanford, California

(1)

Dr. Richard Schamberg  
Rand Corporation  
1700 S. Main Street  
Santa Monica, California

(1)

Dr. Sam Naiditch  
Unified Science Associates  
826 Arroyo Parkway  
Pasadena, California

(1)

Dr. W.S. Emmerich  
Westinghouse Research Laboratories  
Baulah Road, Churchill Borough  
Pittsburgh 35, Pennsylvania

(1)

Dr. R.T. Schneider  
Allison Division  
General Motors Corporation  
Indianapolis, Indiana

(1)

Dr. D.G. Elliott  
Jet Propulsion Laboratory  
Pasadena, California

(1)